ADVANCED INVERTER CONTROL FOR UNINTERRUPTIBLE POWER SUPPLIES AND GRID-CONNECTED RENEWABLE ENERGY APPLICATIONS

By

Shuai Jiang

A DISSERTATION

Submitted to
Michigan State University
in partial fulfillment of the requirements
for the degree of

Electrical Engineering – Doctor of Philosophy

2013

ABSTRACT

ADVANCED INVERTER CONTROL FOR UNINTERRUPTIBLE POWER SUPPLIES AND GRID-CONNECTED RENEWABLE ENERGY APPLICATIONS

By

Shuai Jiang

The advancement of digital signal processors (DSPs) and programmable logic devices in modern power electronics systems offer great control flexibility and capability, providing attractive features particularly for applications in which complex control tasks are involved. This dissertation investigates some DSP based advanced control algorithms for pulse-width modulation (PWM) inverter applications, in particular, voltage regulated inverters connected with AC loads and current regulated inverters connected with utility grids.

Uninterruptible power supply (UPS) is a typical example of voltage regulated inverter applications. It is widely used to supply high quality, continuous and disturbance-free AC power to critical loads such as medical equipments, computers and communication systems. A good UPS system requires not only excellent steady state performances in terms of voltage regulation and total harmonic distortions (THD) regardless of unknown load disturbances but also a fast transient response during load step change.

In this dissertation, a three-phase four-wire AC-DC-AC double conversion UPS system is first studied. Multi-loop control strategies are designed to regulate the system input currents, DC voltages, and output voltages. Next, study will deep dive into a DC-AC three-phase UPS inverter. A high performance repetitive controller (RC) for the voltage regulated three-phase inverter is proposed. The proposed control algorithm can eliminate all the periodic distortions and guarantees a high quality sinusoidal output voltage under unknown and severely distorted loads. A novel 4th-order linear phase infinite-impulse-response (IIR) filter is first used in the RC such that harmonic distortions up to the 19th order are rejected. In order to achieve fast response

during step load transient while still maintaining the low THD feature, a modified synchronousframe approach with significantly reduced delay is later proposed and investigated.

Grid-connected inverters utilizing renewable energy sources (e.g., photovoltaic, wind, fuel cell, etc.) are growing rapidly in recent years along with the constantly growing global demand for electricity. A grid-connected inverter injects a synchronously regulated sinusoidal current to the utility grid with required low THD and high power factor. Using an LCL filter in such a system has been recognized as a small size low cost solution due to its -60dB/dec high frequency attenuation. In this dissertation, a high-resonance-frequency LCL filter with minimal size and cost requirement is designed. A proportional plus repetitive control hybrid strategy is then proposed to achieve very low THD current regulation and high power factor.

Although utility grid is often modeled as an infinite AC voltage source in inverter current control, it can introduce way more complicated resonance issues particularly when long transmission cables are used between the inverter and the main grid. A real example of an HVAC offshore wind farm system with long submarine cables is then investigated and emulated by a scaled-down 120Vac single-phase system. A systematic analysis is carried out and the key passive component parameters that cause high frequency resonances are identified. A notch filter based active damping control is proposed and implemented in the inverter.

When a grid-connected inverter is sourced from photovoltaic (PV) panels, a front-end isolated DC-DC converter is usually incorporated and dedicated control must be employed based on the converter dynamics to achieve both maximum power point tracking (MPPT) and coordination with the 2nd-stage inverter control. A high performance system-level control scheme is designed for the proposed boost-half-bridge converter-inverter system in the PV application.

Dedicated to my beloved wife, Yiwen Dong and our son, Ray Yu Jiang

ACKNOWLEDGMENTS

First of all, I would like to express my sincere thanks to my advisor Dr. Fang Zheng Peng. I am so grateful for his mentoring in the discipline of power electronics and helping me grow from a rookie to a professional researcher. Dr. Peng's rigorous attitude toward academic research, enthusiasms and deep insight in challenging problems set a great example for me to learn from and will continuously guide me in my entire career.

I would like to thank Dr. Joydeep Mitra, Dr. Bingsen Wang and Dr. Guoming Zhu for serving as my Ph. D committee. I've gained so much learning from their wonderful classes and valuable advisories in my dissertation research.

I would also like to thank all my colleagues in the Power Electronics and Motor Drives Laboratory and all my other friends at MSU.

I appreciated the numerous help and inspiring technical suggestions from Dr. Dong Cao, Dr. Wei Qian, Dr. Qin Lei, Dr. Honnyong Cha, Dr. Craig Rogers, Dr. Baoming Ge, Dr. Shao Zhang and Ms. Xi Lu.

I am grateful to Dr. Yuan Li, Dr. Shuitao Yang, Dr. Dan Wang and Dr. Junming Zhang for their insightful suggestions and inspiring technical discussions with me during their visit at MSU.

At the end, I would like to give my special thanks to my wife Yiwen Dong for her selfless love, unconditional support, and constant encouragement, and to my parents Mr. Sanhu Jiang and Ms. Xuequn Yang for their love and care.

TABLE OF CONTENTS

LIST OF TABLES	ix
LIST OF FIGURES	X
CHAPTER 1. Introduction	1
1.1. Background	
1.2. Uninterruptible Power Supplies	
1.3. Renewable Energy Systems Interfaced with Utility Grid	
1.3.1. Grid-Connected Inverter with LCL Filter	
1.3.2. Offshore Wind Farm Inverter Incorporating Long Transmission Cable	
1.3.3. Photovoltaic Inverter System	
1.4. Scope of the Dissertation	
CHAPTER 2. Multi-Loop Control of Three-Phase Four-Wire Online Double Conv	
UPS System	
2.1. System Descriptions and Ratings	
2.2. Multi-Loop Controller Design	
2.2.1. PWM Rectifier Control	
2.2.2. Inverter Control	
2.3. Experimental Results	
2.4. Summary	23
CHAPTER 3. Low THD Repetitive Control of Three-Phase UPS Inverter	24
3.1. Introduction	
3.2. Overview of the Repetitive Control UPS System	25
3.2.1. Repetitive Control Principle	25
3.2.2. Stability Analysis	
3.2.3. Dynamic Response Analysis	30
3.2.4. Practical Design Considerations	31
3.3. Repetitive Controller Design	32
3.3.1. Active Damping Compensator	32
3.3.2. Parameters Selection of the Repetitive Controller	34
3.3.3. Repetitive Control Using Different Low Pass Filters	40
3.4. Experimental Validations	
3.5. Summary	
CHAPTER 4. Synchronous-Frame Repetitive Control with Fast Dynamic Response	49
4.1. Introduction	49
4.2. Repetitive Controller in Synchronous Rotating Frames	51
4.3. Controller Magnitude-Frequency Response	
4.4. Simulation and Experimental Results	57
4.4.1. Compensation of Unbalanced Nonlinear load	

4.4.2. Compensation of Balanced load	61
4.4.3. Transient Responses under Load Step Change	
4.5. Summary	
CHAPTER 5. Design and Control of Grid-Connected Inverter in Renewable	Energy
Applications	
5.1. Introduction	68
5.2. LCL Filter Design	70
5.2.1. Design Procedure of LCL Filter	71
5.2.2. Stability Analysis of LCL Filter Based Grid-Connected Inverter	73
5.3. Current Controller Design	
5.3.1. Inverter Transfer Function Using a Low Pass Filter	
5.3.2. Proportional + Repetitive Current Control Scheme	79
5.4. Experimental Results	86
5.5. Summary	92
CHAPTER 6. Control of an Offshore Wind Farm Grid-Connected Inverter System	
6.1. Introduction	
6.2. Equivalent Model of Offshore Wind Farm Transmission System	
6.3. Frequency Domain Analysis and Controller Design	
6.3.1. Modeling of Long Transmission Cable	
6.3.2. Resonances in the Offshore Wind Farm System	
6.3.3. Notch Filter Based Active Damping Control	
6.3.4. Cable Parameters Uncertainty and Resonance Frequency Auto-Detection	
6.4. Simulation and Experimental Results	
6.5. Summary	129
CHAPTED 7 Control of a Doort Half Dridge Dhatavalta's Micro Inventor System	121
CHAPTER 7. Control of a Boost-Half-Bridge Photovoltaic Micro Inverter System 7.1. Introduction	
7.2. Boost-Half-Bridge Photovoltaic Micro Inverter	
7.2.2. Operation Principle of the Boost-Half-Bridge Converter	
7.3. System Control Description of the PV Micro Inverter	
7.4.1 Converter Peremeters and Voltage Control	
7.4.1. Converter Parameters and Voltage Control	
7.4.2. Analysis of the Converter Dynamics	
7.5.1. MPPT with Ramp-Changed Voltage Command	
7.5.2. Variable Step-Size WFFT Algorithm	
7.6.1. Verification of the Boost-Half-Bridge DC-DC Converter	
7.6.2. Verification of the Grid Current Dynamic Response	
7.7. Summary	130
CHAPTER 8. Conclusion and Recommendation	158
§ 1. Conclusion	

8.2. Recommendation for Future Work	160
BIBLIOGRAPHY	163

LIST OF TABLES

Table 2.1. Parameters of the 3-phase 4-wire double conversion UPS system	12
Table 3.1. System Parameters	33
Table 3.2. Synthesis of $Q(z)z^{k_2}$	37
Table 4.1 Harmonic Sequences In Unbalanced Three-Phase AC Systems	52
Table 5.1. Full-Bridge Inverter Parameters	77
Table 6.1. Parameters of the offshore wind farm system	99
Table 6.2. Parameters of the emulator system	99
Table 7.1. Boost-half-Bridge Converter Parameters.	139

LIST OF FIGURES

Figure 2.1. Typical configuration of an online double conversion UPS system	11
Figure 2.2. AC-DC-AC topology of three-phase four-wire double conversion UPS system 1	12
Figure 2.3. Three-phase four-wire PWM rectifier	13
Figure 2.4. Control block diagram of the PWM rectifier	14
Figure 2.5. PLL routine executed in each sampling cycle (switching cycle)	15
Figure 2.6. Three-phase four-wire inverter	۱7
Figure 2.7. Control block diagram of the inverter.	۱7
Figure 2.8. Bode plot of $G_{inv}(s)$ before and after voltage differential feedback compensation. 1	18
Figure 2.9. Experiment set-up of the 100 kW UPS system	20
Figure 2.10. Grid voltage and current during load turn- on (linear load)	20
Figure 2.11. Output voltage and current during load (linear) step-on	21
Figure 2.12. Output voltage and current during load (linear) step-off	21
Figure 2.13. DC link capacitor voltages and load current during load (linear) step-on	22
Figure 2.14. Grid current, output voltage and output current with non-linear load	22
Figure 3.1. Main circuit of a three-phase UPS inverter. 2	24
Figure 3.2. Block diagram of a typical discrete-time repetitive controlled inverter system 2	26
Figure 3.3. Vector diagrams for stability analysis.	28
Figure 3.4. Phase lead compensation with different k_1	35
Figure 3.5. Bode plots of $Q_e(z)$, $Q_a(z)$, and $Q(z)$	38
Figure 3.6. Locus of vector $H(e^{j\omega T})$ with different K_r . (a) $K_r = 1$. (b) $K_r = 1.8$	39
Figure 3.7. Bode plot of $O(z)$ based on the 4th-order FIR filter and the 4th-order IIR filter 4	11

Figure 3.8. Comparison of system loop gain when using the 4th-order FIR and the 4th-order IIR.
Figure 3.9. Digital implementation structure of the proposed repetitive controller
Figure 3.10. Comparison between the FIR filter based RC and the proposed IIR filter based RC (with 6.6 kW pure rectifier load). (a) Steady state outputs when using the 4th order FIR filter. (b) Harmonic spectrum of the inverter output voltage in (a). (c) Steady state outputs when using the proposed 4th order IIR filter. (d) Harmonic spectrum of the inverter output voltage in (c) 44
Figure 3.11. Steady state outputs with open loop control (with 6.6 kW pure rectifier load) 46
Figure 3.12. Steady state outputs with proposed repetitive control (10 kW pure rectifier load) 46
Figure 3.13. Load step change from 2.8 kW to 10 kW (pure rectifier load)
Figure 3.14. Load step change from 7.5 kW to 15 kW (with line inductor connected rectifier load)
Figure 4.1. System configuration of the three-phase UPS inverter
Figure 4.2. Proposed synchronous-frame repetitive control scheme. 54
Figure 4.3. Frequency response of $ R(z) $ 56
Figure 4.4. Simulated steady state responses under unbalanced nonlinear load when the RC is implemented in (a) Frame #1 only, (b) Frame #1 & Frame #2, and (c) all the three synchronous frames, respectively.
Figure 4.5. Experimental results with unbalanced nonlinear load when the RC is implemented in (a) Frame #1, (b) all the three synchronous frames, (c) harmonic spectrum of the voltage in (b).
Figure 4.6. Experimental results with a balanced nonlinear load using the proposed synchronous-frame RC. (a) Steady state responses. (b) Harmonic spectrum of the voltage in (a)
Figure 4.7. Experimental results with a balanced resistive load using the proposed synchronous-frame RC. (a) Steady state responses. (b) Harmonic spectrum of the voltage in (a)
Figure 4.8. Simulated transient responses for comparison of different repetitive control schemes. A step change is performed on the three-phase bridge rectifier load (2 kW-12 kW). (a) Transient responses when the conventional RC structure is adopted. (b) Transient responses of the proposed synchronous-frame RC
Figure 4.9. Experimental results of transient responses for comparison of different repetitive control schemes. A step change is performed on the three-phase bridge rectifier load (2.6 kW-9.4 kW). (a) Transient responses when the conventional RC structure is adopted. (b) Transient responses of the proposed synchronous-frame RC

Figure 4.10. Transient responses of the proposed synchronous-frame RC. A step change is performed on the balanced resistive load (0-18 kW). (a) Simulation results. (b) Experimenta results.
Figure 5.1. Typical configuration of single-phase grid-connected inverter with LCL filter 69
Figure 5.2. Open-loop Bode plot for different LCL-filter resonance frequencies with grid current feedback. (a) $f_r = 0.47 f_N$. (b) $f_r = 0.94 f_N$
Figure 5.3. Open-loop Bode plot for different LCL-filter resonance frequencies with inverted current feedback. (a) $f_r = 0.47 f_N$. (b) $f_r = 0.94 f_N$
Figure 5.4. Block diagram of the proposed plug-in repetitive controller
Figure 5.5. Root locus of $G_{inv}(z)$. (a) $L_{o1} = L_{o2} = 8.5mH$, (b) $L_{o1} = L_{o2} = 6mH$
Figure 5.6. Bode plot of $K_{p2}G_{inv}(z)$ ($K_{p2} = 50$)
Figure 5.7. Locus of the vector $H(e^{j\omega T_{SW}2})$. (a) $K_r = 0.3$, k_1 is varying; (b) $k_1 = 4$, K_r is varying.
Figure 5.8. Frequency response of $\left C_{prc}(z)G_{inv}(z)\right $
Figure 5.9. (a) Steady state grid voltage and current at heavy load when using the proposed repetitive current controller. (b) Harmonic spectrum in (a). (c) Steady state grid voltage and current at light load when using the proposed repetitive current controller. (d) Harmonic spectrum in (c).
Figure 5.10. (a) Steady state grid voltage and current at heavy load when using the conventional proportional + resonant current controller. (b) Harmonic spectrum in (a). (c) Steady state grid voltage and current at light load when using the conventional proportional + resonant current controller. (d) Harmonic spectrum in (c).
Figure 5.11. Transient responses under load step change. (a) Grid current step change (0.33 A to 1 A). (b) Grid current step change (1 A to 0.33 A)
Figure 6.1. Configuration of a typical HVAC grid-connected offshore wind farm
Figure 6.2. Equivalent single-phase circuit of the HVAC offshore wind farm in per unit scale 96
Figure 6.3. Proposed 120Vac single-phase offshore wind farm emulator system
Figure 6.4. One-phase of a HVAC cable
Figure 6.5 Impedance characteristic of the transmission cable

Figure 6.6. Frequency responses of the lumped LC network input admittance)2
Figure 6.7. Bode plot of $P_{inv}(s)$ under different line impedances)4
Figure 6.8. Bode plot of $P_{inv}(s)$ under different filter capacitances)5
Figure 6.9. Block diagram of proposed current control strategy.)7
Figure 6.10. Bode plots of the notch filter and the proportional resonant (PR) controller 10)9
Figure 6.11. Bode plot of $G_c(s)P_{inv}(s)$ under parameter variations	11
Figure 6.12. Bode plot of $G_c(s)P_{inv}(s)$ with +-20% tolerance of cable parameters	13
Figure 6.13. Bode plot of $G_c(s)P_{inv}(s)$ with +-30% tolerance of cable parameters	15
Figure 6.14. Auto damping control scheme.	17
Figure 6.15. 120Vac emulator system experimental setup	19
Figure 6.16. Simulation waveforms of the cable current and the filter capacitor voltage with the PR controller only	
Figure 6.17. Simulation waveforms of the cable current and the filter capacitor voltage with or notch filter with center frequency at 1.2 kHz.	
Figure 6.18. Simulation waveforms of the cable current and the filter capacitor voltage with the proposed controller	
Figure 6.19. Steady state waveforms and current spectrum when $C_f = 0$. Only one P + resonant controller is implemented.	
Figure 6.20. Steady state waveforms and current spectrum when $C_f = 20uF$ (11.3%). Only or	ne
P + resonant controller is implemented	24
Figure 6.21. Steady state waveforms and current spectrum when $C_f = 20 uF$ (11.3%). One P	
resonant controller and one notch filter are implemented	24
Figure 6.22. Steady state waveforms and current spectrum when $C_f = 20uF$ (11.3%). One P resonant controller and two notch filters are implemented	
Figure 6.23. Dynamic response of the output current with the proposed control implemented. step change from 4A to 8A is applied to the current command	

Figure 7.14. Prototype of the boost-half-bridge PV micro inverter	. 156
Figure 7.13. MPPT of the PV micro inverter system at the steady state. (a) PV voltage current and PV power (solar irradiance: 900 W/m ² @ 50°C) (b) MPPT trajectories (P-V a V curves).	nd I-
Figure 7.12. MPPT of the PV micro inverter system under solar irradiance change. (a) Input output waveforms under solar irradiance change (partial shading to 880 W/m ² @ 50°C) Zoomed-in PV voltage, PV current and PV power in (a). (c) MPPT trajectories (P-V and curves).). (b) l I-V
Figure 7.11. Transient responses of the micro inverter system under solar irradiance ch $(840 \text{ W/m}^2 \text{ to partial shading})$.	
Figure 7.10. Efficiency chart of the boost-half-bridge DC-DC converter.	. 151
Figure 7.9. Transformer voltage and current responses of the boost-half-bridge converter $P_{pv} = 190 \text{ W}$, $v_{pv} = 36.8 \text{ V}$. (b) $P_{pv} = 74 \text{ W}$, $v_{pv} = 44.5 \text{ V}$	
Figure 7.8. Flow chart of the variable step size MPPT	. 148
Figure 7.7. (a) I-V, P-V curves. (b) PV operation zone division based on dP_{pv}/dv_{pv}	. 146
Figure 7.6. Dynamic responses corresponding to the different voltage command general methods in the MPPT. (a) Using a step-changed voltage command. (b) Using a ramp-characteristic command.	nged
Figure 7.5. (a) Half-bridge converter part. (b) Equivalent circuit seen from the LVS DC link.	141
Figure 7.4. Block diagram of the PV voltage regulator	. 140
Figure 7.3. Architecture of the proposed PV micro inverter system control	. 138
Figure 7.2. Idealized transformer voltage and current.	. 136
Figure 7.1. Topology of the boost-half-bridge PV micro inverter	. 134
Figure 6.26. Simulated auto damping waveforms of ifb magnitude, iout magnitude and open gain (iout magnitude over ifb magnitude).	
Figure 6.25. Simulated auto damping waveforms of ifb, iout before and after the band filters.	
Figure 6.24. Dynamic response of the output current with the proposed control implemente step change from 8A to 4A is applied to the current command	

Chapter 1. Introduction

1.1. Background

Modern power electronics applications deal with a broad range of power processing and control from milliwatt level of power management on chip to megawatt level of utility power system. While analog control is still prevalent at lower power level (less than hundreds of watts) with switching frequencies higher than hundreds of kilohertz, the advancement of digital signal processors (DSPs) and programmable logic devices offers great control flexibility and capability, providing attractive features particularly for applications in which complex control tasks are involved. This dissertation investigates some DSP based advanced control algorithms for such applications, in particular, uninterruptible power supplies (UPS) and grid-connected renewable energy systems.

1.2. Uninterruptible Power Supplies

Uninterruptable power supplies (UPS) are widely used to supply high quality, continuous and disturbance-free AC power to critical loads such as medical equipments, computers and communication systems. A good UPS system requires not only excellent steady state performances in terms of voltage regulation and total harmonic distortions (THD) regardless of unknown load disturbances but also a fast transient response during load step change.

Some high performance feedback control techniques such as multi-loop state feedback control [1]-[7], dead-beat control [8], and predictive control [9], [10] have been proposed and investigated. High quality output voltage and fast dynamic response have been demonstrated with these methods. However, the following disadvantages limit the benefits of the above mentioned methods.

- To stabilize the closed-loop system and achieve dynamic stiffness, multiple state variables
 including both voltages and currents are required for sensing. More high-resolution sensors
 result in increased cost.
- High order harmonic distortions caused by load nonlinearity and unbalance can hardly be eliminated. The controller bandwidth is limited intrinsically due to digital implementation.

Selective harmonic compensation employs the idea that each order of harmonic distortions can be compensated individually. This technique is targeted at excellent steady state output and it is implementable either in the stationary frame [15] or in synchronous rotating frames [14], [17]. Nevertheless, excessive computation increases the controller cost and makes it less practical when harmonics above the 13th order need to be compensated.

Repetitive controller (RC) originating from the internal model principle [19] is known as an effective solution for rejection of periodic errors in a dynamic system. The core mechanism of this technique is to incorporate a modified internal model by properly constructing feedback loops of one or a few time delay units. Consequently, periodic errors can be eliminated. A number of repetitive control strategies have been developed for UPS inverters (or constant-voltage-constant-frequency inverters) [20]-[30], grid-connected inverters [31], PWM rectifiers [32], boost DC-DC converters [33], [34], and active power filters [35]-[38]. Among these methods, the conventional RC structure based on the positive feedback loop of a fundamental-period delay unit has gained the largest popularity, for its straightforwardness and excellent harmonic rejection capability (every odd and even harmonic is compensated). However, the control action is postponed by one fundamental period correspondingly, which slows down the dynamic response unavoidably.

Generally, in a three-phase UPS system, the technical concerns can be summarized as follows.

- Harmonic rejection capability. The controller is expected to reject any possible harmonic distortions under general conditions (balanced, unbalanced, nonlinear, etc.).
- Dynamic response. The controller should be able to respond fast to the dynamic load step changes.
- Cost effectiveness. Less high-resolution sensors and acceptable signal processing resources are expected.

1.3. Renewable Energy Systems Interfaced with Utility Grid

1.3.1. Grid-Connected Inverter with LCL Filter

Renewable energy sources are growing rapidly in recent years along with the constantly growing global demand for electricity. Grid-connected voltage source inverter, usually as an essential part in a renewable energy application, injects sinusoidal current to the grid with required low THD and high power factor. Using an LCL filter in such a system has been recognized as an attractive solution to reduce current harmonics around the switching frequency, improve the system dynamic response, and reduce the total size and cost [13], [46].

A common technical concern in designing such an LCL filter based grid-connected inverter is to appropriately select the filter parameters. On the one hand, it is desired to push the resonance frequency of the LCL filter as high as possible in order to save the size and cost, as long as the grid current switching harmonics satisfy with the harmonic distortion standard. On the other hand, the LC resonance would potentially cause system instability and must be carefully dealt

with. Therefore, an optimal design of the LCL filter associated with the grid current control scheme should exist and it is desirable to obtain it.

1.3.2. Offshore Wind Farm Inverter Incorporating Long Transmission Cable

In recent years, offshore wind farms have emerged as one of the most promising renewable energy sources to meet the fast increased energy demand globally. Benefiting from the much stronger wind, more uniform wind speed, and avoidance of audible noises and visual impact, offshore wind farms offer much greater advantages over the onshore technology. A great number of large-scale commercial offshore wind farm projects have been developed in some European countries (United Kingdom, Denmark, Germany, Sweden and the Netherlands) and this number is still increasing [85]-[89].

In general, two types of power transmission technologies can be adopted in offshore wind farms: HVAC and HVDC. High voltage submarine cable, as a link connecting the offshore wind farm and onshore power grid, serves as an indispensable part in both HVAC and HVDC systems. Typically, HVDC transmission requires higher cost compared to HVAC because extra power electronics devices are needed for the AC-to-DC conversion in the substation. However, in HVAC transmission, the high capacitance of the submarine cable causes considerable reactive power. And even worse, LC resonances can occur between the offshore and onshore grids, which can lead to voltage distortions, increased power losses, and even system failure. Therefore, for an offshore wind farm located at a long distance (e.g., larger than 90km) from the seashore, HVDC power transmission becomes more favorable [85]. Intensive studies on HVDC based offshore wind power generation technologies have been carried out [85]-[88]. Comparative evaluations of HVDC and HVAC transmissions have been performed in [85], [89].

It is reported that in existing offshore wind farms, HVAC transmission is so far the most widely adopted approach [85]. In a typical HVAC-connected offshore wind farm [85], [91], a group of wind turbine generators are connected to a central collection point through voltage source converters (VSCs), step-up transformers and local submarine cables. The central point is tied to the onshore main grid through another step-up transformer and the main submarine cable. Each VSC conditions the raw power generated from wind turbine and produces a fine power. However, because of the long distance from the onshore main grid, the grid seen by each VSC is no longer an infinite AC source but a combination of the main grid, transformers and submarine cables. The distributed inductance and capacitance along the HVAC transmission system may result in a series of high frequency resonances, and potentially cause system instability.

Active damping techniques for grid-connected inverters with LCL filters have been widely investigated. Multi-loop feedback strategies in which more than one state variable are sensed can effectively eliminate the conjugate poles and increase phase margins. In addition, filter based damping technique can also compensate the resonant poles without introducing extra sensors. Unfortunately, all the existing active damping techniques are based on the assumption that the inverter is directly tied to an ideal grid. As aforementioned, it is no longer valid to apply these controllers to the offshore wind power applications. Therefore, a systematic study regarding the resonances of the submarine HVAC transmission system incorporating long transmission cables is desired for the guidance of the control strategy design in such a system. Once the model of the offshore wind farm system is built, then it will become much easier to design controllers that can effectively damp the resonances.

1.3.3. Photovoltaic Inverter System

Photovoltaic (PV) inverter is one of the fast growing enabling technologies in grid-connected renewable energy applications. The concept of micro inverter (also known as module integrated converter/inverter) has become a future trend for single-phase grid-connected photovoltaic power systems, for its removal of energy yield mismatches among PV modules, possibility of individual PV module oriented optimal design, independent maximum power point tracking (MPPT), and "plug and play" concept [61], [62]. In general, a PV micro inverter system is often supplied by a low voltage solar panel, which requires a high voltage step-up ratio to produce desired output AC voltage [61]-[63]. Hence, a DC-DC converter cascaded by an inverter is the most popular topology, in which a high frequency transformer is often implemented within the DC-DC conversion stage [64]-[70].

In terms of the pulse-width modulation (PWM) techniques employed by the PV micro inverter system, two major categories are attracting most of the attentions. In the first, PWM control is applied to both of the DC-DC converter and the inverter [64]-[66]. In addition, a constant voltage DC link decouples the power flow in the two stages such that the DC input is not affected by the double-line-frequency power ripple appearing at the AC side. By contrast, the second configuration utilizes a quasi-sinusoidal PWM method to control the DC-DC converter in order to generate a rectified sinusoidal current (or voltage) at the inverter DC link. Accordingly, a line-frequency commutated inverter unfolds the DC link current (or voltage) to obtain the sinusoidal form synchronized with the grid [67]-[70]. Although the latter has the advantage of higher conversion efficiency due to the elimination of high frequency switching losses at the inverter, the double-line-frequency power ripple must be all absorbed by the DC input capacitor, making the MPPT efficiency (defined as the ratio of the energy drawn by the PV inverter within

a certain measuring period at the steady state to the theoretical available energy from the PV module) compromised unless a very large capacitance is used. Moreover, the DC-DC conversion stage requires more challenging control techniques to meet the grid current regulation requirement. Therefore, in terms of the MPPT performance and output current quality, the first category of PV micro inverter is more appropriate and will be studied in this dissertation.

MPPT is performed by the boost-half-bridge DC-DC converter. Numerous MPPT techniques have been studied and validated, for example, perturb & observe (P & O) method [76]-[79], incremental conductance method [80], ripple correlation method [81], reduced current sensor method [82], etc. Different techniques have shown different trade-offs among the steady state MPPT efficiency, the transient tracking speed, and the control complexity [83], [84].

Another critical concern for MPPT implementation is the dynamics of the specific converter adopted. In [78], an optimal P & O method has been developed to limit the negative effect of the converter dynamic responses on the MPPT efficiency. In [79], a closed-loop control technique has been proposed to minimize the PV voltage oscillation. However, the converter dynamic behavior associated with the MPPT operation can also influence the converter efficiency and functioning, which has been rarely discussed before. For example, the MPPT methods using step-changed perturbations on the PV voltage (or current) or the converter duty cycle periodically may sometimes cause problems such as inrush current, LC oscillation, magnetic saturation, etc. These undesirable transient responses can result in higher power losses or even circuit malfunctioning; and of course, they are different from case to case.

1.4. Scope of the Dissertation

This dissertation starts from the study of a three-phase four-wire online double conversion UPS system. A typical three-phase four-wire online double conversion UPS system consists of

static bypass circuits, a power factor correction rectifier, an inverter, and a DC-DC charger connected with a battery stack. In this dissertation, multi-loop control strategies are developed for the double conversion UPS system excluding the battery charger and the bypass circuit control. Input current regulation, DC link voltage regulation and balancing, and the output voltage regulation are realized. A novel DC link voltage balancing technique will be proposed. Experimental results under different test conditions will be included to demonstrate the controller performances.

Next, advanced repetitive control techniques will be investigated for the voltage regulation of the three-phase UPS inverters. A low THD repetitive control strategy will be proposed to achieve optimal steady state voltage regulation. Then an improved synchronous-frame repetitive control approach will be introduced to enhance the dynamic performances. Experimental results and comparisons among different control strategies will be provided to verify the controller performances.

For the grid-connected renewable energy applications, the study starts from a grid-connected voltage source inverter, which is commonly used as the grid interface in almost every renewable energy system. The feasibility of using a high-resonance-frequency LCL filter with minimal size and cost requirement is studied and verified. A proportional plus repetitive control hybrid strategy is then proposed to regulate the grid current and power factor. A conventional proportional plus resonant controller is also designed for the comparison purpose.

Most of the time when designing the controller in a grid-connected inverter system, the grid is typically presumed as an infinite voltage source or a first-order single inductor. However, this assumption can become untrue particularly when the power transmission system connecting the inverter and the main grid is using long transmission cables.

Next, a more specific case study is then carried out on an HVAC offshore wind farm system, which incorporates long submarine transmission cables. In this dissertation, the entire system is modeled by per unit values and emulated by a scaled-down 120Vac single-phase system. A lumped LC network is adopted to model the high-frequency characteristics of the HVAC undersea cable. A systematic analysis based on the frequency-domain approach is carried out. The key parameters of system passive components that affect high-frequency resonances are identified. A notch filter based active damping control strategy is then proposed to stabilize the closed-loop system. In order to adapt the proposed damping control to more general cases where the long transmission cable parameters are unknown, a simple auto tuning algorithm is also investigated. Experimental tests are carried out to validate the theoretical analysis as well as the proposed active damping method.

Finally, a boost-half-bridge PV micro inverter system is proposed. The grid current control strategy introduced earlier can be directly applied here. The system control strategies will be discussed, particularly in terms of the maximum power point tracking algorithm. Experimental results will be included to examine the micro inverter system performances.

Chapter 2. Multi-Loop Control of Three-

Phase Four-Wire Online Double Conversion

UPS System

2.1. System Descriptions and Ratings

The online double conversion UPS system is widely used for supplying constant and disturbance-free power to sensitive equipment loads. When the grid power environment is "noisy", or voltage sags frequently happen, or power outages sometimes occur, the online UPS system is able to decouple the load from the grid such that the load can be well protected. On the other side, the power factor correction function of the online double conversion UPS system ensures the input current of high power factor and minimal harmonic distortions when the load is of nonlinearity and absorbs harmonically distorted current. Therefore, the online double conversion UPS system is also able to protect the grid from pollutions generated by the loads.

Figure 2.1 shows the typical configuration of an online double conversion UPS system. It is composed of static bypass SCRs, a power factor correction (PFC) rectifier, a DC-DC battery charger connected with a battery stack, an inverter, and a common DC link. The static bypass SCRs switches the UPS system between online mode and standby mode. In addition, the PFC rectifier regulates the grid current to be sinusoidal and unity power factor, meanwhile the inverter feeds a sensitive equipment load with regulated sinusoidal voltage. Finally, the DC-DC battery charger controls the charging and discharging of the batteries during normal operation mode and power sags or outage mode.

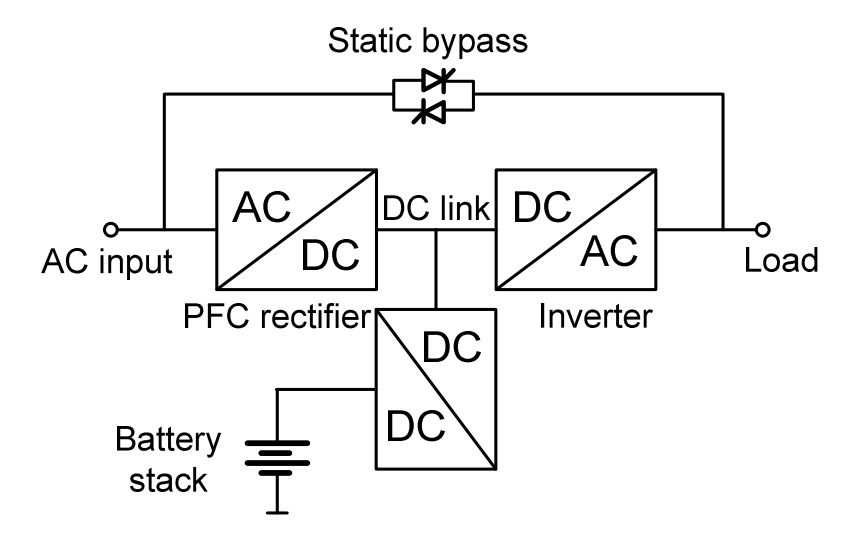


Figure 2.1. Typical configuration of an online double conversion UPS system.

In this chapter, a three-phase four-wire online double conversion UPS system is studied. Instead of studying the entire UPS system control strategies, this dissertation will focus more on the main AC-DC-AC power conversion control in this chapter. Figure 2.2 shows the three-phase four-wire back-to-back double conversion UPS topology excluding the DC-DC charger and the static bypass circuit.

To achieve the goal of maintaining constant output voltage irrespective of load disturbances, some high performance feedback control methods have been proposed [1]-[10]. A grid-connected PWM rectifier with low pass filter (L, LC, or LCL) is usually required to draw a sinusoidal current from the grid at a close-to-unity power factor and simultaneously achieve DC link voltage regulation. LCL filter is superior for its fast high frequency attenuation characteristics and is proved to have significant advantages in higher power applications [13]. Several high performance controllers have been adopted (for rectifiers or similarly, grid-connected inverters) with high power factor and small THD of grid current [11]-[13].

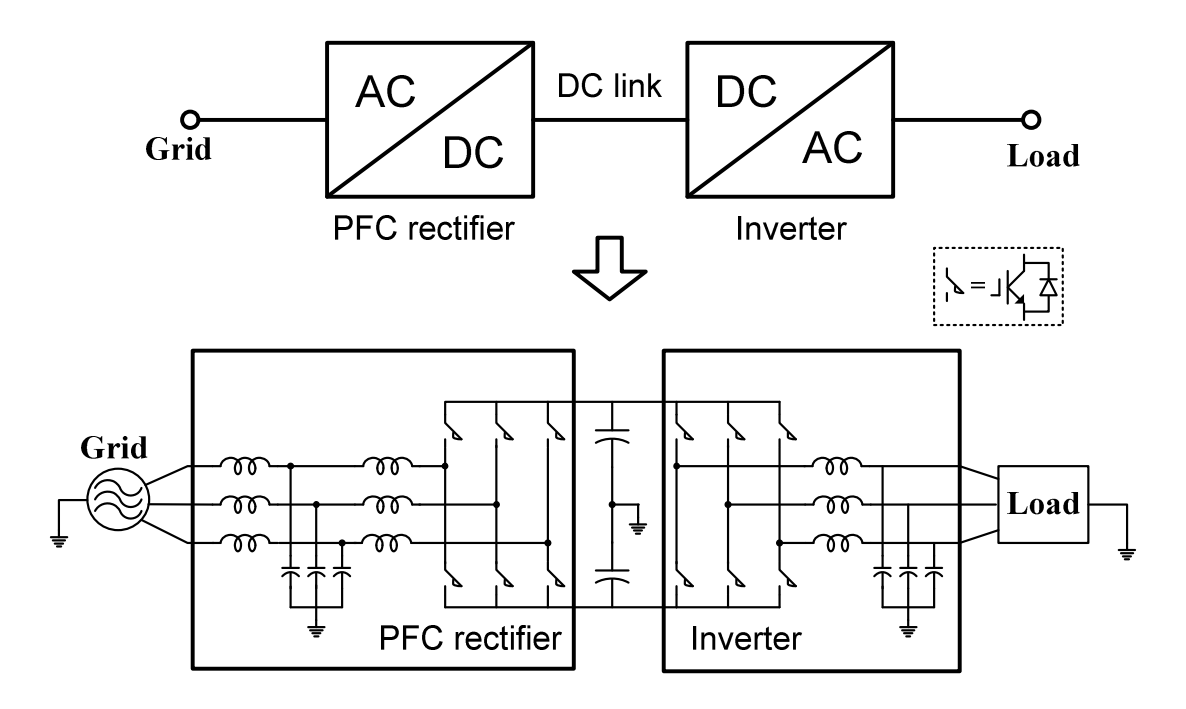


Figure 2.2. AC-DC-AC topology of three-phase four-wire double conversion UPS system.

Table 2.1. Parameters of the 3-phase 4-wire double conversion UPS system

Parameters	Values
Nominal line-to-line voltage	480 V
DC link voltage	830 V
Nominal power	100 kW
Fundamental frequency	57~63 Hz
Switching frequency	10 kHz
Input filter inductance (grid side)	100 uH
Input filter inductance (rectifier side)	250 uH
Input filter capacitance	20 uF
Output filter inductance	250 uH
Output filter capacitance	150 uF
DC link capacitor	9.4 mF

Among all the reported control algorithms, multi-loop state feedback control schemes have attracted the most attention among researchers because of the ease of implementation and good

performances. In this dissertation, multi-loop state feedback control strategies are implemented with both the PWM rectifier and the inverter.

Table 2.1 provides the system parameters.

2.2. Multi-Loop Controller Design

2.2.1. PWM Rectifier Control

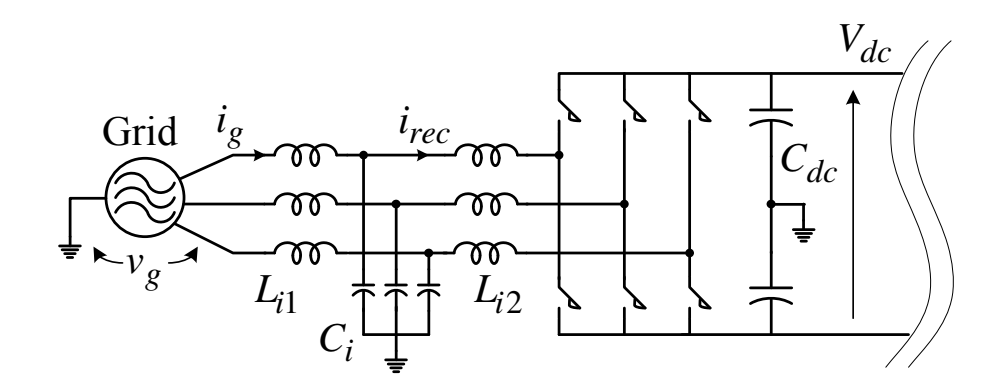


Figure 2.3. Three-phase four-wire PWM rectifier.

The three-phase four-wire PWM rectifier is shown in Figure 2.3. In Figure 2.4, the control block diagram of the PWM rectifier is illustrated. The DC link voltage is fed back to the outer voltage loop, and controlled through a PI compensator with lower bandwidth. The DC link voltage reference is set to be a little above the minimum required DC link voltage for normal operation of both the PWM rectifier and inverter.

The inner current loop regulates the rectifier current for power factor correction. To adapt the system to a varying grid frequency (57 Hz~63 Hz), a phase lock loop (PLL) algorithm is synthesized as in Figure 2.5 to generate the instantaneous sinusoid angle for the inner current loop reference.

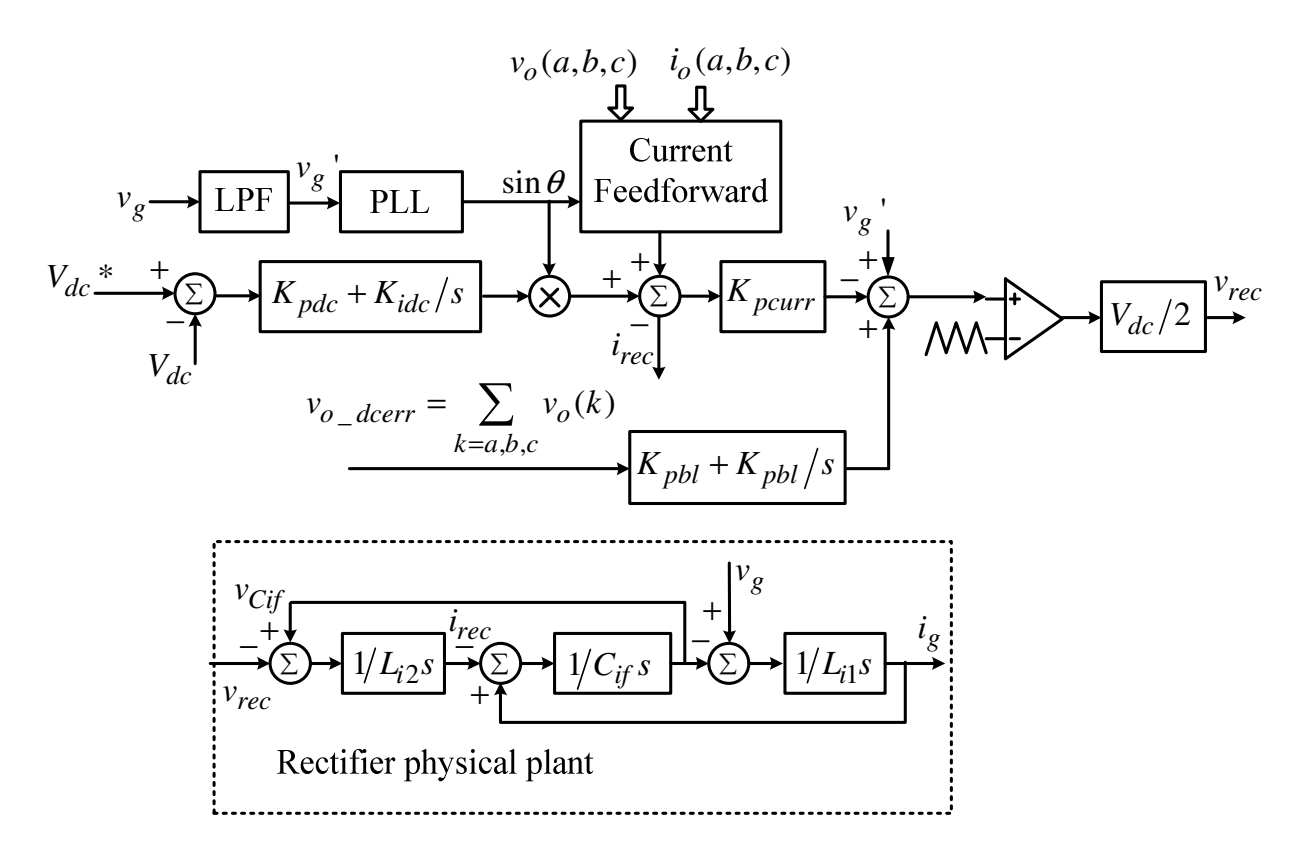


Figure 2.4. Control block diagram of the PWM rectifier.

The PLL routine detects the zero-crossing of grid voltage every fundamental cycle. A low pass filter is added for better rejection of high frequency ripples and noises from the grid voltage, thus good robustness is achieved. A counter is incorporated to update the total number of sampling cycles in one fundamental period. Then the instantaneous sinusoid angle can be calculated as in (2.1).

$$\theta = 2\pi \frac{K(i)}{N} \tag{2.1}$$

Where K(i) represents the counter value in the *ith* sampling cycle after the latest zero-crossing point, N is the total number of sampling cycles in one fundamental period.

The proposed PLL can synchronize with the grid voltage in only one fundamental period and provide very fast dynamic response when grid frequency varies.

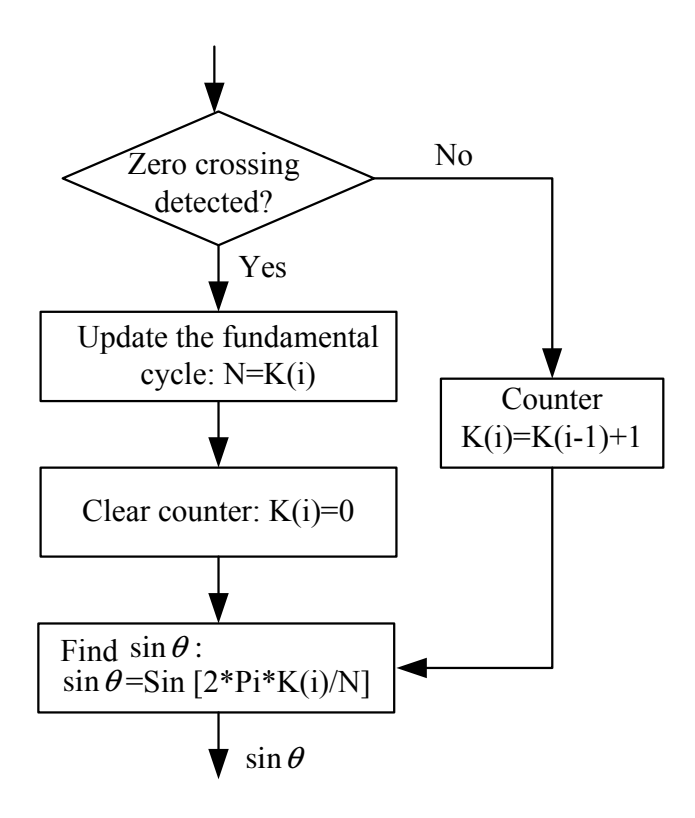


Figure 2.5. PLL routine executed in each sampling cycle (switching cycle).

During step load, the inverter output power changes instantly. For best regulation of the DC link voltage during such a transient, the rectifier current must be adjusted to the correct level in the fastest way. Hence, the input and output power are balanced. To compensate the relatively lower bandwidth of the outer voltage loop for dynamic stiffness, the inverter output power is calculated and fed forward to generate the instantaneous current command, which is shown in (2.2), where *T* is the fundamental period.

$$I_{recff}^{*} = \sin \theta \cdot \sqrt{\frac{2}{3\sum_{k=a,b,c} v_g^{2}(k)}} \cdot \frac{1}{T} \int_{t}^{t+T} \sum_{k=a,b,c} v_o(k) i_o(k) dt$$
 (2.2)

However, it is noteworthy that one must be very careful to implement the feed forward by calculating the instantaneous load power. Either an excessive or an inadequate feed forward would jeopardize the improvement of the dynamic response.

A well known problem associated with three-phase four-wire PWM rectifier is the DC capacitor voltage imbalance. The input current measurement errors usually can cause a DC offset in the sensed current [11]. The offset is then amplified by the inner current controller, which eventually leads to the DC capacitor voltage imbalance. This imbalance weakens the effective utilization of DC link voltage and forces to increase the DC link voltage in order to guarantee the correct operation of both the rectifier and inverter. As a result, the system efficiency and device stress are becoming worse.

In order to address the above mentioned voltage imbalance, an additional balancing controller must be incorporated. Unlike the conventional balancing control methods which often need to sense both of the capacitor voltages, here, a method only requiring one DC link voltage sensor is proposed, and thus cost can be reduced.

Specifically, while intentionally leaving the DC steady state error at the inverter side controller, the DC component of inverter output can be extracted as shown in (2.3) and fed back to a PI controller. The PI output is added to the final SPWM reference directly. Therefore, with only one DC voltage sensor implemented the DC voltage imbalance and inverter output DC offset are both eliminated.

$$v_{o_dcerr} = \sum_{k=a,b,c} v_o(k)$$
 (2.3)

In the three-phase four-wire UPS system, an LCL filter is employed to interface the PWM rectifier and grid. LCL filter is superior for its better performance in terms of high frequency

attenuation. To perform the PFC function, one can directly sense the grid current i_g for feedback control, or sense the rectifier bridge input current i_{rec} for indirect control. The details of the current control technique will be discussed in Chapter 5.

2.2.2. Inverter Control

The three-phase four-wire inverter is shown in Figure 2.6. In Figure 2.7, the control block diagram of the inverter is illustrated.

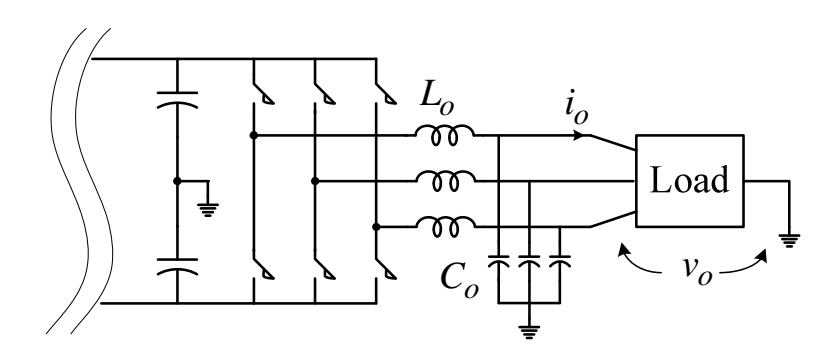


Figure 2.6. Three-phase four-wire inverter.

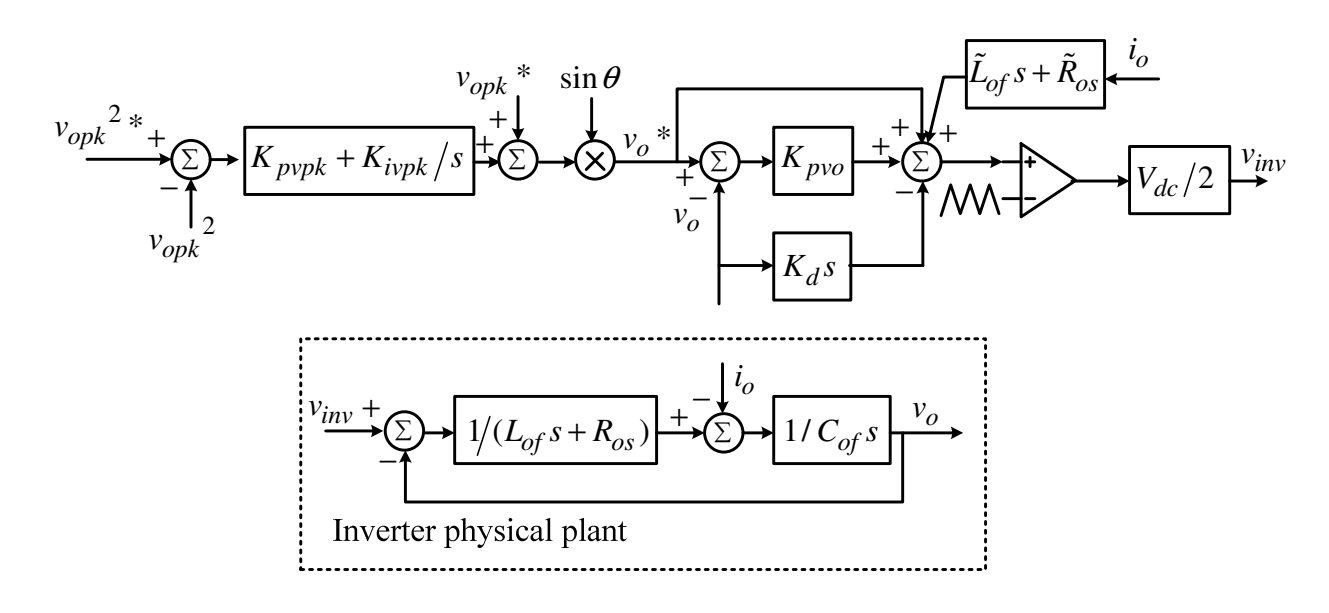


Figure 2.7. Control block diagram of the inverter.

Instantaneous voltage feedback plus reference feed forward play the major roles in the inverter voltage control. Proportional controller is used for better stability and leaving a steady state DC error. This DC error is utilized at the rectifier side for DC capacitor voltage balancing. Until the DC error is diminished to zero, the rectifier keeps compensating the DC voltage imbalance.

The second order LC filter has conjugate poles around 5160 rad/s, causing the LC resonance. Neglecting the equivalent series resistance of the inductor, the LC filter transfer function $G_{inv}(s)$ is given by (2.4).

$$G_{inv}(s) = \frac{1}{L_{of} C_{of} s^2 + 1}$$
 (2.4)

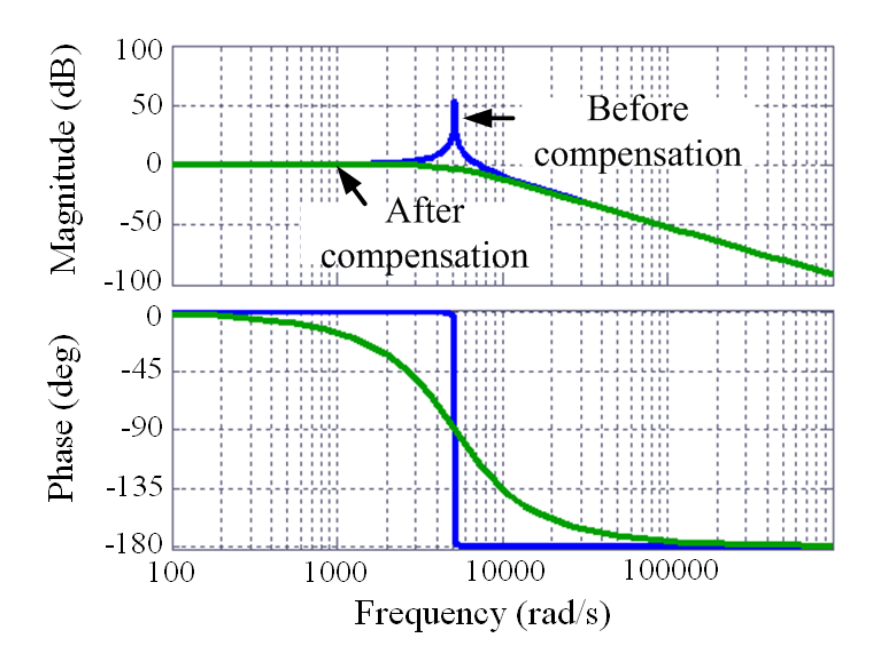


Figure 2.8. Bode plot of $G_{inv}(s)$ before and after voltage differential feedback compensation.

(For interpretation of the references to color in this and all other figures, the reader is referred to the electronic version of this dissertation.)

To actively damp this resonance, a well known technique is to feed back the capacitor current to the inner current loop [1]. However, this requires an additional current sensor. Physically, the capacitor current is proportional to its voltage differential. Therefore, in this chapter, the capacitor voltage differential multiplying a constant gain K_d is fed back to form the inner active damping loop, compensating the LC plant with an optimal damping ratio (set to 0.707).

Figure 2.8 gives the bode plots of the LC filter before and after the active damping compensation, respectively. To further improve the inverter voltage controller's dynamic response during step load as well as enhance its capability of dealing with non-linear load, the load disturbance decoupling is injected based on the estimated filter inductance and equivalent series resistance. Hence, the influence of load perturbation can be minimized.

An additional outer loop for peak voltage (2.5) control is added. It augments the inner loops to completely eliminate the steady state error of inverter voltage magnitude, and thus the inverter output voltage is always regulated as rated level.

$$v_{opk} = \sqrt{\frac{2}{3} \sum_{k=a,b,c} v_o^2(k)}$$
 (2.5)

2.3. Experimental Results

The multi-loop control strategies for the 100 kW three-phase four-wire double conversion UPS system are implemented with Texas Instruments TMS320F2407 digital signal processor. Figure 2.9 shows the system experiment set-up. 75kW linear load and 50 kW non-linear diode rectifier load are tested to verify the controllers' performance, respectively. High power factor (0.99) and low THD (3.2%) are achieved with the input current as shown in Figure 2.10. Figure

2.13 demonstrates the dynamic stiffness and balancing of the DC link capacitor voltage during load step change.

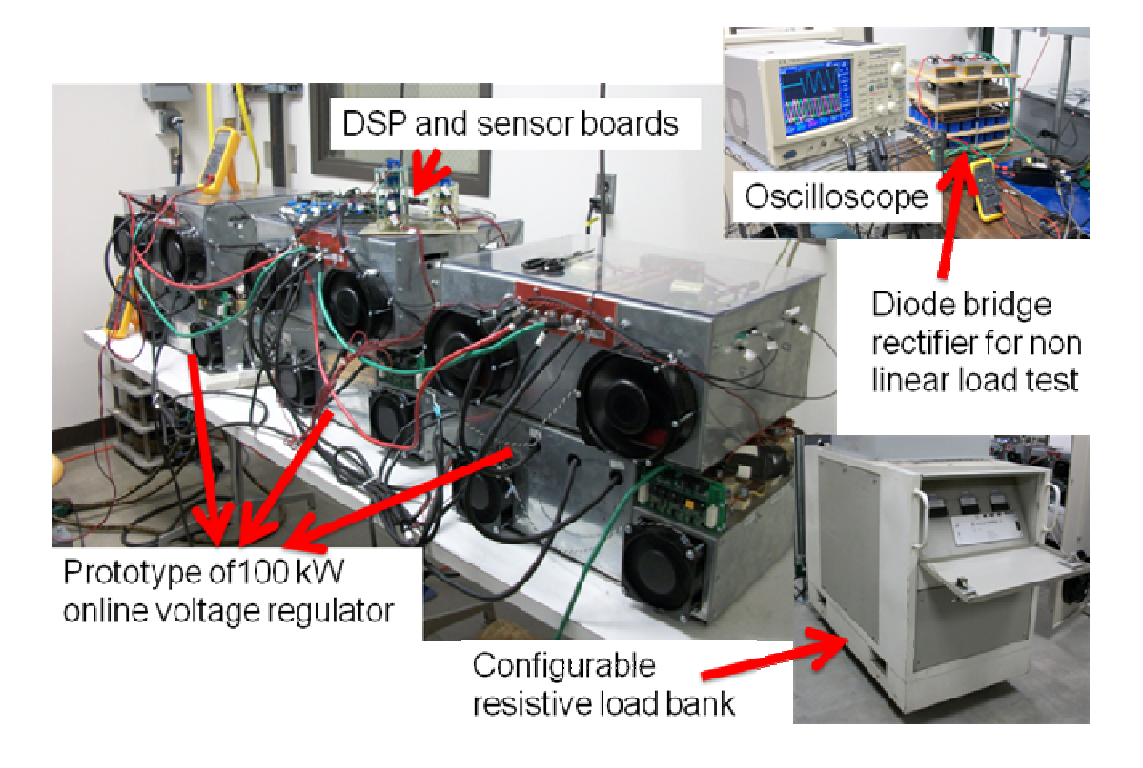


Figure 2.9. Experiment set-up of the 100 kW UPS system.

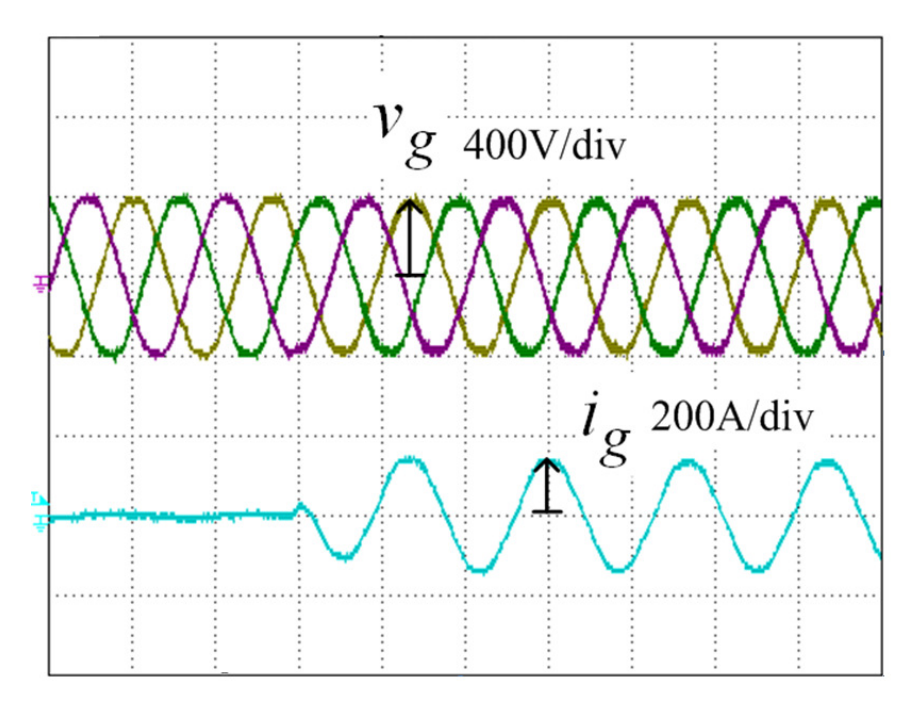


Figure 2.10. Grid voltage and current during load turn- on (linear load).

In Figure 2.11 and Figure 2.12, fast dynamic response and good steady state regulation are exhibited. Figure 2.14 shows the inverter output voltage regulation under non-linear load condition. A THD of 3.9% is achieved.

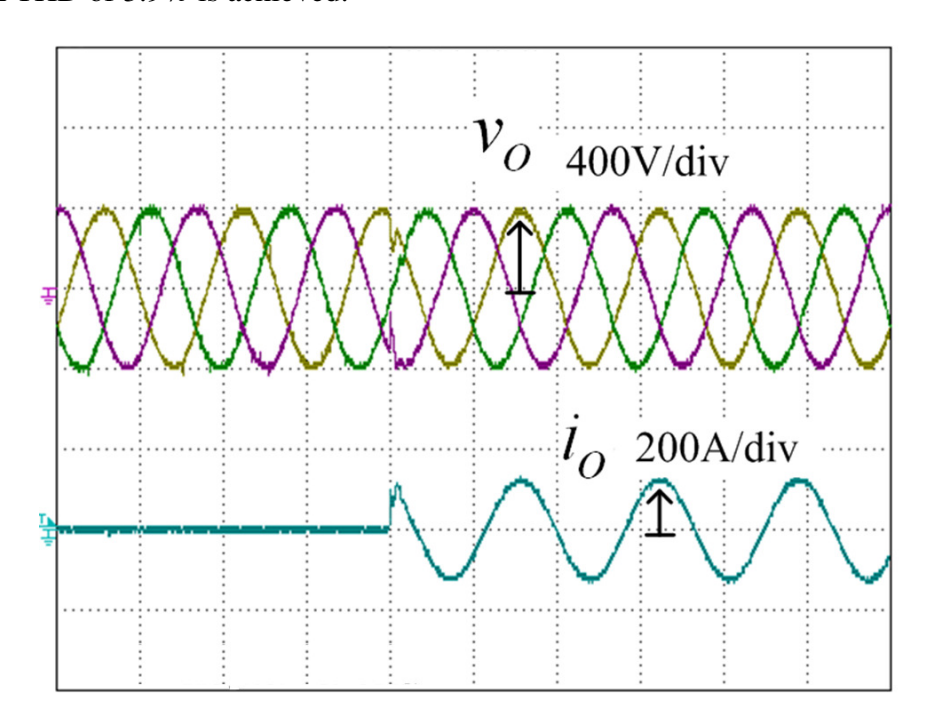


Figure 2.11. Output voltage and current during load (linear) step-on.

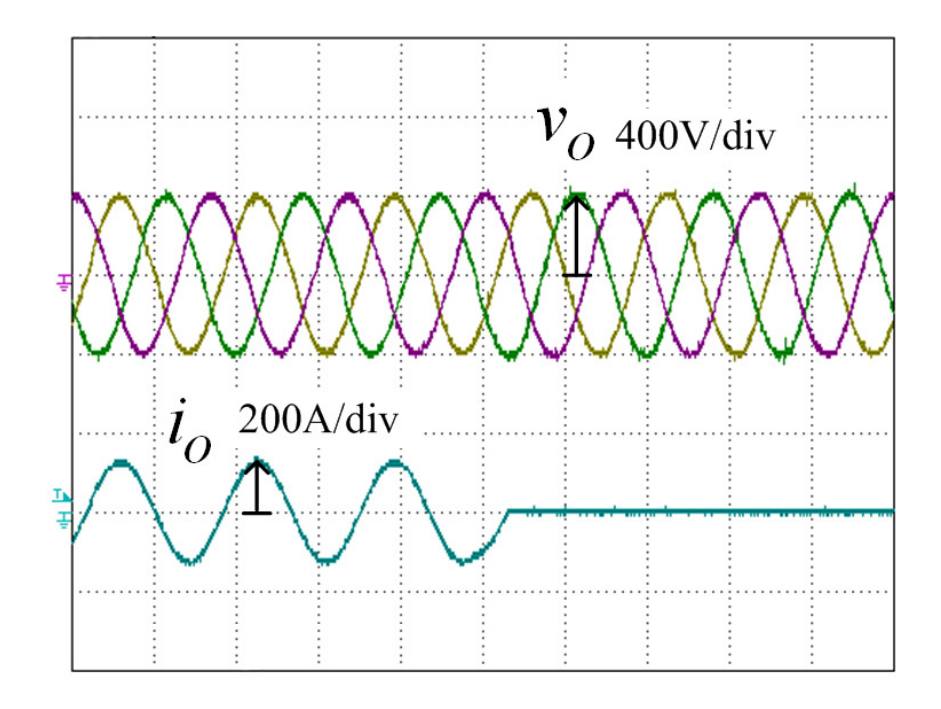


Figure 2.12. Output voltage and current during load (linear) step-off.

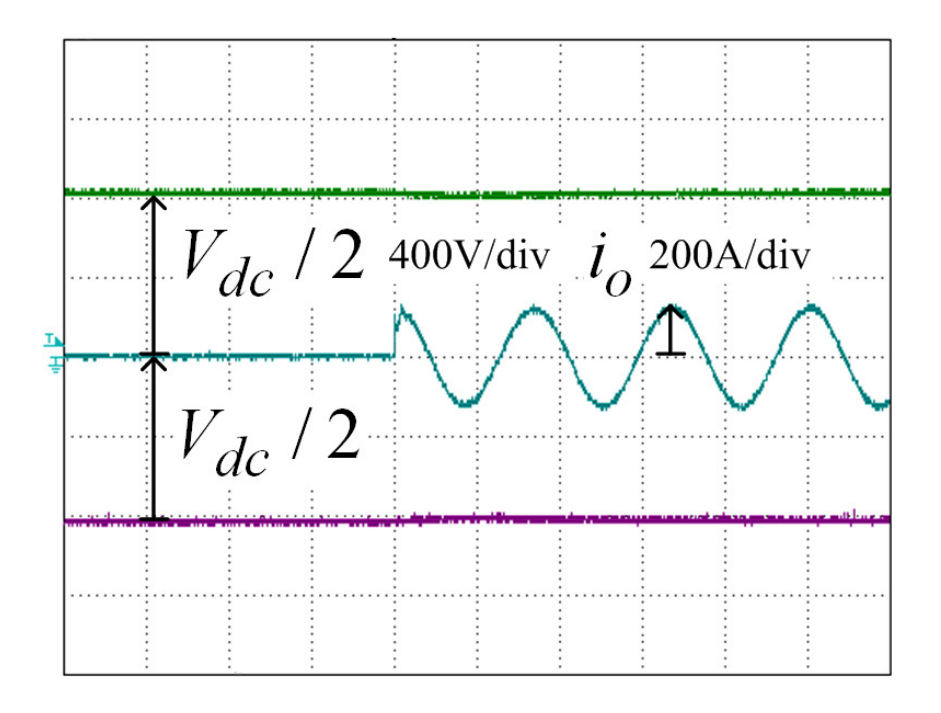


Figure 2.13. DC link capacitor voltages and load current during load (linear) step-on.

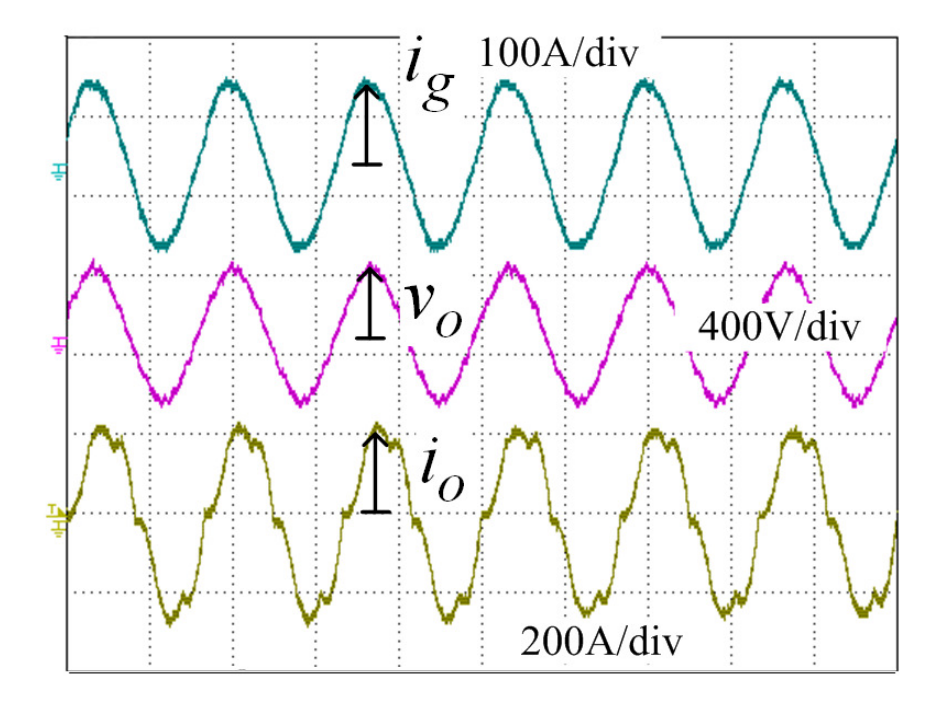


Figure 2.14. Grid current, output voltage and output current with non-linear load.

2.4. Summary

In this chapter, multi-loop state feedback control strategies for three-phase four-wire online double conversion UPS system are discussed and verified experimentally.

At the input LCL filter, the rectifier current is fed back and regulated for power factor correction. By feeding forward the inverter output power so as to generate an instantaneous command for the inner current loop, dynamic stiffness of the DC link voltage is obtained during load step change.

The imbalance of DC capacitor voltage is an inherent drawback with three-phase four-wire PWM rectifiers, which causes higher device voltage stresses and reduced efficiency due to insufficient utilization of DC link voltage. The proposed control strategies intentionally leave a steady state DC error with the inverter voltage control loop, and feed back this DC error to a dedicated voltage balancing controller at the rectifier side. Therefore, the inverter output DC error and DC link capacitor voltage imbalance are eliminated simultaneously.

At the inverter side, peak voltage outer loop, voltage reference feed forward, instantaneous voltage and active damping inner loops, assisted with load disturbance decoupling are employed to achieve good steady state and transient performances.

Chapter 3. Low THD Repetitive Control of

Three-Phase UPS Inverter

3.1. Introduction

In this chapter, the three-phase UPS inverter is studied. Figure 3.1 shows the most commonly used topology of a three-phase UPS inverter.

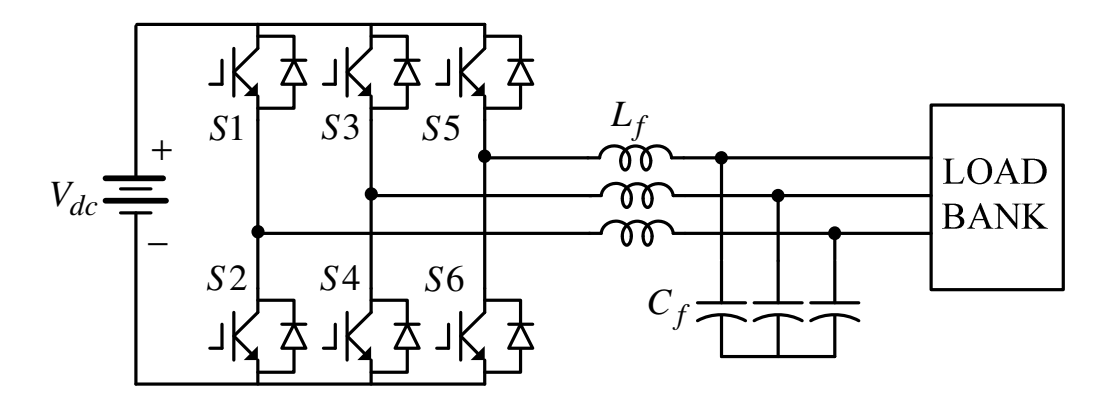


Figure 3.1. Main circuit of a three-phase UPS inverter.

Repetitive control originating from the internal model principle [19] is well known as a nearperfect solution for rejection of periodic distortions in a dynamic system. The core mechanism of
this technique is to incorporate a modified internal model based on a time delay unit.

Consequently, periodic errors can be eliminated. A number of repetitive control strategies have
been developed for UPS inverters [20]-[30], grid-connected inverters/rectifiers [31], [32], and
active power filters [35]-[38]. Generally, a non-causal zero-phase low pass filter Q(z) is often
placed on the positive feedback path of RC. Most commonly, Q(z) is selected as a low order
FIR filter. Furthermore, a compensator S(z) is designed and placed on the controller forward
path in order to modify the magnitude characteristics of the inverter plant. Both Q(z) and S(z)

are incorporated to guarantee system stability and achieve excellent low frequency harmonic compensations at the price of sacrificing high order (>13th-order) harmonic rejection capability.

However, in a UPS inverter, the nonlinear load harmonic distortions can be all the way to the 19th-order or even higher. Furthermore, the design of S(z) usually requires precise knowledge of the LC filter parameters, resulting in higher design complexity and weakened robustness. In this chapter, a high performance repetitive controller is proposed, by utilizing a 4th-order linear phase IIR filter Q(z). It maintains a close to unity magnitude in its pass band and rolls off very fast above the cut-off frequency. Benefiting from this feature, S(z) is no longer needed which simplifies the controller design and enhances the controller robustness. Furthermore, harmonics up to the 19th order can be well compensated and a good stability margin is also achieved. In order to obtain good dynamic response, a more precise feed forward containing both the voltage reference and load disturbance decoupling term is added.

3.2. Overview of the Repetitive Control UPS System

3.2.1. Repetitive Control Principle

Figure 3.2 shows the typical block diagram of a repetitive control based UPS inverter system in the discrete-time domain. The repetitive controller is plugged into the main control loop and assisted by a reference feed-forward path for better steady-state and transient performances. All the repetitive disturbances such as the distorted non-linear load, LC filter parameter drifting, dead-time effect, are represented by d(z). $v_r(z)$ and v(z) are the control reference and output voltage, respectively. $\varepsilon(z)$ is the tracking error.

A second-order inverter system with LC filter is commonly associated with the conjugate pole pair on the imaginary axis, which leads to instability under no load/light load condition.

Therefore, either an inner current loop or an active damping loop will be helpful for the stability compensation. For simplification, here $G_c(z)$ represents the stabilized inverter plant.

In order to achieve fast dynamic response, the voltage reference feed forward as well as the disturbance decoupling feed forward are added. In practice, the disturbance decoupling term can be calculated by multiplying the load current and the inductor impedance.

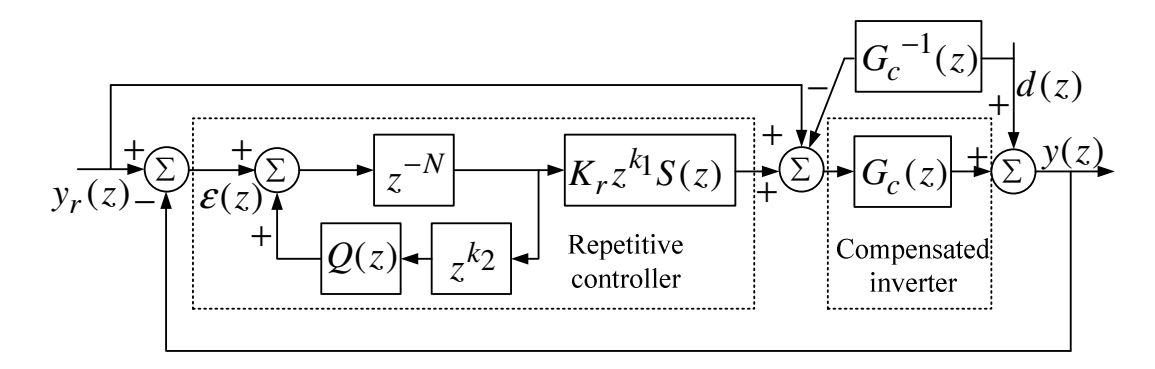


Figure 3.2. Block diagram of a typical discrete-time repetitive controlled inverter system.

The core of the repetitive controller is called the modified internal model (3.1), which is denoted by the positive feedback loop in Figure 3.1. z^{-N} is the time delay unit essential to a repetitive controller. In practice, it occupies N memory units for data storage in a digital signal processor. Most commonly N equals to the number of samples in one fundamental period (denoted as N_0).

$$C(z) = \frac{z^{-N}}{1 - O(z)z^{k_2}z^{-N}}$$
(3.1)

The original internal model incorporates a unity gain in the positive feedback path such that the tracking error $\mathcal{E}(z)$ is integrated based on the repetitive period. In an asymptotically stable closed-loop system, this error will eventually approach zero when the system reaches equilibrium. However in practice, the internal model is often modified by incorporating a filter Q(z) instead of the unity gain. Although this manipulation results in a sacrifice in terms of error

convergence and reference tracking accuracy, it does increase the system stability margin at the mean time. Q(z) is often designed as either a close-to-unity constant for easy implementation, or a low pass filter which only sacrifices the high frequency harmonic distortion rejection. Once Q(z) is a low pass filter, it must have a linear phase characteristic such that the phase delay can be precisely compensated to zero by a non-causal phase lead unit z^{k_2} .

S(z) is a compensator which modifies the magnitude and phase response of $G_c(z)$ for better harmonic rejection at higher frequency. z^{k_1} is another non-causal phase lead term. It compensates the phase delay introduced by both $G_c(z)$ and S(z). K_r is a constant gain. It is tuned together with Q(z) for optimum control operation.

3.2.2. Stability Analysis

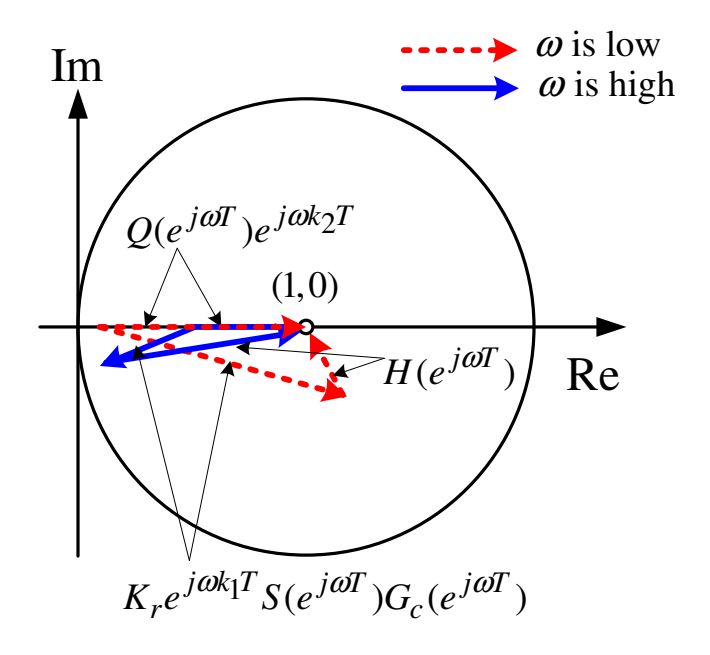
Applying Mason's rule to the block diagram in Figure 3.2, the tracking error $\mathcal{E}(z)$ in relation to the reference $v_r(z)$ and disturbance d(z) can be derived

$$\varepsilon(z) = v_r(z) \frac{[1 - G_c(z)][1 - Q(z)z^{k_2}z^{-N}]}{1 - z^{-N}[Q(z)z^{k_2} - K_r z^{k_1}S(z)G_c(z)]} - d(z) \frac{1 - Q(z)z^{k_2}z^{-N}}{1 - z^{-N}[Q(z)z^{k_2} - K_r z^{k_1}S(z)G_c(z)]}$$
(3.2)

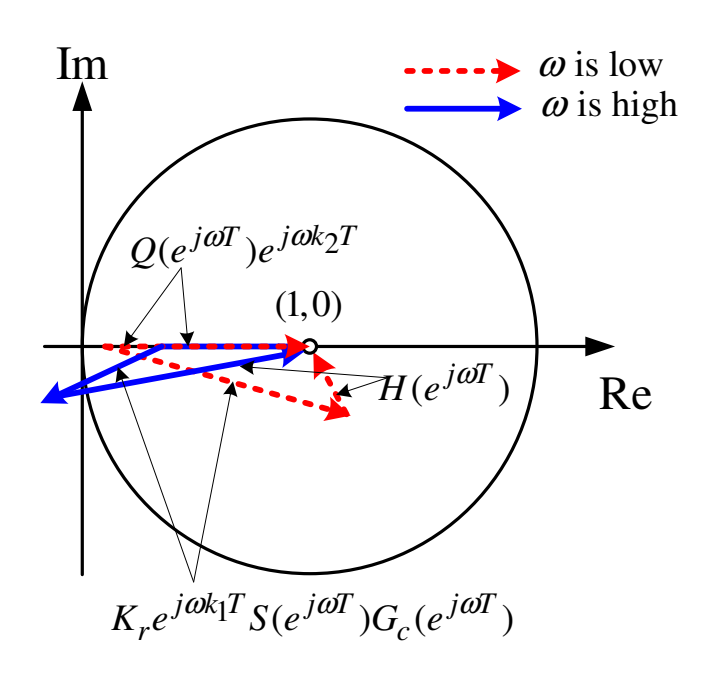
With further manipulation on (3.2), the error convergence is expressed as

$$\varepsilon(z) = \varepsilon(z)z^{-N} [Q(z)z^{k_2} - K_r z^{k_1} S(z) G_c(z)]$$

$$+ [v_r(z) - v_r(z) G_c(z) - d(z)] [1 - Q(z)z^{k_2} z^{-N}]$$
(3.3)



(a) Stable condition



(b) Unstable condition

Figure 3.3. Vector diagrams for stability analysis.

Let $H(z)=Q(z)z^{k_2}-K_rz^{k_1}S(z)G_c(z)$. One can observe that the tracking error $\mathcal{E}(z)$ is bounded if

$$|H(e^{j\omega T})| = |Q(e^{j\omega T})e^{j\omega k_2 T} - K_r e^{j\omega k_1 T} S(e^{j\omega T}) G_c(e^{j\omega T})| < 1$$
(3.4)

where $\omega \in [0, \pi/T]$, T is the sampling period. In other words, when ω increases from zero to the Nyquist frequency, as long as $H(e^{j\omega T})$ is confined within the unity circle, the repetitive control system is asymptotically stable.

Figure 3.3 illustrates the stability conditions geometrically. Assume that $Q(e^{j\omega T})e^{j\omega k_2T}$ is a zero-phase low pass filter, and thus it is always along the real axis. In Figure 3.3(a), both $Q(e^{j\omega T})e^{j\omega k_2T}$ and $K_re^{j\omega k_1T}S(e^{j\omega T})G_c(e^{j\omega T})$ exhibit considerable magnitude attenuation when ω increases from zero to the Nyquist frequency such that $H(e^{j\omega T})$ never exceeds the unity circle. Therefore, the system stability is guaranteed. By contrast, Figure 3.3(b) represents the unstable condition, in which $|H(e^{j\omega T})|$ is larger than unity when $K_re^{j\omega k_1T}S(e^{j\omega T})G_c(e^{j\omega T})$ reaches a negative phase close to -180° at high frequency.

From the above analysis, one can perceive the general design criteria to meet the stability requirement:

1) Low pass filter is a better choice than a close-to-unity constant for $Q(e^{j\omega T})e^{j\omega k_2T}$. And more importantly, $Q(e^{j\omega T})e^{j\omega k_2T}$ is preferred to have fast roll-off rate above the cut-off frequency. This can be explained by examining the locus of vector $H(e^{j\omega T})$. At high frequency region, a small magnitude of $Q(e^{j\omega T})e^{j\omega k_2T}$ will help with preventing $H(e^{j\omega T})$ from exceeding the unity circle.

- 2) $K_r e^{j\omega k_1 T} S(e^{j\omega T}) G_c(e^{j\omega T})$ must demonstrate a low pass characteristic. K_r must have an upper limit and differs according to the roll-off rate of $Q(e^{j\omega T})e^{j\omega k_2 T}$. The same reason as explained in 1) is applied here.
- 3) The phase shift of $K_r e^{j\omega k_1 T} S(e^{j\omega T}) G_c(e^{j\omega T})$ should be as small as possible when ω increases. This can be achieved by carefully tuning the non-causal phase lead compensator z^{k_1} .

3.2.3. Dynamic Response Analysis

From (3.3), the tracking error will have fast convergence when |H(z)| is small. Assume $Q(z)z^{k_2}$ has a close-to-unity pass-band gain. At low frequencies within the pass band of $Q(z)z^{k_2}$, Eq. (3) can be further simplified in approximation as

$$\mathcal{E}(z) = \mathcal{E}(z)z^{-N}H(z) \tag{3.5}$$

Theoretically, if |H(z)|=0, the tracking error $\mathcal{E}(z)$ can be eliminated in one repetition period. However, it is unrealistic to make |H(z)| zero for all ω . In practice, |H(z)| is usually designed to be close to zero in the pass band of $Q(z)z^{k_2}$.

From (3.5), it is noticeable that another factor significantly affecting the dynamic response is z^{-N} . A long control delay will not only result in slow error convergence but also increase the magnitude of tracking error during transients. Hence, a large z^{-N} becomes intolerant particularly when fast dynamic response is desirable, and thus it demerits the advantage of repetitive control. Therefore, how to minimize the delay effectively becomes a vital consideration for the controller design. The method of minimizing N will be discussed in Chapter 4.

Steady state tracking error is another key criterion to evaluate a controller's performance. Notifying that the tracking error is periodic and $z^{-N} = 1$ at the steady state, the steady state error is obtained as (3.6) by simplifying (3.2).

$$\begin{split} |\mathcal{E}(e^{j\omega T})| &= |v_r(e^{j\omega T})| \left| \frac{[1 - G_c(e^{j\omega T})][1 - Q(e^{j\omega T})e^{j\omega k_2 T}]}{1 - H(e^{j\omega T})} \right| \\ &+ |d(e^{j\omega T})| \left| \frac{1 - Q(e^{j\omega T})e^{j\omega k_2 T}}{1 - H(e^{j\omega T})} \right| \end{split} \tag{3.6}$$

Equation (3.6) reveals that $|1-Q(e^{j\omega T})e^{j\omega k_2T}|/|1-H(e^{j\omega T})|$ determines the harmonic rejection capability of the controller. Equivalently, a small $|1-Q(e^{j\omega T})e^{j\omega k_2T}|/|1-H(e^{j\omega T})|$ indicates high repetitive peaks of the open loop gain.

3.2.4. Practical Design Considerations

From previous analysis, $Q(z)z^{k_2}$ and $K_rz^{k_1}S(z)G_c(z)$ are both vital important in repetitive controller design. Most commonly, $Q(z)z^{k_2}$ is realized by either a close-to-unity constant or a low-order zero-phase low-pass filter. Specifically, non causal zero-phase finite impulse response (FIR) filter is the most popular choice. On the other side, a lot of efforts have been placed on design of S(z) to compensate the magnitude and phase response of inverter plant and attenuate the repetitive peaks of the open loop gain.

However, the design of S(z) inevitably suffers constraints from the LC filter parameters in order to achieve accurate compensation. Moreover, using S(z) to attenuate the loop gain is less efficient. This is explainable by taking a look at Fig. 3(b). If $Q(z)z^{k_2}$ does not have enough roll-off above the cut-off frequency, $K_r z^{k_1} S(z) G_c(z)$ needs to be very small to avoid exceeding the unity circle. Contradictorily, $K_r z^{k_1} S(z) G_c(z)$ must be maintained as close to unity in a wide

frequency range for better harmonic rejection and fast error convergence. These two requirements toughen the design of S(z) even further.

In this chapter, a practical design of the repetitive controller module is proposed.

Instead of using a low-order filter of slow transition from pass band to stop band, the proposed design will introduce a high performance $Q(z)z^{k_2}$ which obtains great flatness in pass band and sharp roll-off above the cut-off frequency. In this case, S(z) will play a much less sensitive role in the entire controller. Hence, one can simply set S(z)=1. The second-order low pass filter $G_c(z)$ with phase-lead compensation from z^{k_1} is capable enough for high frequency attenuation. Furthermore, the design of $Q(z)z^{k_2}$ has minimal reliance on the inverter physical parameters, which enhances the controller's robustness.

As mentioned previously, faster error convergence requires not only a smaller $|H(e^{j\omega T})|$ but more importantly a reduced time delay z^{-N} . Chapter III will introduce the proposed technique in which the time delay is effectively reduced to one sixth of the fundamental period. Chapter IV will go through the detailed design of $Q(z)z^{k_2}$ and $K_rz^{k_1}G_c(z)$.

3.3. Repetitive Controller Design

The proposed repetitive controller is implemented for an 18kW three-phase UPS inverter. The system parameters are listed in Table 3.1.

3.3.1. Active Damping Compensator

A UPS inverter system with output LC filter generally requires a multi-loop control strategy for voltage regulation. The outer loop is dedicated to achieve satisfactory steady state performance, while the inner loop usually improves the transient response as well as the system

stability. Either inductor current or capacitor current feedback is valid for forming the inner loop [6]. But they both require high resolution current sensors, resulting in an increased total cost.

Table 3.1. System Parameters

Parameters	Values	
Nominal line-to-line voltage	208 V	
DC link voltage	415 V	
Fundamental frequency	60 Hz	
Switching frequency	10.8 kHz	
Sampling frequency	10.8 kHz	
Rated output power	18 kW	
Output filter capacitance	150 uF	
Output filter inductance L_f	250 uH	

Another approach is to utilize the capacitor voltage differential feedback [40]. It is easy to understand that the capacitor voltage differential is equivalent to the capacitor current. This approach eliminates high-resolution current sensors and effectively reduces cost. Hence, this method will be incorporated in the proposed control scheme as a pre-compensator to stabilize the inverter plant. In practice, in order to avoid the high frequency noises caused by the differential calculation, either an analog low pass filter in the sensing circuitry or a digital filter will be helpful.

 K_d denotes the gain along the capacitor voltage differential feedback path. The capacitor voltage differential feedback equivalently modifies the LC filter transfer function by inserting a damping term K_ds into the denominator. Then the compensated inverter plant and corresponding damping ratio can be derived

$$G_c(s) = \frac{1}{L_f C_f s^2 + K_d s + 1}$$
 (3.7)

$$\xi = \frac{K_d}{2\sqrt{L_f C_f}} \tag{3.8}$$

Set $\xi = 0.707$, then $K_d = 2.74 \times 10^{-4}$. Applying Tustin transformation to (3.7), $G_c(z)$ in the discrete time domain is obtained

$$G_c(z) = \frac{0.04096 + 0.08193z^{-1} + 0.04096z^{-2}}{1 - 1.352z^{-1} + 0.5154z^{-2}}$$
(3.9)

3.3.2. Parameters Selection of the Repetitive Controller

a) Determination of z^{k_1}

After $G_c(z)$ is obtained, the next step is to determine the non-causal phase lead compensator z^{k_1} . It is worth noting that the phase delay of $G_c(z)$ is non-linear in relation to the frequency, and meanwhile the real $G_c(z)$ will deviate from (3.9) because of inverter parameter uncertainties and discretization errors. Therefore, z^{k_1} just performs rough compensation within a certain frequency range in order to achieve increased phase margin and enhanced stability.

The magnitude and phase responses of $G_c(z)z^{k_1}$ when $k_1 = 2,3,4$ are illustrated in Figure 3.4. A minimum phase displacement below 10^4 rad/s (1952 Hz) is achieved when $k_1 = 3$. The phase displacement above 10^4 rad/s is uncritical since at higher frequencies the system open loop gain goes below 0 dB. But in reality, the extra delay caused by the DSP software computation, sensing of state variables and gate drive circuitry must be all taken into account. It is typically $1\sim2$ switching/sampling cycles. Hence, the optimum value of k_1 must be further tuned during experimental tests.

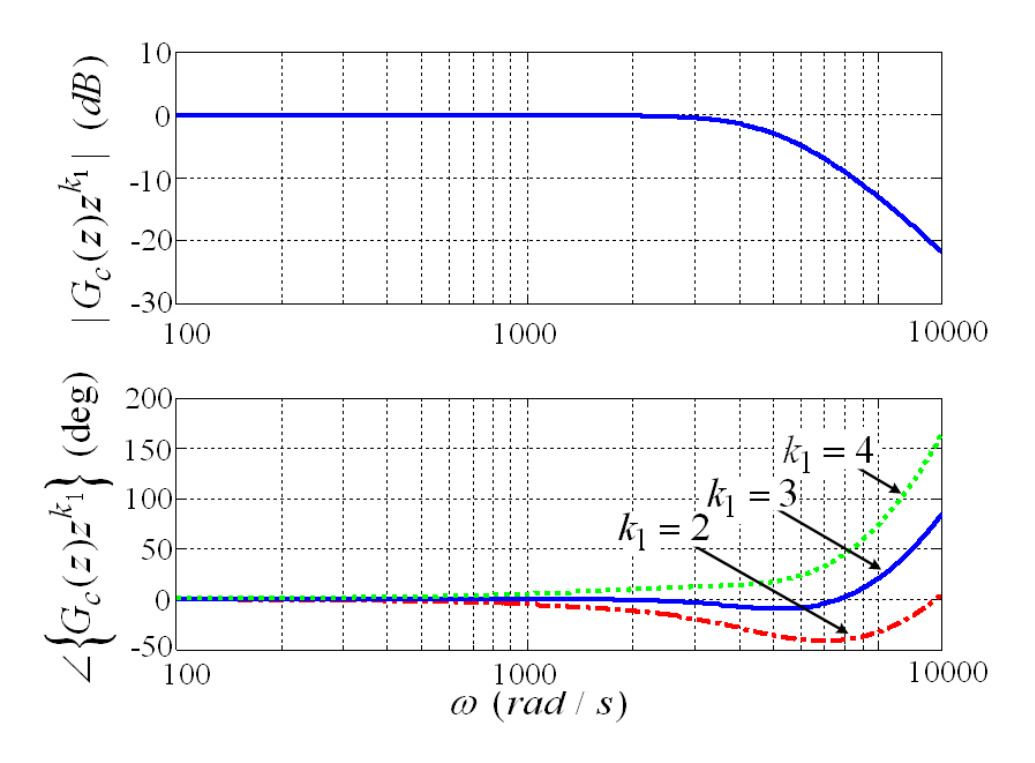


Figure 3.4. Phase lead compensation with different k_1 .

b) Synthesis of $Q(z)z^{k_2}$

As previously discussed, $|1-Q(e^{j\omega T})e^{j\omega k_2T}|/|1-H(e^{j\omega T})|$ directly indicates the steady state tracking error of the stationary frame repetitive controller. Thus, $Q(z)z^{k_2}$ must be designed very close to unity within a wide frequency range. Nevertheless, stability is always the first priority for any controller design. As aforementioned, $Q(z)z^{k_2}$ must reach enough attenuation at high frequencies to guarantee the stability. These two contradictory requirements imply a necessary sacrifice in terms of the steady state error if a poor Q(z) with slow high-frequency roll off is selected.

Digital FIR filter is convenient for design and has been implemented in many existing repetitive controllers. It has intrinsic linear phase as long as its impulse response is either symmetric or anti-symmetric. A linear phase FIR can be precisely compensated by a non-causal

phase lead term to achieve zero phase delay. However, to obtain high performance, which is represented by great flatness in pass band, high magnitude attenuation in stop band, and fast transition in between, the required filter order increases sharply.

On the other hand, linear phase IIR filter requires a much lower order compared to FIR with a given set of parameters, particularly when a high quality filter is to be synthesized [39]. Less multiplier terms results in reduced computation burden and lower cost of implementation.

Elliptic filter is known as the one that has the fastest roll-off rate with the given amount of ripple. Therefore, it is a good candidate for Q(z) synthesis. In order to achieve linear phase, an all-pass phase equalizer can be placed in cascade. In order to reach a good compromise between the computation complexity and filter performance, a 2nd-order elliptic filter (denoted by $Q_e(z)$) and a 2nd-order all-pass phase equalizer (denoted by $Q_a(z)$) will be very practical and good enough. $Q_e(z)$ and $Q_a(z)$ are expressed as

$$Q_e(z) = \frac{b_0 + b_1 z^{-1} + b_2 z^{-2}}{1 + a_1 z^{-1} + a_2 z^{-2}}$$
(3.10)

$$Q_a(z) = \frac{a_2' + a_1'z^{-1} + z^{-2}}{1 + a_1'z^{-1} + a_2'z^{-2}}$$
(3.11)

Benefiting from the phase compensation term z^{k_1} in the loop forward path, the cut-off frequency of $Q_e(z)$ (denoted as ω_e) can be pushed even higher than $1/\sqrt{L_f C_f}$, predicting a good rejection to very high order harmonics. But for stability concerns, ω_e is recommended not to exceed 10^4 rad/s.

For an elliptic filter, the pass-band ripple is typically a conflicting parameter to the roll-off rate in the transition band. Likewise, for an all-pass filter, the phase equalization precision and

the effective compensation range also need trade-off. Therefore, an iterative design approach is necessary for obtaining the optimal $Q_e(z)$ and $Q_a(z)$. Furthermore, it is always important to keep in mind that the group delay of Q(z) must be multiples of the sampling period T such that it can be precisely compensated to zero by z^{k_2} . Table 3.2 lists the details of $Q(z)z^{k_2}$ synthesized in MATLAB.

Table 3.2. Synthesis of $Q(z)z^{k_2}$

	$b_0 = 0.1385, b_1 = 0.2564,$ $\omega_e = 10487 \text{ rad/s}$	
$Q_e(z)$ 2nd-order	$b_2 = 0.1385;$	Pass band ripple: 0.04 dB
	$a_1 = -0.7599, a_2 = 0.2971$ Pass band gain: 0.993~0.9	
	$a_1' = -0.6151,$	Linear phase region:
$Q_a(z)$ 2nd-order	$a_2' = 0.1019$	ω ∈ [0,8816] rad/s
Q(z) 4th-order	$Q(z) = Q_e(z)Q_a(z)$	
z^{k_2}	k ₂ = 5	

The bode plots of the synthesized $Q_e(z)$, $Q_a(z)$, and Q(z) are shown in Figure 3.5. The effective compensation region of $Q_a(z)$ is from 0 to 8816 rad/s (1404 Hz) and the group delay of Q(z) is exactly tuned to be 5 switching/sampling cycles. It is observed that based on a cut-off frequency around 10^4 rad/s, the proposed Q(z) still retains a gain of 0.93 at the frequency of the 19th-order harmonic (1140 Hz).

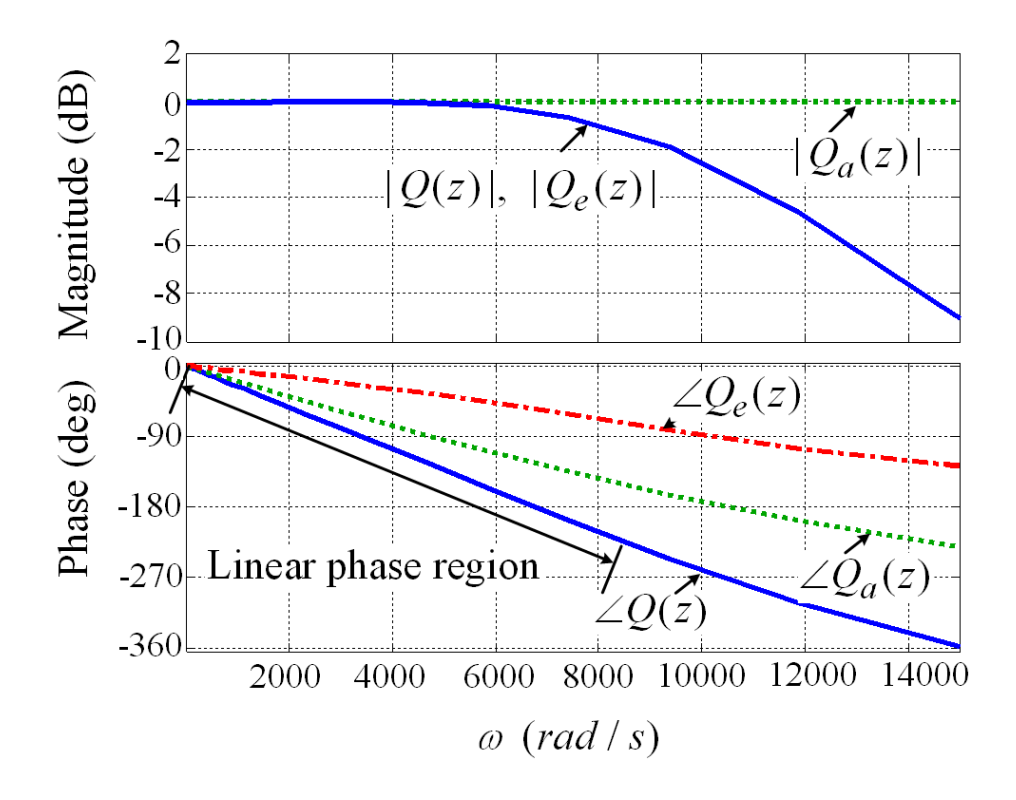


Figure 3.5. Bode plots of $Q_e(z)$, $Q_a(z)$, and Q(z).

c) Selection of K_r

In general, the constant gain K_r is co-designed with $Q(z)z^{k_2}$. A higher cut-off frequency of Q(z) can bring better high-frequency harmonic rejection, but a smaller K_r must be selected accordingly to meet the stability requirement. Unfortunately, reducing K_r will increase $|1-Q(e^{j\omega T})e^{j\omega k_2T}|/|1-H(e^{j\omega T})|$ at lower frequencies, which leads to a larger steady state error in terms of low order harmonic compensations. If Q(z) has a moderate cut-off frequency, the system stability can be guaranteed in a wider range of K_r . Given the Q(z) in Table 3.2, the locus of the vector $H(e^{j\omega T})$ can be plotted in Figure 3.6(a) and 3.6(b), where $K_r=1$ and $K_r=1.8$ respectively.

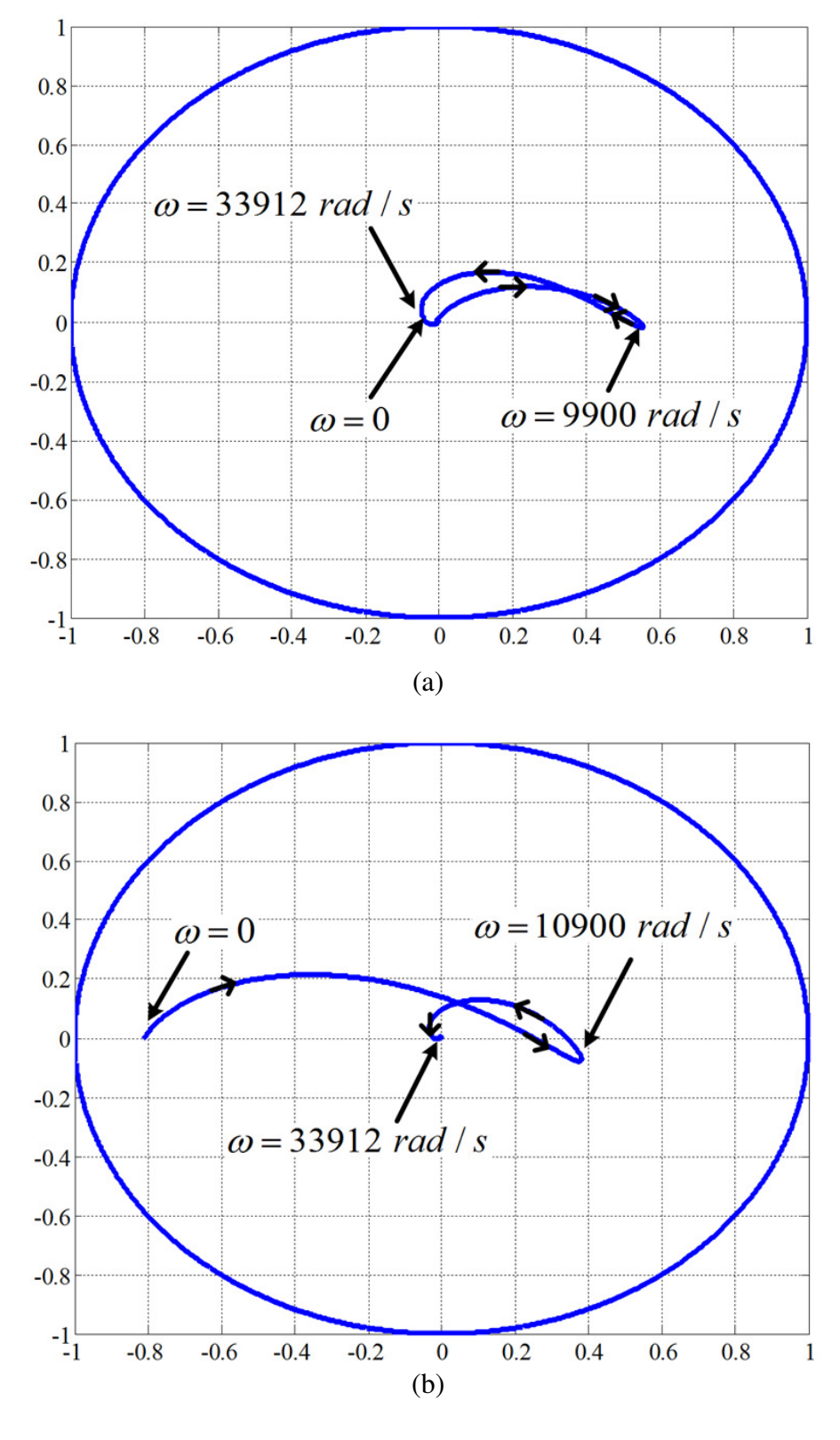


Figure 3.6. Locus of vector $H(e^{j\omega T})$ with different K_r . (a) $K_r = 1$. (b) $K_r = 1.8$.

In both cases, $H(e^{j\omega T})$ is confined within the unity circle, which means the system is stable. But in Figure 3.6(b), the starting point of $H(e^{j\omega T})$ moves towards the stability boundary and thus a smaller stability margin is indicated. In addition, even though a smaller steady state error can be expected with a larger K_r , the dynamic response is sacrificed according to (3.5). In fact, thanks to the close-to-unity gain of Q(z) in its pass band, the steady state error is almost negligible with $K_r = 1$. Therefore, taking both the stability and the dynamic response into account, $K_r = 1$ is the most appropriate choice.

3.3.3. Repetitive Control Using Different Low Pass Filters

It has been found that a FIR filter with lower than 4th order is most frequently selected for Q(z) in previous repetitive controllers. Hence, it is desirable to compare the controller performance with incorporation of the 4th-order FIR and the proposed 4th-order IIR respectively. A 4th-order zero-phase FIR filter for Q(z) is designed

$$Q(z) = 0.0293 + 0.1760z^{-1} + 0.5868z^{-2} + 0.1760z^{-3} + 0.0293z^{-4}$$
(3.12)

 $k_2 = 2$ is selected for zero phase compensation. The 4th-order FIR and the proposed 4th-order IIR have the same peak gain of 0.9975 in the pass band, while the cut-off frequencies are both around $10^4 \, rad \, / \, s$.

Figure 3.7 shows the bode plots of the two cases. It can be observed that the 4th-order IIR has much less magnitude attenuation than the FIR when ω varies from 0 to 7000rad / s.

From Figure 3.2, the transfer function of the repetitive controller can be expressed as

$$R_0(z) = \frac{z^{-N_0}}{1 - Q(z)z^{k_2}} K_r z^{k_1}$$
(3.13)

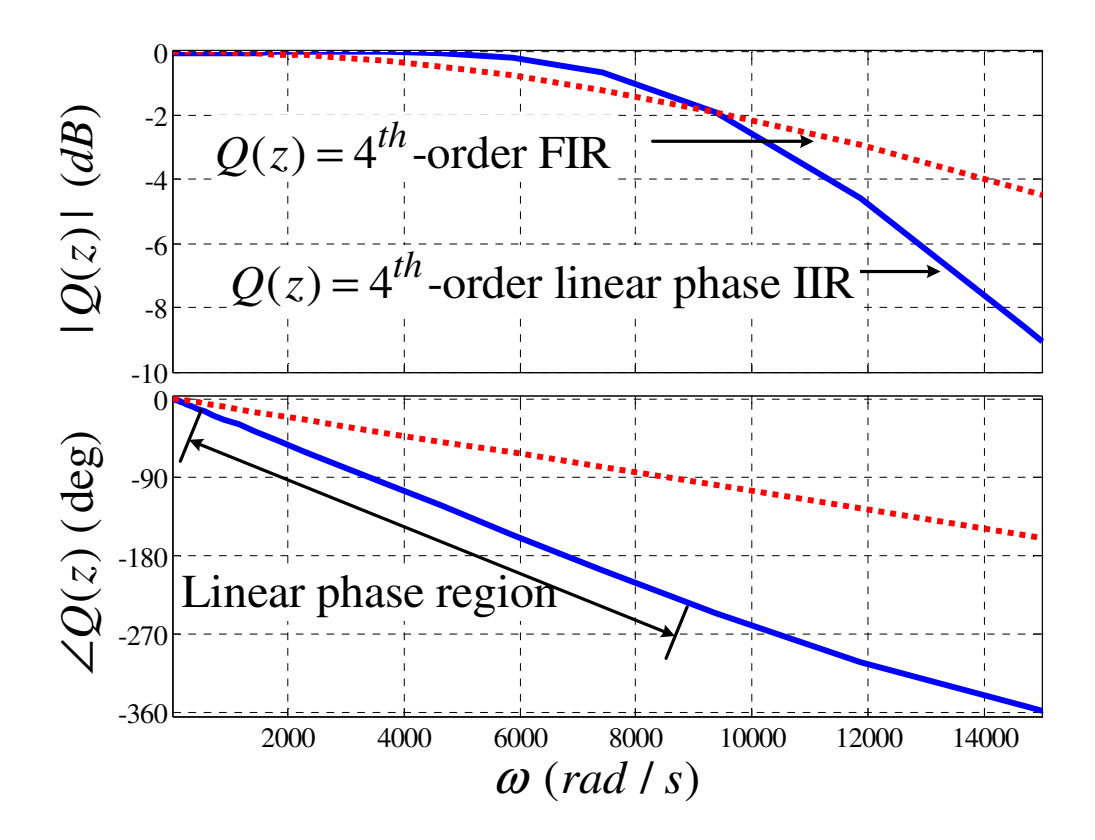


Figure 3.7. Bode plot of Q(z) based on the 4th-order FIR filter and the 4th-order IIR filter.

The open loop gain $|R_0(z)G_c(z)|$ can be plotted as Figure 3.8 shows. The cross-over frequency is $\omega_{cr} = 10^4 \, rad \, / \, s$ for both cases. The magnitude of $|R_0(z)G_c(z)|$ at each harmonic frequency determines the controller's capability of rejection to the corresponding order harmonic disturbance. It can be observed that with incorporation of the 4th-order IIR, $|R_0(z)G_c(z)|$ is maintained higher than +40dB for the harmonics up to 13th order. Even at 19th-order harmonic frequency, $|R_0(z)G_c(z)|$ is still close to +20dB.

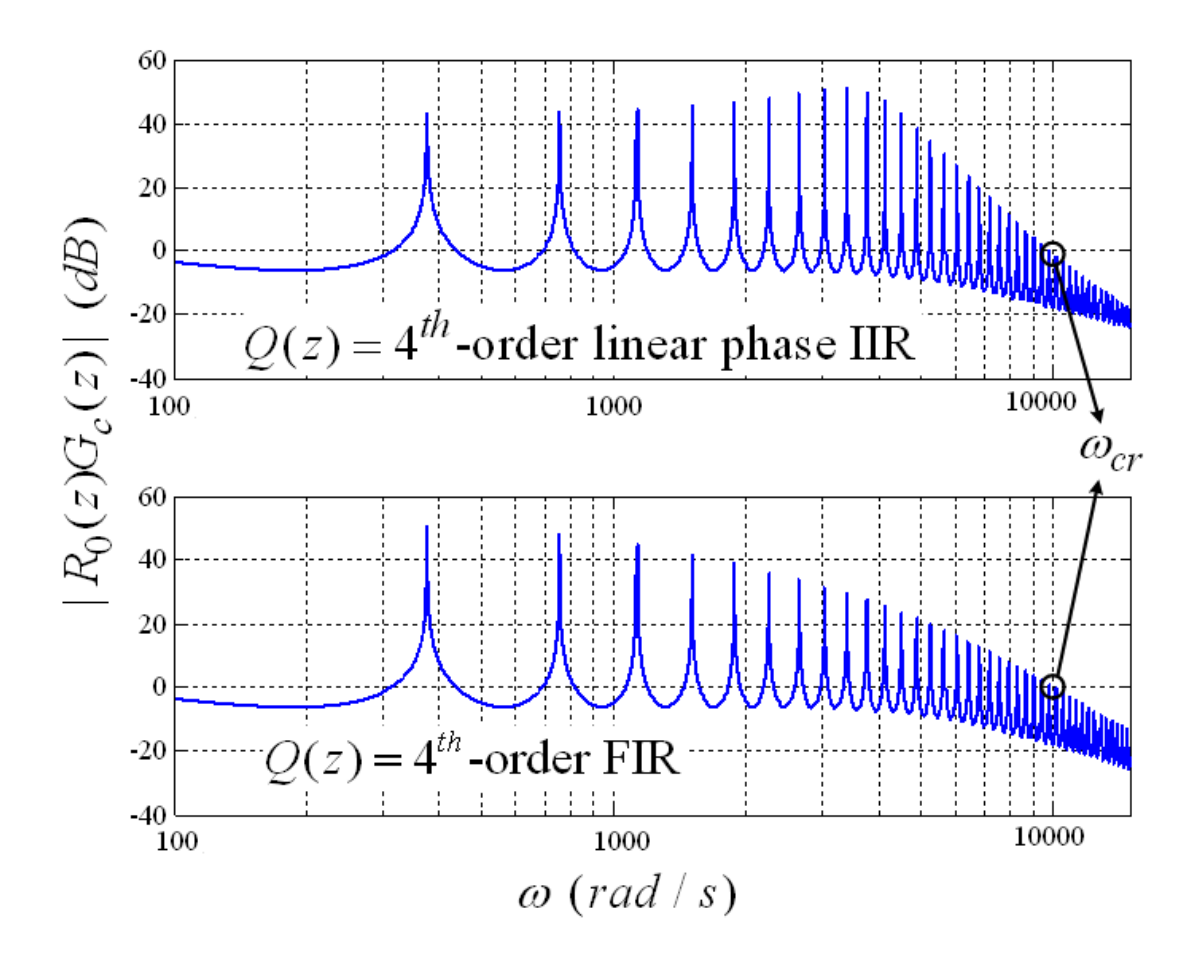


Figure 3.8. Comparison of system loop gain when using the 4th-order FIR and the 4th-order IIR.

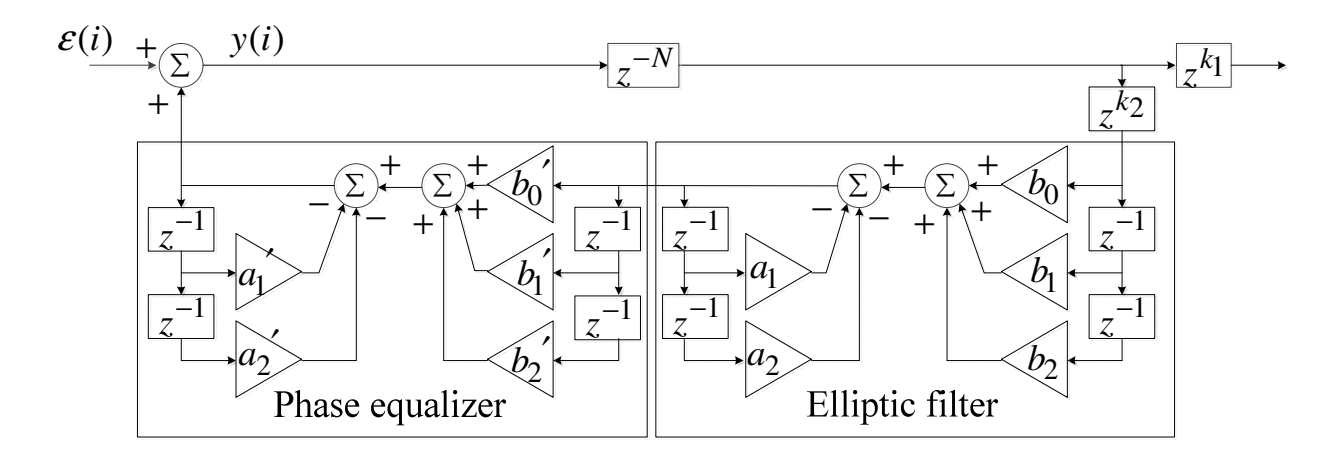


Figure 3.9. Digital implementation structure of the proposed repetitive controller.

On the other hand, when using the 4th-order FIR, $|R_0(z)G_c(z)|$ drops to +20dB at the 13th order and +10dB at the 19th order. Therefore, the proposed 4th-order IIR is much more advantageous than the 4th-order FIR in the repetitive control system.

Figure 3.9 shows the digital implementation structure of the repetitive controller shown in Figure 3.2.

3.4. Experimental Validations

Experiments have been carried out on an 18 kW three-phase inverter prototype. The comparison between the 4th-order FIR filter based RC and the proposed 4th-order IIR filter based RC is shown in Figure 3.10. Steady state waveforms and harmonic spectrums in both cases are provided when the inverter is connected to a severely distorted diode rectifier load. It can be seen that the proposed 4th-order IIR filter based RC is much more superior than the FIR filter based RC. Figure 3.11 shows the steady state waveforms with open loop feed forward control. Figure 3.12 shows the steady state waveforms with a much heavier rectifier load (55%) connected. The output voltage THD is still as low as 1.73%. Figure 3.13 and Figure 3.14 demonstrate the transient responses of the proposed repetitive controller. Due to the one fundamental period delay in the modified internal model, the repetitive controller generally takes several (3~5) fundamental cycles to eliminate the tracking error.

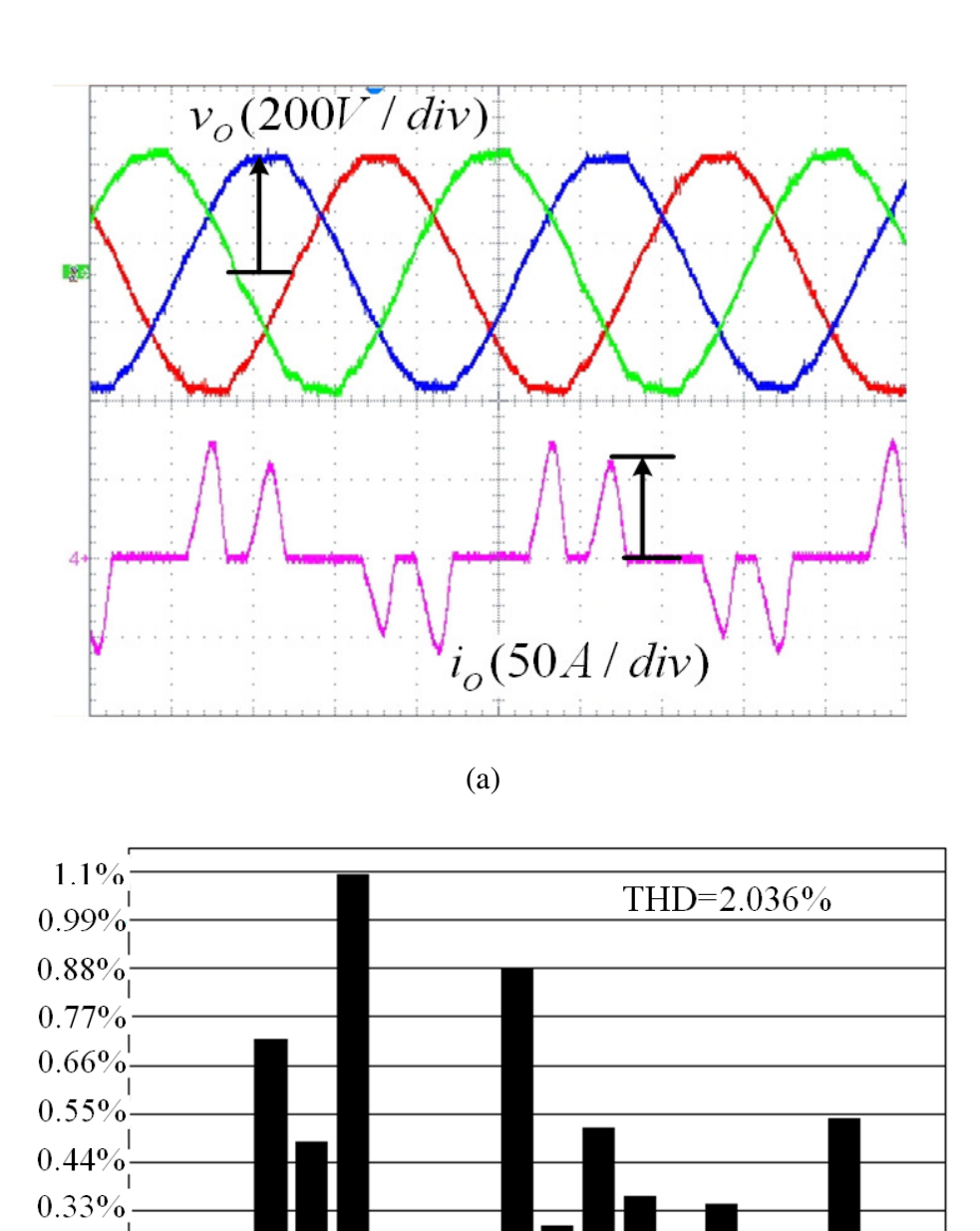


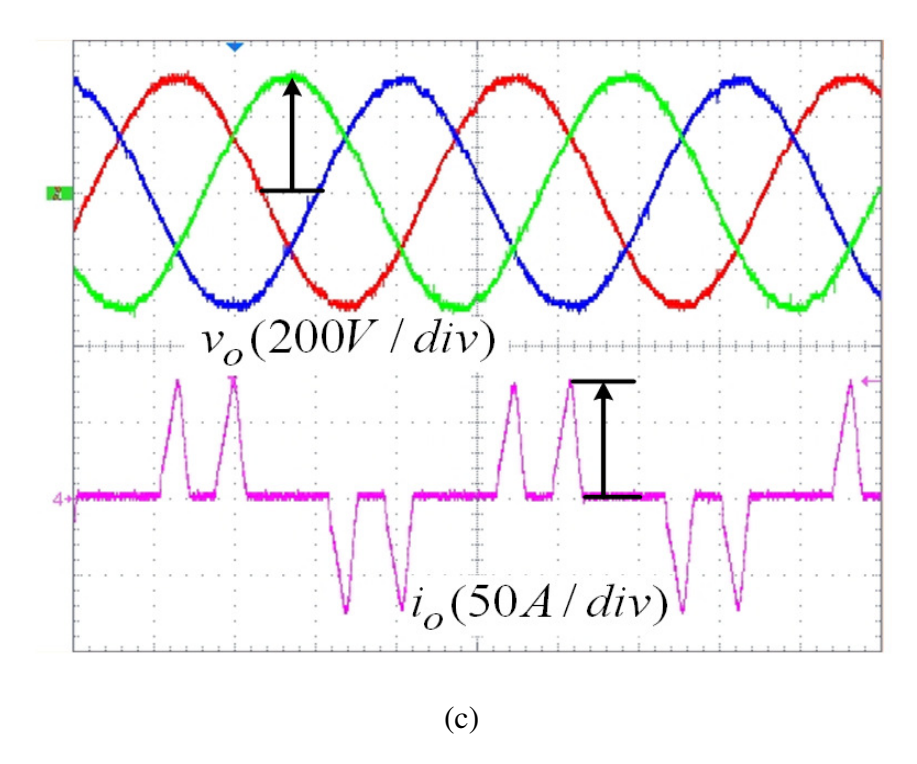
Figure 3.10. Comparison between the FIR filter based RC and the proposed IIR filter based RC (with 6.6 kW pure rectifier load). (a) Steady state outputs when using the 4th order FIR filter. (b) Harmonic spectrum of the inverter output voltage in (a). (c) Steady state outputs when using the proposed 4th order IIR filter. (d) Harmonic spectrum of the inverter output voltage in (c).

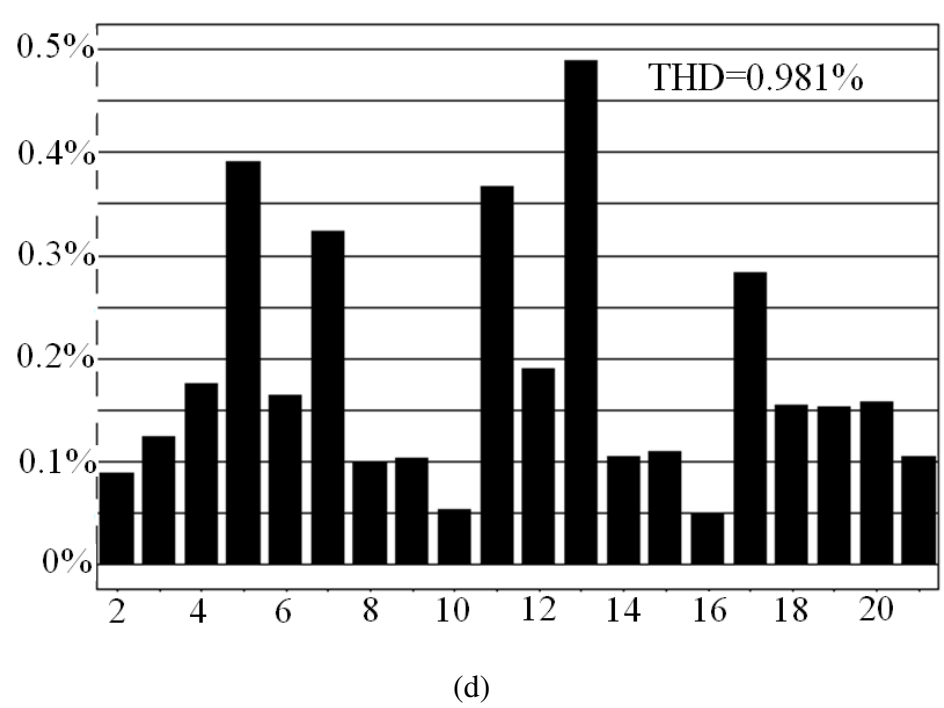
(b)

0.22% 0.11% 0%

Ż

Figure 3.10 (cont'd).





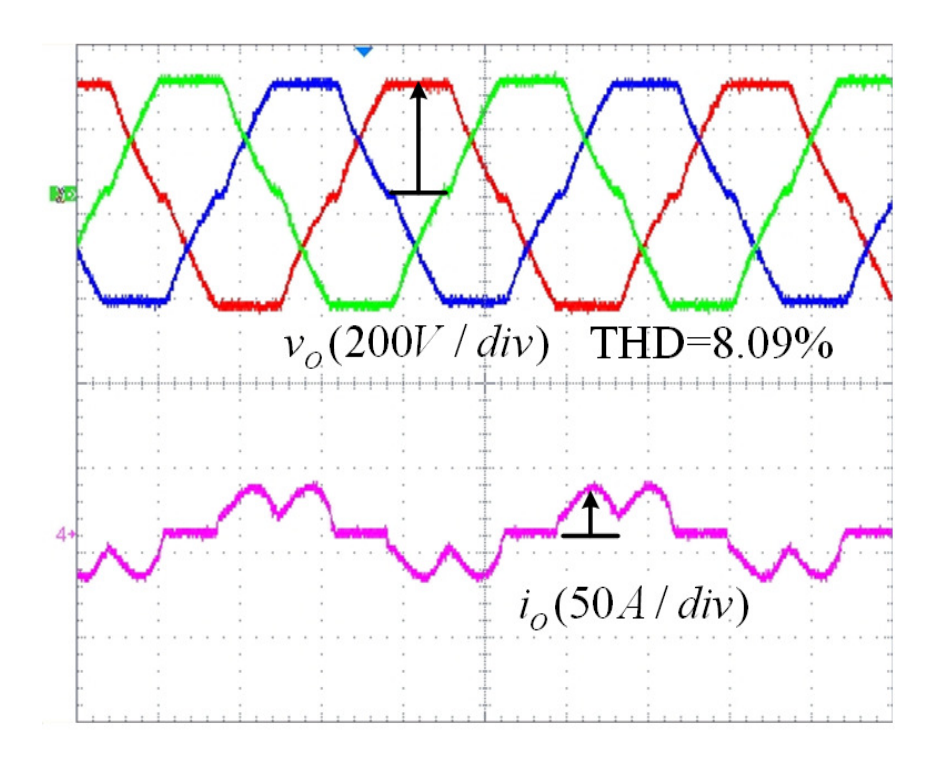


Figure 3.11. Steady state outputs with open loop control (with 6.6 kW pure rectifier load).

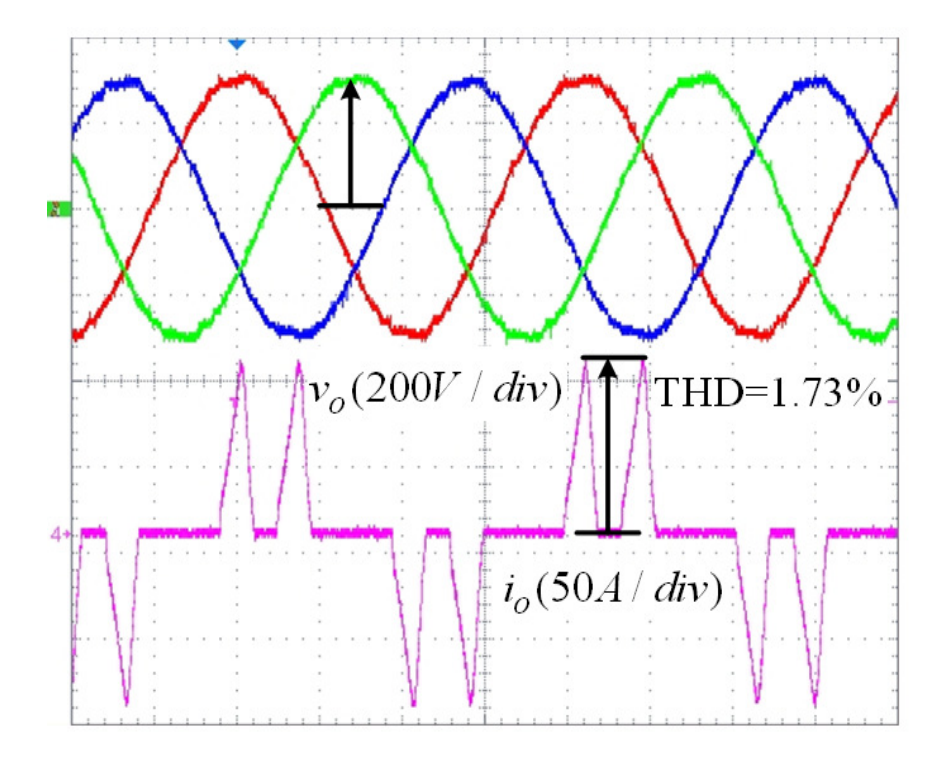


Figure 3.12. Steady state outputs with proposed repetitive control (10 kW pure rectifier load).

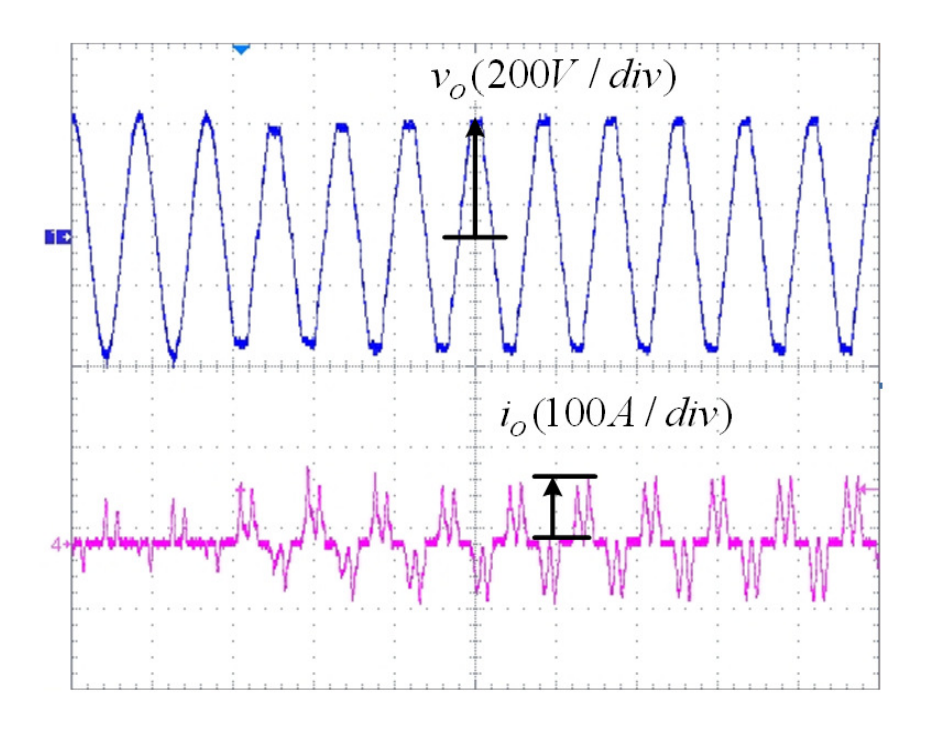


Figure 3.13. Load step change from 2.8 kW to 10 kW (pure rectifier load).

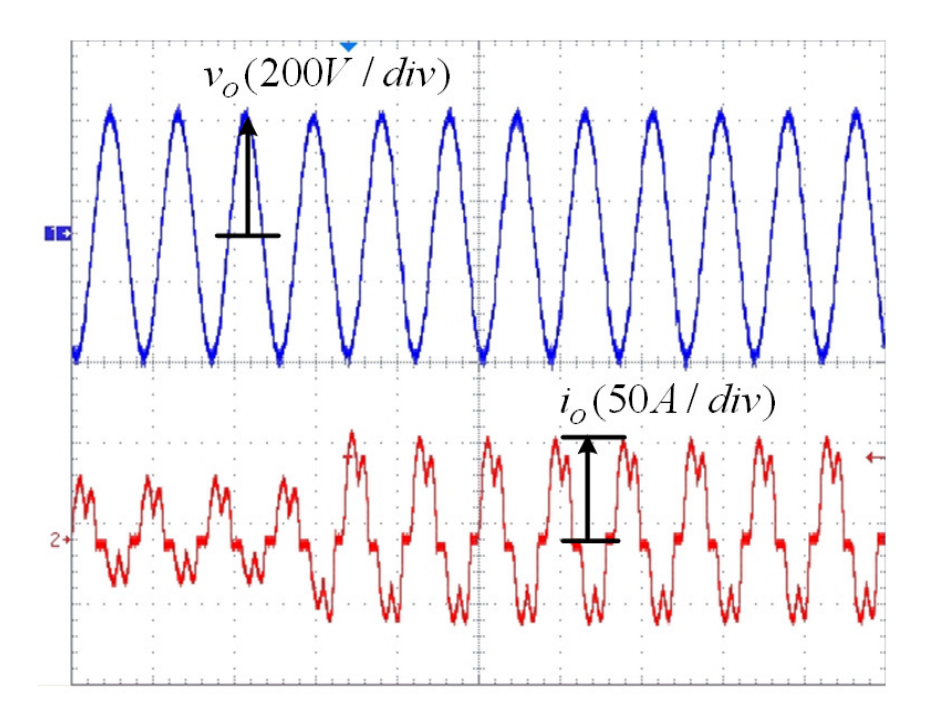


Figure 3.14. Load step change from 7.5 kW to 15 kW (with line inductor connected rectifier load).

3.5. Summary

In this chapter, a high performance repetitive controller is proposed for three-phase UPS inverters. A 4th-order linear phase IIR filter Q(z) is synthesized and placed on the positive feedback path inside the RC. Compared to the low order FIR filters which are commonly used in the existing RCs, the proposed 4th-order IIR filter exhibits great pass band flatness and a fast high frequency roll-off rate. Benefiting from this feature, the compensator S(z) in the control forward path is eliminated and a good stability margin is obtained, which indicates a strong robustness of the controller. More importantly, the proposed RC demonstrates very high loop gains at harmonic frequencies up to the 19th order. Hence, very low output voltage THD can be guaranteed even when a heavily distorted nonlinear load is connected. Even though dynamic response can be improved with the help of the voltage reference feed forward and load disturbance decoupling feed forward, the fundamental period delay in the internal model still slows down the tracking error convergence. In the next chapter, an improved repetitive control technique in terms of the dynamic response will be introduced and discussed.

Chapter 4. Synchronous-Frame Repetitive

Control with Fast Dynamic Response

4.1. Introduction

A high performance repetitive control strategy for three-phase UPS inverters is introduced in last chapter. Outstanding steady state voltage regulation with very low total harmonic distortions has been achieved. However, the control action is postponed by one fundamental period correspondingly, which slows down the dynamic response unavoidably. In order to improve the dynamic response, many improved repetitive controller structures have been proposed and investigated.

As most AC systems only contain odd harmonics in their Fourier series expansions while even harmonics are normally regarded as negligible, repetitive controllers aimed at compensating only the odd harmonics have been proposed [27], [30], [36], [37]. In these odd-harmonic RCs, the time delay is reduced to a half of the fundamental period such that an improvement of the controller dynamic response can be expected. Furthermore, unnecessary compensations on the even harmonics are eliminated in order to avoid the waste of control efforts and the possibility of re-injecting distortions at the even harmonic frequencies. A further progress of repetitive control has been achieved particularly in three-phase applications, by selecting only the $(6n\pm1)$ th (n=0,1,2,...) harmonics for compensation [38]. In [38], the authors start from constructing an RC to compensate all the 6nth (n=0,1,2,...) harmonics in the synchronous frame, and then derive the equivalent stationary-frame controller transfer function according to the frequency

shift mechanism. The $(6n\pm1)$ th-harmonic RC obtains enhanced frequency selectivity and small computation complexity, and the maximum control delay is further reduced to 1/3 of the fundamental period. Nevertheless, under severe conditions, a three-phase AC system may contain not only the $(6n\pm1)$ th (n=0,1,2,...) harmonics but also the triplen harmonics (3nth, n=1,3,5...). In this case, a controller capable of compensating all the odd harmonics would be more desirable.

As a result, in a three-phase AC system, the technical concerns for the repetitive controller design can be summarized as follows.

- Harmonic rejection capability. The controller is expected to reject any possible harmonic distortions under general conditions (balanced, unbalanced, nonlinear, etc.).
- Dynamic response. Auxiliary state feedback controllers can be plugged-in to enhance the dynamic response [22]-[29], [36]. However, with reduced weight of the RC, steady state performance can possibly be sacrificed. Therefore, an RC with fast response to disturbances itself, or in other words, an RC with minimized internal time delay, is very desirable.

In this chapter, an improved repetitive control scheme for three-phase UPS inverters is proposed. Instead of using the stationary-frame implementation, the RC as discussed previously is placed into three different synchronous frames, where the odd harmonics can be all transformed to the 6n (n = 0,1,2,...) multiples of the fundamental frequency. Resultantly, by designing the repetitive controller as a compensator for 6nth (n = 0,1,2,...) harmonics in the synchronous frames, the harmonic distortions under severely unbalanced and nonlinear loads can be well rejected. More importantly, the repetitive control time delay is minimized to 1/6 of the

fundamental period. A significant improvement of the dynamic response is obtained without sacrificing any steady state performance.

4.2. Repetitive Controller in Synchronous Rotating Frames

In an AC system, the d-q reference transformation substantially performs the frequency shift on all system signals. Hence, any harmonic regulators designed in synchronous d-q frames will behave as frequency-shifted transfer functions when viewing from the stationary frame. This characteristic associated with synchronous frame transformation has been utilized skillfully for both voltage and current regulations of PWM inverters [14], [17], [18].

Before embarking on the controller design in synchronous frames, it is very important to get idea of the frequency-shift mechanism when converting signals from the stationary frame to a synchronous rotating frame. Assume ω_0 is the fundamental frequency. Generally speaking, a balanced three-phase AC system only contains $(6n\pm1)$ th (n=0,1,2...) harmonics. But in the synchronous frame rotating at $+\omega_0$, the $(6n\pm1)\omega_0$ (n=0,1,2...) components are all shifted to the multiples of $6\omega_0$. This useful feature significantly simplifies the synchronous-frame harmonic regulator design under balanced conditions: only the 6nth (n=0,1,2...) harmonics need to be compensated.

However, a good three-phase UPS inverter system must meet the voltage regulation requirement under both balanced and unbalanced load conditions. When the load is unbalanced and nonlinear, harmonics will include all the odd-order components, each of which contains both the positive sequence and the negative sequence (assume that the system discussed in this chapter does not have the neutral path and thus no zero sequence harmonic exists.). Therefore, not only are the 6nth (n = 0,1,2...) harmonics visible in the synchronous frame rotating at $+\omega_0$

but also other orders of harmonics. Consequently, designing regulators for 6nth (n = 0,1,2...) harmonics in only one rotating frame will be inadequate.

Table 4.1 Harmonic Sequences In Unbalanced Three-Phase AC Systems

Harmonic order in	Sequence	Harmonic order in synchronous frames rotating at $\omega_{k\pm}(k=1,3)$		
stationary frame		$\omega_{l+} = +\omega_0$	$\omega_{l-} = -\omega_0$	$\omega_{3+} = +3\omega_0$
1	Positive	0	-(Note 1)	-
	Negative	-	0	-
3	Positive	-	-	0
	Negative	-	-	6
5	Positive	-	6	-
	Negative	6	-	-
7	Positive	6	-	-
	Negative	-	6	-
9	Positive	-	-	6
	Negative	-	-	12
11	Positive	-	12	-
	Negative	12	-	-
13	Positive	12	-	-
	Negative	-	12	-
15	Positive	-	-	12
	Negative	-	-	18
17	Positive	-	18	-
	Negative	18	-	-
19	Positive	18	-	
	Negative	-	18	-

Note 1: "-" stands for harmonic orders other than 6nth (n = 0,1,2...).

Now consider three different synchronous frames. Define the three frames as Frame #1 (rotating at $+\omega_0$), Frame #2 (rotating at $-\omega_0$), and Frame #3 (rotating at $+3\omega_0$), respectively. Table 4.1 summarizes the harmonic sequences (up to the 19th order) and frequency shifts in

these three frames in an unbalanced system. It is worth noting that all the positive and negative sequence components of the $(6n\pm1)$ th (n=0,1,2...) harmonics are substantially converted to 6nth (n=0,1,2...) harmonics in either Frame #1 or Frame #2. Likewise, the triplen harmonics are all shifted to $6n\omega_0$ (n=0,1,2...) in Frame #3. As a result, if regulators for 6nth (n=0,1,2...) harmonics are placed in all of the three selected synchronous frames, the system will be capable of coping with unbalanced conditions.

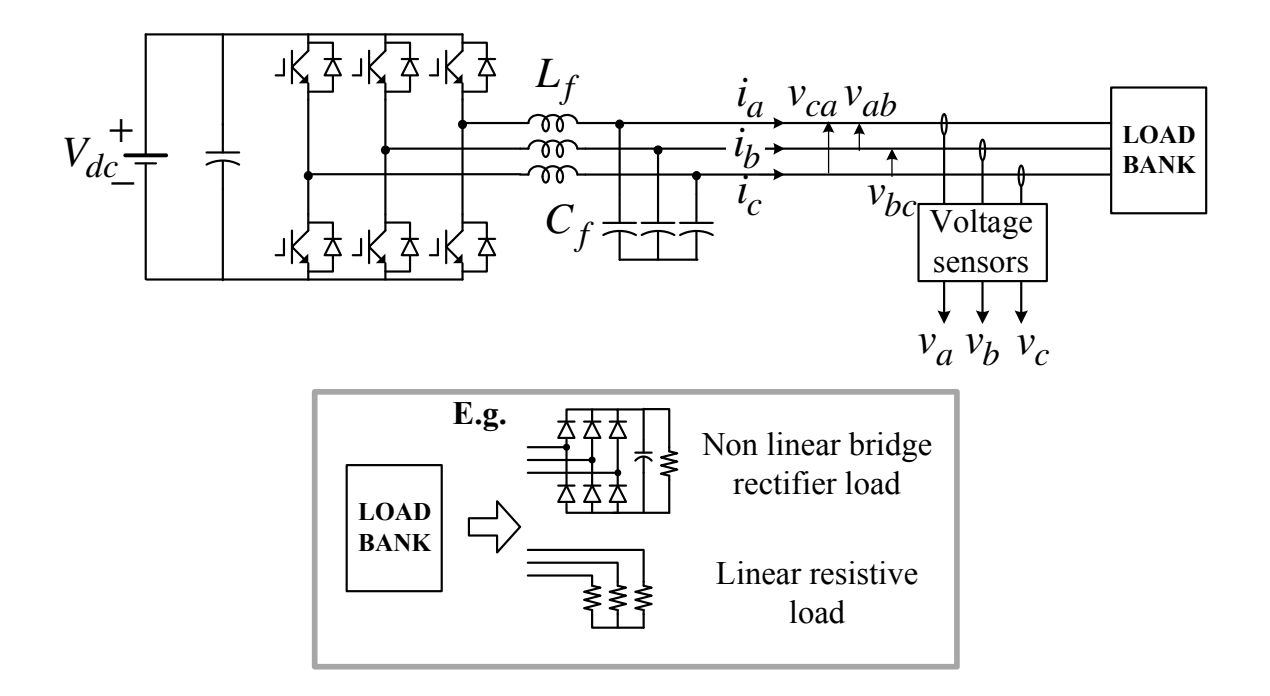


Figure 4.1. System configuration of the three-phase UPS inverter.

Come back to the repetitive control. The conventional repetitive controllers are designed for rejection of all the odd and even harmonics at the price of introducing a fundamental period delay. However, from the above discussions, the required time delay can be significantly reduced from one fundamental period to its 1/6, with the repetitive controller placed into the three synchronous frames given in Table 4.1. Meanwhile, the controller still preserves the capability of rejecting all the possible harmonics in the system.

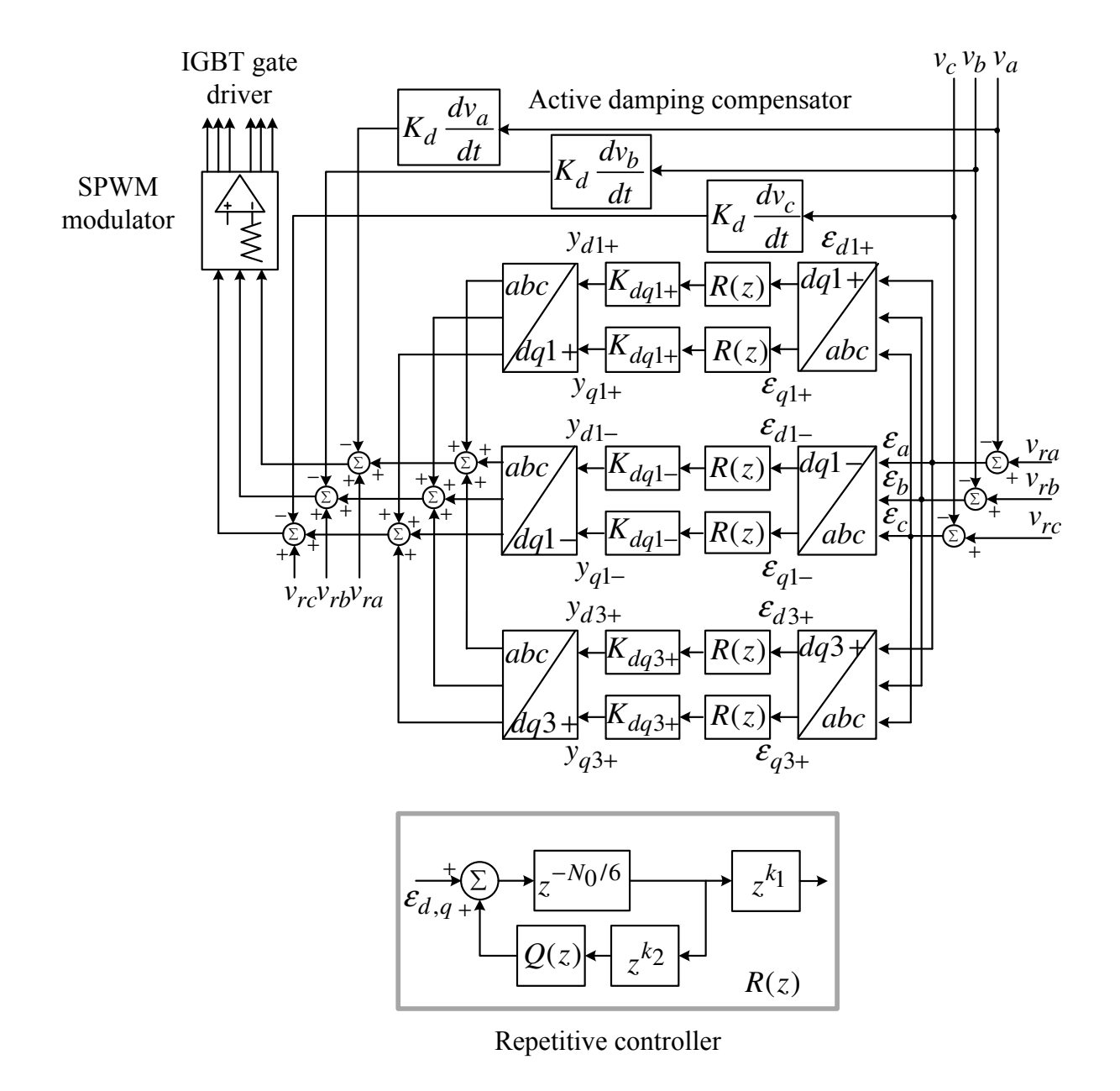


Figure 4.2. Proposed synchronous-frame repetitive control scheme.

The system configuration of the three-phase UPS inverter is shown in Figure 4.1. The proposed synchronous-frame repetitive control scheme is shown in Figure 4.2. It incorporates the RC illustrated in Figure 3.2 into the three synchronous frames. R(z) denotes the RC transfer function. N is reduced to $N_0/6$. The constant gain associated with each RC in each forward path can be extracted out and assigned as K_{dq1+} , K_{dq1-} , and K_{dq3+} respectively.

As a result, the process of the synchronous-frame RC design can be summarized as: 1) Design the RC based on the conventional stationary-frame structure as shown in Figure 3.2; synthesize Q(z) and tune the parameters of k_1 , k_2 and K_r , respectively. 2) Plug it into the three synchronous frames rotating at $+\omega_0$, $-\omega_0$, and $+3\omega_0$, respectively; assign N as $N_0/6$. 3) Perform a fine tuning on K_{dq1+} , K_{dq1-} and K_{dq3+} , respectively.

4.3. Controller Magnitude-Frequency Response

Plug the repetitive controller into the three synchronous frames rotating at $+\omega_0$, $-\omega_0$, and $+3\omega_0$, respectively, and assign $N=N_0$. R(z) shown in Figure 4.2 can be described as

$$R(z) = \frac{z^{-N_0/6}}{1 - Q(z)z^{k_2}z^{-N_0/6}} z^{k_1}$$
(4.1)

Let us start from considering a simple case: the three-phase system is balanced. From Chapter III, it is known that the repetitive controller in Frame #1 is adequate to reject all the $(6n\pm1)$ th (n=0,1,2...) harmonics. In this case, K_{dq1+} can be selected as equal to K_r ($K_r=1$), and K_{dq1-} , K_{dq3+} can be simply set to zero.

Now consider a more general case that the load is both unbalanced and nonlinear. Under this condition, K_{dq1-} and K_{dq3+} should no longer be zero. The RC in Frame #1 combined with the one in Frame #2 cancels all the positive and negative sequence components of $(6n\pm1)$ th (n=0,1,2...) harmonics. Meanwhile, the RC in Frame #3 compensates all the triplen harmonics. It is worth noting that the selection of K_{dq1+} , K_{dq1-} and K_{dq3-} is always restricted by the stability requirement and the amount of unbalanced power is considerably lower than the

balanced power in most cases. Therefore, it is reasonable to assign K_{dq1-} and K_{dq3+} with smaller weight compared to K_{dq1+} . In practice, $K_{dq1+}=1$ and $K_{dq1-}=K_{dq3+}=0.3$ are selected.

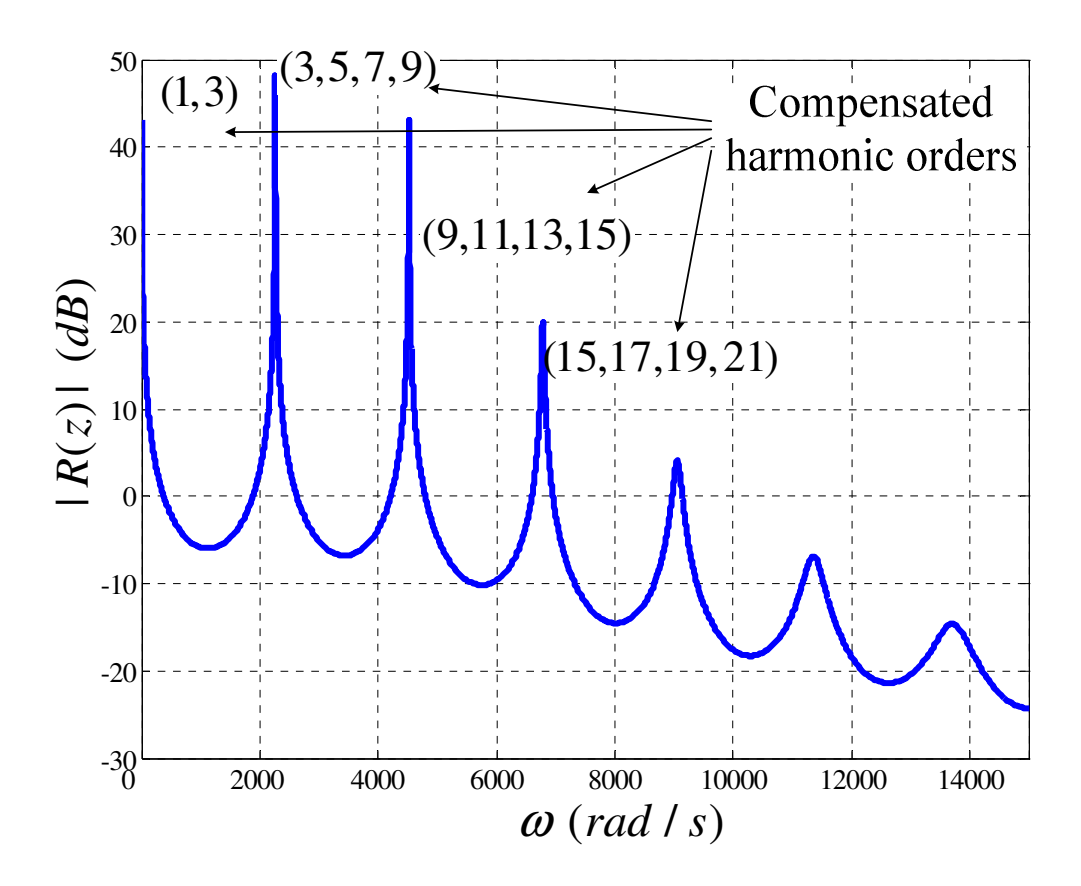


Figure 4.3. Frequency response of |R(z)|.

Once K_{dq1+} , K_{dq1-} and K_{dq3+} are determined, the magnitude of |R(z)| directly affects the controller's harmonic rejection capability. |R(z)| can be plotted as shown in Figure 4.3. From Figure 4.3, the first three peaks are higher than +40dB and compensate all the odd harmonics up to the 13th order. The 4th peak of |R(z)| is around +20dB and compensates the 15th, 17th, and 19th harmonics. Hence, the proposed controller obtains a good rejection to the high order harmonics.

4.4. Simulation and Experimental Results

All the simulation and experimental results are carried out based on the 18 kW three-phase UPS inverter system depicted in Figure 4.1. The system parameters have been given in Table 3.1. One 16-bit fixed-point processor TI TMS320LF2407 is used to control the system in the experiment.

4.4.1. Compensation of Unbalanced Nonlinear load

The capability of the proposed synchronous-frame RC to reject harmonics under unbalanced nonlinear load is verified by the simulation and experimental results shown in Figure 4.4 and Figure 4.5, respectively. The output line-to-line voltages are denoted by v_{ab} , v_{bc} and v_{ca} , respectively. i_a , i_b and i_c represent the load currents. The phase voltage tracking errors are represented by ε_a , ε_b and ε_c , respectively. In Figure 4.4, a 15 kW balanced three-phase resistive load is connected to the inverter output. In addition, a 3 kW single-phase bridge rectifier load is connected across Phase a and Phase b in order to create the unbalance and nonlinearity. Three cases are simulated and compared, which are 1) the RC is implemented in Frame #1 only (Figure 4.4(a)); 2) the RC is implemented in both Frame #1 and Frame #2; 3) the RC is implemented in all the three synchronous frames (Figure 4.4(c)). It can be observed that only when the repetitive controller is incorporated into all the three synchronous frames simultaneously, the voltage tracking errors can be greatly minimized.

Similar results are also obtained from the experiment. In Figure 4.5, a 2.6 kW single-phase bridge rectifier load is connected between Phase a and Phase b. Considering that the harmonic distortions are mainly contributed by the unbalanced nonlinear portion of the load, the resistive load used in the simulation is removed in this case.

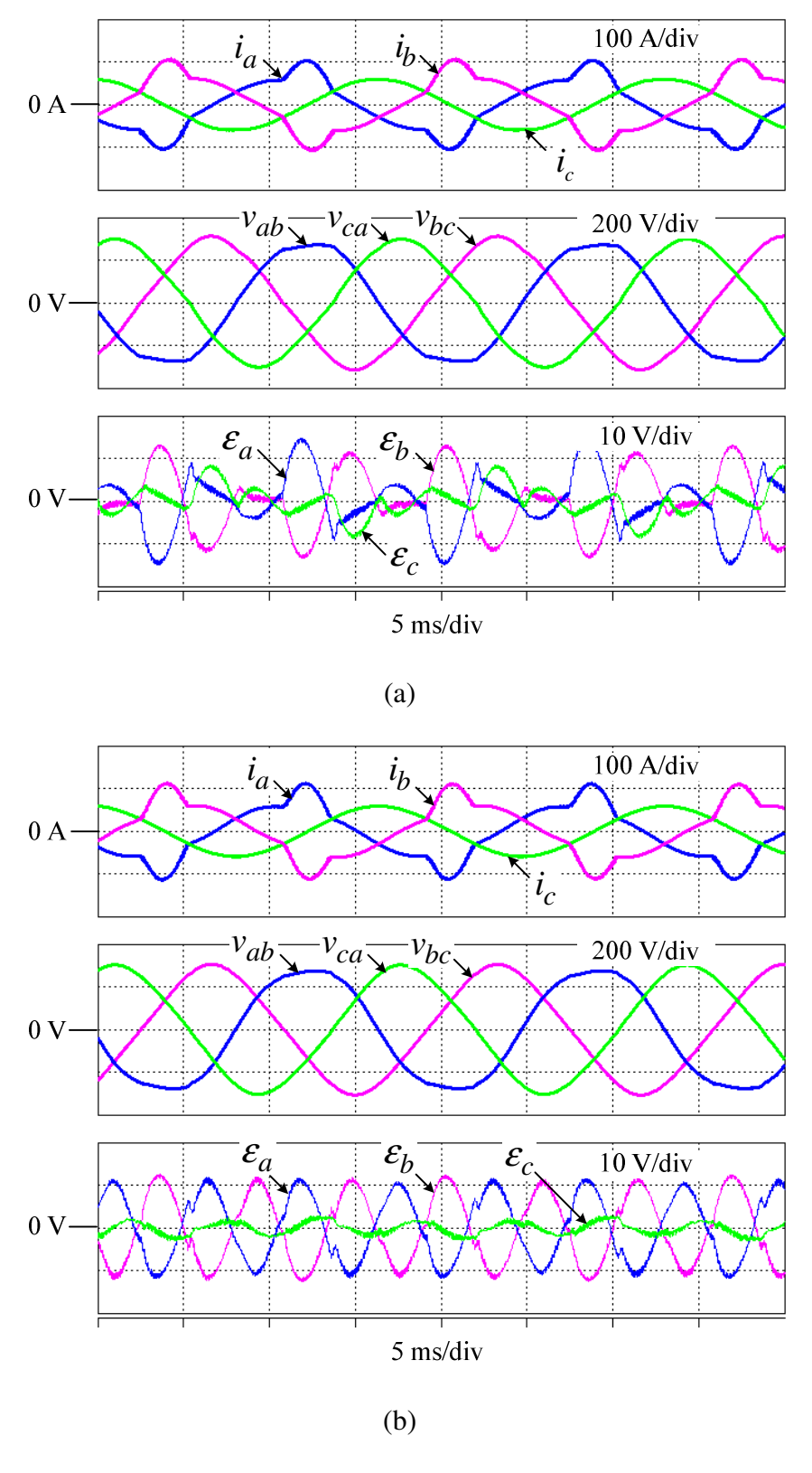


Figure 4.4. Simulated steady state responses under unbalanced nonlinear load when the RC is implemented in (a) Frame #1 only, (b) Frame #1 & Frame #2, and (c) all the three synchronous frames, respectively.

Figure 4.4 (cont'd).

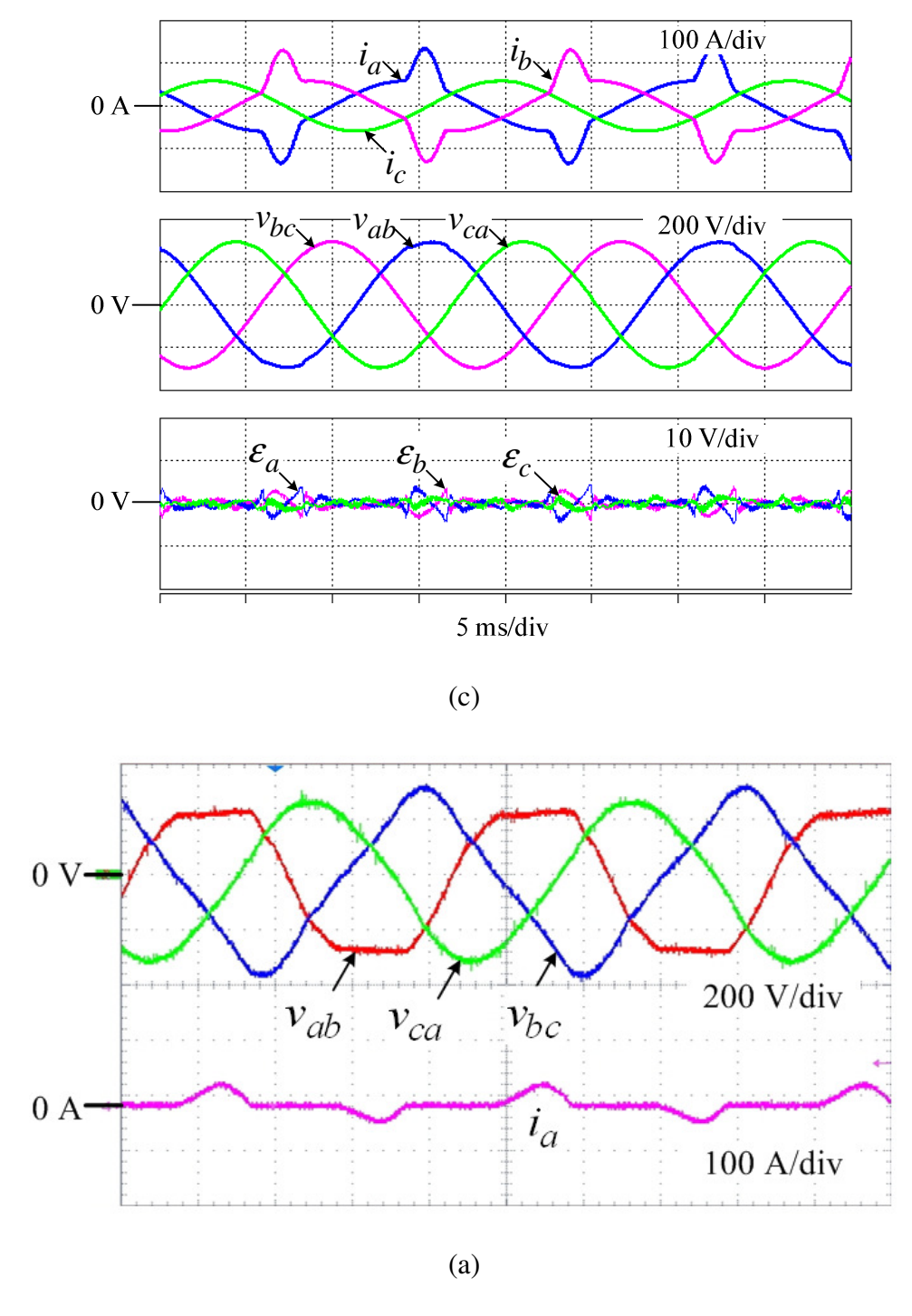
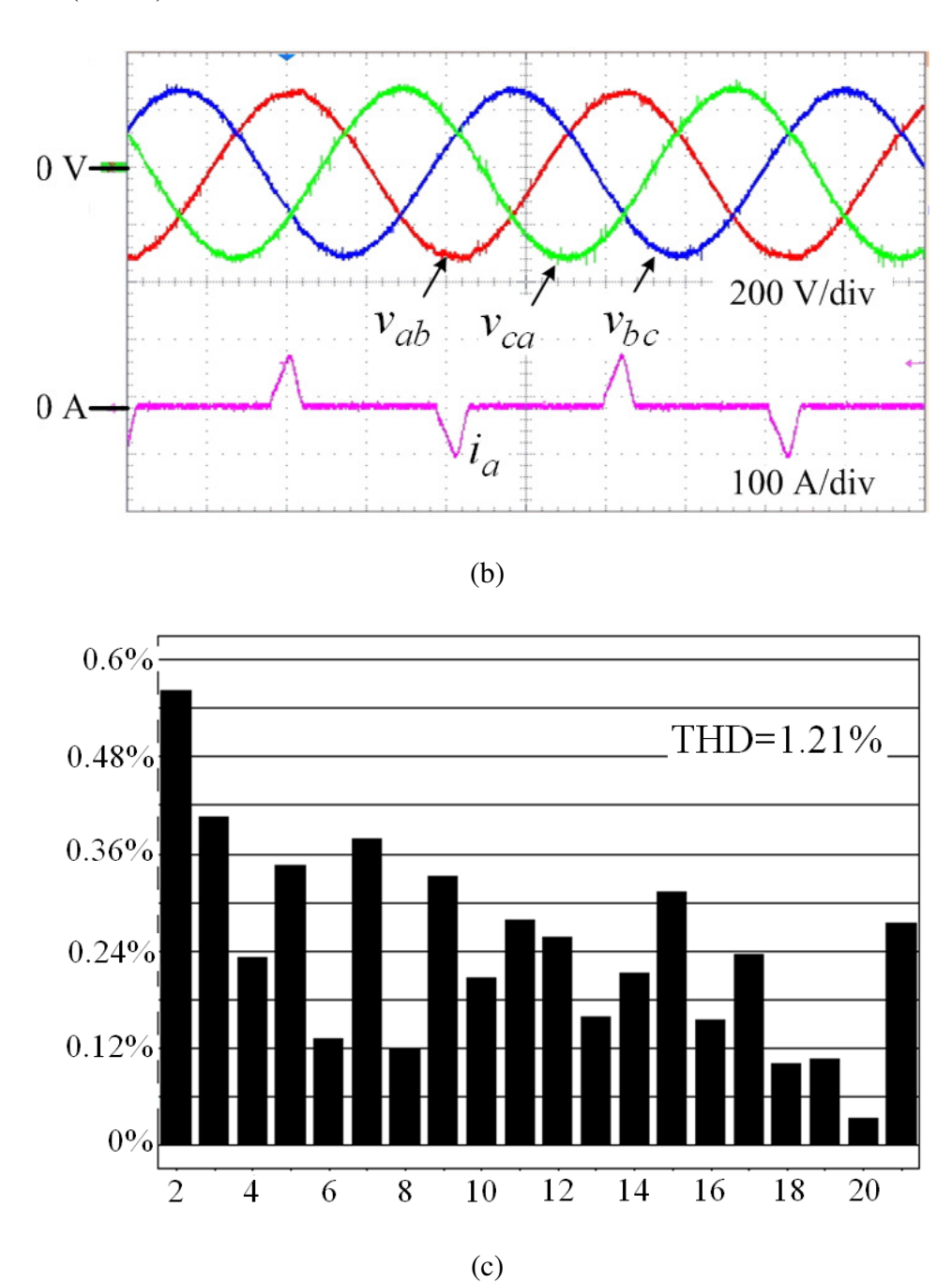


Figure 4.5. Experimental results with unbalanced nonlinear load when the RC is implemented in (a) Frame #1, (b) all the three synchronous frames, (c) harmonic spectrum of the voltage in (b).

Figure 4.5 (cont'd).



Experimental tests are performed with the RC implemented in Frame #1 only (Figure 4.5(a)) and all the three frames (Figure 4.5(b) and (c)), respectively. It can be seen that the experimental results agree with the simulated waveforms very well. By implementing the proposed controller,

the steady state voltage THD is 1.21%, which indicates excellent harmonic compensations for the unbalanced nonlinear load.

4.4.2. Compensation of Balanced load

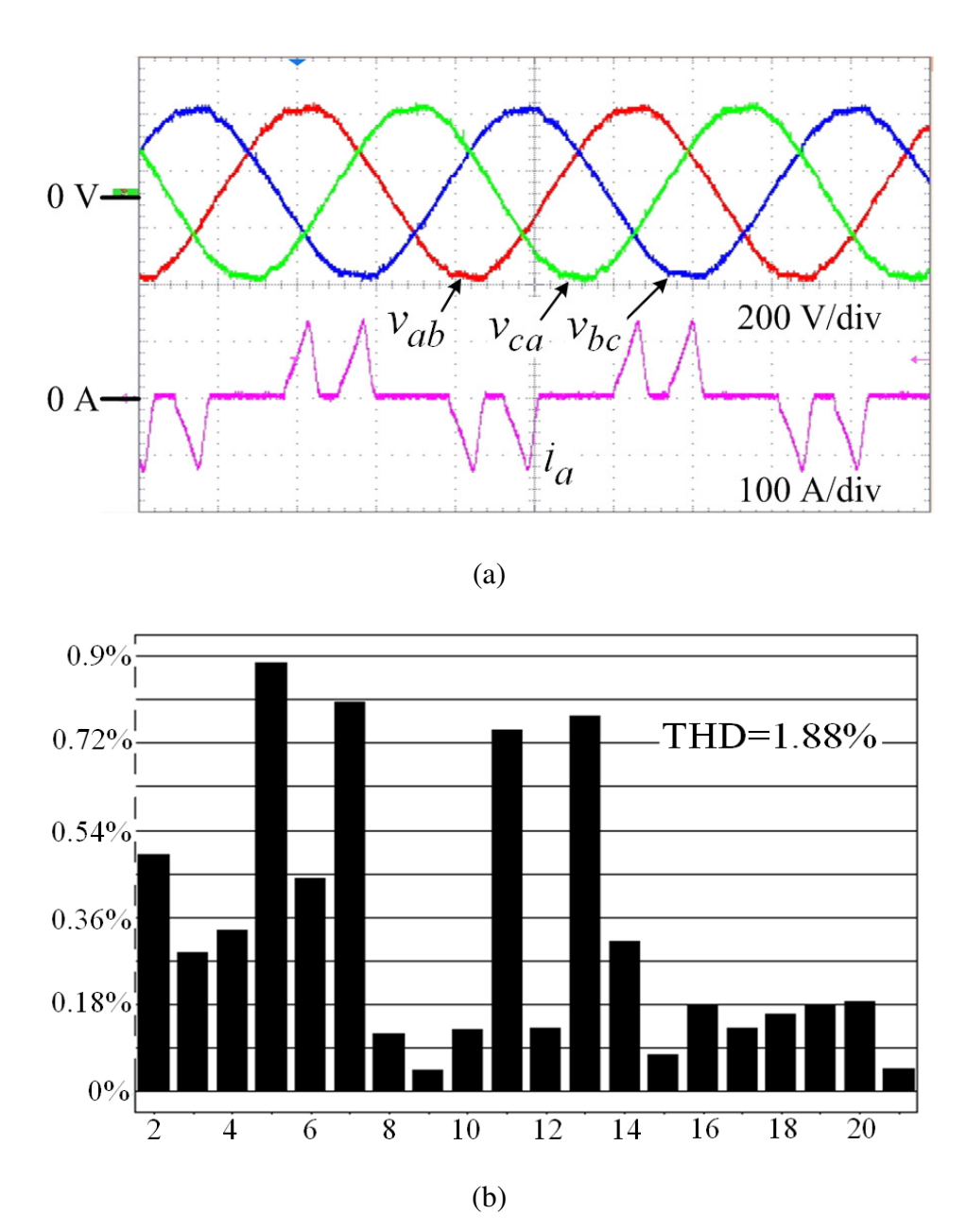


Figure 4.6. Experimental results with a balanced nonlinear load using the proposed synchronous-frame RC. (a) Steady state responses. (b) Harmonic spectrum of the voltage in (a).

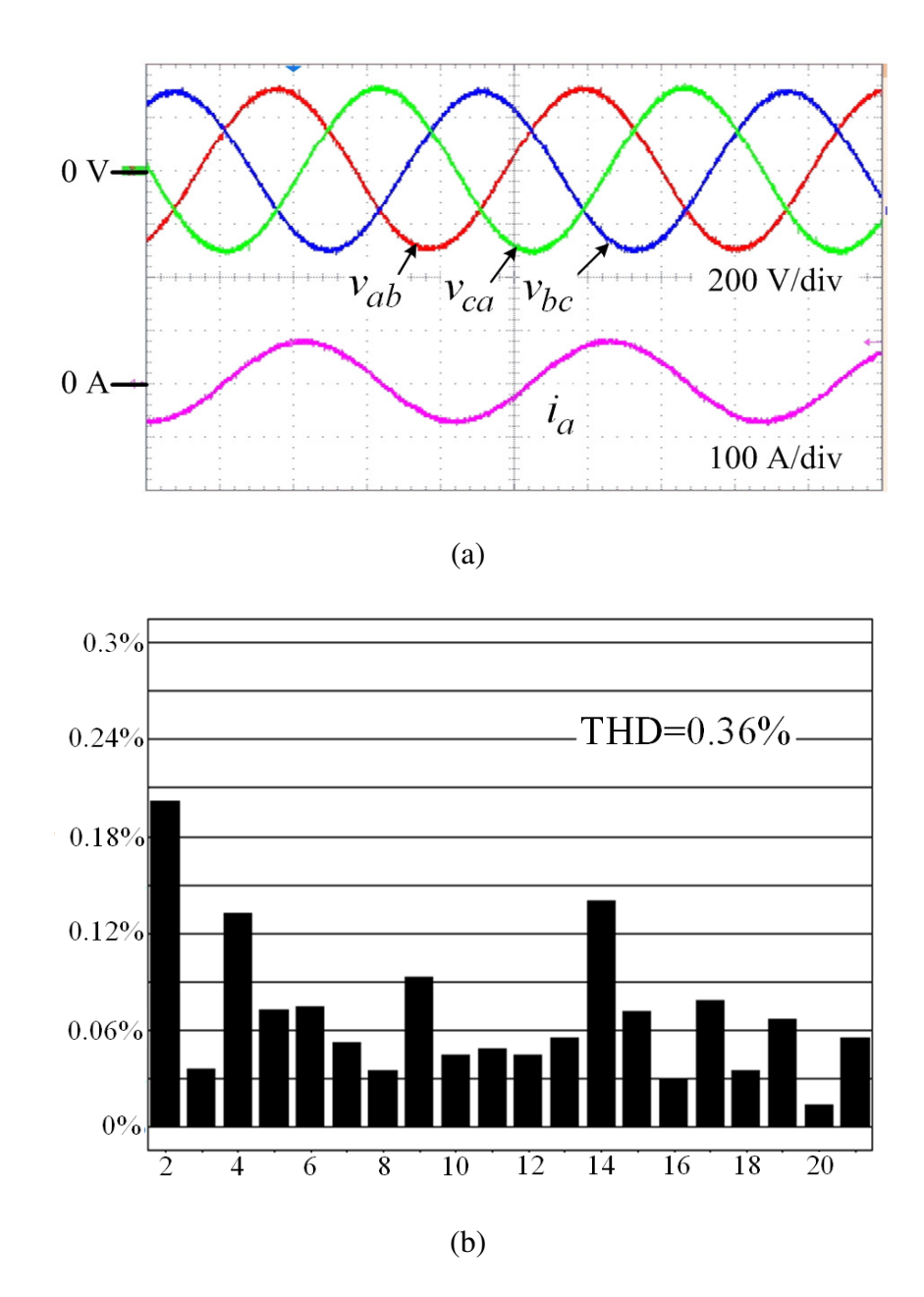


Figure 4.7. Experimental results with a balanced resistive load using the proposed synchronous-frame RC. (a) Steady state responses. (b) Harmonic spectrum of the voltage in (a).

The steady state operation of the inverter when connected with a three-phase bridge rectifier load is shown in Figure 4.6. 2/3 of the nominal power (12kW) is reached. Under such an extreme load condition, the output current exhibits a crest factor as high as 4.2. It can be seen that a very low voltage THD (1.88%) is still guaranteed. When the inverter feeds a balanced three-phase

resistive load at the nominal power (18 kW), an ultra-low THD of 0.36% is demonstrated, as shown in Figure 4.7.

4.4.3. Transient Responses under Load Step Change

To validate the controller's dynamic response, simulation and experimental results are provided in Figure 4.8-Figure 4.10. In Figure 4.8 and Figure 4.9, a step-changed three-phase bridge rectifier load is implemented. The RC is first adopted based on the conventional stationary-frame architecture (depicted in Figure 3.2) where $N=N_0$ and $K_r=1$. Results are obtained in Figure 4.8(a) and Figure 4.9(a). Then, comparisons are made by relocating the RC into Frame #1-Frame #3 in which $N = N_0 / 6$, $K_{dq1+} = 1$, and $K_{dq1-} = K_{dq3+} = 0.3$, as shown in Figure 4.8(b) and Figure 4.9(b). The same parameters of Q(z), k_1 and k_2 as selected in Chapter 3 are applied in both cases. It can be seen that the dynamic performance of the proposed synchronous-frame approach is much superior over the conventional RC scheme. Under the step change of a heavily distorted nonlinear load, the load current distortion is apparently shaped by the instantaneous voltages. Slow convergence of the voltage errors also causes slow load current recovery and thus results in more non-repetitive distortions during the transients. This effect adversely affects the controller dynamic responses even further when the conventional repetitive control architecture is applied. The transient responses of the proposed synchronous-frame RC under a balanced linear resistive load are shown in Figure 4.10. A step change from zero to the nominal power (18 kW) is performed. From Figure 4.8-Figure 4.10, the feature of fast transient responses of the proposed controller is verified; a good agreement between the simulation and experimental results is obtained.

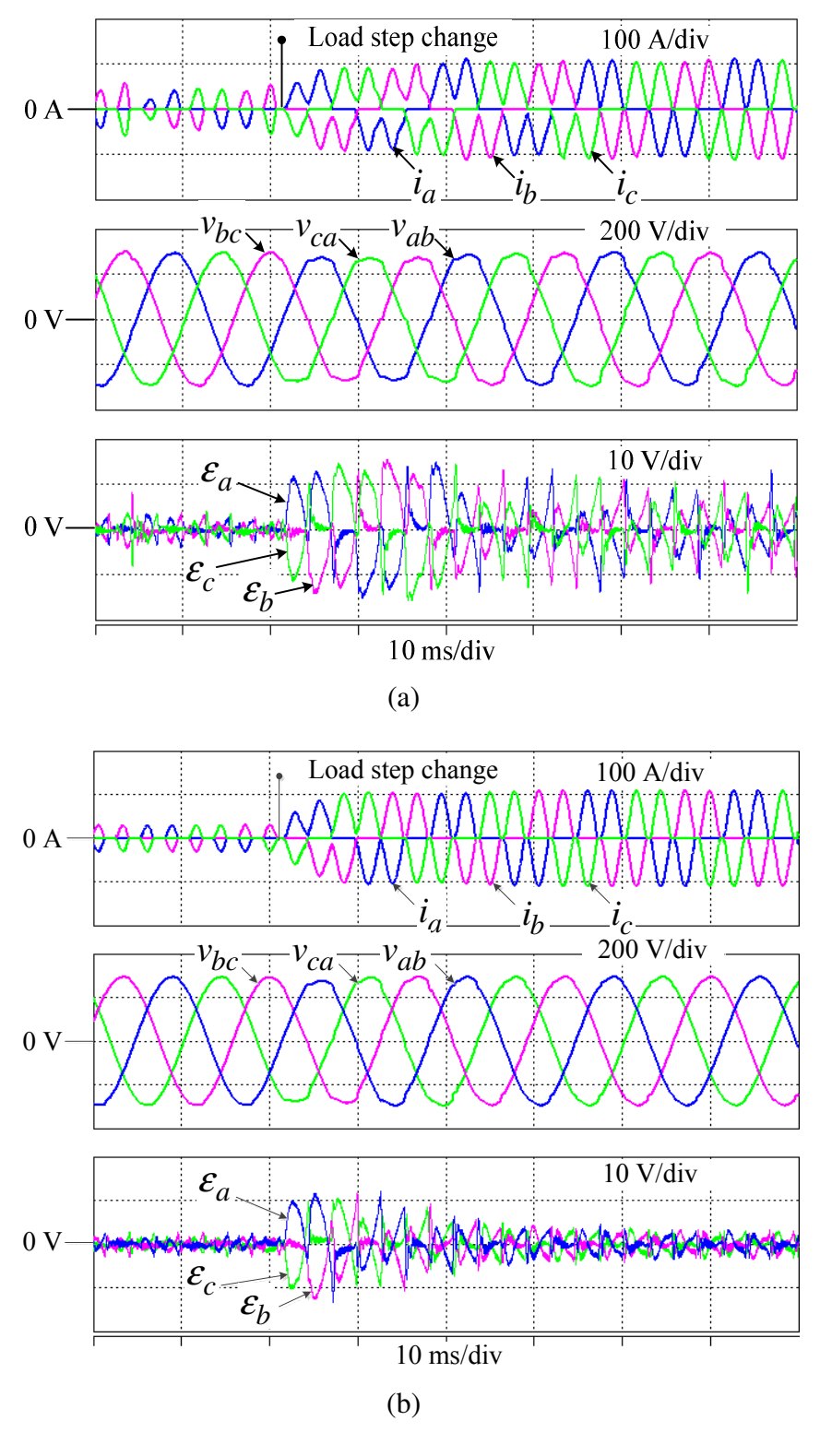


Figure 4.8. Simulated transient responses for comparison of different repetitive control schemes. A step change is performed on the three-phase bridge rectifier load (2 kW-12 kW). (a) Transient responses when the conventional RC structure is adopted. (b) Transient responses of the proposed synchronous-frame RC.

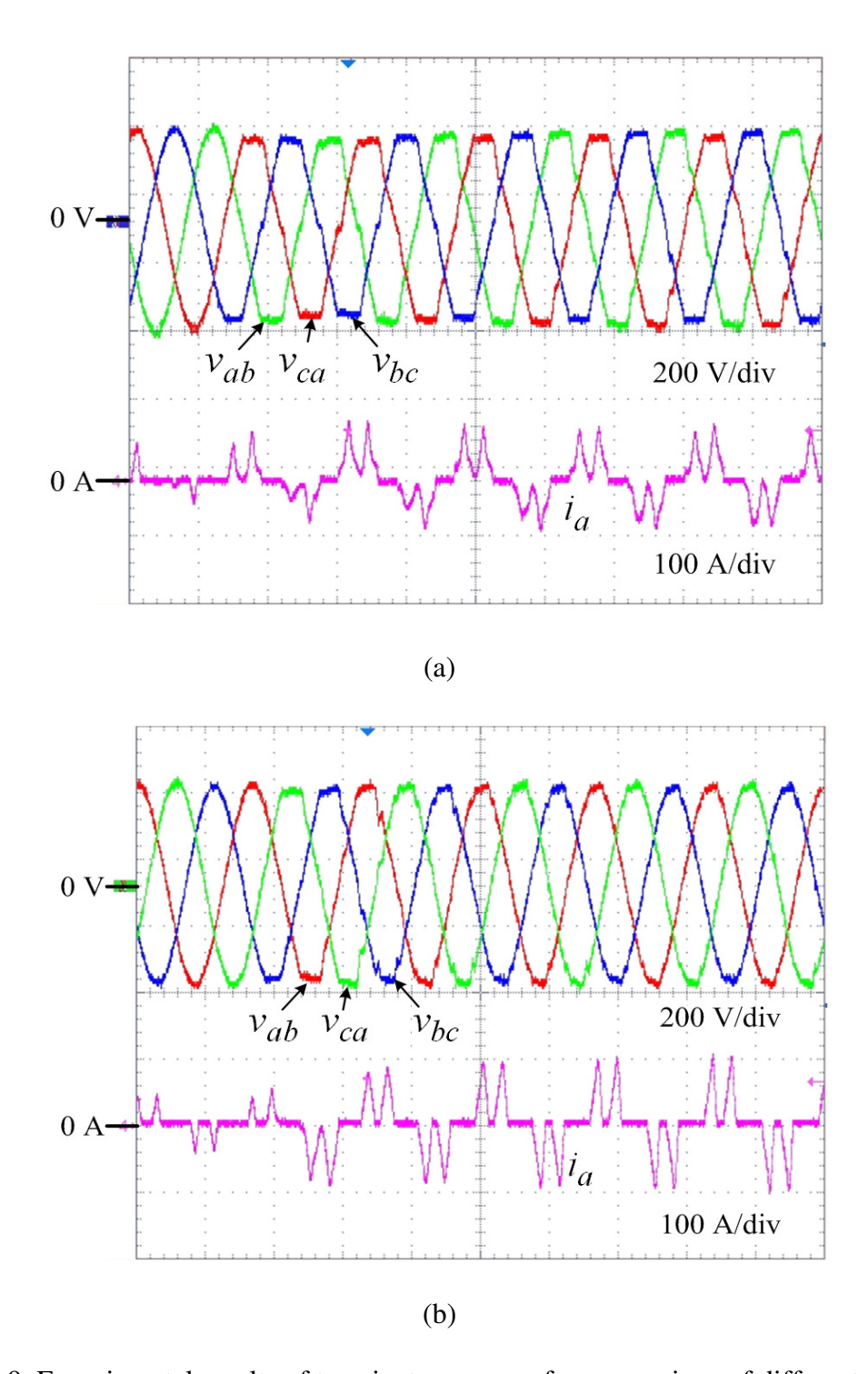


Figure 4.9. Experimental results of transient responses for comparison of different repetitive control schemes. A step change is performed on the three-phase bridge rectifier load (2.6 kW-9.4 kW). (a) Transient responses when the conventional RC structure is adopted. (b) Transient responses of the proposed synchronous-frame RC.

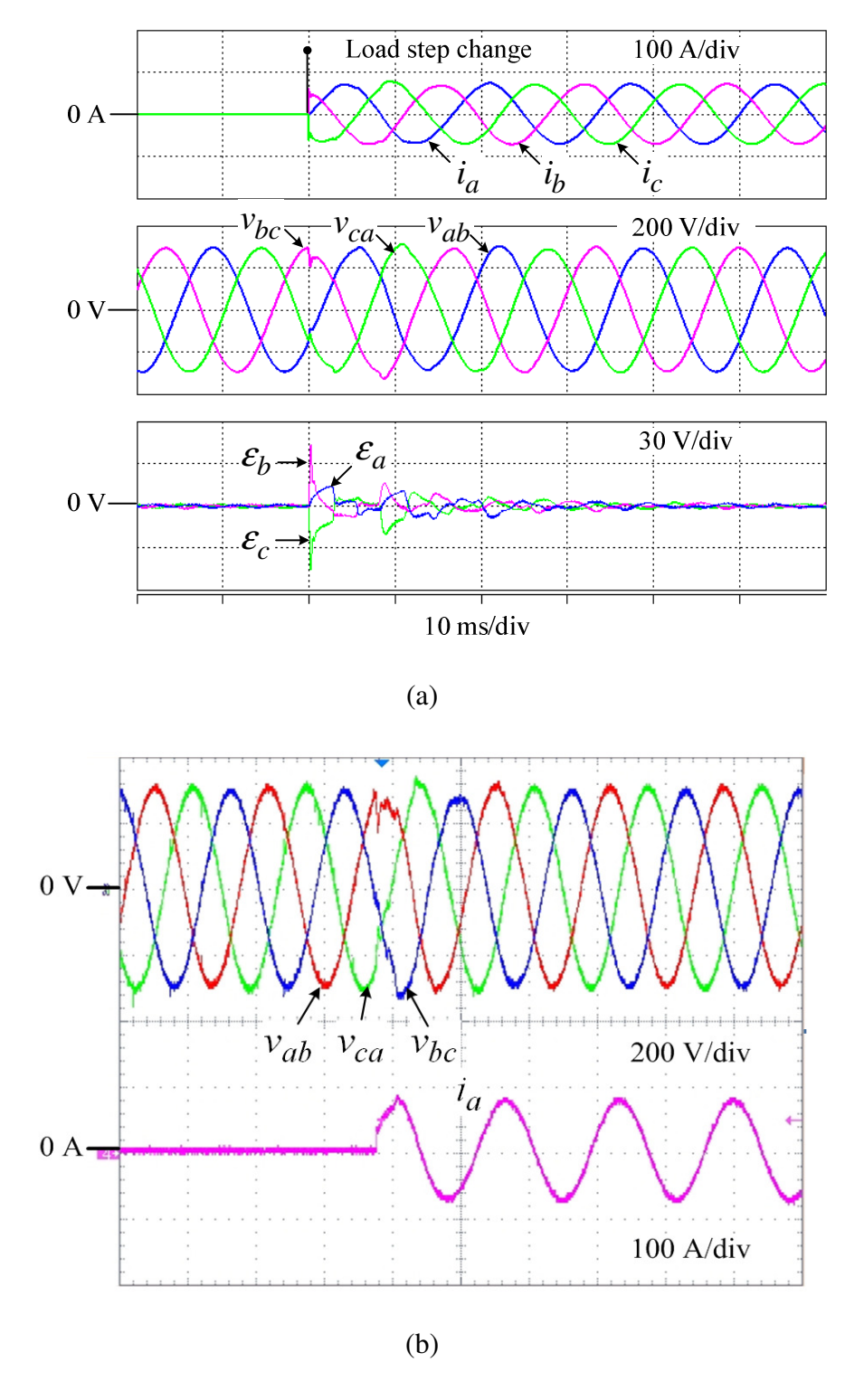


Figure 4.10. Transient responses of the proposed synchronous-frame RC. A step change is performed on the balanced resistive load (0-18 kW). (a) Simulation results. (b) Experimental results.

4.5. Summary

In this chapter, a new synchronous-frame repetitive control strategy has been presented for three-phase UPS inverters. By designing the repetitive controller to compensate the 6nth (n = 0,1,2...) harmonics in three different synchronous rotating frames, all the stationary-frame odd harmonic distortions including both the ($6n\pm1$)th (n=0,1,2...) and the triplens are eliminated. Therefore, the voltage regulation requirement can be satisfied under general load conditions (balanced, unbalanced, nonlinear, etc.). Conventional repetitive control schemes suffer the drawback of slow dynamic responses caused by the long internal time delay, which is usually equal to one fundamental period. The proposed synchronous-frame repetitive controller minimizes the time delay to 1/6 of the fundamental period and significantly enhances the dynamic responses without sacrificing any steady state performance.

Simulation and experimental results have been provided for validation of the proposed controller's performances. The promising features including low THD and fast dynamic responses make the proposed controller very competitive for three-phase UPS inverter systems.

Chapter 5. Design and Control of Grid-Connected Inverter in Renewable Energy

Applications

5.1. Introduction

Renewable energy sources are growing rapidly in recent years along with the constantly growing global demand for electricity. Grid-connected voltage source inverter, usually as an essential part of a grid-connected renewable energy system, injects sinusoidal current to the grid with required low THD and high power factor. Using an LCL filter in such a system has been recognized as an attractive solution to reduce current harmonics around the switching frequency, improve the system dynamic response, and reduce the total size and cost [46].

Figure 5.1 shows the typical configuration of an LCL filter based single phase grid-connected inverter in photovoltaic applications. The inverter DC link interfaces with a PV panel either directly or through an intermediate DC-DC conversion stage. The DC-link voltage is usually controlled by the inverter through adjusting the amount of current injected to the grid.

In this chapter, more concentration will be on the current control regardless of the DC-link voltage regulation. For the LCL filter, the low frequency dynamics are usually controlled by a current control loop while the high frequency resonant poles are usually damped by modifying the output filter through adding extra dissipative passive elements (passive damping) or by modifying the feedback control structures (active damping).

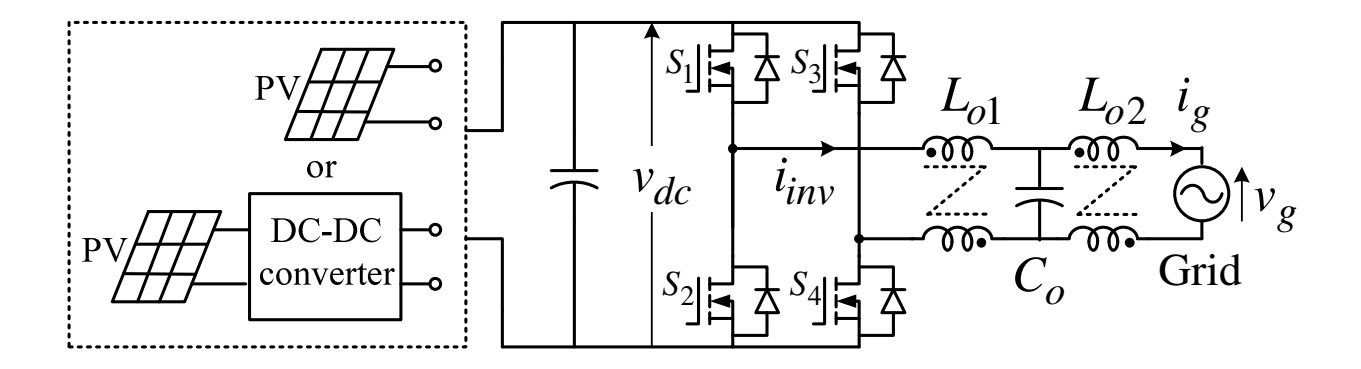


Figure 5.1. Typical configuration of single-phase grid-connected inverter with LCL filter.

The advantage of active damping is its lossless feature, but they are also more sensitive to parameter uncertainties. Moreover, in digital control systems, the effectiveness of active damping is also limited by the controller sampling frequency [53], [57].

On the other hand, thanks to the -60dB/dec attenuation rate above the resonance frequency of the LCL filter, it is possible to push the resonance frequency to be very high (close to a half of the switching frequency) without compromising the ability of filtering out the harmonics associated with the pulse width modulation [46]. With a high resonance frequency, the LCL filter will exhibit promising features such as small size, reduced cost, and low power losses. However, with a limited sampling frequency, active damping becomes a very challenging task.

It has been shown that a current controller without introducing any damping method can also be stabilized, as long as the LCL filter parameters and the current sensor location are properly selected [58]. Nevertheless, stability will be lost when the resonance frequency is very high (40%~50% of the sampling/switching frequency). Therefore, in this chapter, the stability conditions are discussed when the LCL filter has different resonance frequencies. A simple approach, which is to feed back the inverter side current and implement a first order low pass filter on the current feedback path, is proposed to obtain stability naturally when using a high-resonance-frequency LCL filter.

On the other hand, the current controller performance is evaluated by the output current total harmonic distortions (THD), power factor and dynamic response. Repetitive control (RC) is known as an effective solution for elimination of periodic harmonic errors and has been previously investigated and validated in the UPS systems [20]-[30], active power filters [35]-[38], boost-based PFC circuits [33], [34], and grid-connected inverters/PWM rectifiers [31], [32]. In Chapter 3, a 4th-order linear phase infinite impulse response (IIR) filter has been synthesized for the RC based UPS systems. This IIR filter is implemented to obtain very high system open loop gains at a large number of harmonic frequencies such that the harmonic rejection capability is greatly enhanced. In this chapter, a plug-in repetitive current controller is proposed. It is composed of a proportional part and an RC part, to which the previously designed IIR filter is accommodated. The proposed current controller exhibits the following superior features:

- 1) High power factor is obtained.
- 2) Current harmonic distortions (up to the 13th-order) caused by the grid voltage non-ideality are minimized.
 - 3) Outstanding current regulation is guaranteed in a wide range of load conditions.
 - 4) Fast dynamic response is achieved during load step change.

5.2. LCL Filter Design

In Figure 5.1, a full-bridge inverter is adopted. Sinusoidal current with a unity power factor is supplied to the grid through a third-order LCL filter (L_{o1} , L_{o2} and C_{o}). i_{inv} and i_{g} are the output AC current at the inverter side and the grid side, respectively. v_{g} is the grid voltage. The grid voltage v_{g} is sensed to extract the instantaneous sinusoidal angle θ_{g} , which is commonly known as the phase lock loop (PLL). i_{inv} represents the grid current reference.

5.2.1. Design Procedure of LCL Filter

The LCL filter is incorporated to effectively attenuate the switching frequency ripple and the even higher frequency harmonics. Compared to the first-order inductor filter, the LCL filter has a -60dB/dec attenuation rate above its resonant frequency. Therefore, with LCL filter, it is very feasible to push the resonance frequency above 1/3 of the switching frequency and the current switching ripple reduction still satisfies the requirement.

However, if the LC resonance peak is not properly considered in the filter design or no damping is implemented, it makes no sense even the filter itself already achieves sufficient high frequency attenuation. Therefore, it must be an iterative design procedure such that we are able to push the LCL resonance frequency as close to the upper limit as possible, and simultaneously guarantees from the side of controller design that the resonance poles won't cause instability or can be damped.

In addition, two different current feedback schemes can both be good to use: inverter side inductor current feedback and grid side inductor current feedback. In terms of the low frequency characteristics, both of the two feedback schemes almost have no difference. This is because the reactance of the filter capacitor is very large at low frequency such that the inverter side current is approximately equal to the grid side current, except for the switching frequency ripples. Nevertheless, once considering the high frequency characteristics of the two feedback schemes, particularly the LC resonance, these two current feedback schemes will become totally different. In order to optimally design the LCL filter to achieve lowest cost size, it is also necessary to examine both of the two feedback schemes, respectively.

Hence, here is the design procedure of the LCL filter:

- 1. Determine the inverter side inductance based on the current switching ripple requirement. Typically, the inductor current peak-to-peak ripple is around 30%~40% of the peak current of the fundamental frequency.
- 2. Calculate the resonance (double pole) frequency of the LCL filter based on the requirement for grid-side current switching ripple attenuation.
- 3. Determine the LCL filter capacitor value based on the requirement of the allowable reactive power absorbed by the inverter, which is typically 5%. It is noteworthy that the higher capacitance we select, the more reactive power is circulating between the inverter and the capacitor, which essentially decreases the inverter efficiency. Furthermore, if the inverter side current feedback is chosen, the capacitor selection is also limited by the power factor requirement.
- 4. Analyze the control loop stability of using two current feedback schemes, respectively. When the LCL resonance frequency is selected to its upper limit determined from Step 2, it is usually very difficult to implement the active damping technique because the resonance frequency could be very close to the Nyquist frequency (half of the switching frequency), which hits the physical limit in digital control. Therefore, it is desirable to find other means to avoid the instability even without using active damping.
- 5. If the control loop stability is not achievable without using active damping, then gradually decrease the LC resonance frequency, which means increasing the filter size and cost. Repeat Step 4 to analyze the stability of using two feedback schemes, respectively, until find the LCL filter parameters satisfies all the above requirements.

5.2.2. Stability Analysis of LCL Filter Based Grid-Connected Inverter

The frequency response of the third-order LCL filter is to be examined before the current controller design. Assuming that a simple proportional controller is used, the stability of the LCL filter based system can be studied by Bode plots and Nyquist stability criterion.

The Nyquist criterion in the Bode plots indicates that the number of -180° crossings in the phase-frequency response only needs to be counted in the frequency range with gains above 0 dB. In order to obtain stability or no right half plane poles, the number of the positive crossings N+ must be equal to the number of negative crossings N-. Any other cases indicate instability [58].

As both the grid current feedback and inverter current feedback are considered in this chapter, the following two transfer functions of a lossless LCL filter from the inverter output voltage to the ac output current are of interest:

$$G_{iinv}(s) = \frac{i_{inv}(s)}{i_{inv}(s)} = \frac{(L_{o2}C_os^2 + 1)e^{-sT_d}}{L_{o1}L_{o2}Cs^3 + (L_{o1} + L_{o2})s}$$
(5.1)

$$G_{ig}(s) = \frac{i_g(s)}{v_{inv}(s)} = \frac{1}{L_{o1}L_{o2}Cs^3 + (L_{o1} + L_{o2})s}e^{-sTd}$$
(5.2)

and the resonance frequency and the zero point frequency in (5.1) can be expressed as

$$\omega_r = \sqrt{\frac{r_1 r_2 C_o + L_{o1} + L_{o2}}{L_{o1} L_{o2} C_o}}$$
 (5.3)

$$\omega_0 = \sqrt{\frac{1}{L_{o2}C_o}} \tag{5.4}$$

For the stability analysis, the discrete control model is used. A simple proportional controller is assumed to be in the loop, which is considered as integration to the control plant. With reasonable proportional gains, the peak gain at the resonance frequency will be mostly likely above 0 dB. The computational delay which is approximately one and a half sampling period is considered in practice, which is represented by T_d . Therefore, the LCL transfer function discretized with a zero-order hold will be adopted for analysis. Define f_s , f_N and f_r as the sampling frequency, Nyquist frequency (half of the sampling frequency) and LCL resonance frequency.

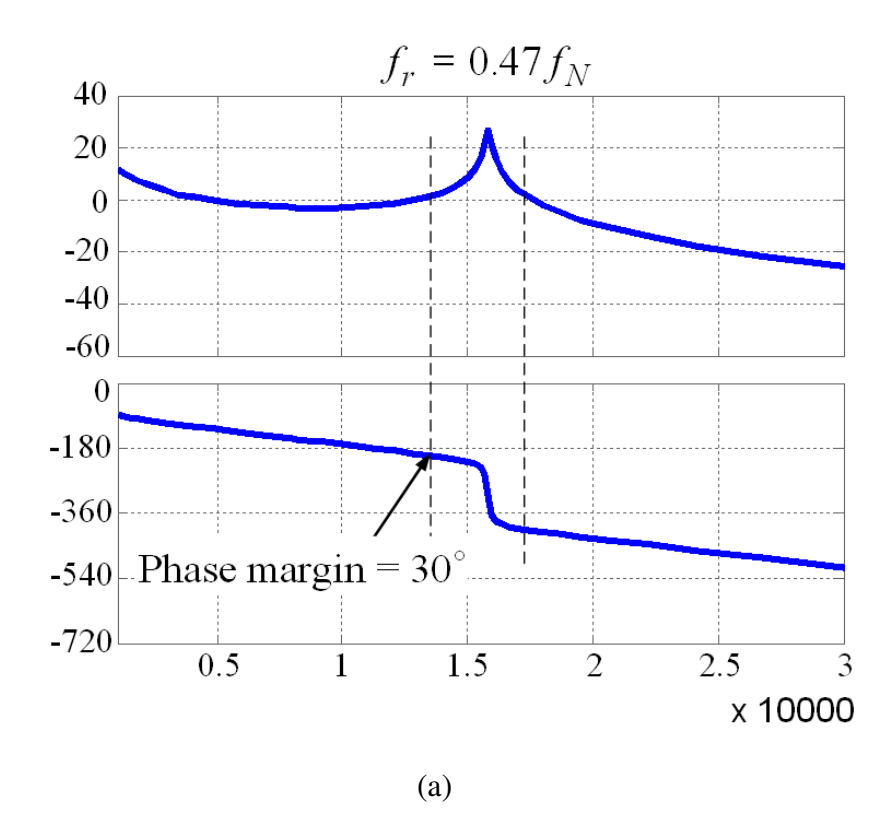
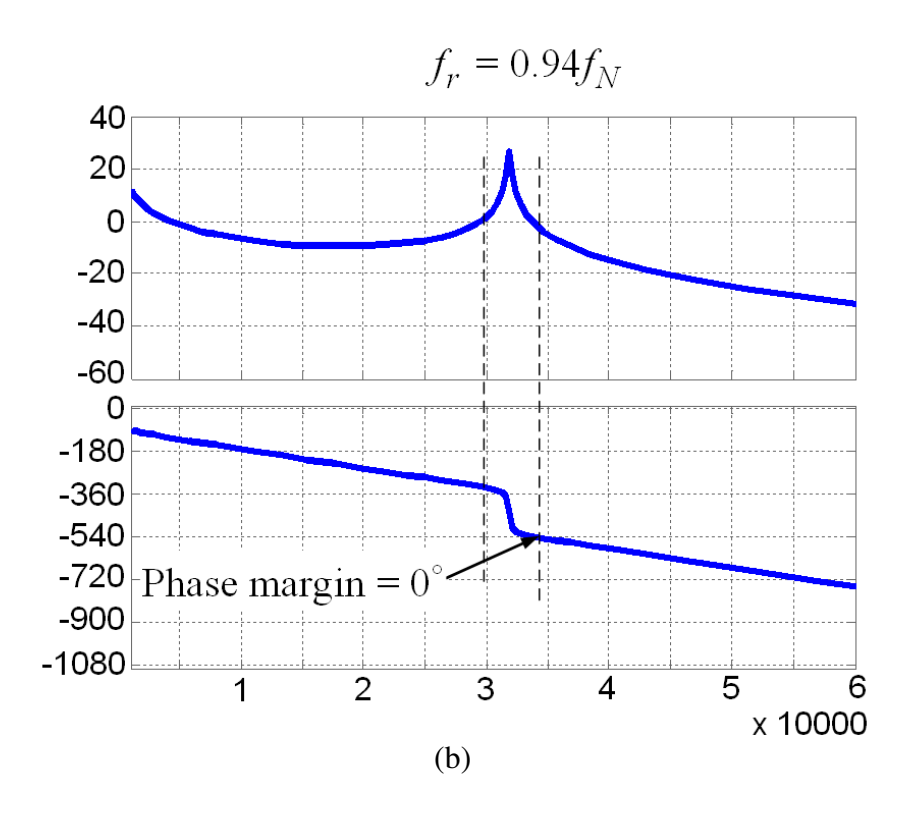


Figure 5.2. Open-loop Bode plot for different LCL-filter resonance frequencies with grid current feedback. (a) $f_r = 0.47 f_N$. (b) $f_r = 0.94 f_N$.

Figure 5.2 (cont'd).



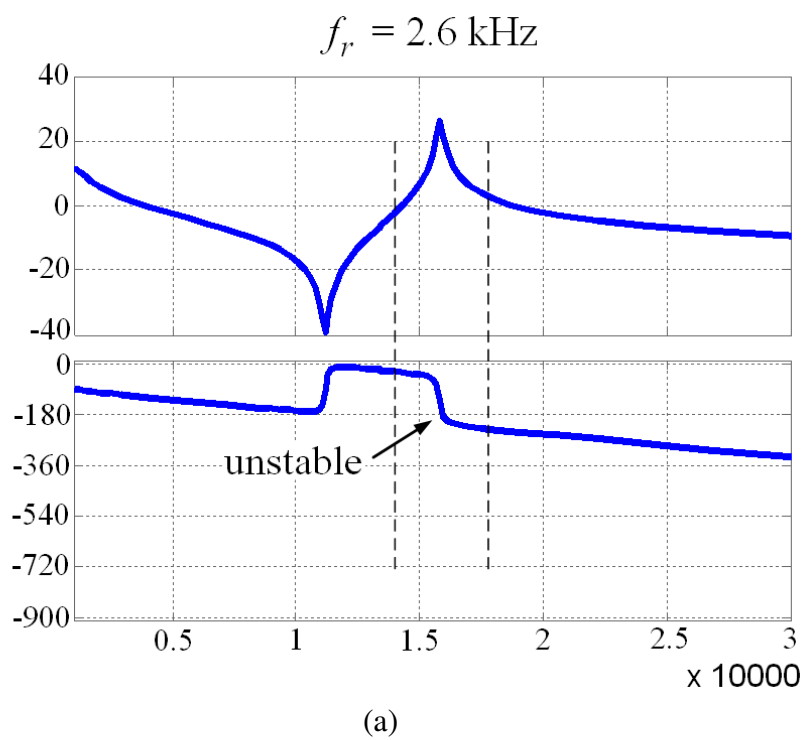


Figure 5.3. Open-loop Bode plot for different LCL-filter resonance frequencies with inverter current feedback. (a) $f_r = 0.47 f_N$. (b) $f_r = 0.94 f_N$.

Figure 5.3 (cont'd).

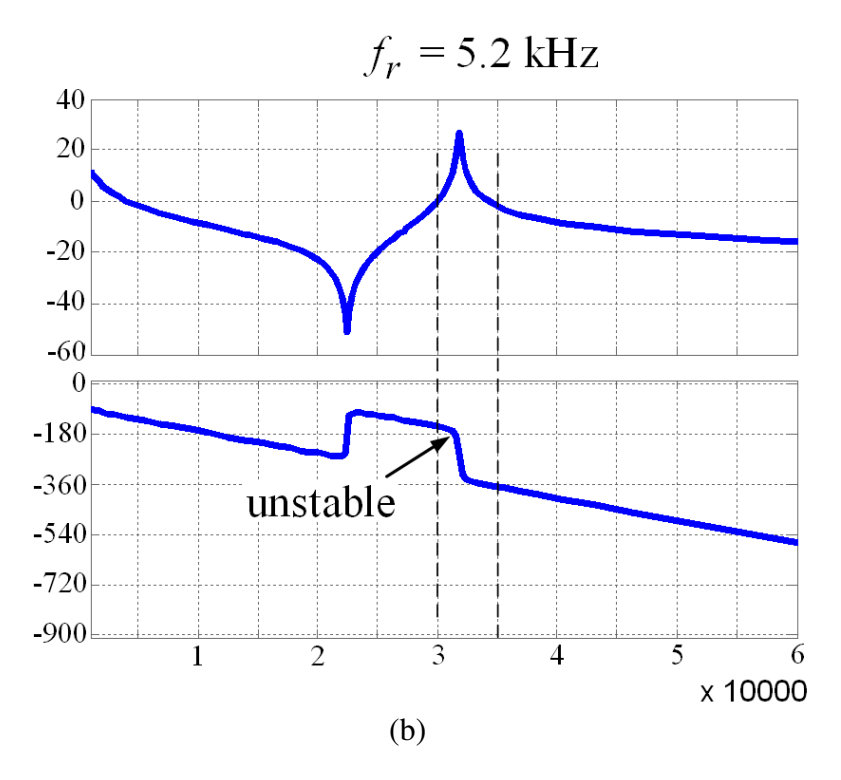


Figure 5.2 and Figure 5.3 show the open loop Bode diagrams when different LCL-filter resonance frequencies are selected. In Figure 5.2, the grid current feedback is adopted. It can be seen that when f_r is selected as a lower value, the system will be stable. Once f_r is moving to a higher value, which is close to the Nyquist frequency f_N , the phase curve will exhibit further delay around f_r . The maximum phase delay will reach -540° and results in instability. Likewise, when the inverter current feedback is used, as shown in Figure 5.3, the system is always unstable when f_r is moving from $0.47 f_N$ to $0.94 f_N$. However, it is noticeable that with the inverter current feedback, the minimum phase delay is almost -180° when f_r equals to $0.94 f_N$.

Moreover, it is very desirable to design the LCL filter with a resonance frequency as high as possible, given the condition that the switching ripple attenuation is not compromised. Because

of the -60dB/dec high frequency attenuation, we are still able to obtain a switching ripple less than 2% even when $f_r = f_N$. It is worth noting that in Figure 5.3(b), the system will become stable as long as a little more phase delay can be added around the resonance frequency, making the phase delay between -180° and -540° around f_r . The simplest effective method is to place a low pass filter in the loop. On the one side, the low pass filter is able to cancel out some of the switching ripple noises. On the other side, the low pass filter can also introduce more phase delay to the system and help to obtain desired phase margin at the two 0 dB crossing points. The details will be discussed in the next section.

5.3. Current Controller Design

In this chapter, the LCL parameters are selected by following the guidelines as previously discussed. The current sensor is placed at the inverter side instead of the grid side. Table 5.1 summarizes the key parameters of the full-bridge inverter.

Table 5.1. Full-Bridge Inverter Parameters

HVS DC link voltage	370V
Switching frequency	10.8 kHz
Sampling frequency	10.8 kHz
Rated output power	210 W
Grid voltage	180 V ~ 240 V
Grid line frequency	60 Hz
Filter inductor (L_{o1}, L_{o2})	8.5 mH
Filter capacitor (C_o)	330 nF

5.3.1. Inverter Transfer Function Using a Low Pass Filter

The control-output-to-inverter-current transfer function in the continuous time domain can be derived as

$$G_{LCL}(s) = \frac{(L_{o2}C_{o}s^{2} + r_{2}C_{o}s + 1)e^{-sT_{d}}}{L_{o1}L_{o2}Cs^{3} + (r_{1}L_{o2} + r_{2}L_{o1})C_{o}s^{2} + (r_{1}r_{2}C_{o} + L_{o1} + L_{o2})s + r_{1} + r_{2}}$$
(5.5)

where r_1 and r_2 represent the equivalent series resistance of L_{o1} and L_{o2} , respectively. Based on the power loss estimation of the inductors, $r_1 = 1.4\Omega$ and $r_2 = 1.0\Omega$. From (5.5), the LC resonance frequency is

$$\omega_r = \sqrt{\frac{r_1 r_2 C_o + L_{o1} + L_{o2}}{L_{o1} L_{o2} C_o}}$$
 (5.6)

The system hardware and software delay is summarized as T_d , which is typically around one and a half sampling period ($T_d = 140 \mu s$). In order to reduce the switching noises in the sensed inverter current as well as obtain extra phase delay around the resonance frequency, an analog low pass filter (5.7) is placed on the current feedback path.

$$F_{LPF}(s) = \frac{\omega_{fc}}{s + \omega_{fc}} \tag{5.7}$$

The cut-off frequency is chosen as $\omega_{fc} = 4 \times 10^4 \, rad \, ls$. Therefore, by using the zero-order hold discretization scheme, the entire plant combining (5.5) and (5.7) can be discretized as

$$G_{inv}(z) = \frac{0.00265z^{-2} + 0.00548z^{-3} + 0.00474z^{-4} + 0.00559z^{-5} + 0.000254z^{-6}}{1 + 0.5468z^{-1} - 0.5653z^{-2} - 0.9606z^{-3} + 0.024z^{-4}}$$
(5.8)

5.3.2. Proportional + Repetitive Current Control Scheme

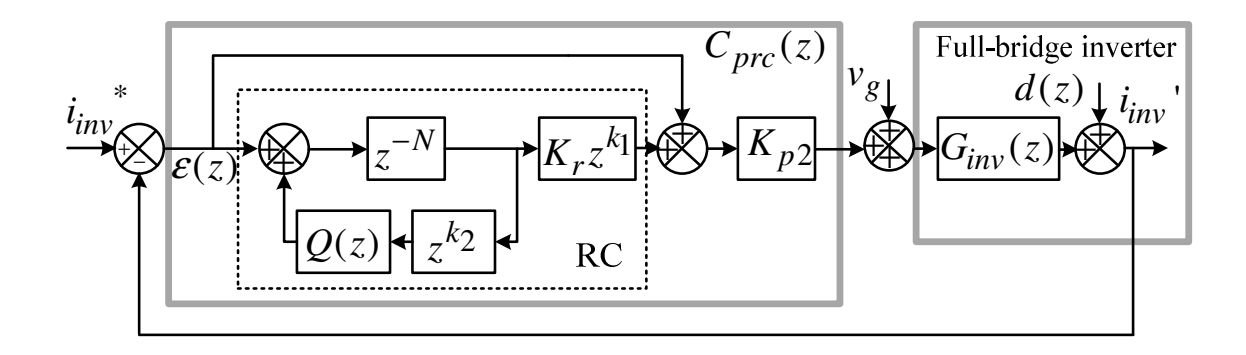


Figure 5.4. Block diagram of the proposed plug-in repetitive controller.

The plug-in digital repetitive controller is designed as Figure 5.4 shows. The conventional proportional controller with a gain of K_{p2} is incorporated to guarantee fast dynamics. The RC is then plugged into the system and operates in parallel with the proportional controller.

 $\mathcal{E}(z)$ and d(z) represent the tracking error and the repetitive disturbances, respectively.

The modified internal model, which is denoted by the positive feedback loop inside the RC, plays the most critical role in the proposed current regulator. z^{-N} is the time delay unit where N denotes the number of samples in one fundamental period. In an ideal RC, a unity gain is along the positive feedback path such that all the repetitive errors based on the fundamental period are completely eliminated when the system reaches equilibrium. However, in order to obtain a sufficient stability margin, a zero-phase low pass filter is often incorporated rather than the unity gain. This can be realized by cascading a linear phase low pass filter Q(z) and a non-causal phase lead compensator z^{k_2} . z^{k_1} is another non-causal phase lead unit which compensates the phase lag of $G_{inv}(z)$, particularly at high frequencies. Here k_1 and k_2 both stand for the number of sampling periods. K_r is the constant gain unit that determines the weight of the RC in the whole control system.

From Figure 5.4, the transfer function of the entire plug-in RC current regulator can be described as

$$C_{prc}(z) = \frac{K_r K_{p2} z^{-N} z^{k_1}}{1 - Q(z) z^{k_2} z^{-N}} + K_{p2}$$
 (5.9)

Determination of K_{p2} can be guided by examining the root locus of $G_{inv}(z)$. In practice, the filter inductors L_{o1} and L_{o2} are subject to parameter variation due to the permeability roll-off at high power. Hence, $L_{o1} = L_{o2} = 8.5mH$ and $L_{o1} = L_{o2} = 6mH$ are both plugged into (5.5) to plot the root locus of $G_{inv}(z)$, as shown in Figure 5.5.

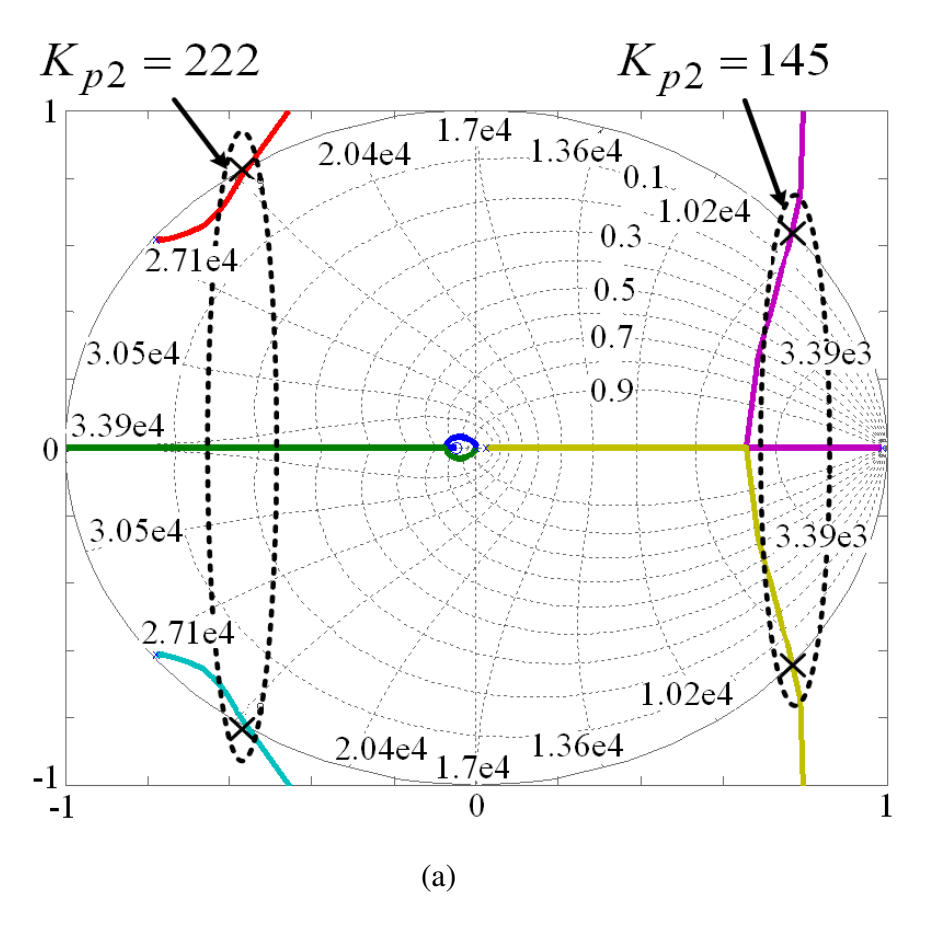
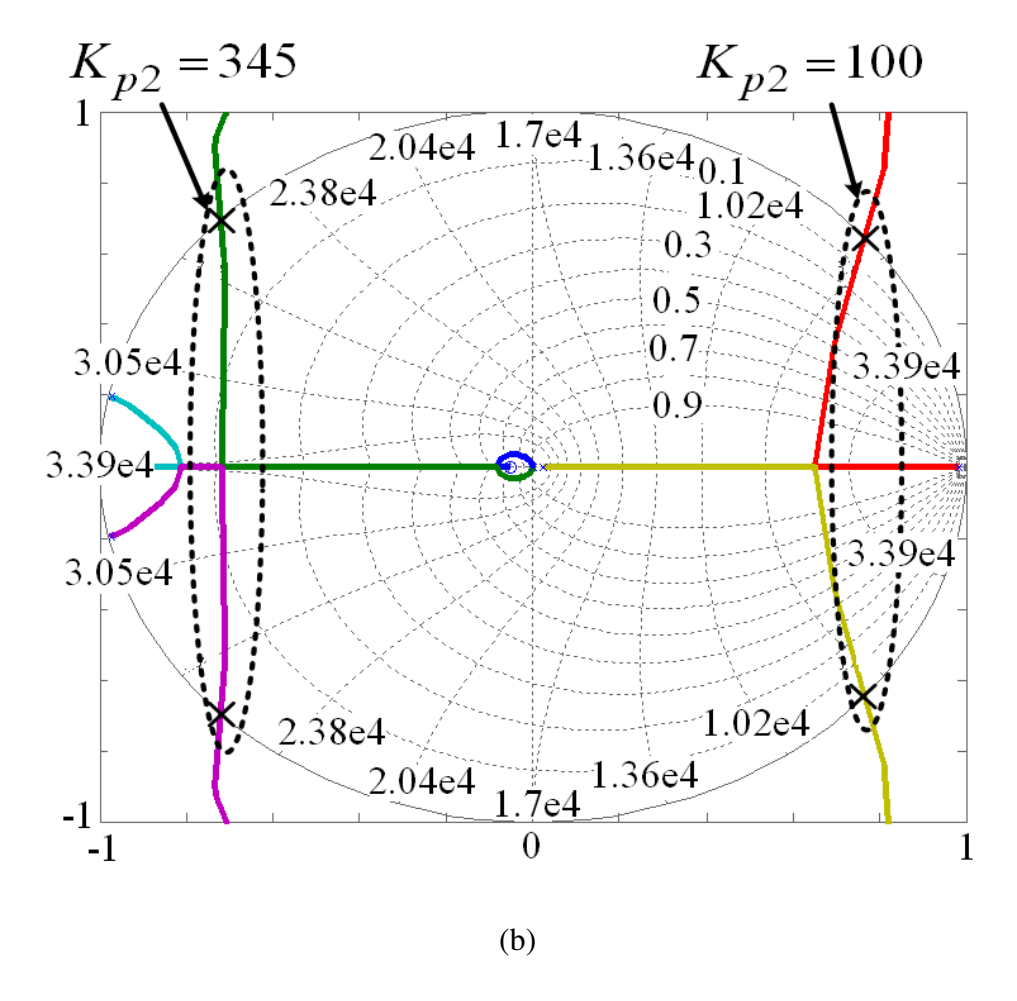


Figure 5.5. Root locus of $G_{inv}(z)$. (a) $L_{o1}=L_{o2}=8.5mH$, (b) $L_{o1}=L_{o2}=6mH$.

Figure 5.5 (cont'd).



Equation (5.8) is modified accordingly for the case $L_{o1} = L_{o2} = 6mH$. Two pairs of conjugate poles appear on the unity circle as shown in Figure 5.5(a) and (b), representing the critical stable conditions. Hence, $K_{p2} < 145$ and $K_{p2} < 100$ are the stability requirements in the two cases respectively. In order to guarantee a sufficient stability margin, $K_{p2} = 50$ is selected.

Figure 5.6 shows the bode plot of $K_{p2}G_{inv}(z)$ when $K_p=50$. Considering the LCL filter parameters uncertainty, the inductor with 8.5 mH each and 6 mH each are considered, respectively. The phase margin is greater than 40° as shown in Figure 5.6, indicating a good stability.

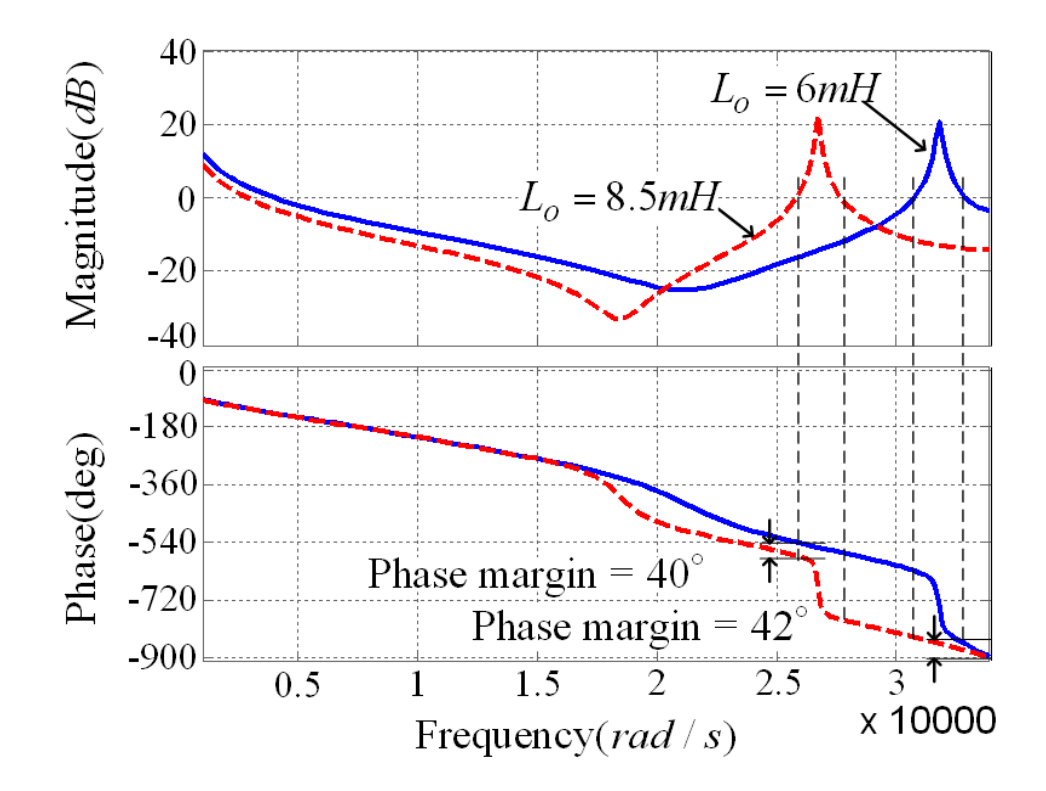


Figure 5.6. Bode plot of $K_{p2}G_{inv}(z)$ ($K_{p2} = 50$).

From Figure 5.4, the tracking error $\mathcal{E}(z)$ can be derived as

$$\varepsilon(z) = \varepsilon(z)z^{-N} \left[Q(z)z^{k_2} - \frac{K_r K_{p2} z^{k_1} G_{inv}(z)}{1 + K_{p2} G_{inv}(z)} \right]$$

$$+ \left[\frac{1 - Q(z) z^{k_2} z^{-N}}{1 + K_{p2} G_{inv}(z)} \right] \left[i_{inv}^*(z) - d(z) \right]$$
(5.10)

It is noticeable that a larger K_{p2} will result in a smaller tracking error during the transient because the second summation term on the right side of (5.10) is reduced. This exactly explains the function of the proportional control part.

Let
$$|H(z)|_{z=e} j\omega T_{sw2} = \left| Q(z)z^{k_2} - \frac{K_r K_{p2} z^{k_1} G_{inv}(z)}{1 + K_{p2} G_{inv}(z)} \right|, \ \omega \in [0, \frac{\pi}{T_{sw2}}], \text{ in which } T_{sw2} \text{ is also the}$$

sampling period. A sufficient condition for the system stability is

$$\left| H(e^{j\omega T_{SW2}}) \right| < 1 \tag{5.11}$$

With further manipulation on (5.10), the steady state error can be derived as

$$\left| \mathcal{E}(z) \right| = \left| i_{inv}^*(z) - d(z) \right| \frac{1 - Q(z)z^{k_2}}{\left[1 + K_{p2}G_{inv}(z) \right] \left[1 - H(z) \right]}$$
 (5.12)

From (5.11) and (5.12), the general design criteria of Q(z) for obtaining a good stability as well as a small steady state error can be summarized as: 1) Q(z) must have sufficient attenuation at high frequencies; 2) Q(z) must be close to unity in a frequency range which covers a large number of harmonics; 3) $Q(z)z^{k_2}$ must have a zero phase when Q(z) is close to unity.

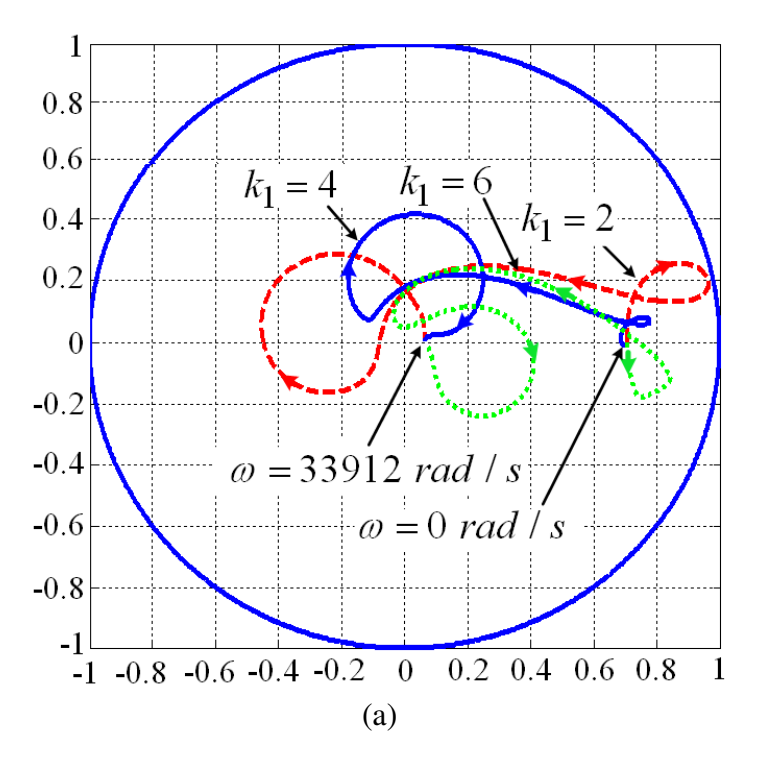
In Chapter 3, a 4th-order linear phase IIR filter is synthesized for the repetitive voltage controller for UPS systems. Compared with the conventional linear phase finite impulse response (FIR) filters used for the repetitive control, the linear phase IIR filter exhibits a flat gain in the pass band and a much faster roll off in the transition band, when the filter order is given [39]. Hence, it is a good candidate for the repetitive current controller here as well.

In practice, Q(z) is synthesized by cascading a 2nd-order elliptic filter $Q_e(z)$ and a 2nd-order all-pass phase equalizer $Q_a(z)$. Q(z), $Q_e(z)$ and $Q_a(z)$ are expressed by (5.13)-(5.15).

$$Q(z) = Q_e(z)Q_a(z) \tag{5.13}$$

$$Q_e(z) = \frac{0.1385 + 0.2564z^{-1} + 0.1385z^{-2}}{1 - 0.7599z^{-1} + 0.2971z^{-2}}$$
(5.14)

$$Q_a(z) = \frac{0.1019 - 0.6151z^{-1} + z^{-2}}{1 - 0.6151z^{-1} + 0.1019z^{-2}}$$
(5.15)



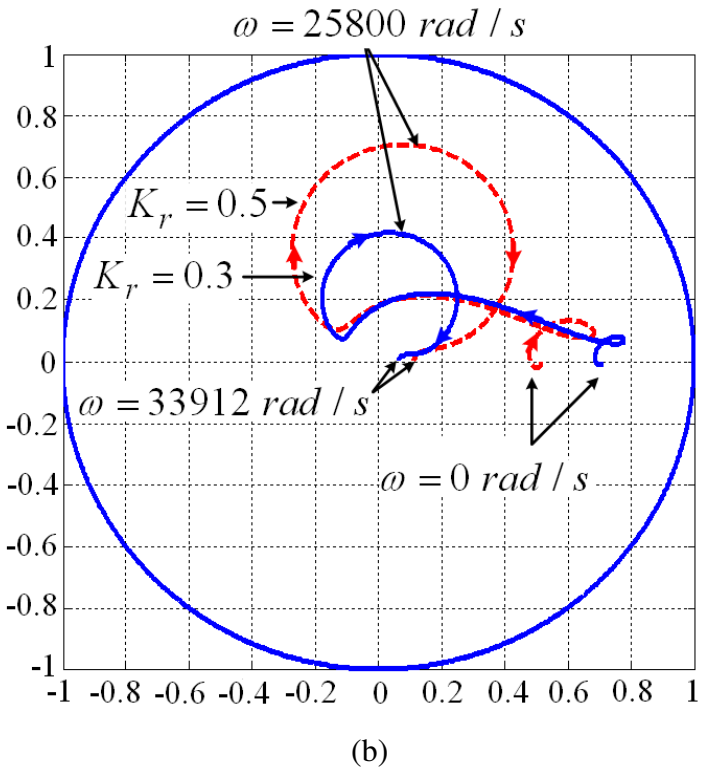


Figure 5.7. Locus of the vector $H(e^{j\omega T_{SW2}})$. (a) $K_r = 0.3$, k_1 is varying; (b) $k_1 = 4$, K_r is varying.

The bode plots of $Q_e(z)$, $Q_a(z)$ and Q(z) are referred to Figure 3.5. The linear phase region of Q(z) is from 0 to 1403 Hz (8816 rad/s). $k_2 = 5$ is selected to compensate the phase delay of Q(z) to zero. The maximum pass band gain and the cut-off frequency of Q(z) is 0.9975 and 1670 Hz, respectively.

The locus of $H(e^{j\omega T_{SW2}})$ is useful for guiding the selection of K_r and k_1 . The fundamental principle for choosing K_r and k_1 is that $H(e^{j\omega T_{SW2}})$ should keep a sufficient margin from the unity circle when ω increases from 0 to the nyquist frequency π/T_{SW2} . When K_r and k_1 are assigned with different values, $H(e^{j\omega T_{SW2}})$ can be plotted in Figure 5.7(a) and (b). In Figure 5.7(a), K_r is fixed, $k_1 = 4$ renders a good stability margin. Likewise, $K_r = 0.3$ would be an appropriate choice from Figure 5.7(b).

 $\left|C_{prc}(z)G_{inv}(z)\right|$ denotes the open loop gain of the plug-in repetitive control system. In particular, the magnitude of $\left|C_{prc}(z)G_{inv}(z)\right|$ at the frequencies of the fundamental as well as high order harmonics determines the steady state tracking error. $\left|C_{prc}(z)G_{inv}(z)\right|$ is plotted in Figure 5.8. It can be observed that the open loop gain peaks are higher than 40 dB and 20 dB at the harmonic frequencies up to the 9th order and 13th order respectively, which yields an excellent harmonic rejection capability.

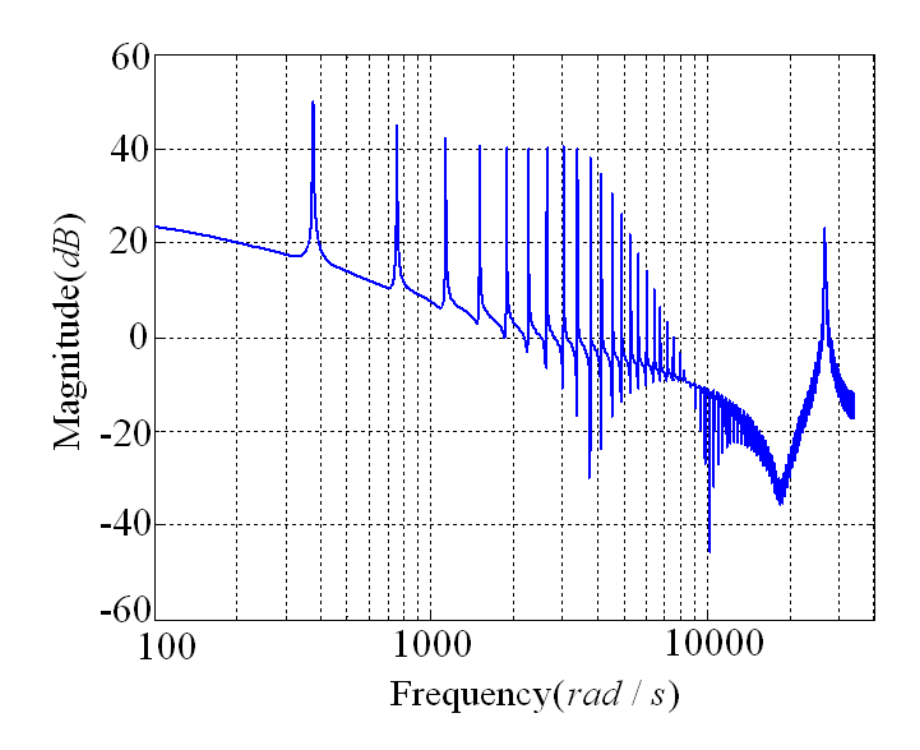
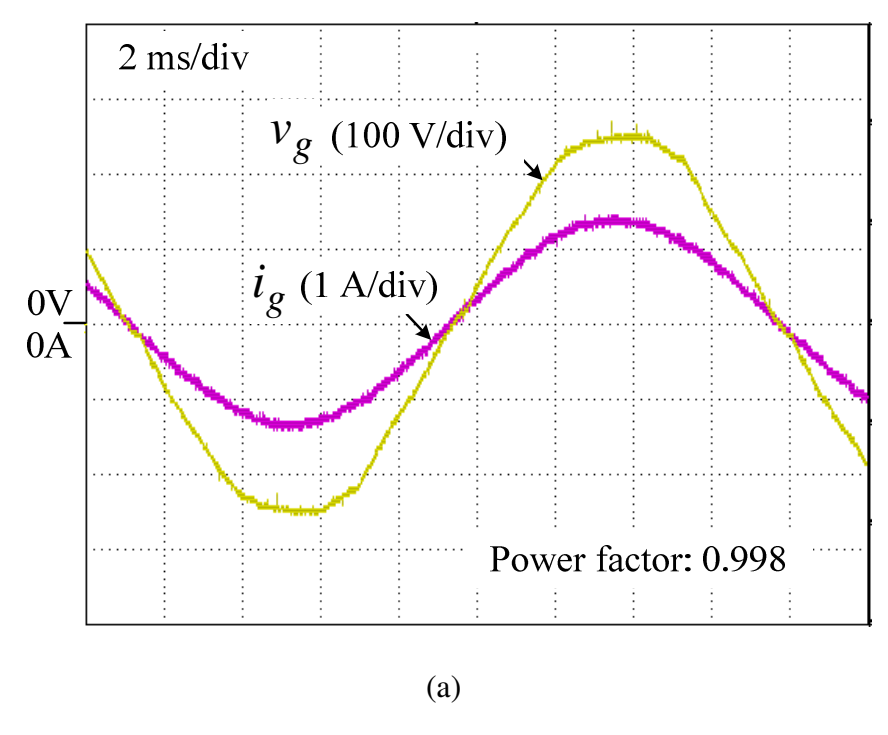


Figure 5.8. Frequency response of $\left|C_{prc}(z)G_{inv}(z)\right|$.

5.4. Experimental Results

A 210 W single-phase inverter with an output LCL filter has been built and experimentally tested in the laboratory. The inverter is controlled by the 32-bit digital signal processor (TI TMS320F28035). The validity of the LCL filter design as well as the plug-in repetitive current controller design are verified by the following experimental results.

The steady state grid voltage and current waveforms and the corresponding harmonic spectrums are depicted in Figure 5.9. Both heavy load and light load conditions are tested to verify the current controller performance. As can be seen from Figure 5.9(a), the proposed plugin RC achieves a THD as low as 1.31% and a high power factor of 0.998 under heavy load. Low THD (3.721%) and high power factor (0.99) are still obtained even when the load is reduced by 2/3, as shown in Figure 5.9(c).



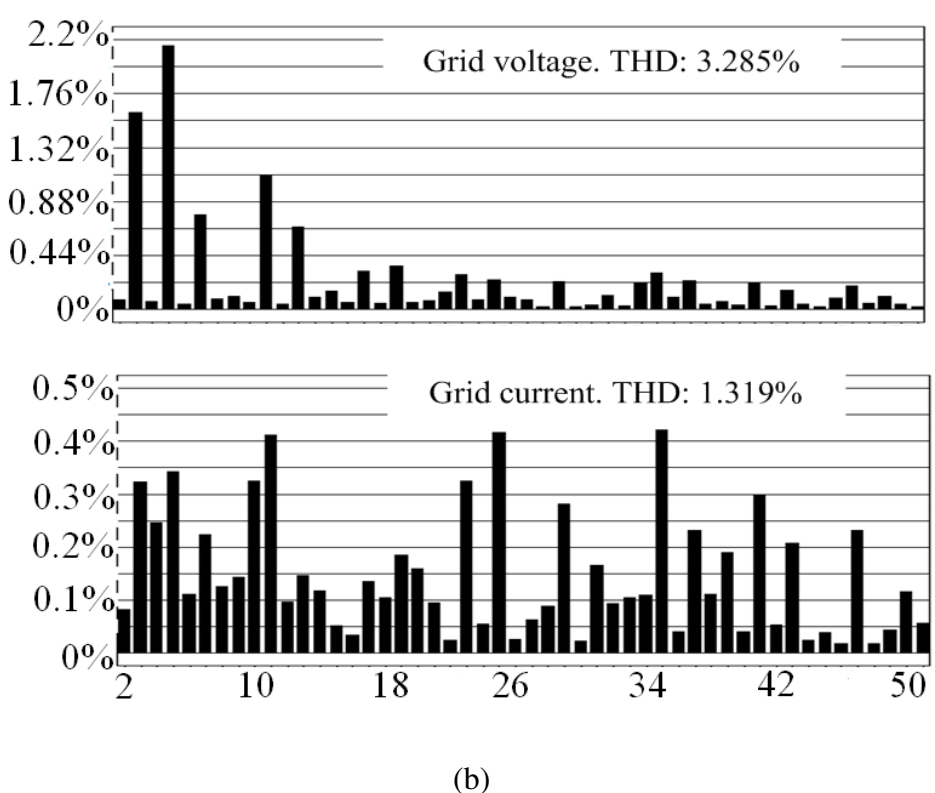
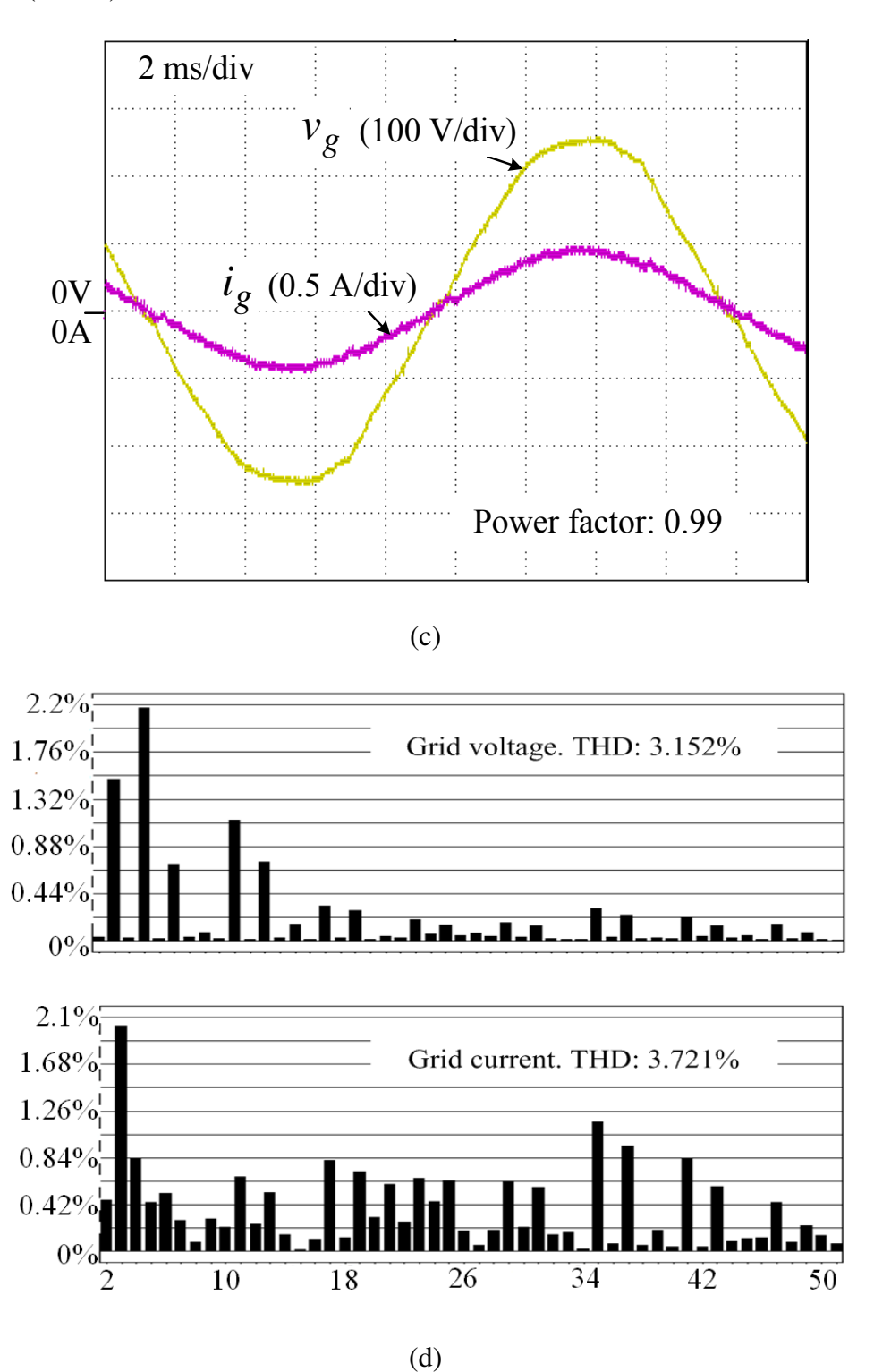


Figure 5.9. (a) Steady state grid voltage and current at heavy load when using the proposed repetitive current controller. (b) Harmonic spectrum in (a). (c) Steady state grid voltage and current at light load when using the proposed repetitive current controller. (d) Harmonic spectrum in (c).

Figure 5.9 (cont'd).



Comparison has been made by testing the single-phase inverter system with conventional proportional + resonant controller (Figure 5.10).

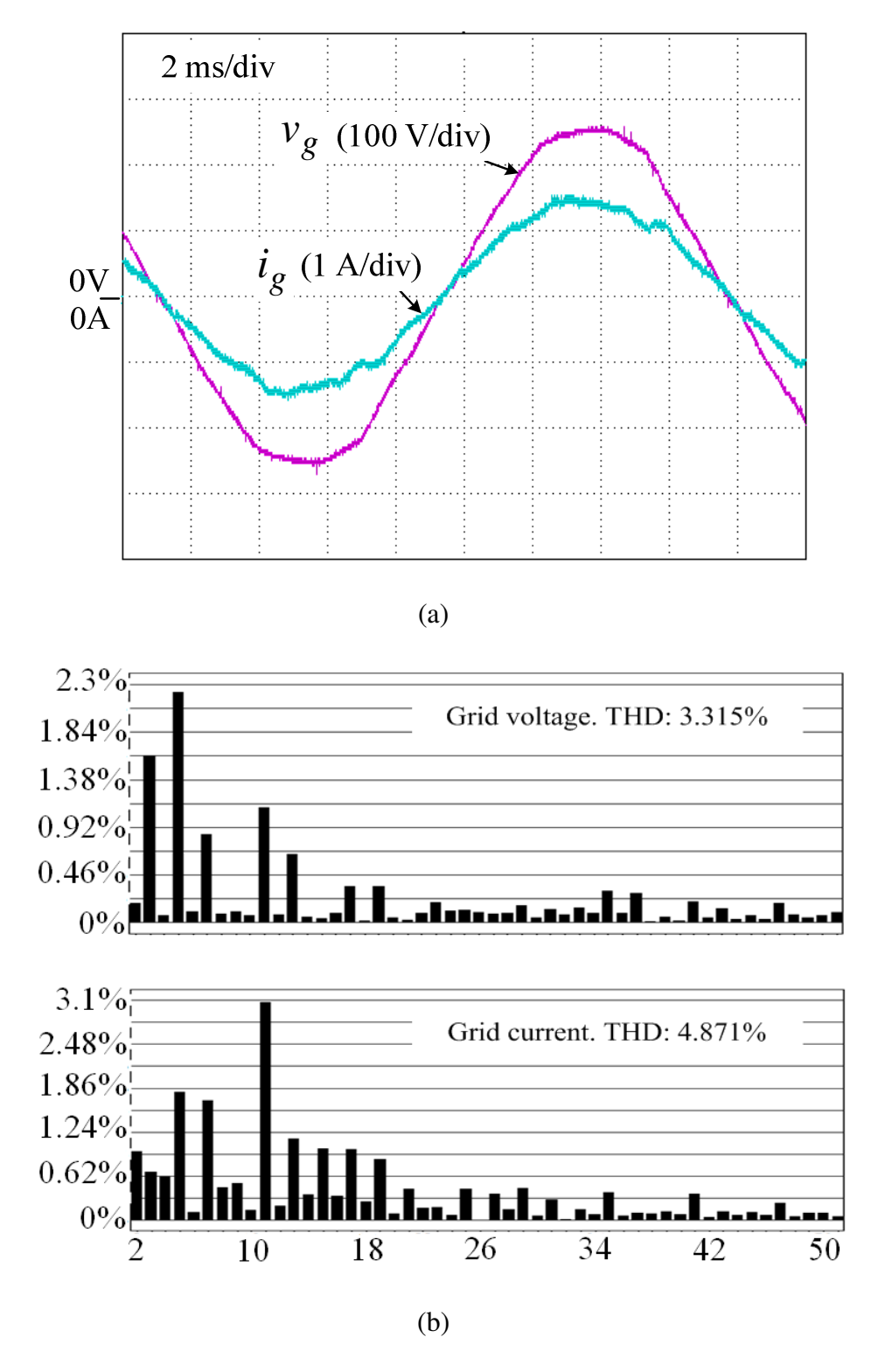
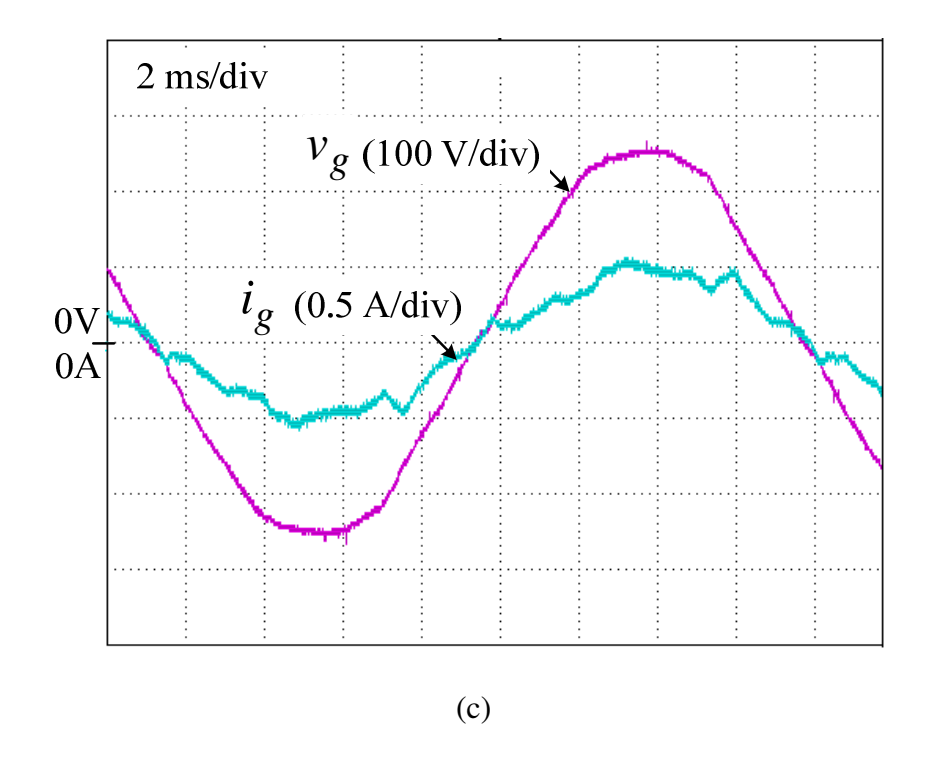
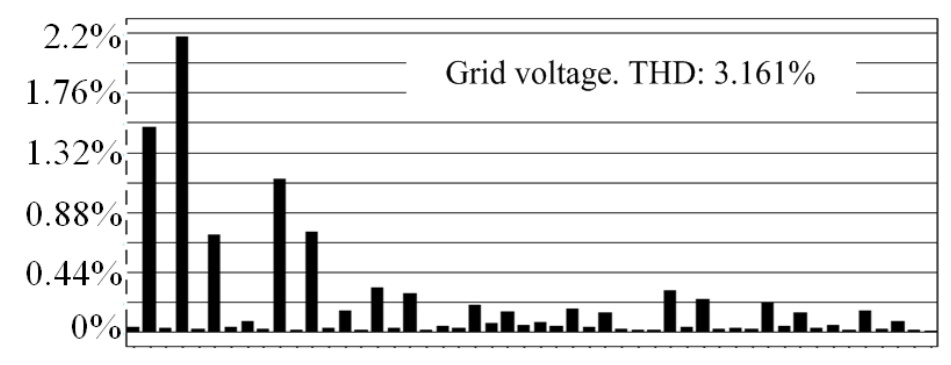
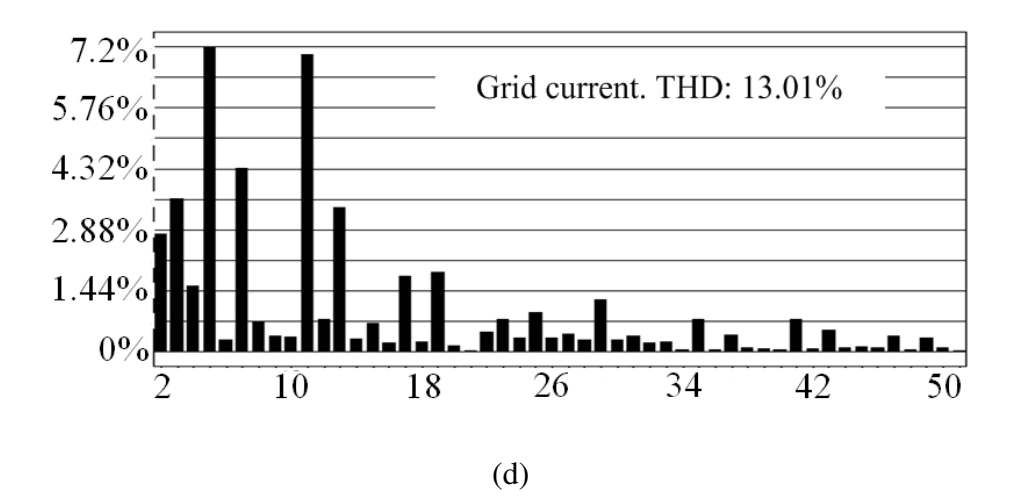


Figure 5.10. (a) Steady state grid voltage and current at heavy load when using the conventional proportional + resonant current controller. (b) Harmonic spectrum in (a). (c) Steady state grid voltage and current at light load when using the conventional proportional + resonant current controller. (d) Harmonic spectrum in (c).

Figure 5.10 (cont'd).







The conventional proportional + resonant controller is designed with the same bandwidth of the proposed repetitive + proportional controller. In this case, the controller does not possess harmonic compensation capabilities and thus the current regulation is much worse than the previous case. Especially for the light load condition, the current THD goes as high as 13%, which is considerably higher than the 5% criterion.

Dynamic responses of the plug-in RC are verified by the experimental results in Figure 5.11. Figure 5.11(a) and (b) show the results when the full-bridge inverter is tested independently. In Figure 5.11(a) and (b), the grid current reference is step changed from 0.33 A to 1 A and 1 A to 0.33 A, respectively. The proportional part in the plug-in RC enables the controller to respond to the abrupt reference change promptly. Meanwhile, the RC part cancels the harmonic distortions in several fundamental cycles following the step change.

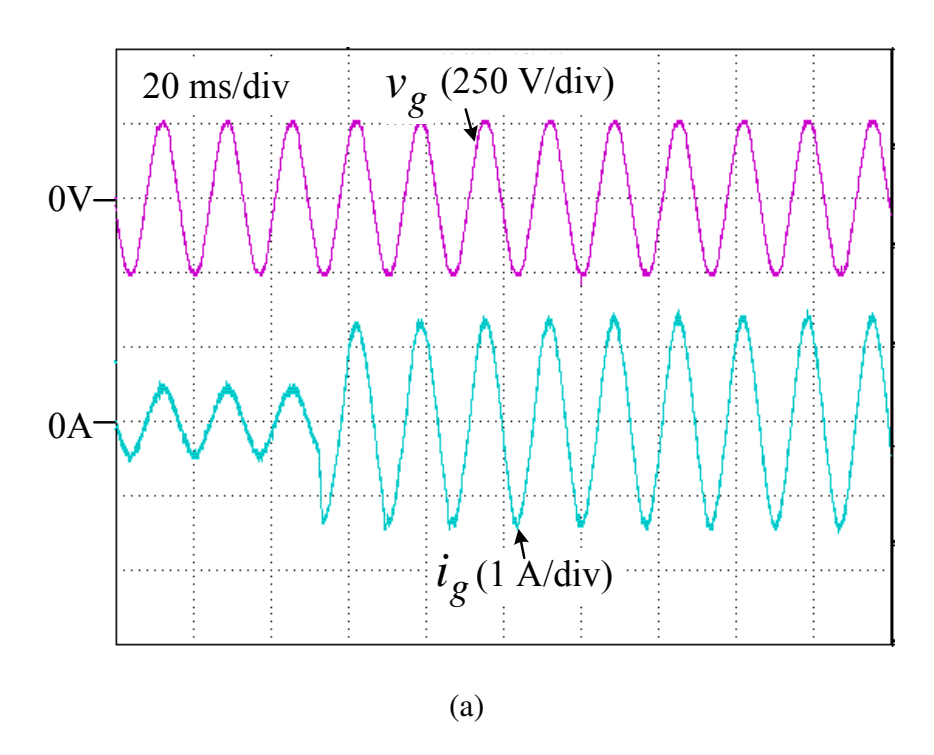
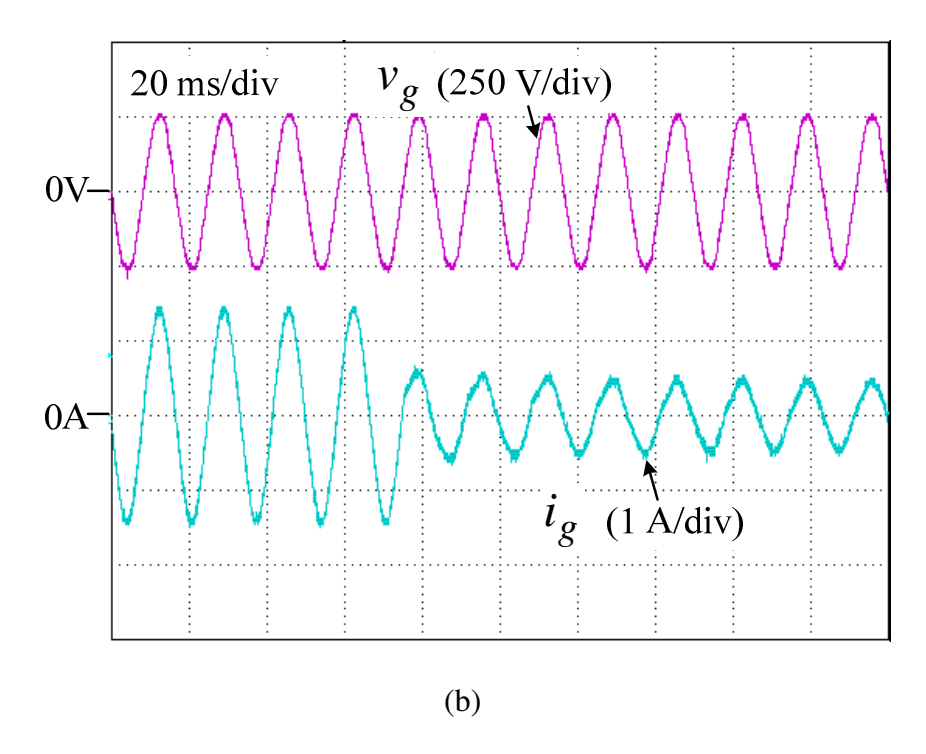


Figure 5.11. Transient responses under load step change. (a) Grid current step change (0.33 A to 1 A). (b) Grid current step change (1 A to 0.33 A).

Figure 5.11 (cont'd).



5.5. Summary

A single-phase inverter based on a LCL filter for grid-connected photovoltaic systems has been presented in this chapter The LCL filter is designed with very high resonance frequency such that the filter size, cost and power loss can reduced significantly. A plug-in repetitive current regulator was proposed and illustrated. By properly selecting the current sensor locations as well as placing a first order low pass filter on the feedback path, the control loop does not require any extra damping method and is significantly simplified. With only one current sensor used, low cost of the controller is achieved. Simulation and experimental results of the 210 W prototype were shown to verify the performance of the LCL filter based grid-connected inverter system and the current control strategy. Moreover, the current injected to the grid is regulated precisely and stiffly. High power factor (> 0.99) and low THD (1.32% ~ 3.72%) are obtained under both heavy load and light load conditions.

Chapter 6. Control of an Offshore Wind

Farm Grid-Connected Inverter System

6.1. Introduction

Power electronic converter plays an important role in distributed generation and in integration of renewable energy sources into electrical grid. Taking modern wind turbine as an example, it is inevitable to adapt back-to-back voltage source inverter (VSI) for grid connection via either HVAC or HVDC transmission cable. Among the existing offshore wind farms, the HVAC interconnection has been widely used, such as in Denmark's Horns Rev wind farm, Nysted wind farm, United Kingdom's Barrow wind farm and so on. Figure 6.1 (a) shows the diagram of a typical wind generation system with HVAC transmission. In practice, a group of wind generators are connected to an onshore collection point through VSI, step-up transformers and HVAC submarine cables.

It is well-known that switching-mode power converter (i.e., VSI) would generate harmonics, which potentially pollute the connected utility. To prevent the pollution of the utility by high-frequency current ripple, an filter, typically LC type, is usually installed at the output of the inverter. The capacitor is used to provide a low-impedance path for the high-frequency components. Generally, the transmission line is usually simplified as an inductor for the convenience of grid-connected inverter design. Hence, the inverter actually outputs with an equivalent LCL filter.

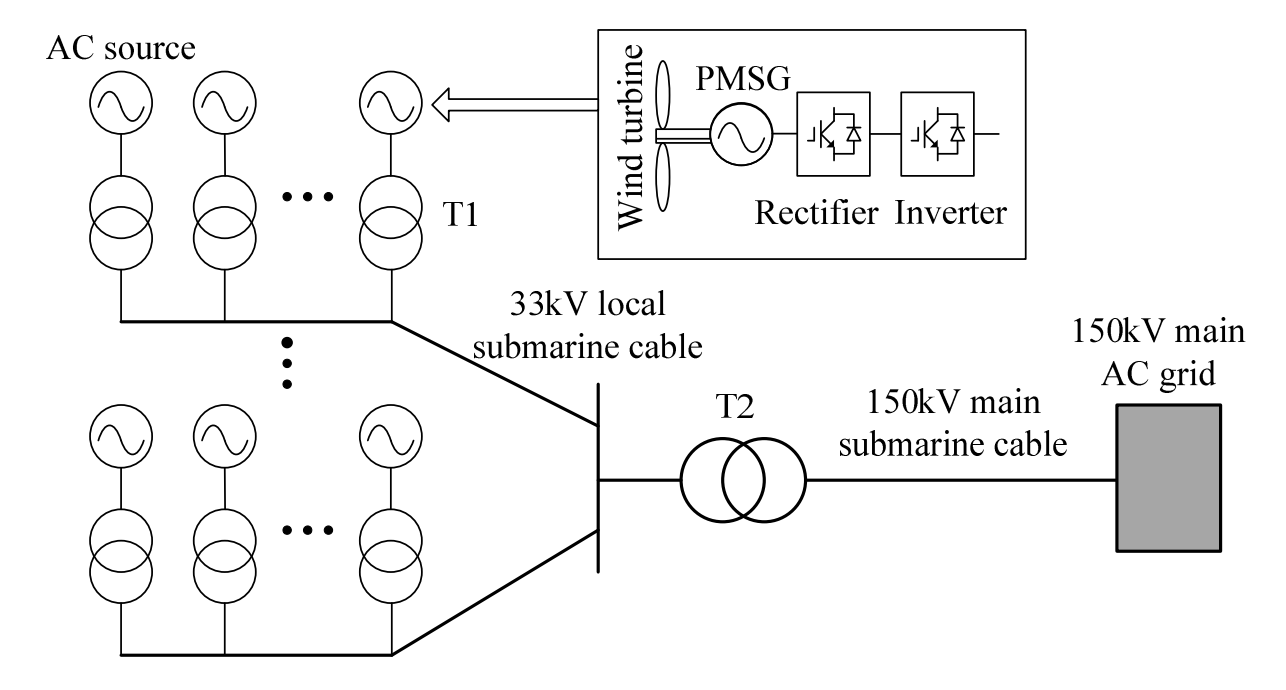


Figure 6.1. Configuration of a typical HVAC grid-connected offshore wind farm.

Passive and active damping techniques are often used to attenuate the resonant peaks caused by LCL filter. However, the passive damping causes a decrease of the overall system efficiency because of the losses on the additional components. Alternatively, multi-loop and filter-based active damping techniques were developed to eliminate the resonant peaks instead of adding any passive devices. In the multi-loop based damping, more system state variables are involved into the control loop to guarantee the system stability [100]-[102]. That means two or even more control loops are required to damp the system resonant peaks. In the filter-based damping methods, a higher order controller (filter) is used to regulate the low-frequency dynamics and damp the potential unstable high-frequency dynamics [58]. The design of the filter can be divided into analogy-based and digital based approaches. In both cases, this class of the active damping methods has the advantage that it does not need more sensors.

As aforementioned, the transmission line is usually equivalent as the inductor. However, because of relative long distance from the onshore main grid, the distributed inductance and

capacitance along the HVAC transmission system is too significant to be ignored [89], [95]. Typically in the range of 100–150 kvar/km for 33-kV cross-linked polyethylene (XLPE) cables, 1000 kvar/km for 132-kV XLPE cables, and 6–8 Mvar/km for 400-kV XLPE cables [85]. Due to the high capacitance of the cable, the inverter filter and the transformer leakage inductance as illustrated in Figure 6.1, a series of resonances may occur between the onshore and offshore grids that leads to a distortion in the shape of the voltage/current, which in turn, potentially result in system instability. According to the authors' knowledge, no systematic study regarding the resonances of the submarine HVAC transmission system has been reported.

In this chapter, a per-unit scale single-phase equivalent model of the HVAC connected wind generation system is developed. The system modeling is firstly derived with consideration of the HVAC cable characteristics and then frequency domain analysis is provided for better understanding of system essential behavior. Due to the high order of LC configuration, the system open-loop transfer function exhibits a series of significant high-frequency resonant peaks, which makes the control loop gain of conventional controller quite small in order to guarantee system stability. Consequently, the steady state error of the system output (i.e., current) is unable to track a sinusoidal reference. Hence, in this chapter, a cascaded notch-filter based active damping method is proposed to address the resonant peaks. Furthermore, the proposed controller also consists of proportional- resonant component to reduce steady-state error of the output current. In order to facilitate the simulations and experimental tests that are carried out later on, all per unit parameters are proportionally reconstructed into actual values in the 120Vac emulator system. The simulation and experimental results validate the findings of resonances and the performance of the proposed controller. Since in practical applications, the transmission cable parasitic parameters has a considerable amount of uncertainty, an auto tuning algorithm is then

discussed, which can automatically detect the system resonance frequencies and thus the damping controller notch frequencies can be placed much more accurately.

6.2. Equivalent Model of Offshore Wind Farm Transmission System

Considering the offshore wind farm system shown in Figure 6.1, if every wind turbine generator and the associated VSC are identical, all these distributed power sources can be simply considered as one single source [90]. To make the analysis more convenient, the system in Figure 6.1 can be further simplified into a per unit scale single-phase AC system, where all the transformers are eliminated. Figure 6.2 shows the simplified equivalent model of the offshore wind farm.

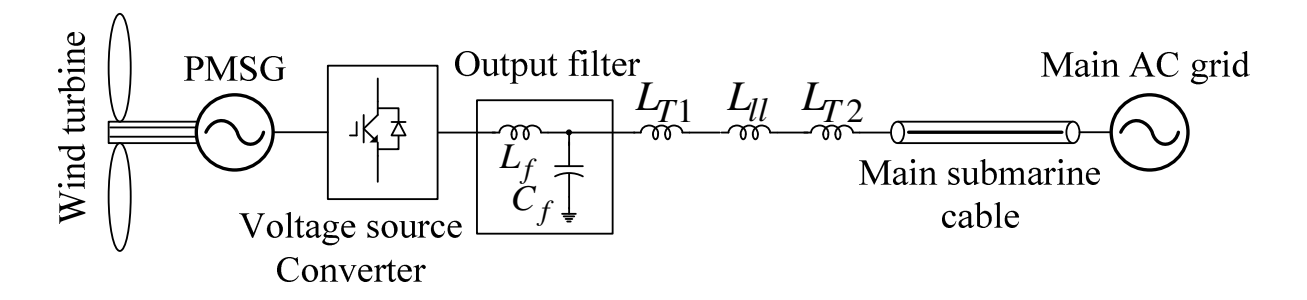


Figure 6.2. Equivalent single-phase circuit of the HVAC offshore wind farm in per unit scale.

In Figure 6.2, the wind turbine is connected to a permanent magnet synchronous generator (PMSG) and then fed to a VSC. L_f and C_f represent the VSC's output filter tank. The impedance of transformer T1, the local 33kV submarine cable, and the impedance of transformer T2, which are shown in Figure 6.1, are represented by L_{T1} , L_{Il} , L_{T2} . The main HVAC submarine cable is connected between T2 and the onshore main grid.

In this dissertation, our main interest is concentrated on the resonance issues after the VSC. Hence, an emulator system shown in Figure 6.3 can be further developed, where the wind turbine generator and VSC are represented by one single-phase inverter. L_{T1} , L_{ll} , L_{T2} in Figure 6.2 are merged together as one single inductor L_r . r_f and r_r stand for the equivalent series resistance (ESR) along with L_f and L_r .

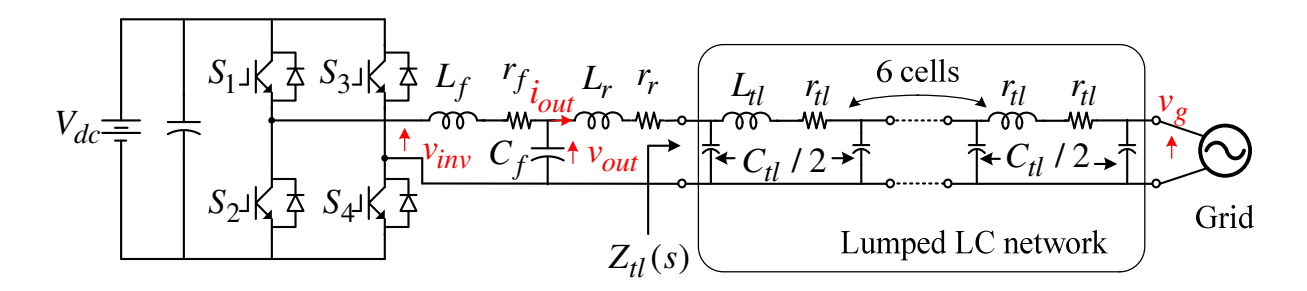


Figure 6.3. Proposed 120Vac single-phase offshore wind farm emulator system.

The high frequency characteristic of the 150kV submarine cable has a significant impact on the entire system frequency response. Therefore, the submarine cable modeling is very critical here. It is known that submarine cable has large shunt capacitance. For long distance transmission, the transmission line effect can no longer be neglected. In practice, a transmission line can be mimicked by a lumped LC network with finite number of cells [95], [96]. More number of cells gives better equivalence in terms of high-frequency characteristics. In reality, due to the significant impact of the conductor skin effect at high frequencies, the ESR along the submarine cable becomes dominant, giving sufficient passive damping naturally. In practice, a total of 6 cells of π model will be far enough to mimic the submarine cable, as shown in Figure 6.3. L_{tl} , C_{tl} and r_{tl} represent the series inductance, shunt capacitance and ESR in each cell.

Considering the skin effect in a cylindrical conductor, the ESR in each cell can be expressed in Laplace form as given in (6.1). r_{tl0} is the ESR at f_0 , where the skin depth equals to the radius of the conductor.

$$r_{tl}(s)\Big|_{s=j2\pi f} = r_{tl0} \cdot \frac{1}{1 - \left(1 - \sqrt{\frac{j2\pi f_0}{s}}\right)^2}$$
 (6.1)

 $Z_{tl}(s)$ is the input impedance of submarine cable seen from the offshore end. The transfer function from the inverter output voltage $v_{inv}(s)$ to the output current $i_{out}(s)$ is represented by $P_{inv}(s)$, as given by (6.2).

$$P_{inv}(s) = \frac{i_{out}(s)}{v_{inv}(s)} = \frac{1}{\left[sL_r + r_r + Z_{tl}(s)\right] + sC_f(sL_f + r_f)\left[sL_r + r_r + Z_{tl}(s) + \frac{1}{sC_f}\right]}$$
(6.2)

The key parameters of the offshore wind farm for study is summarized in Table 6.1. The system has a rated power capacity of 3MVA. 45km ABB XLPE cable is used for the 150kV HVAC power transmission. According to the cable datasheet, the calculated ESR loss is around 3.6% at 60Hz. However, if skin effect is taken into account, the calculated ESR loss increases to 14.1% at 1kHz and 23.62% at 3kHz, respectively, according to (6.1). The local line impedance L_r , which is a summation of the transformer impedance and the local 33kV submarine cable impedance, is regarded as an uncertain parameter here and can vary from 1% p.u. to 15% p.u. depending on the specific system.

Table 6.1. Parameters of the offshore wind farm system

HVAC transmission voltage	150 kV
Rated power	3 MVA
Local line impedance (L_r)	2% ~15%
Fundamental frequency	60 Hz
Main cable length	45 km
Main cable type	ABB XLPE
Main cable cross section area	630 sqmm
Main cable resistivity	0.0146 Ohm/1000 ft

Table 6.2. Parameters of the emulator system

Nominal voltage	120V
Nominal current	8A
Local line impedance (L_r)	1% ~15% p.u.
Output filter inductance (L_f)	700 uH (1.76% p.u.)
Output filter capacitance (C_f)	0 ~ 50uF (0~28.3% p.u.)
Lumped LC network cell No.	6 cells
Inductance per cell (L_{tl})	700 uH (1.76% p.u.)
Capacitance per cell (C_{tl})	3 uF (1.7% p.u.)
ESR per cell (r_{tl0})	72.5 mOhm (0.48% p.u.)
Sampling/switching frequency	10kHz

Keeping the per unit values of the system parameters in Table 6.1 constant, the scaled-down emulator system depicted in Figure 6.3 can be developed with the parameters listed in Table 6.2. For simplification, it is assumed that the ESR r_r and r_f are both around 1% p.u..

6.3. Frequency Domain Analysis and Controller Design

6.3.1. Modeling of Long Transmission Cable

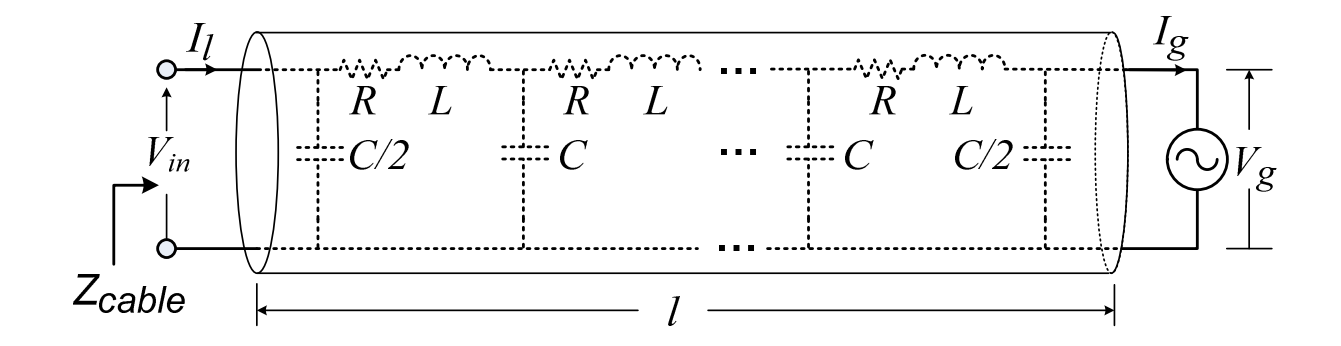
Figure 6.4 shows the schematic diagram of one-phase HVAC cable as well as its impedance characteristic. As illustrated in Figure 6.4(a), the input impedance of a lossless transmission cable terminated with an ideal voltage source is defined as

$$Z_{tl} = Z_C \frac{Z_g / Z_C + \tanh(\gamma l)}{(Z_g / Z_C) \tanh(\gamma l) + 1}$$
(6.3)

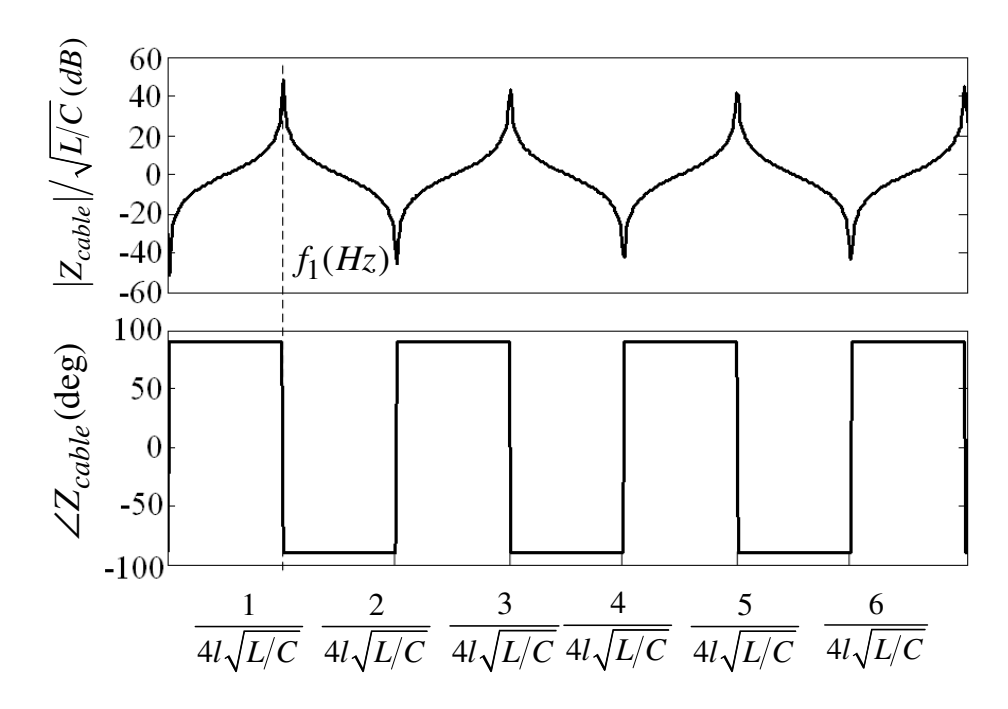
Where $Z_g = V_g/I_g$ is the grid-side impedance. $\gamma = \sqrt{z \cdot y}$ is called the propagation constant and $Z_C = \sqrt{z/y}$ is called the characteristic impedance of the line. $z = \omega L$ and $y = \omega C$ are the per unit length series impedance and shunt admittance of the cable, respectively. From (6.3), Z_{tl} of the lossless transmission line is a transcendental function with an infinite number of j-axis poles and zeros. Figure 6.4(b) shows the theoretical Z_{tl} of the transmission cable, when Z_g is zero.

On the other hand, it is worthy to point out that the current density in AC circuits is greater near the outer surface of the conductor, which is so-called skin effect. Near to the center of the conductor there are more lines of magnetic force than near the rim. This causes an increment in the inductance toward the center and the current tends to crowd toward the outer surface. As a sequence, with the increase of operating frequencies, the effective cross section area of the conductor would decrease and thereby the ESR along the cable becomes dominant, giving sufficient passive damping naturally. Hence, with the concern of conductor skin effect, the poles and zeros as shown in Figure 6.4(b) could be attenuated accordingly when the frequency

increases. Figure 6.5 shows the impedance of a transmission cable with concern of skin effect. The cable parameter used here is listed in Table 6.1 and Table 6.2.



(a) Schematic diagram



(b) Impedance of a cable of length *l* terminated in a short circuit

Figure 6.4. One-phase of a HVAC cable

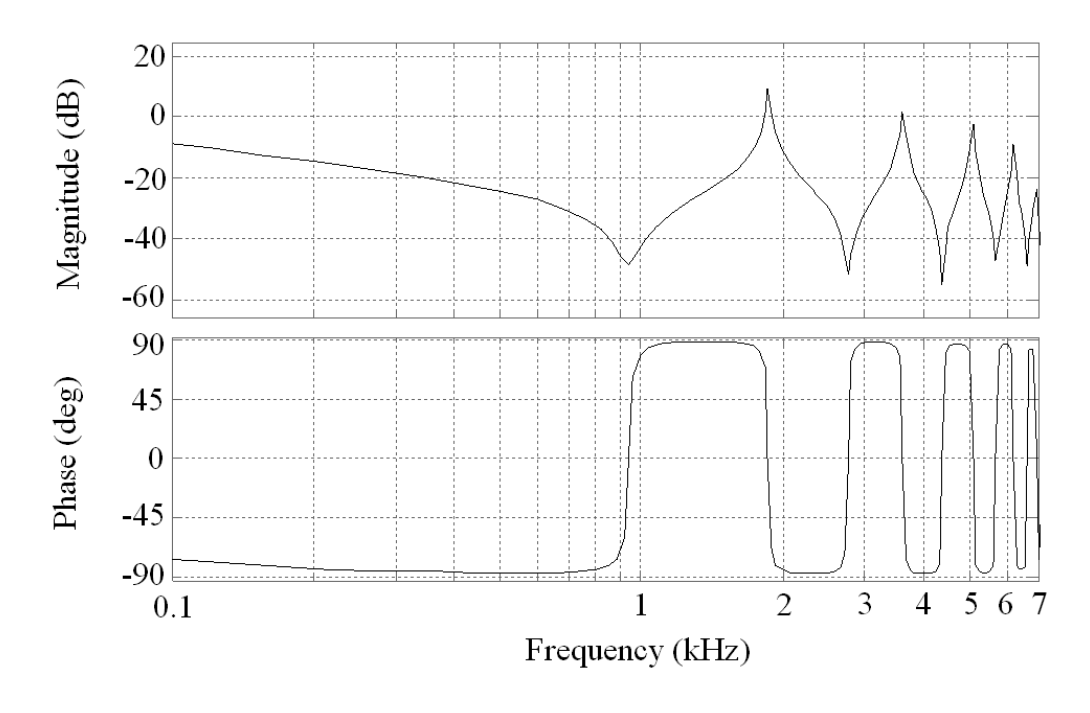


Figure 6.5 Impedance characteristic of the transmission cable

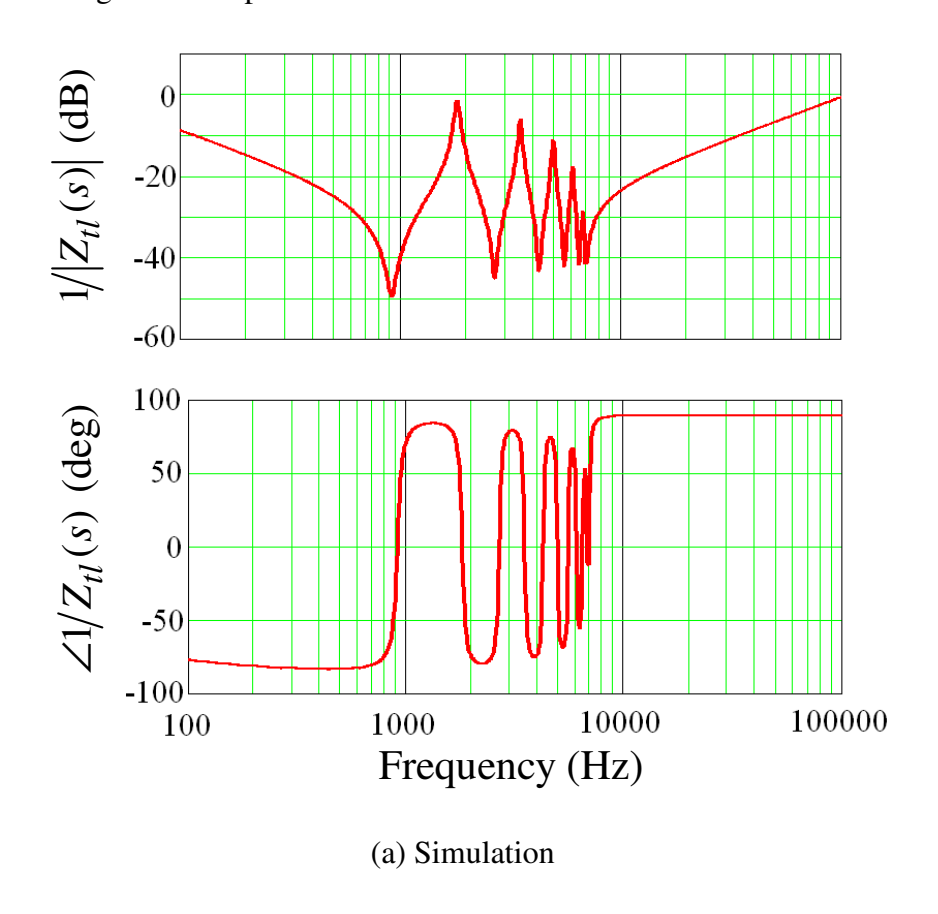
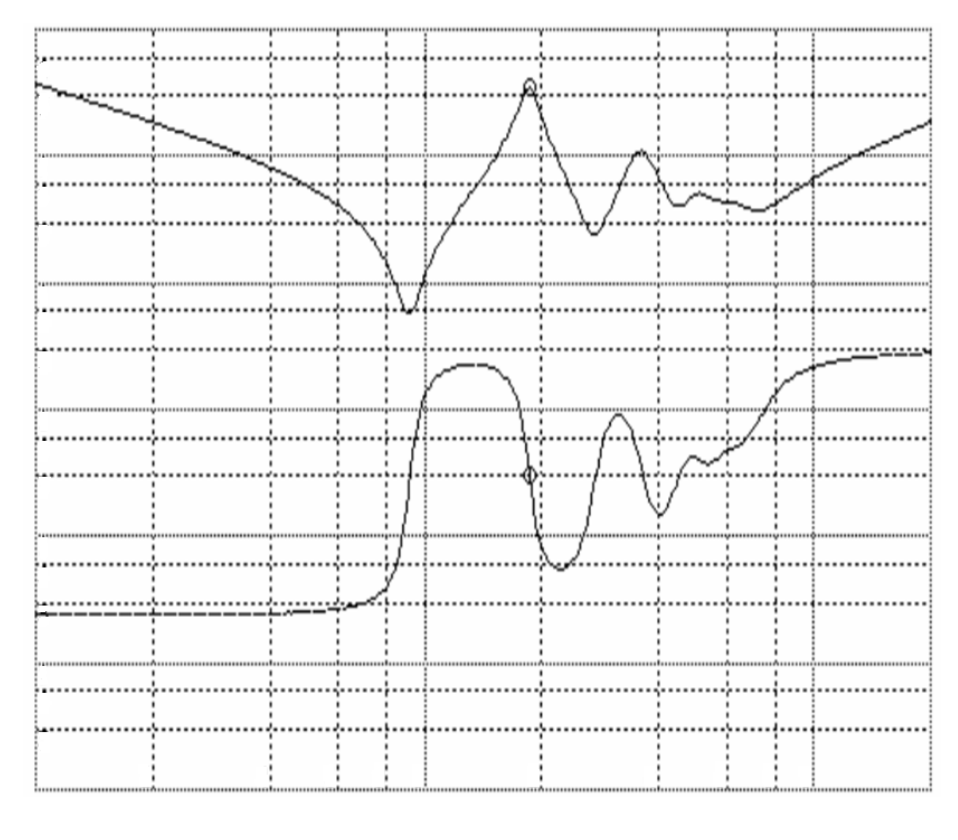


Figure 6.6. Frequency responses of the lumped LC network input admittance.

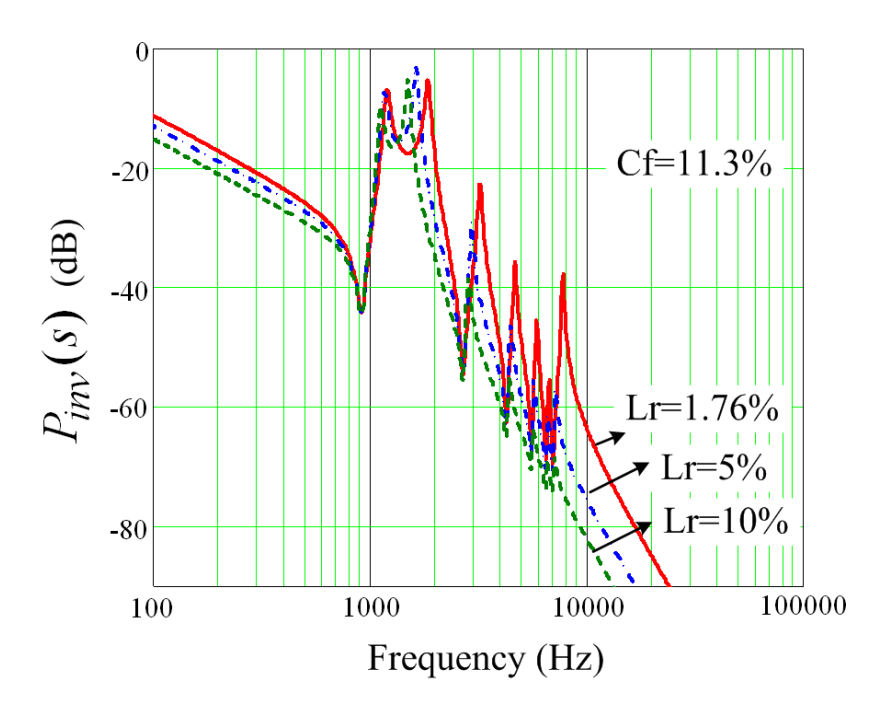
Figure 6.6 (cont'd).



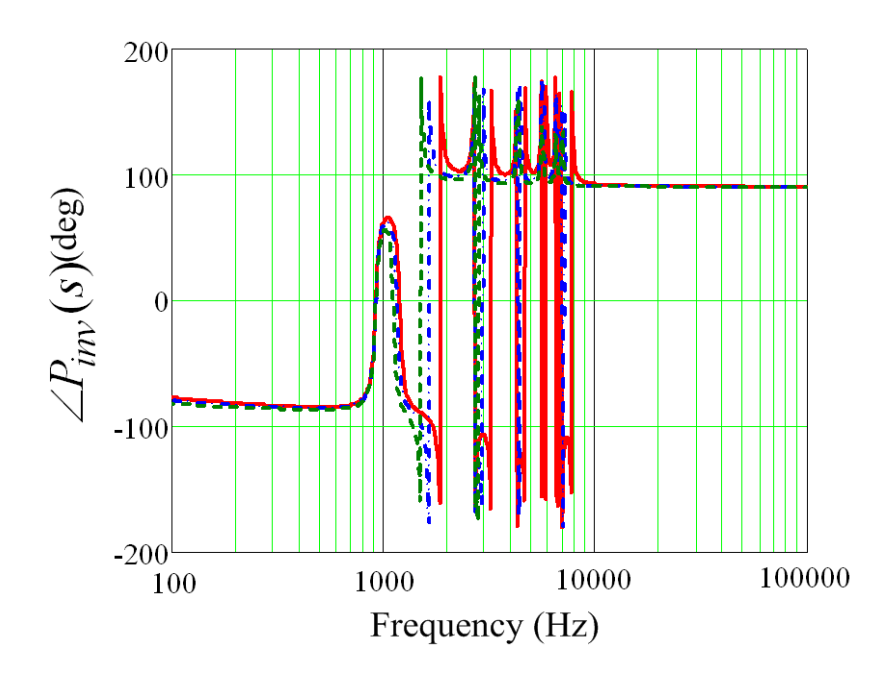
(b) Experiment

The input admittance response of the lumped LC network used to mimic the submarine cable is shown in Figure 6.6. Figure 6.6(a) gives the frequency domain simulation result based on the cable parameters listed in Table 6.1 and Table 6.2. The first resonance poles are located around 1.8kHz. Due to skin effect, the resonance peaks have more damping at higher frequencies. A prototype of 6-cell lumped LC network was built and tested in the laboratory. Figure 6.6(b) shows the experimental measurement. Because of the greatly increased inductor core loss at higher frequencies, more damping was observed compared to the simulation result. Nevertheless, it is still good enough to verify the concept.

6.3.2. Resonances in the Offshore Wind Farm System



(a) Magnitude-frequency response

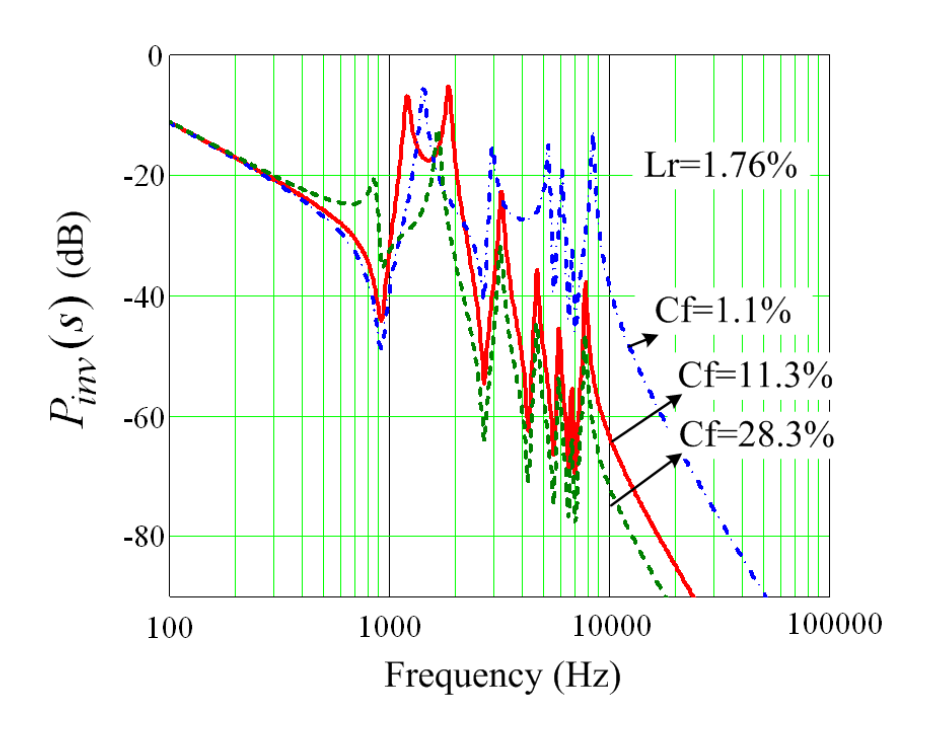


(b) Phase-frequency response

Figure 6.7. Bode plot of $P_{inv}(s)$ under different line impedances.

Since the output current i_{out} is the control target, the transfer function from the inverter output voltage v_{inv} to i_{out} , represented by $P_{inv}(s)$, is of our interest. From (6.2), the bode diagram of $P_{inv}(s)$ can be plotted as in Figure 6.7 and Figure 6.8.

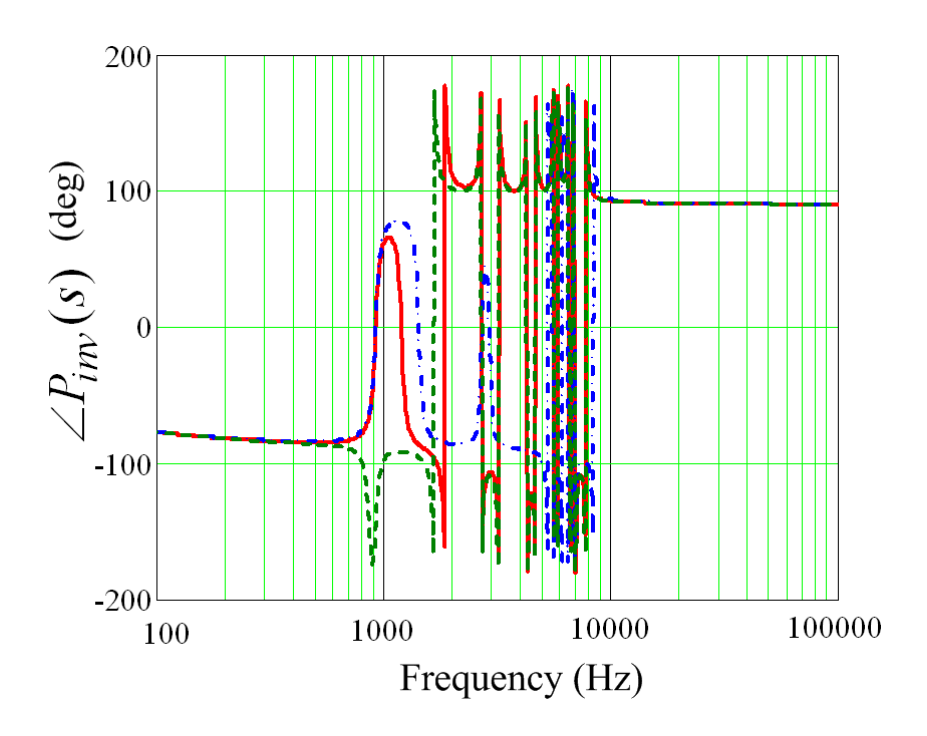
In Figure 6.7, the output filter capacitance is fixed to 20uF (11.3% p.u.), $P_{inv}(s)$ is plotted under different local line impedances (L_r). If $P_{inv}(s)$ is multiplied by a gain K_p to obtain a cross-over frequency around 240Hz, it is noticeable that better gain margin at high-frequency resonance peaks can be achieved when higher L_r is selected.



(a) Magnitude-frequency response

Figure 6.8. Bode plot of $P_{inv}(s)$ under different filter capacitances.

Figure 6.8 (cont'd).



(b) Phase-frequency response

In Figure 6.8, L_r is fixed to 1.76% p.u., $P_{inv}(s)$ is plotted under different output filter capacitance (C_f). Likewise, higher C_f brings better high frequency attenuations of $P_{inv}(s)$. One particular example is that C_f is not implemented in the output filter. In this case, multiple high-frequency resonance peaks will exceed 0dB, making the system extremely difficult to compensate.

Therefore, a conclusion can be drawn from the above analysis: larger L_r and C_f leads to more desirable high-frequency characteristics of $P_{inv}(s)$. But on the other side, larger L_r and C_f simultaneously result in more reactive power flowing in the transmission system.

Consider a worst case in which L_r is very small (assumed as 1.76%). From Nyquist law, in order to actively compensate the high-frequency resonance poles, the controller sampling

frequency should be sufficiently higher than twice of the resonance frequencies. In high power converters, switching and sampling frequencies typically do not exceed 10kHz. Resultantly, a practical active damping compensator should only compensate the first two resonance peaks (below 2kHz). Based on this constraint, the filter capacitance C_f is selected as 20uF (11.3%) minimum.

6.3.3. Notch Filter Based Active Damping Control

A current control strategy is proposed as shown in Figure 6.9.

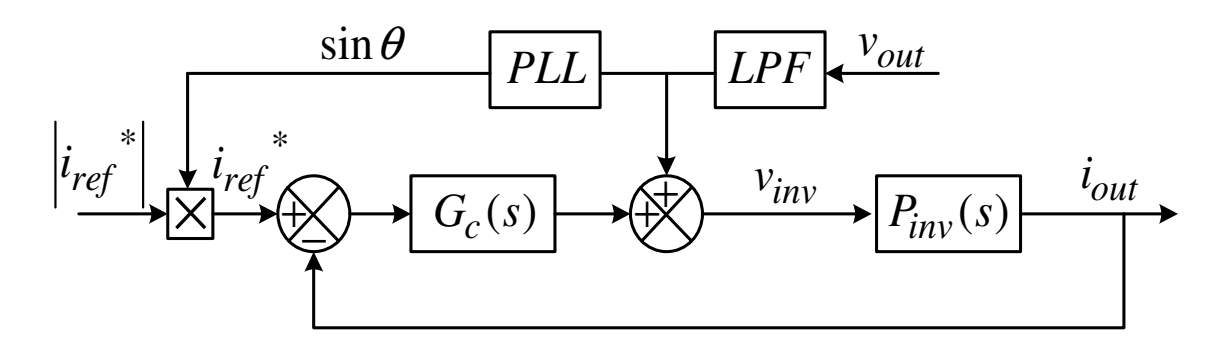


Figure 6.9. Block diagram of proposed current control strategy.

As aforesaid, it is possible to make the system stable by drastically reducing the proportional gain of the PI controller. However, this yields poor bandwidth and disturbance rejection capability. Hence it will be not considered here. The requirement for the potential control strategies is to obtain resonance damping while preserving reasonable bandwidth as well as stability and robustness margins.

To achieve this target, filter-based damping strategies will be explored to address the resonance peaks of the system open-loop transfer function $G_C(s)$ Pinv(s) as illustrated in Figure 6.9. The performance/effectiveness of filter-based damping techniques will be evaluated by the following two criterions: The first one is to attenuate the resonance peak of the gain response. However, as the resonance peak is very high, a rather sharp filter characteristic is required.

Otherwise, the closed-loop bandwidth is decreased considerably. On the other hand, it is required to avoid 180 degree crossings in the frequency range with a gain above 0-dB. Note that the gain and phase responses cannot be modified separately.

With the above theoretical analysis, notch filter is found very suitable to damp the gain resonance since its stop-band filter characteristic. Hence, the notch filter aims to damp the resonant peaks of the open loop transfer function. The continuous transfer function of the standard notch filter can be expressed as,

$$G_{notch,i} = \frac{s^2 + m_i \omega_i s + \omega_i^2}{s^2 + n_i \omega_i s + \omega_i^2}$$
(6.4)

Where, ω_i is the notch frequency where signal can be mostly attenuated by the filter. The deepness and wideness of the notch filter will be decided by the damping of the zeros and of the poles of the filter, respectively. Actually, the notch filter is often used to filter out the undesired signal in the specific frequency only. Figure 6.10(a) shows the bode plot of the notch filter. It has a V-shape magnitude characteristic, with the gain remaining fairly close to unity up to the neighborhood of the notch point, then falling off abruptly with a descending rate much greater than that of a second-order filter. This behavior is suitable for canceling out the resonant peak without appreciable attenuation at lower frequencies.

Again, the multiple resonant frequencies are existed with the consideration of the cable characteristic. It is required to attenuate multiple resonance peaks by notch filters in order to maintain system stability. As a sequence, the so-called cascaded notch-filter (multiple notch filters in series) is proposed to damp the significant resonance peaks. The order of the cascaded notch filter is determined by the number of peaks, of which the magnitude is above 0-dB.

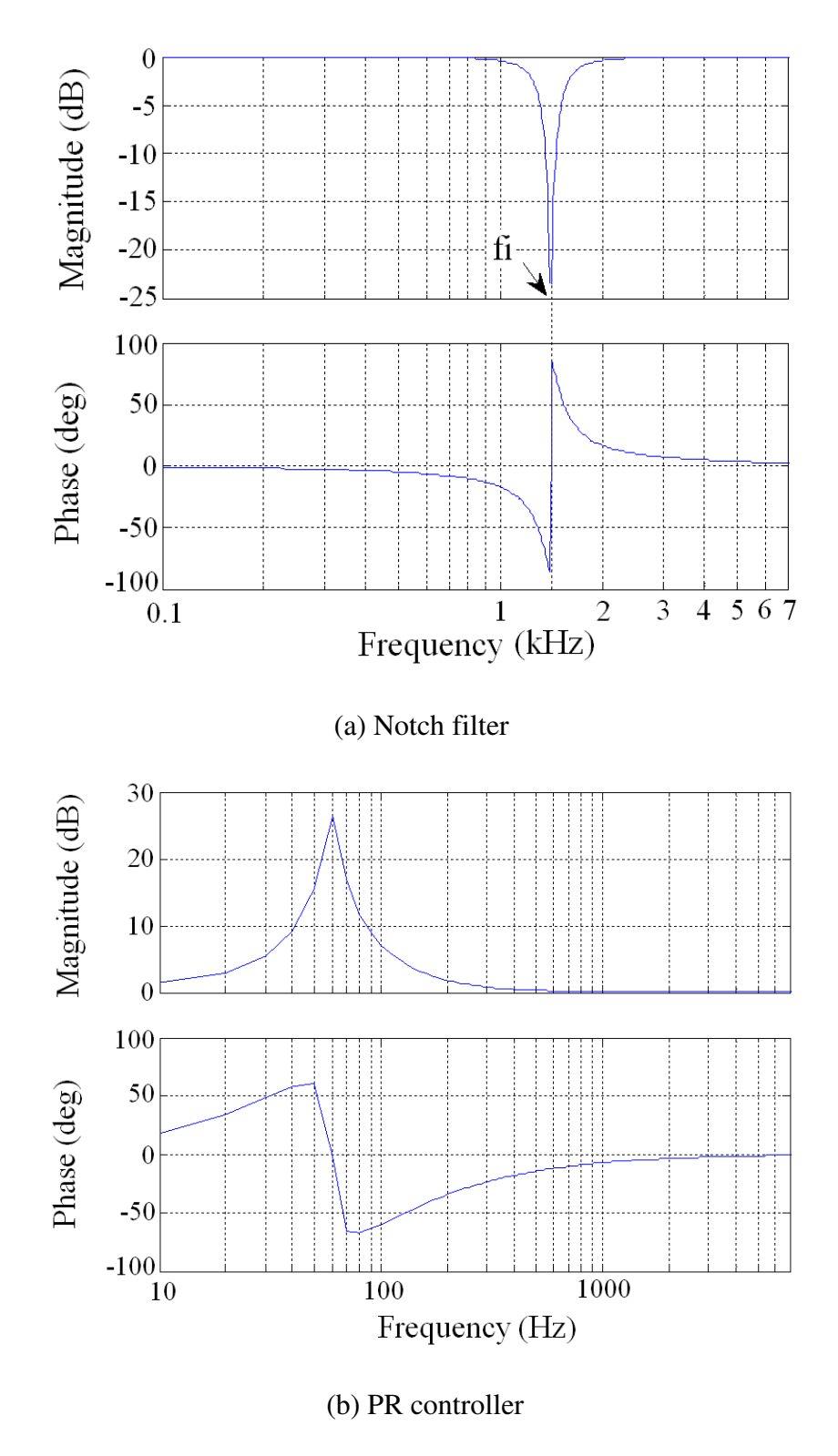


Figure 6.10. Bode plots of the notch filter and the proportional resonant (PR) controller

On the other hand, proportional-resonant (PR) controller is able to provide high gain at fundamental frequency and thus reduces the steady-state error. The expression of a proportional resonant controller is as follows:

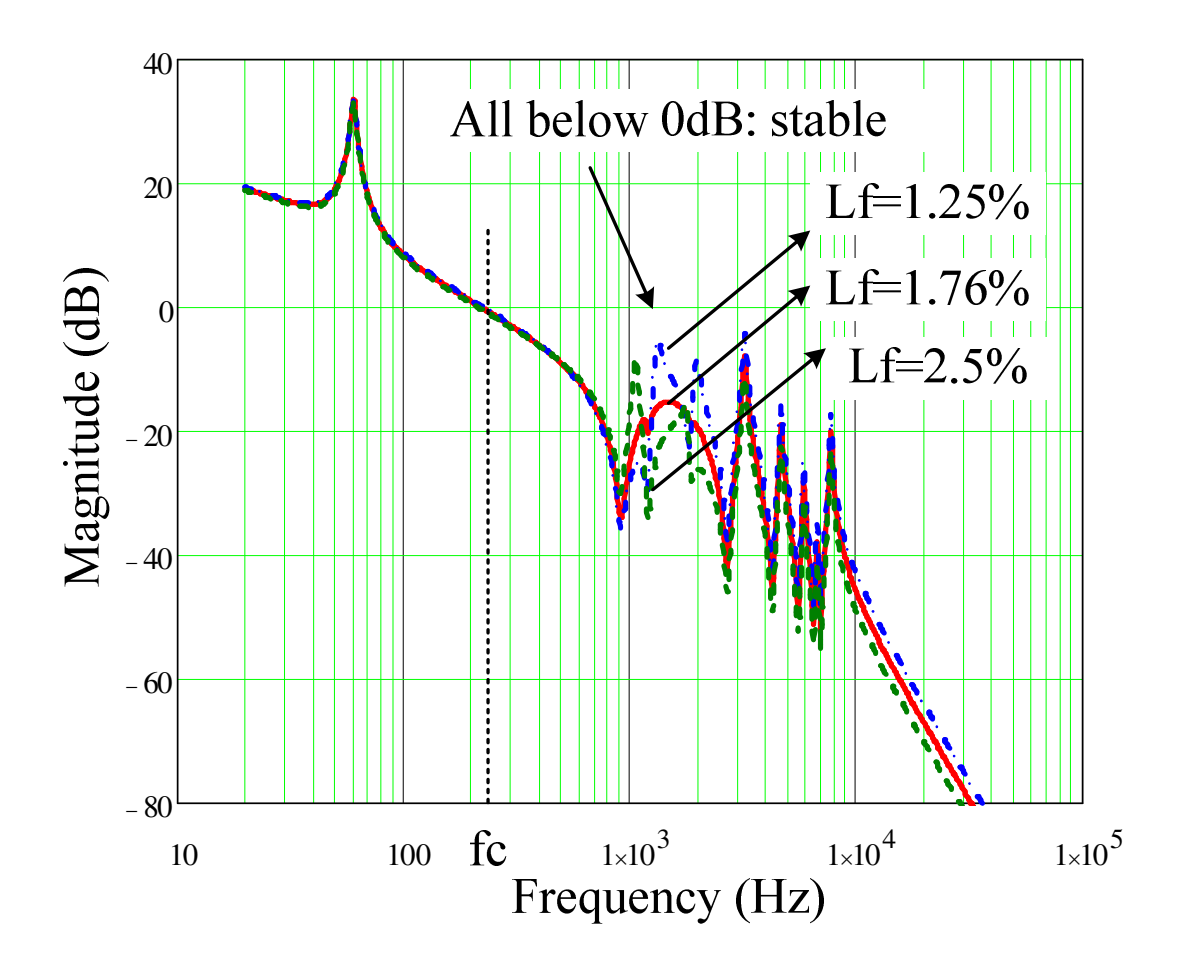
$$G_{PR} = K_P + \frac{2K_R\omega_C s}{s^2 + 2\omega_C s + (\omega_0^2)}$$
(6.5)

Where, ω_C is the equivalent bandwidth of the controller. K_P and K_R are the proportional and resonant gain, respectively. ω_0 is the frequency that needs a high gain on it. ω_C needs to be set as small as possible because a large ω_C will introduce a phase lag toward the crossover frequency and thus decreases the phase margin. Figure 6.10(b) shows the bode plots of the PR controller.

The voltage across C_f (v_{out}) is sensed for PLL and feed forward. In order to reduce the sensitivity of v_{out} to the high frequency disturbances, a low pass filter is incorporated here. The proposed current controller $G_c(s)$ is expressed in (6.6). Two notch filters are cascaded for the active damping compensation. The two notch filters are aligned at 1.2 kHz and 1.85 kHz, respectively. The controller delay is expressed as $e^{-1.5sT_s}$.

$$G_{c}(s) = \left[K_{p} + \frac{2K_{R}\omega_{c}s}{s^{2} + 2\omega_{c}s + \omega_{0}^{2}}\right] \cdot \left[\frac{s^{2} + m_{1}\omega_{n1}s + \omega_{n1}^{2}}{s^{2} + n_{1}\omega_{n1}s + \omega_{n1}^{2}}\right] \cdot \left[\frac{s^{2} + m_{2}\omega_{n2}s + \omega_{n2}^{2}}{s^{2} + n_{2}\omega_{n2}s + \omega_{n2}^{2}}\right] \cdot e^{-1.5sT_{s}}$$
(6.6)

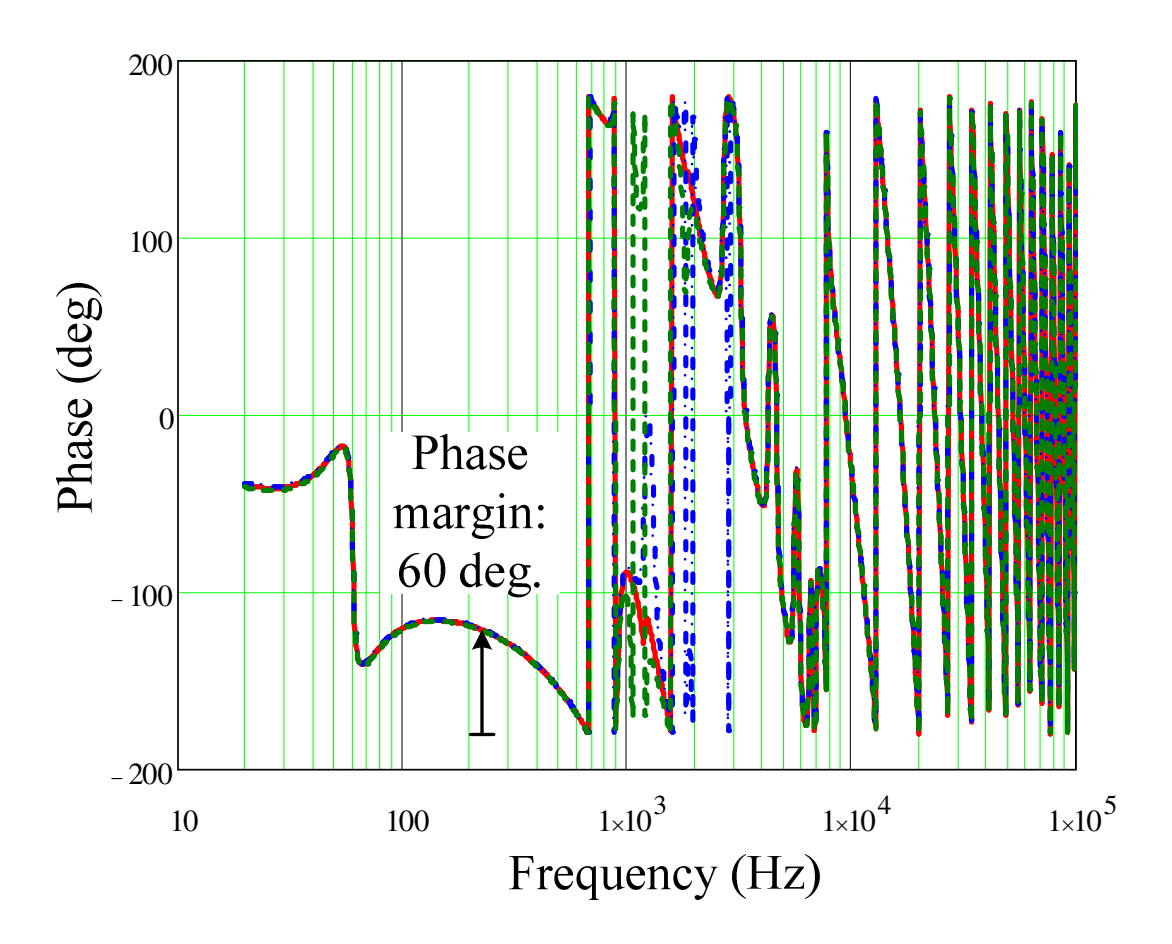
The system bode diagram after compensation is plotted in Figure 6.11. Within a certain range of the filter inductance variation, for example 1.25% p.u. ~2.5% p.u. here, the compensated high-frequency resonance poles are well below 0 dB. A phase margin of 60 degrees is achieved at the cross-over frequency 240Hz.



(a) Magnitude frequency response

Figure 6.11. Bode plot of $G_c(s)P_{inv}(s)$ under parameter variations.

Figure 6.11 (cont'd).



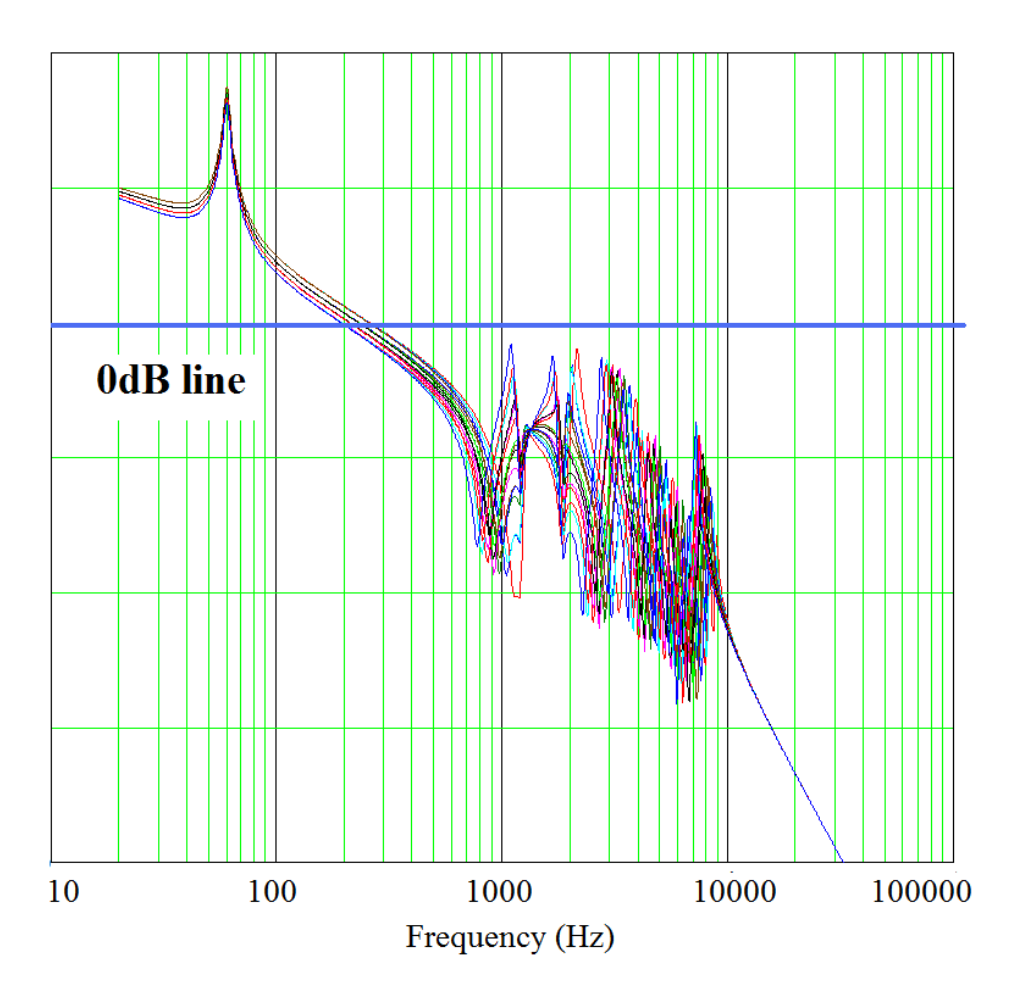
(b) Phase frequency response

6.3.4. Cable Parameters Uncertainty and Resonance Frequency Auto-Detection

Based on the previously proposed notch filter damping control technique, one particular question will come up. What if the cable resonance frequencies are not aligned with the notch frequencies due to cable parameters uncertainty? Therefore, it is desired to also analyze the damping controller performance given a certain parameters variation range.

Figure 6.12 shows the open loop transfer function bode plot when the transmission cable has a +-20% tolerance of its inductance and capacitance.

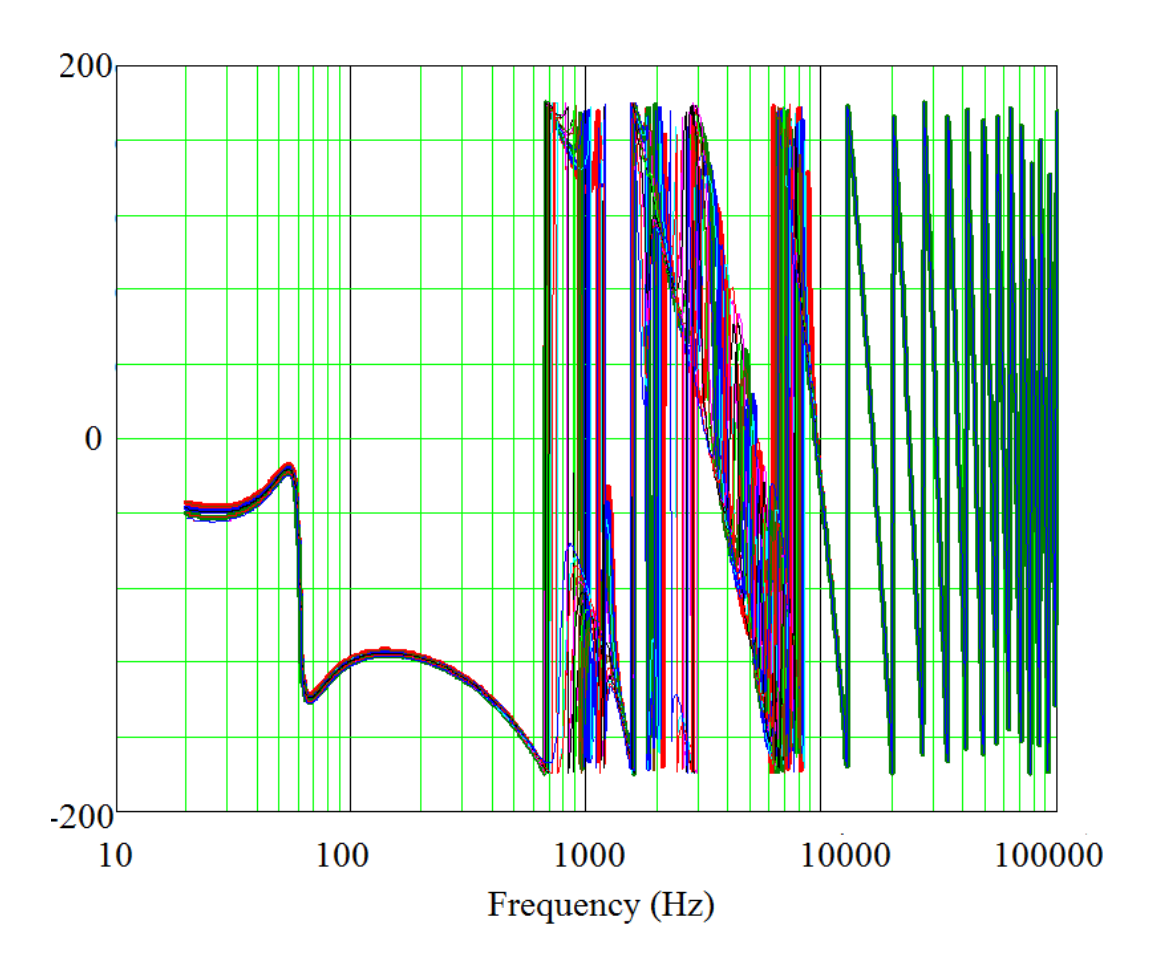
From Figure 6.12(a), it is shown that the notch filter can appropriately damp the resonance peaks under 0dB within the +-20% cable parameter tolerance, even when the notch frequency is not exactly aligned with the resonance frequencies. However, we can see the gain margin is not very large especially when the cable inductance and capacitance are both located at the lower boundary (-20%). From Figure 6.12(b), there's minimal impact from the cable parameter to the phase margin at the 0dB cross-over frequency due to the cable parameter tolerances.



(a) Magnitude frequency response

Figure 6.12. Bode plot of $G_c(s)P_{inv}(s)$ with +-20% tolerance of cable parameters.

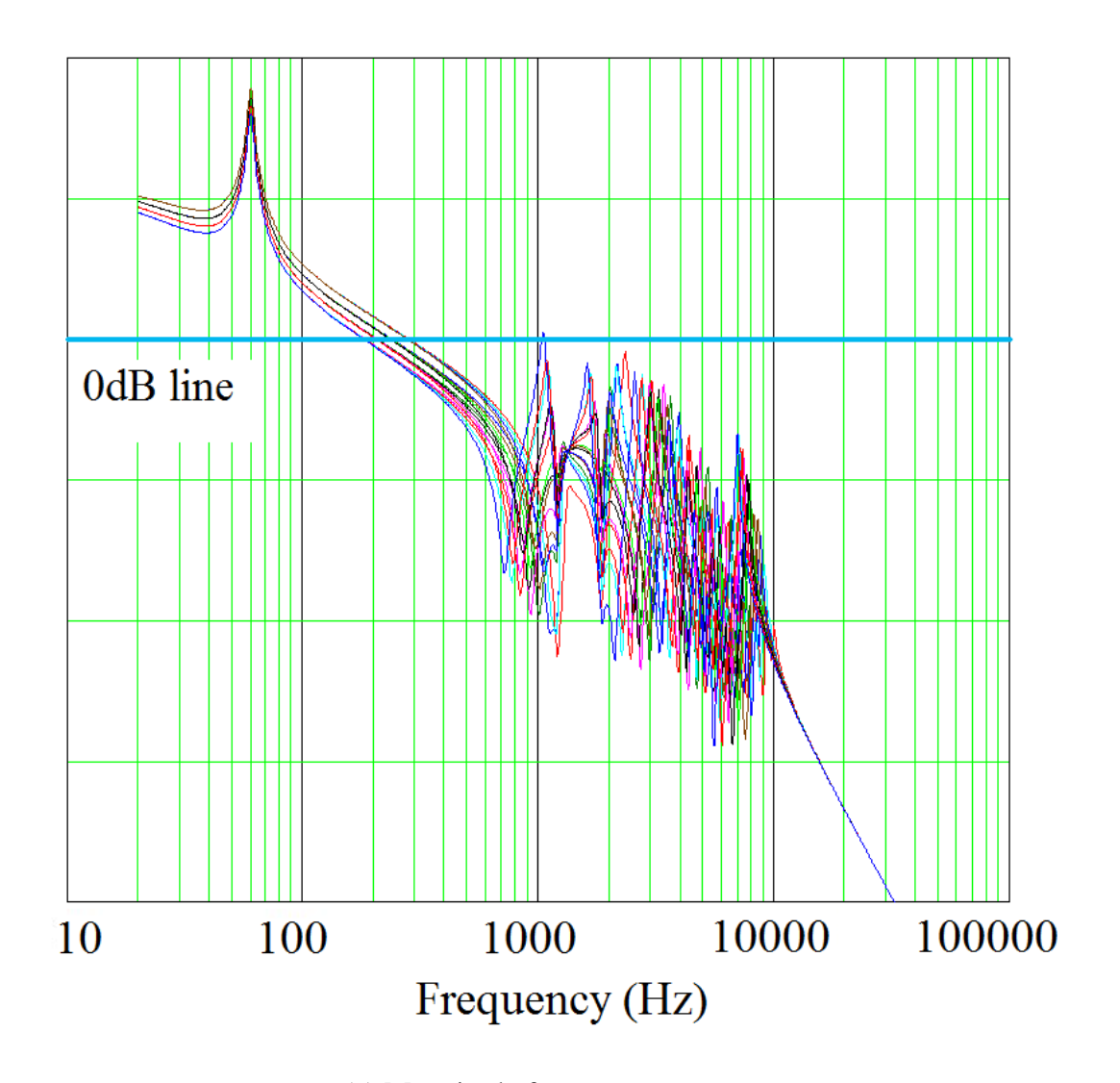
Figure 6.12 (cont'd).



(b) Phase frequency response

Figure 6.13 shows the open loop transfer function bode plot when the transmission cable has a +-30% tolerance of its inductance and capacitance. It can be seen that when the inductance and capacitance are both reduced by 30%, the first resonance peak of the loop gain curve is above 0dB, which results in instability.

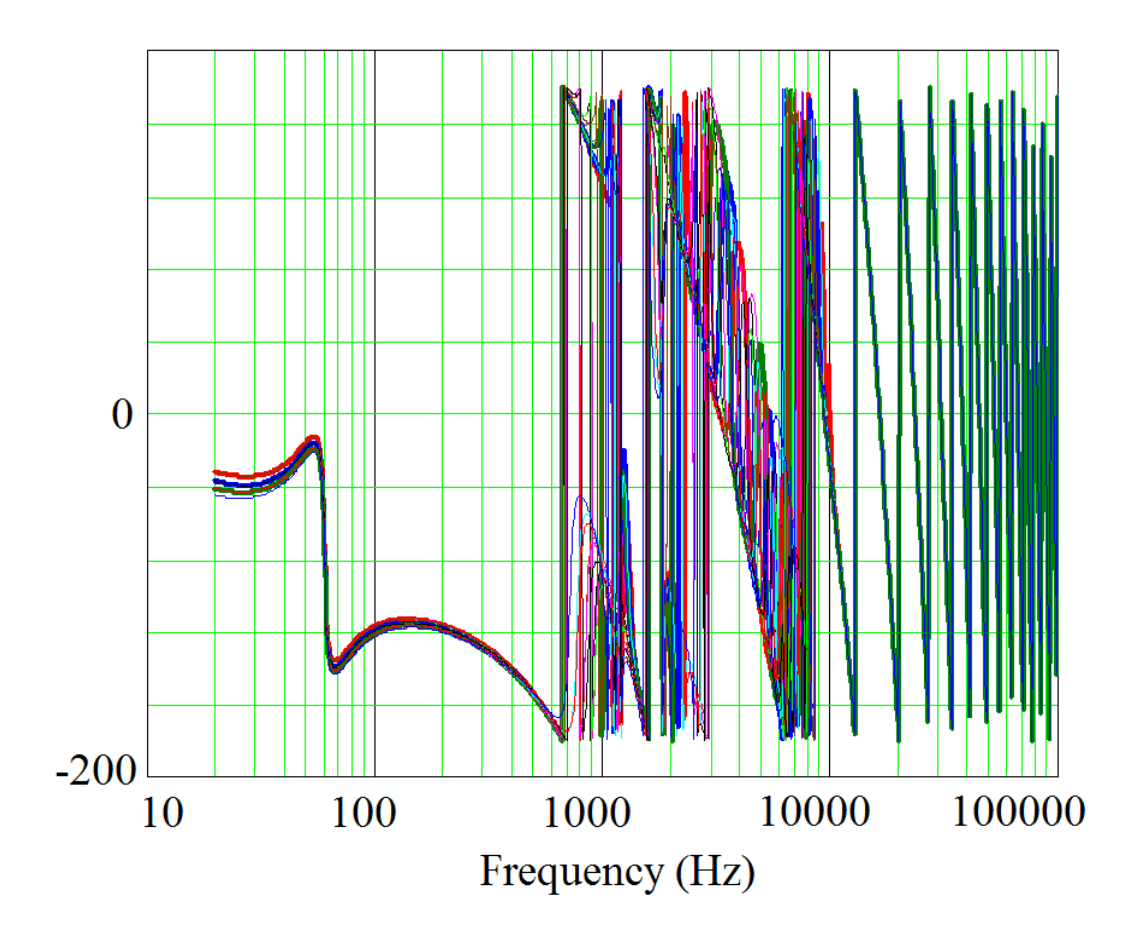
Fortunately, with the advancement of digital control, it is possible to automatically detect the resonance frequencies of the system ($P_{inv}(s)$). Figure 6.14 shows the auto damping control scheme particularly designed for the interested offshore wind farm system.



(a) Magnitude frequency response

Figure 6.13. Bode plot of $G_c(s)P_{inv}(s)$ with +-30% tolerance of cable parameters.

Figure 6.13 (cont'd).



(b) Phase frequency response

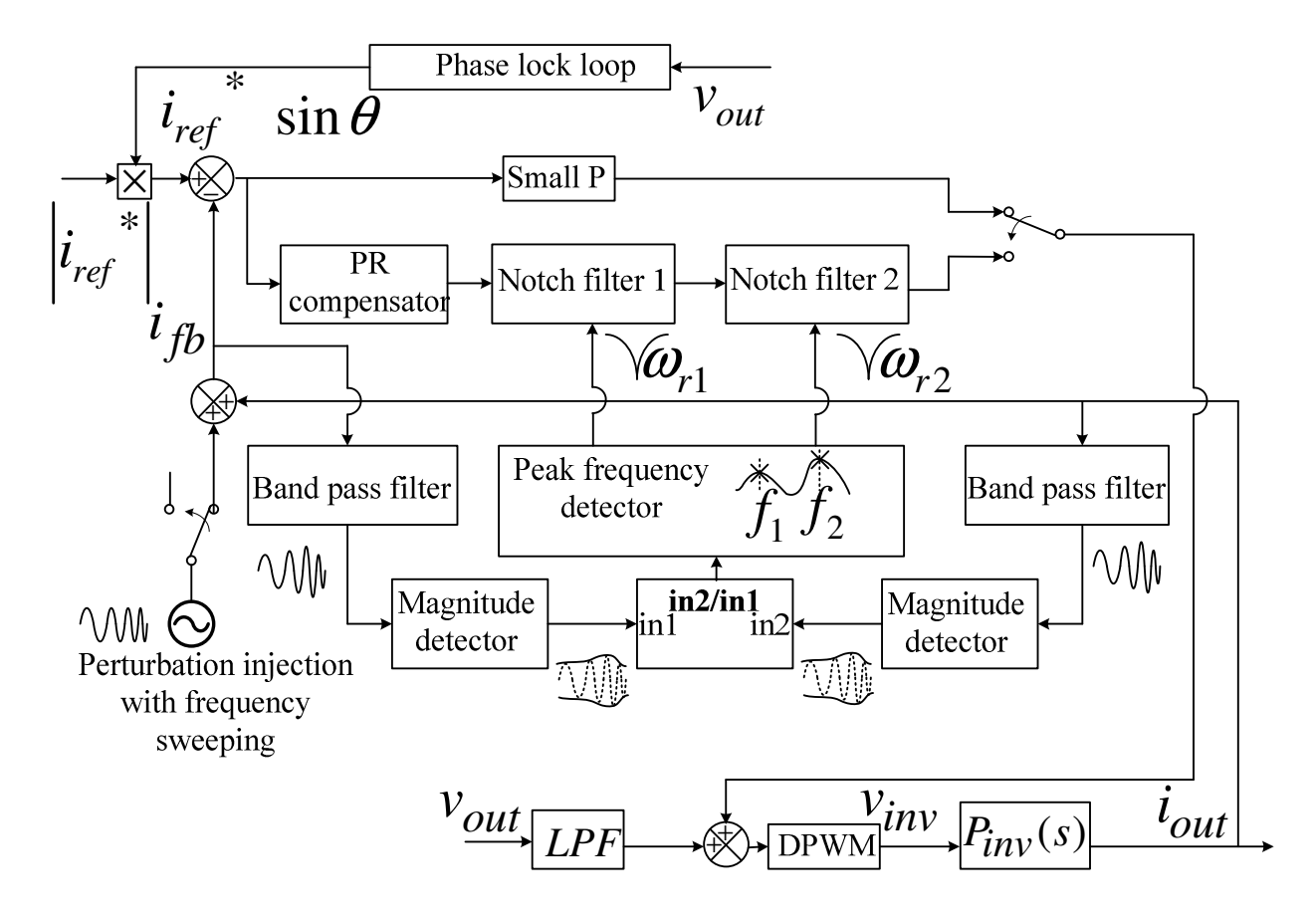


Figure 6.14. Auto damping control scheme.

An offshore wind farm emulator system composed of a full-bridge single-phase inverter, an LC filter, a line inductor, a lumped LC network with 6 π -model cells, and a 120Vac grid has been set up in the laboratory. L_r is selected as 700uH (1.76%).

The concept in Figure 6.14 is to automatically search for the transmission system resonant frequencies during inverter start up. Once the system resonance frequencies are detected after the inverter start up, then align the notch filter frequencies with the resonances.

Steps of the auto damping control scheme:

1. Use a low gain P controller which guarantees the closed-loop system stability. This is very important since if the stability is not guaranteed, the resonances occurring in the system will affect the voltage and current measurement accuracy during the auto damping scheme running.

On the opposite, a stable system with low proportional gain will guarantee the convergence of the auto damping scheme.

- 2. Inject a pure sinusoidal perturbation signal into to the current feedback signal.
- 3. Sweep the frequency of the perturbation signal within the interested frequency range. Measure the small signal gain from the modified current feedback to the original current feedback.
- 4. Find the peaks of the measured small signal gain and the associated frequencies. Tune the notch filter frequencies accordingly.
 - 5. Switch from the low gain P controller to the desired PR + notch filter controller.

This auto damping control scheme is very similar to the function of a network analyzer, which sweeps the frequency of the injected perturbation signal and measures the transfer function from the system input to the output such that the frequency response of any unknown system can be recorded. In practice, once the real offshore wind farm system using long undersea cables is built, the system parameters are relatively fixed, except for the change caused from temperature, ocean flow, and other environmental factors. Therefore, the control in a real offshore wind farm system does not require continuous online measurement of the system physical characteristics. The proposed auto damping scheme can be activated once a while for calibration purposes.

Due to page limit and the scope of this dissertation, more details of the proposed auto damping technique will not be discussed, which is left for future work.

6.4. Simulation and Experimental Results

An offshore wind farm emulator system composed of a full-bridge single-phase inverter, an LC filter, a line inductor, a lumped LC network with 6 π -model cells, and a 120Vac grid has been set up in the laboratory as Figure 6.15 shows. L_r is selected as 700uH (1.76%).

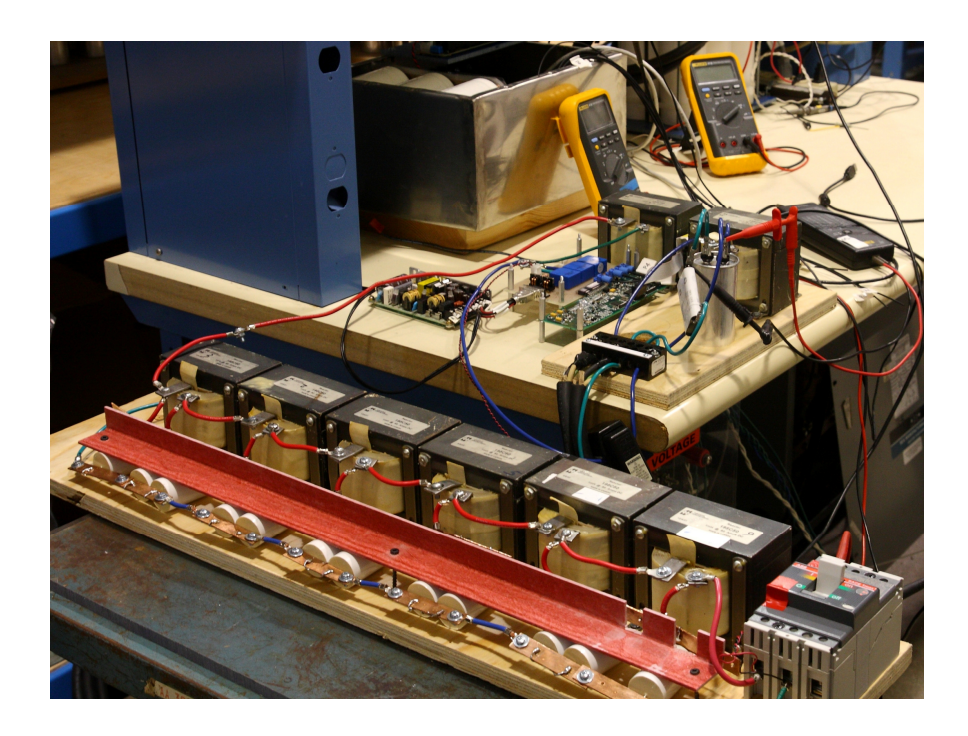


Figure 6.15. 120Vac emulator system experimental setup.

For the purpose of the system stability, the proportional gain Kp of the current controller is limited due to the peaks existing at the resonant frequencies of the open loop transfer function, as illustrated in Figure 6.7. Hence, the control loop gain for the traditional strategy (the PI controller) is quite small, and thereby the steady-state error of the system output will be significant. To address this challenge, the PR controller is used to replace the PI controller for purpose of reducing steady-state error.

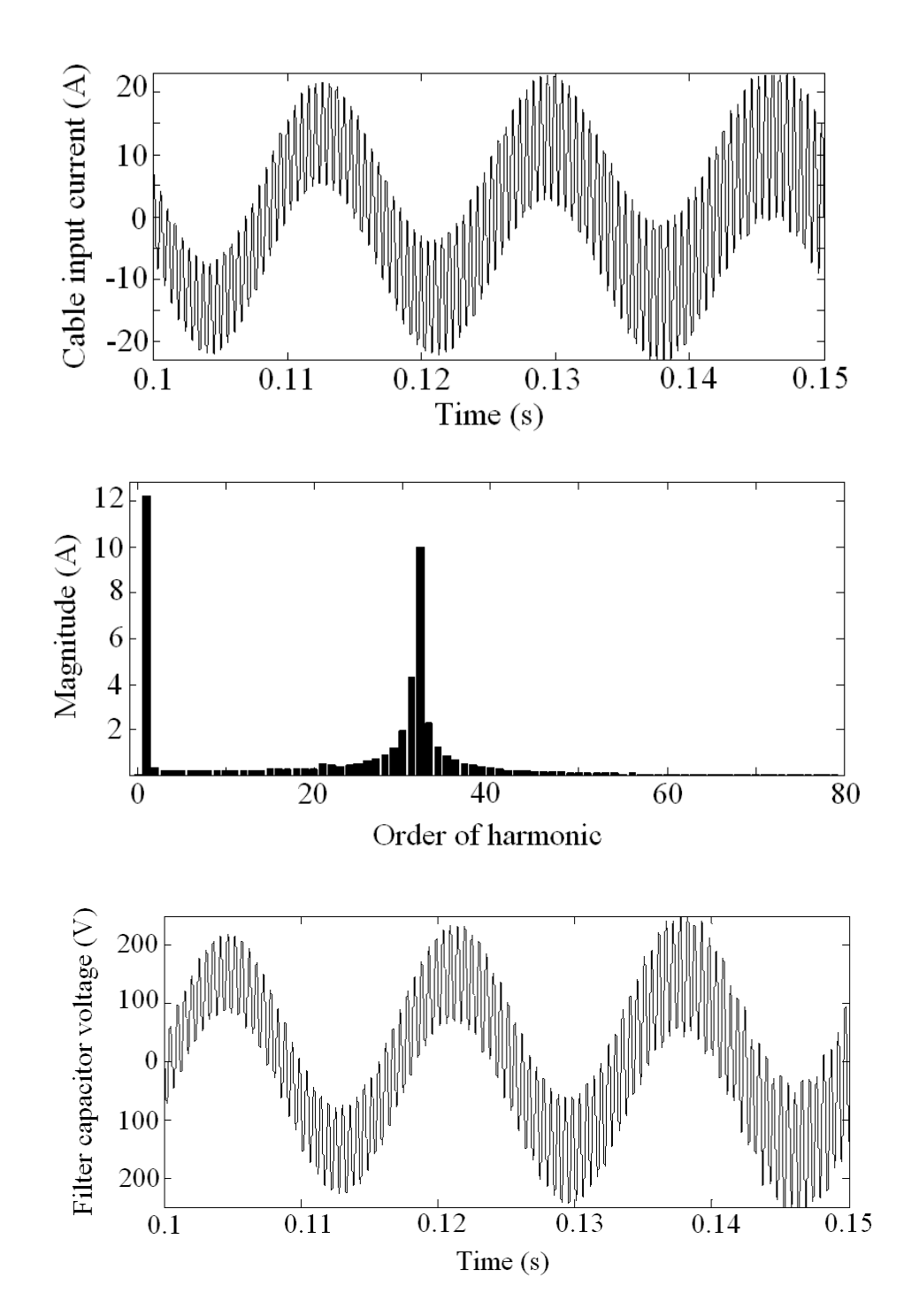


Figure 6.16. Simulation waveforms of the cable current and the filter capacitor voltage with the PR controller only.

Figure 6.16 shows the simulation results of the filter capacitor voltage, the input current of the cable and its spectrum analysis with the PR controller only. The system would be unstable due to the resonant peaks. From the current spectrum analysis, it can be found that a series of resonant

frequencies are existed from around 1.2 kHz to 2 kHz, which is coordinated with the aforementioned theoretical analysis.

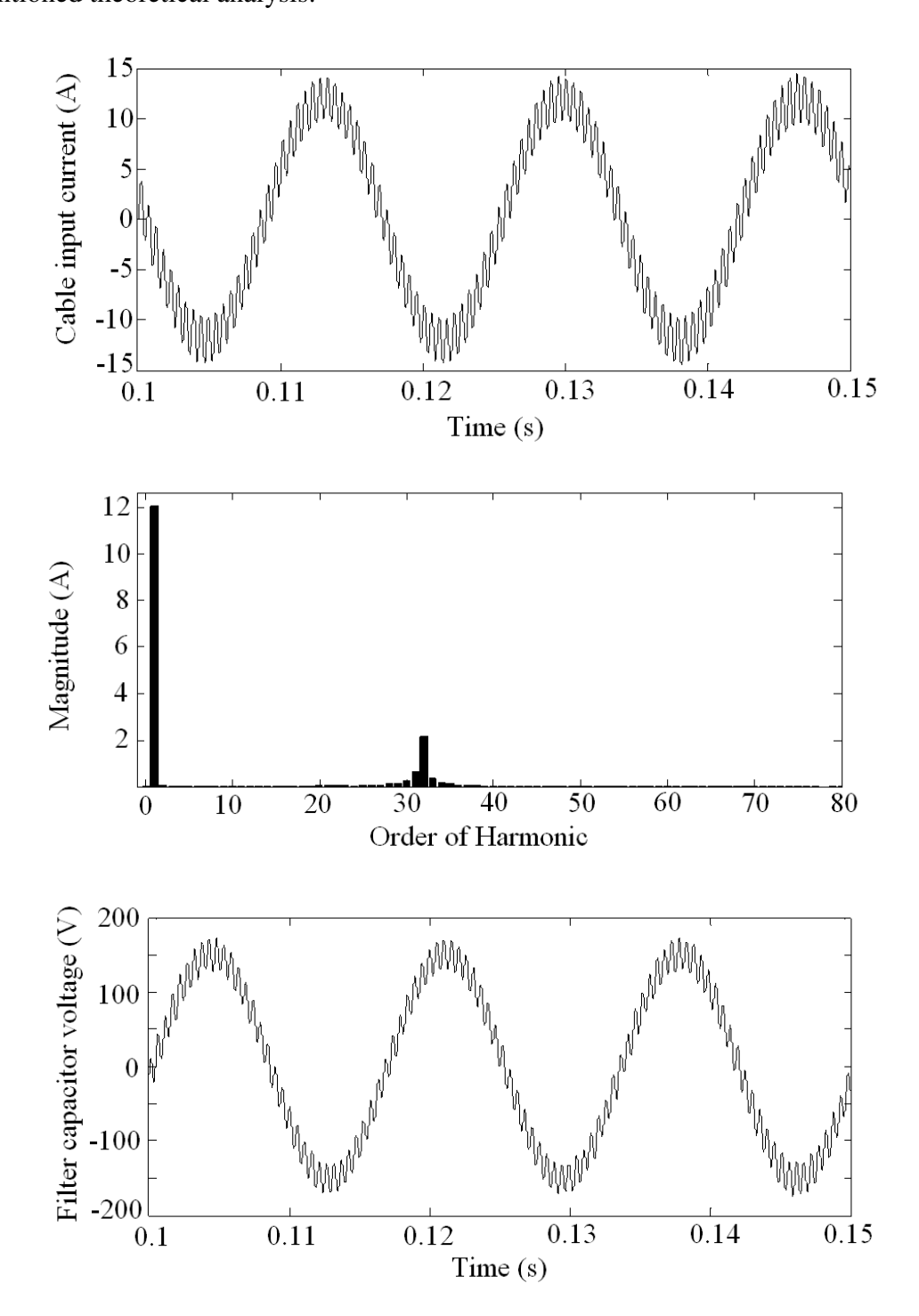


Figure 6.17. Simulation waveforms of the cable current and the filter capacitor voltage with one notch filter with center frequency at 1.2 kHz.

As a result, there are significant resonances both in the cable current and filter capacitor voltage, and thereby cause system unstable. Hence, the conventional system would encounter the challenge of system stability with the consideration of the transmission cable characteristics.

With the compensated strategy, the cascaded notch filter is adapted to compensate the resonant peaks caused by the system setup. In case of one notch filter centered frequency at 1.2 kHz, the compensated results of the capacitor voltage, the cable current and its spectrum analysis are illustrated in Figure 6.17. To some extent, the resonant phenomenon can be relieved by the notch filter since one of the resonant peak can be attenuated, however, the other significant peak at 1.8 kHz is still there.

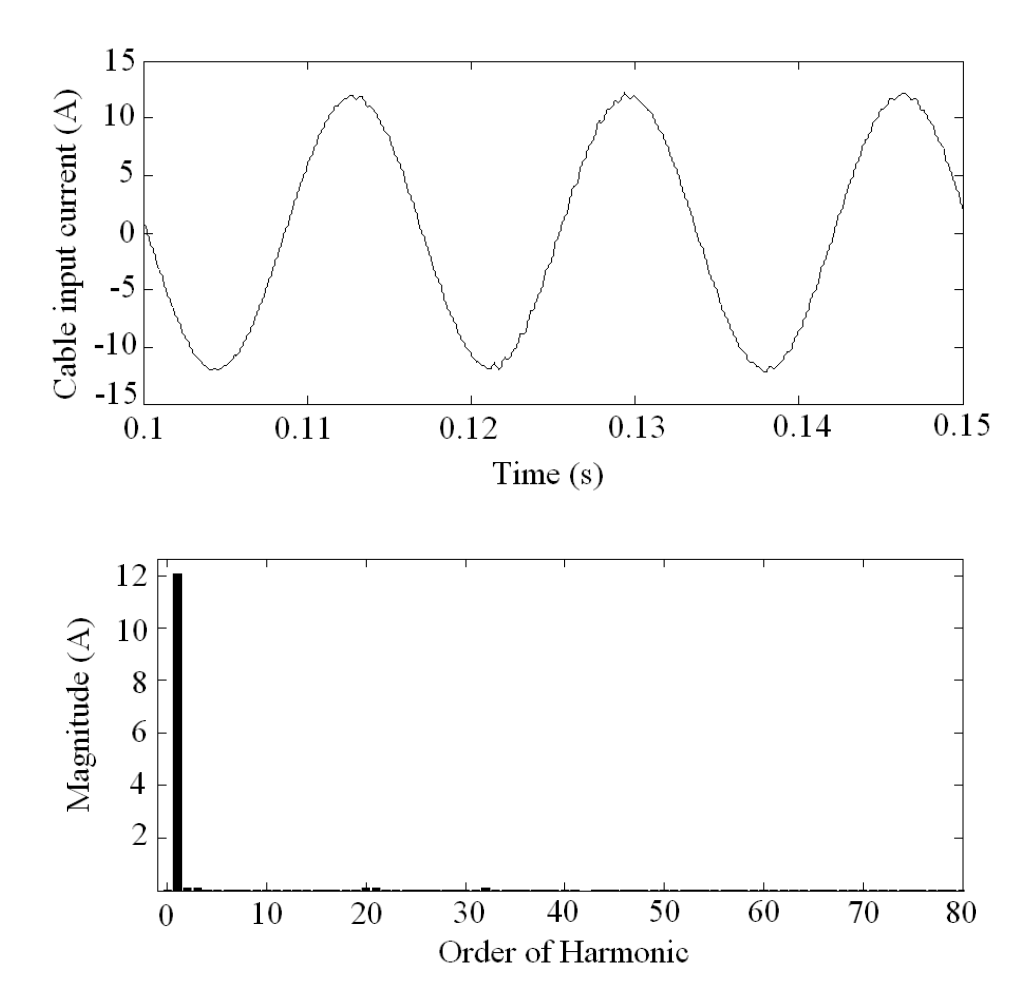


Figure 6.18. Simulation waveforms of the cable current and the filter capacitor voltage with the proposed controller.

Figure 6.18 (cont'd).

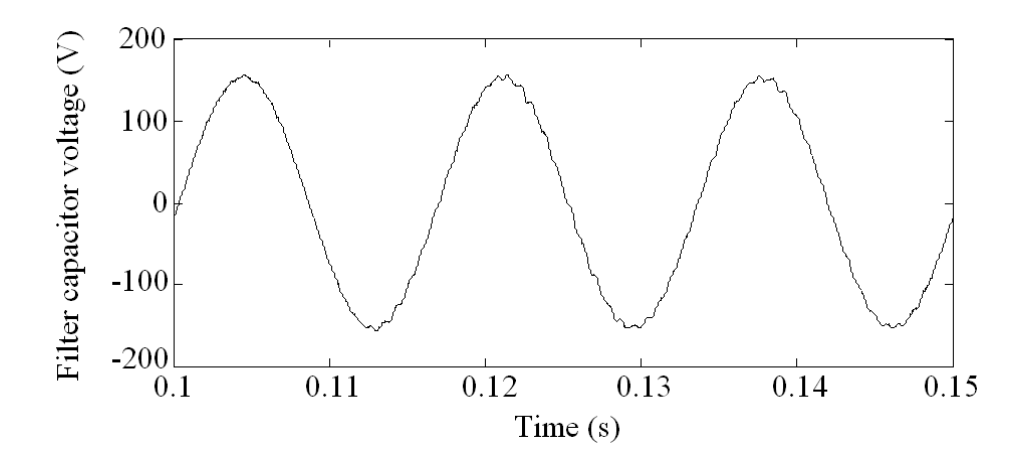


Figure 6.18 shows the simulation results of the capacitor voltage, the cable current with the proposed controller: the PR and two notch filters (1.2kHz and 1.8 kHz).

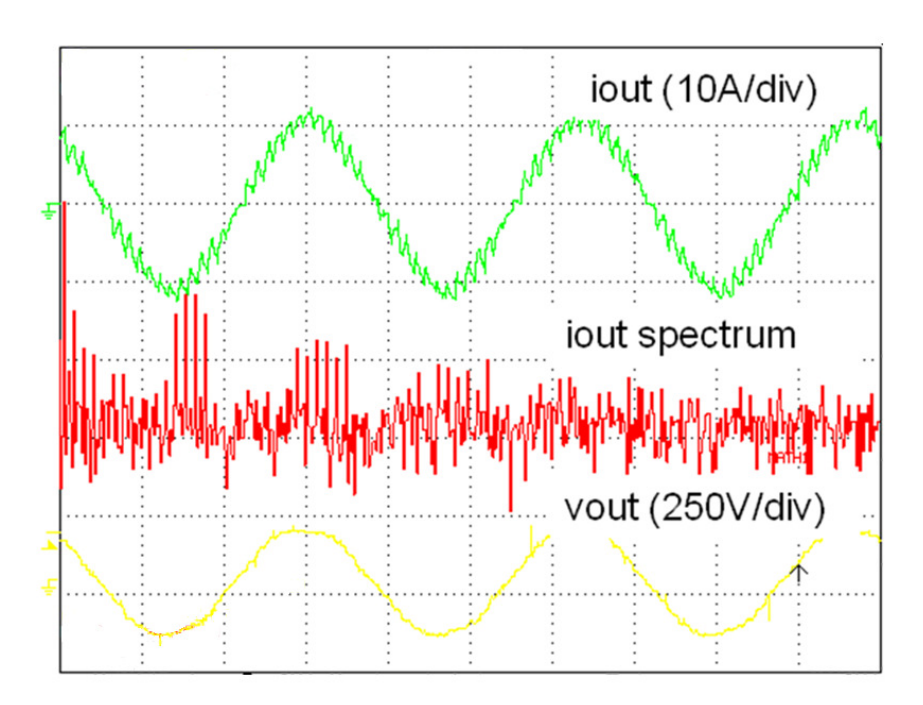


Figure 6.19. Steady state waveforms and current spectrum when $C_f = 0$. Only one P + resonant controller is implemented.

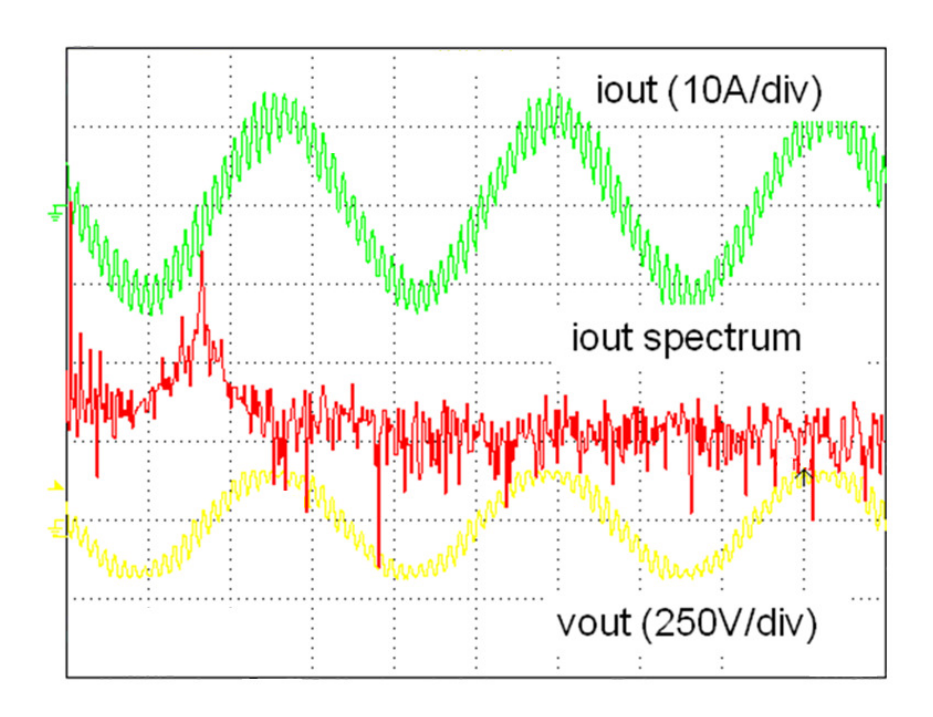


Figure 6.20. Steady state waveforms and current spectrum when $C_f = 20 uF$ (11.3%). Only one P + resonant controller is implemented.

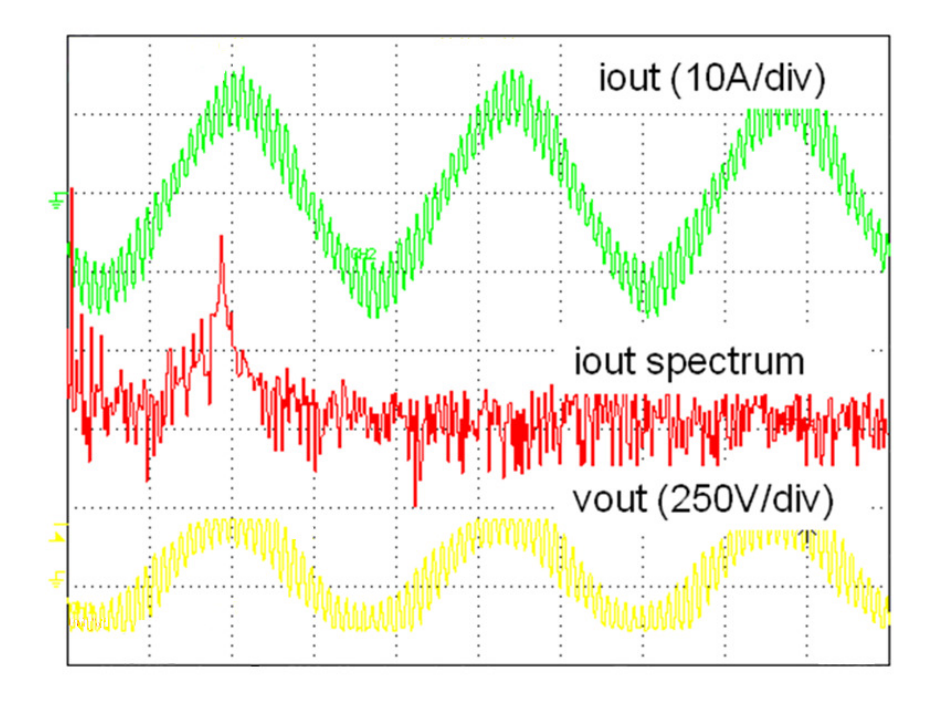


Figure 6.21. Steady state waveforms and current spectrum when $C_f = 20 uF$ (11.3%). One P + resonant controller and one notch filter are implemented.

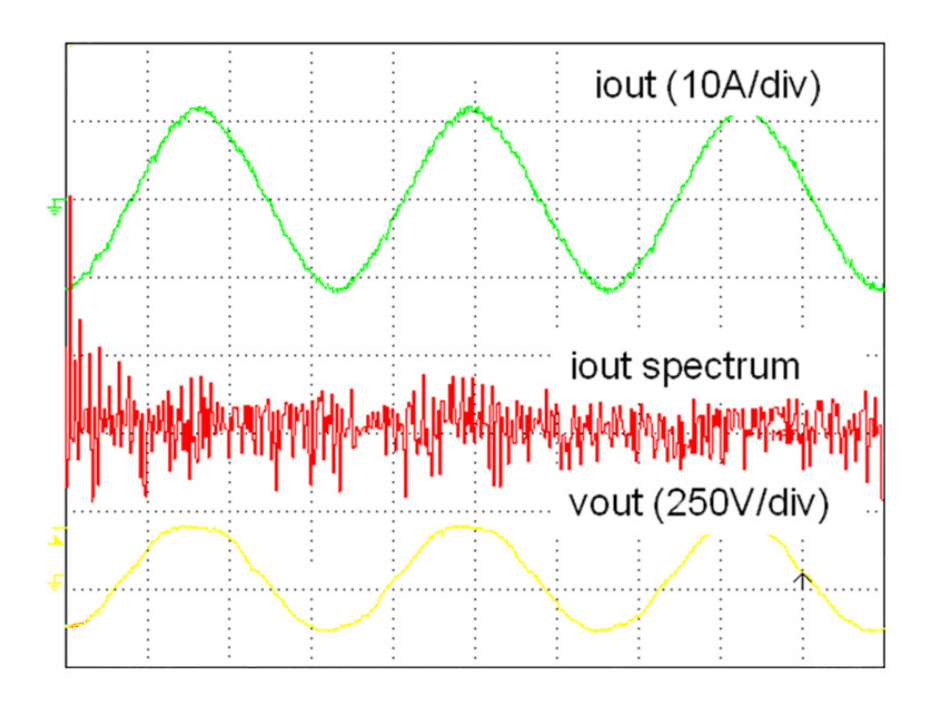


Figure 6.22. Steady state waveforms and current spectrum when $C_f = 20 uF$ (11.3%). One P + resonant controller and two notch filters are implemented.

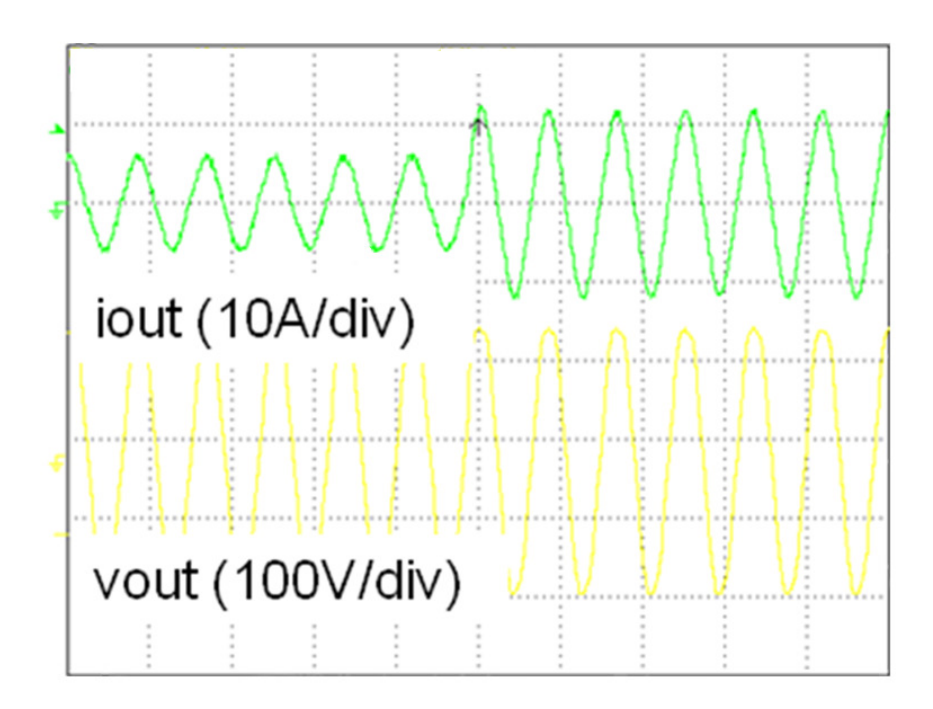


Figure 6.23. Dynamic response of the output current with the proposed control implemented. A step change from 4A to 8A is applied to the current command.

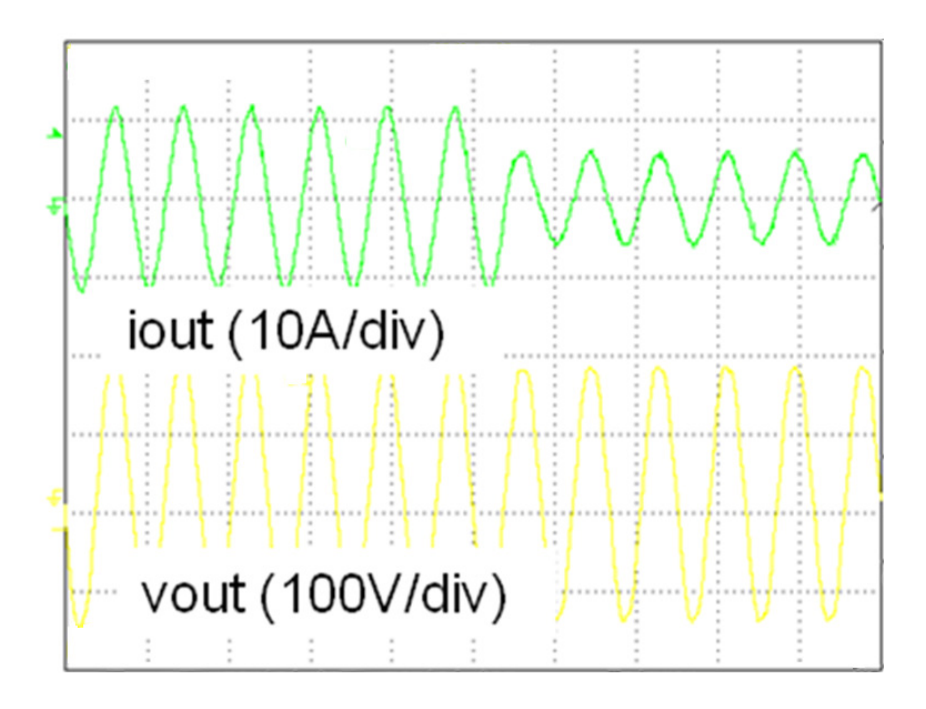


Figure 6.24. Dynamic response of the output current with the proposed control implemented. A step change from 8A to 4A is applied to the current command.

It can be found that the resonant phenomenon can be completely attenuated, which is coordinated with the theoretical analysis. The simulation has exhibited the resonant problem of the conventional control method with consideration of cable characteristics, and the effectiveness of the proposed control strategy is also verified by the simulation.

In Figure 6.19, the output voltage, output current and its frequency spectrum are captured when the filter capacitor C_f is disconnected. Only one P + Resonant controller is implemented in this case. As can be seen from Figure 6.19, multiple resonances can be observed at around 1.6 kHz, 3.2 kHz, 5 kHz, etc. After a 20uF capacitor is connected, the output waveforms are shown in Figure 6.20. Without implementation of notch filters, resonance occurs at around 1.6 kHz, which exactly stands for the unstable poles in the closed-loop system.

In Figure 6.21, the first notch filter given in (6.6) is implemented in the controller, while other set-ups are kept unchanged from Figure 6.20. It can be seen that the resonance frequency is

shifted a bit higher to around 1.85 kHz. In Figure 6.22, both of the two notch filters in (6.6) are implemented. In this case, the first two resonance peaks depicted in Figure 6.7 and Figure 6.8 are well compensated, and the closed-loop system is stabilized. A THD of 2.34% is achieved with the output current.

Dynamic response of the proposed current controller is verified through Figure 6.23 and Figure 6.24. The current tracking commands in both cases have a step change from 4A to 8A and from 8A to 4A, respectively. Good stability and fast transient response are achieved.

The simulation results of the auto damping control depicted in Figure 6.14 are presented in Figure 6.25 and Figure 6.26, respectively. The auto detection of the system resonance peaks is performed during the first 500ms upon the inverter start up. Here, the sinusoidal perturbation signal is linearly swept from 1kHz to 2kHz during the 500ms. The control gain is initially set to have a very low bandwidth such that the system stability is guaranteed during the auto detection procedure.

In Figure 6.25, the inverter output current (iout) and the modified feedback current with perturbation injection (ifb) are shown. It can be seen that both currents have included the fundamental 60Hz components as well as some high frequency disturbance components. After the band pass filter, the disturbance components with the same frequency of the injected perturbation signal are filtered out, also shown as in Figure 6.25.

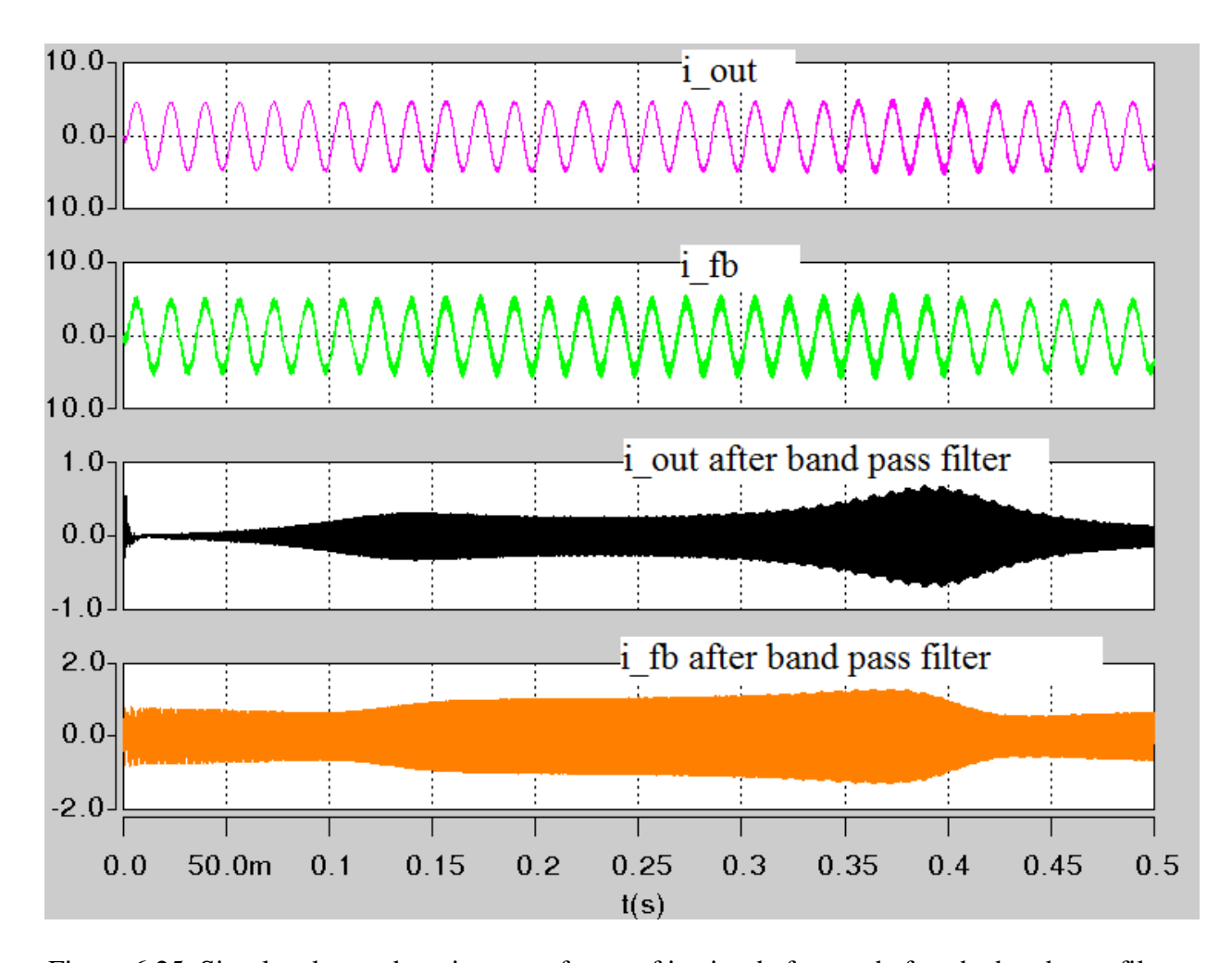


Figure 6.25. Simulated auto damping waveforms of ifb, iout before and after the band pass filters.

After the band pass filter, both currents are sent to magnitude detectors in order to obtain their magnitude information at the injected perturbation frequency. Taking a division of these two magnitudes, the open loop gain from ifb to iout is obtained, as shown in Figure 6.26. Based on the measured loop gain, it is very easy to detect the resonance peak frequencies (f1 and f2). In this case, f1 is 1.2kHz and f2 is 1.8kHz. Notch filter frequency can be then aligned with f1 and f2 such that auto damping is achieved.

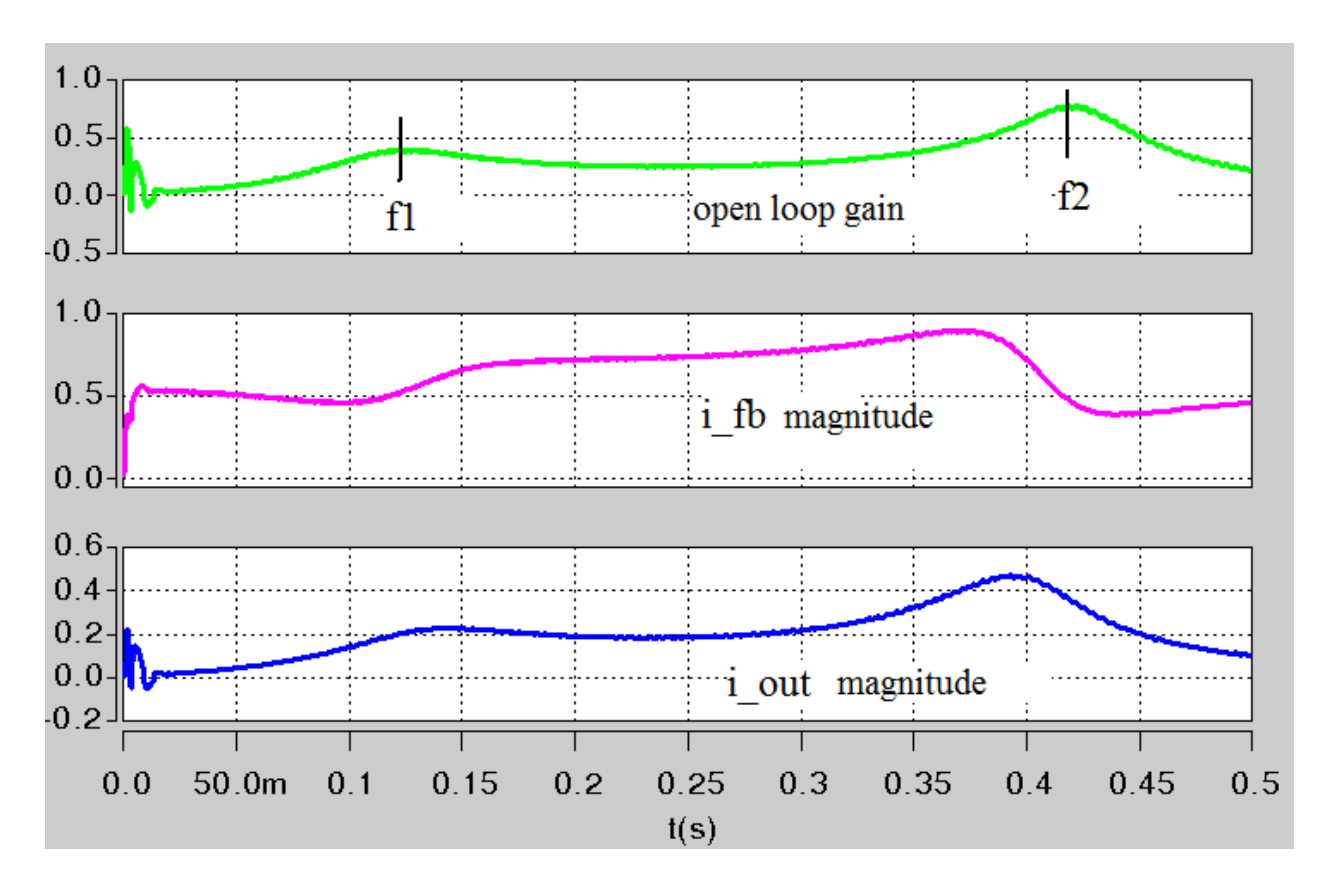


Figure 6.26. Simulated auto damping waveforms of ifb magnitude, iout magnitude and open loop gain (iout magnitude over ifb magnitude).

6.5. Summary

The resonance issues associated with HVAC grid-connected offshore wind farms have been investigated in this chapter. Most of the existing offshore wind farms are using HVAC power transmission systems, which in general consists of wind turbine generators, voltage source converters, step-up transformers and submarine cables. In particular, the main submarine cable connecting the offshore wind farm and onshore grid exhibits high shunt capacitance, which can cause severe high-frequency resonance issues. In order to better understand this problem, a per unit scale equivalent circuit model has been developed for the offshore wind farm system. A full-bridge inverter connected to the 120Vac grid through an output LC filter, a line inductor and a lumped LC network with finite number of cells has been implemented to emulate the offshore

wind farm. Frequency domain analysis has been carried out to identify the key passive components that have significant impact on the system high-frequency characteristics. It has been found that larger local line inductance and output filter capacitance can give more desirable system high-frequency responses. A notch filter based active damping compensator has been proposed to stabilize the emulator system. Furthermore, the validity of the proposed notch filter based damping control is studied given a certain range of the transmission cable parameters uncertainty. It has been shown that the proposed damping method can guarantee stability given a +-20% inductance and capacitance variations. In order to adapt the proposed damping control to a more general case: the transmission system parameters are unknown, an auto damping control technique is briefly presented and discussed. Simulation and experimental results have been provided to verify the theoretical analysis and the validity of the proposed control strategy.

Chapter 7. Control of a Boost-Half-Bridge

Photovoltaic Micro Inverter System

7.1. Introduction

The concept of micro inverter (also known as module integrated converter/inverter) has become a future trend for single-phase grid-connected photovoltaic (PV) power systems, for its removal of energy yield mismatches among PV modules, possibility of individual PV module oriented optimal design, independent maximum power point tracking (MPPT), and "plug and play" concept [61], [62]. In general, a PV micro inverter system is often supplied by a low voltage solar panel, which requires a high voltage step-up ratio to produce desired output AC voltage [61]-[63]. Hence, a DC-DC converter cascaded by an inverter is the most popular topology, in which a high frequency transformer is often implemented within the DC-DC conversion stage [64]-[70].

In terms of the pulse-width modulation (PWM) techniques employed by the PV micro inverter system, two major categories are attracting most of the attentions. In the first, PWM control is applied to both of the DC-DC converter and the inverter [64]-[66]. In addition, a constant voltage DC link decouples the power flow in the two stages such that the DC input is not affected by the double-line-frequency power ripple appearing at the AC side. By contrast, the second configuration utilizes a quasi-sinusoidal PWM method to control the DC-DC converter in order to generate a rectified sinusoidal current (or voltage) at the inverter DC link. Accordingly, a line-frequency commutated inverter unfolds the DC link current (or voltage) to obtain the sinusoidal form synchronized with the grid [67]-[70]. Although the latter has the advantage of

higher conversion efficiency due to the elimination of high frequency switching losses at the inverter, the double-line-frequency power ripple must be all absorbed by the DC input capacitor, making the MPPT efficiency (defined as the ratio of the energy drawn by the PV inverter within a certain measuring period at the steady state to the theoretical available energy from the PV module) compromised unless a very large capacitance is used. Moreover, the DC-DC conversion stage requires more challenging control techniques to meet the grid current regulation requirement. Therefore, in terms of the MPPT performance and output current quality, the first category of PV micro inverter is more appropriate and will be adopted in this dissertation.

A boost dual-half-bridge DC-DC converter for bidirectional power conversion applications was first proposed in [71] and then further investigated in [72]-[74]. It integrates the boost converter and the dual-half-bridge converter together by using minimal number of devices. High efficiency is realizable when the zero voltage switching (ZVS) technique is adopted. By replacing the secondary half bridge with a diode voltage doubler, a new boost-half-bridge converter can be derived for unidirectional power conversions [75]. In this chapter, the boost-half-bridge converter is incorporated as the DC-DC conversion stage for the grid-connected PV micro inverter system. Benefiting from its circuit simplicity, ease of control and minimal semiconductor devices, the promising features such as low cost, high efficiency and high reliability are obtained.

A full-bridge PWM inverter with an output LCL filter is incorporated to inject synchronized sinusoidal current to the grid. In general, its performance is evaluated by the output current total harmonic distortions (THD), power factor and dynamic response. The controller discussed in Chapter 5 can be utilized here.

MPPT is performed by the boost-half-bridge DC-DC converter. Numerous MPPT techniques have been studied and validated, for example, perturb & observe (P & O) method [76]-[79], incremental conductance method [80], ripple correlation method [81], reduced current sensor method [82], etc. Different techniques have shown different trade-offs among the steady state MPPT efficiency, the transient tracking speed, and the control complexity [83], [84].

Another critical concern for MPPT implementation is the dynamics of the specific converter adopted. In [78], an optimal P & O method has been developed to limit the negative effect of the converter dynamic responses on the MPPT efficiency. In [79], a closed-loop control technique has been proposed to minimize the PV voltage oscillation. However, the converter dynamic behavior associated with the MPPT operation can also influence the converter efficiency and functioning, which has been rarely discussed before. For example, the MPPT methods using step-changed perturbations on the PV voltage (or current) or the converter duty cycle periodically may sometimes cause problems such as inrush current, LC oscillation, magnetic saturation, etc. These undesirable transient responses can result in higher power losses or even circuit malfunctioning; and of course, they are different from case to case. In this chapter, the dynamics of the boost-half-bridge converter is carefully studied for guiding the MPPT design. A customized MPPT producing a ramp-changed PV voltage is then developed for practice. In addition, for the purpose of fast tracking and high MPPT efficiency, the power-voltage (P-V) curve of the PV module is divided into three different operation zones, where the MPPT step size is varied accordingly.

7.2. Boost-Half-Bridge Photovoltaic Micro Inverter

7.2.1. Boost-Half-Bridge PV Micro Inverter Topology

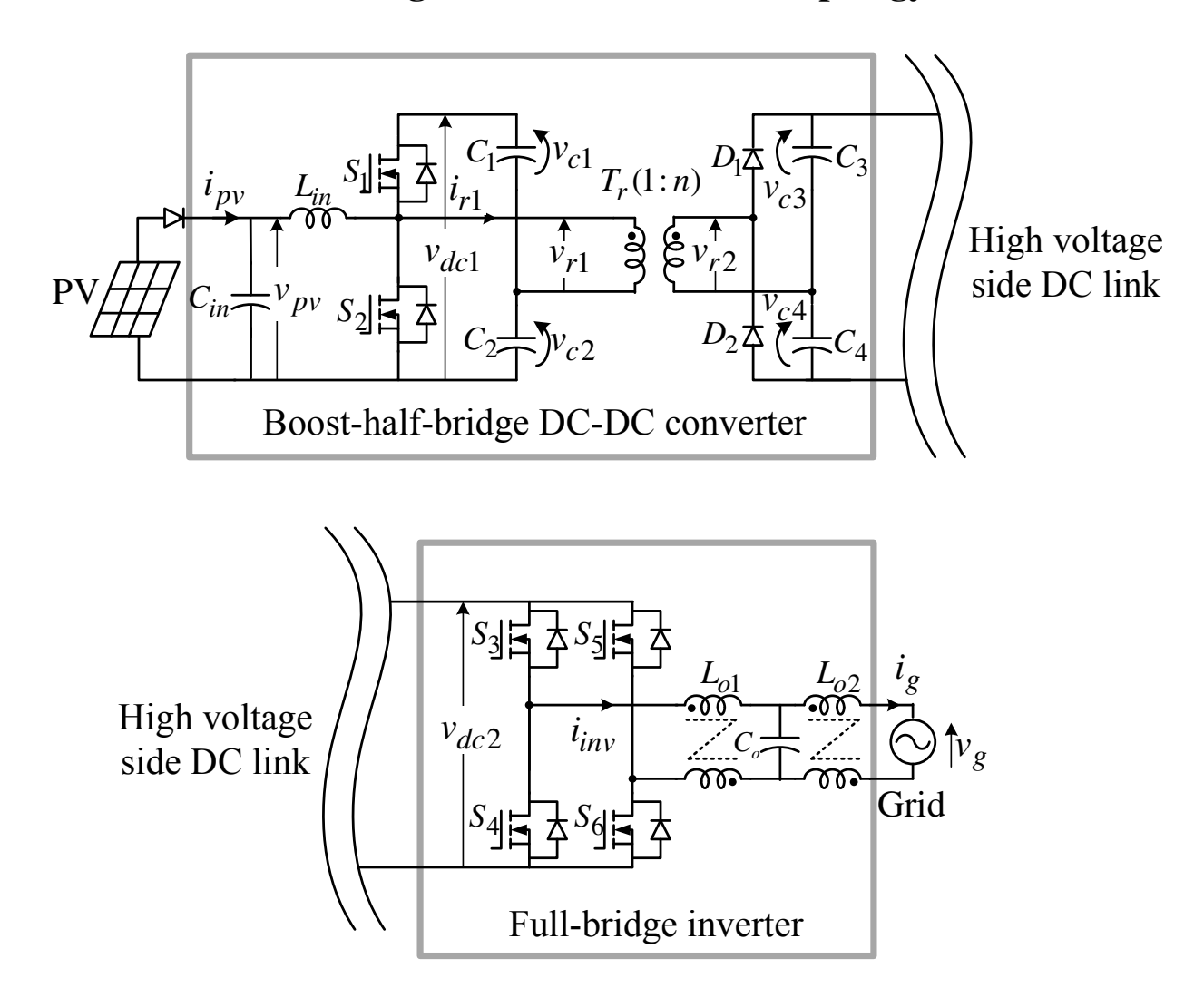


Figure 7.1. Topology of the boost-half-bridge PV micro inverter.

The boost-half-bridge micro inverter topology for grid-connected photovoltaic systems is depicted in Figure 7.1. It is composed of two decoupled power processing stages. In the front-end DC-DC converter, a conventional boost converter is modified by splitting the output DC capacitor into two separate ones. C_{in} and L_{in} denote the input capacitor and boost inductor, respectively. The center taps of the two MOSFETs (S_1 and S_2) and the two output capacitors

 $(C_1 \text{ and } C_2)$ are connected to the primary terminals of the transformer T_r , just similar to a half-bridge. The transformer leakage inductance reflected to the primary is represented by L_s and the transformer turns ratio is 1:n. A voltage doubler composed of two diodes $(D_1 \text{ and } D_2)$ and two capacitors $(C_3 \text{ and } C_4)$ is incorporated to rectify the transformer secondary voltage to the inverter DC link.

A full-bridge inverter composed of 4 MOSFETs $(S_3 \sim S_6)$ using SPWM control serves as the DC-AC conversion stage. Sinusoidal current with a unity power factor is supplied to the grid through a third-order LCL filter $(L_{o1}, L_{o2} \text{ and } C_o)$.

Other symbol representations are defined as follows. The duty cycle of S_1 is denoted by d_1 . The switching period of the boost-half-bridge converter is T_{sw1} . The PV current and voltage are represented by i_{pv} and v_{pv} , respectively. The voltages across C_1 , C_2 , C_3 and C_4 are denoted by v_{c1} , v_{c2} , v_{c3} and v_{c4} , respectively. The transformer primary voltage, secondary voltage and primary current are denoted as v_{r1} , v_{r2} and i_{r1} , respectively. The low voltage side (LVS) DC link voltage is v_{dc1} and the high voltage side (HVS) DC link voltage is v_{dc2} . The switching period of the full bridge inverter is T_{sw2} . The output AC currents at the inverter side and the grid side are represented by i_{inv} and i_g , respectively. The grid voltage is v_g .

7.2.2. Operation Principle of the Boost-Half-Bridge Converter

The boost-half-bridge converter is controlled by S_1 and S_2 with complementary duty cycles. Neglect all the switching dead bands for simplification. The idealized transformer operating waveforms are illustrated in Figure 7.2. When S_1 is on and S_2 is off, v_{r1} equals to v_{c1} . When S_1 is off and S_2 is on, v_{r1} equals to $-v_{c2}$. At the steady state, the transformer volt-sec is always automatically balanced. In other words, the primary volt-sec A_1 (positive section) and A_2 (negative section) are equal. So are the secondary volt-sec A_3 (positive section) and A_4 (negative section). Normally, D_1 and D_2 are on and off in a similar manner as S_1 and S_2 , but with a phase delay t_{pd} due to the transformer leakage inductance. Ideally, the transformer current waveform is determined by the relationships of $v_{c1} \sim v_{c4}$, the leakage inductance L_s , the phase delay t_{pd} , and S_1 's turn-on time d_1T_{sw1} [72].

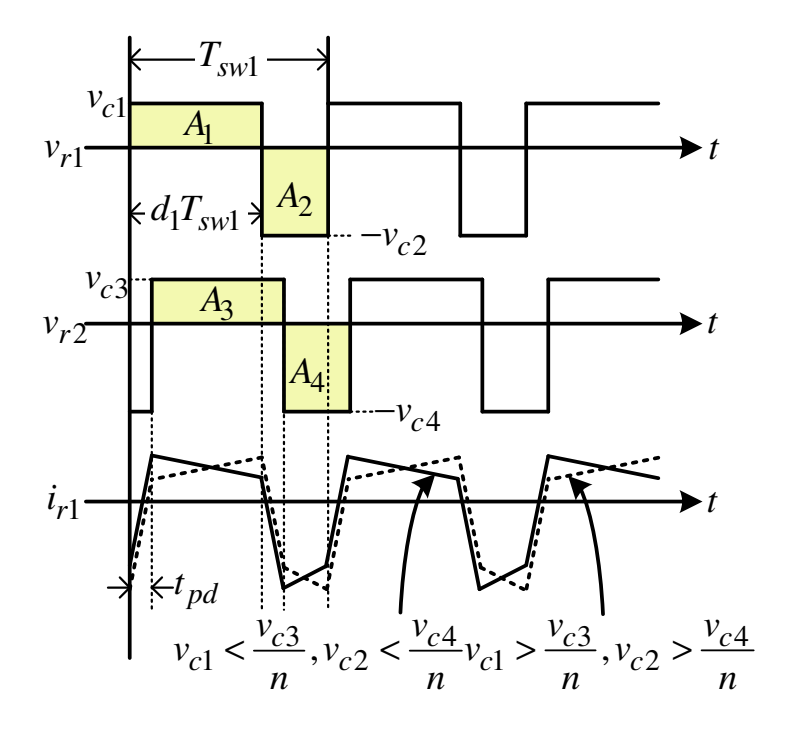


Figure 7.2. Idealized transformer voltage and current.

In order to reach an optimal efficiency of the boost-half-bridge converter, ZVS techniques can be considered for practical implementation, as guided by [72]. It is worth noting that engineering trade-offs must be made between the reduced switching losses and increased conduction losses when soft switching is adopted. Detailed optimal design processes of the boost-half-bridge converter will not be addressed here.

For simplicity, hard switching is employed and the transformer leakage inductance is regarded as small enough. Therefore, Eq. (7.1) and (7.2) can be derived as follows.

$$v_{c1} = \frac{(1 - d_1)}{d_1} v_{pv}, \ v_{c2} = v_{pv}, \ v_{dc1} = \frac{v_{pv}}{d_1}$$
 (7.1)

$$v_{c3} = \frac{n(1-d_1)}{d_1} v_{pv}, \ v_{c4} = nv_{pv}, \ v_{dc2} = \frac{nv_{pv}}{d_1}$$
 (7.2)

When viewing from the full-bridge inverter, the boost-half-bridge converter just operates identically as a conventional boost converter, but with the extra features of the galvanic isolation as well as the high step-up ratio. The simple circuit topology with minimal use of semiconductor devices exhibits a low total cost and good reliability.

7.3. System Control Description of the PV Micro Inverter

An all digital approach is adopted for the control of the boost-half-bridge PV micro inverter system as Figure 7.3 shows. The PV voltage v_{pv} and current i_{pv} are both sensed for calculation of the instantaneous PV power P_{pv} , the PV power variation ΔP_{pv} , and the PV voltage variation Δv_{pv} . The MPPT function block generates a reference $v_{pv}^{}$ for the inner loop of the PV voltage regulation, which is performed by the DC-DC converter. At the inverter side, the grid voltage v_g is sensed to extract the instantaneous sinusoidal angle θ_g , which is commonly known as the phase lock loop (PLL). The inverter output current i_{inv} is pre-filtered by a first-order low pass filter on the sensing circuitry to eliminate the high frequency noises. The filter output i_{inv} is then fed back to the plug-in repetitive controller (as discussed in Chapter 5) for the inner loop regulation. Either v_{dc1} or v_{dc2} can be sensed for the DC link voltage regulation as the outer loop.

In practice, the LVS DC link voltage v_{dc1} is regulated for cost effectiveness. The grid current and the LVS DC link voltage references are represented by i_{inv}^{*} and v_{dc1}^{*}, respectively.

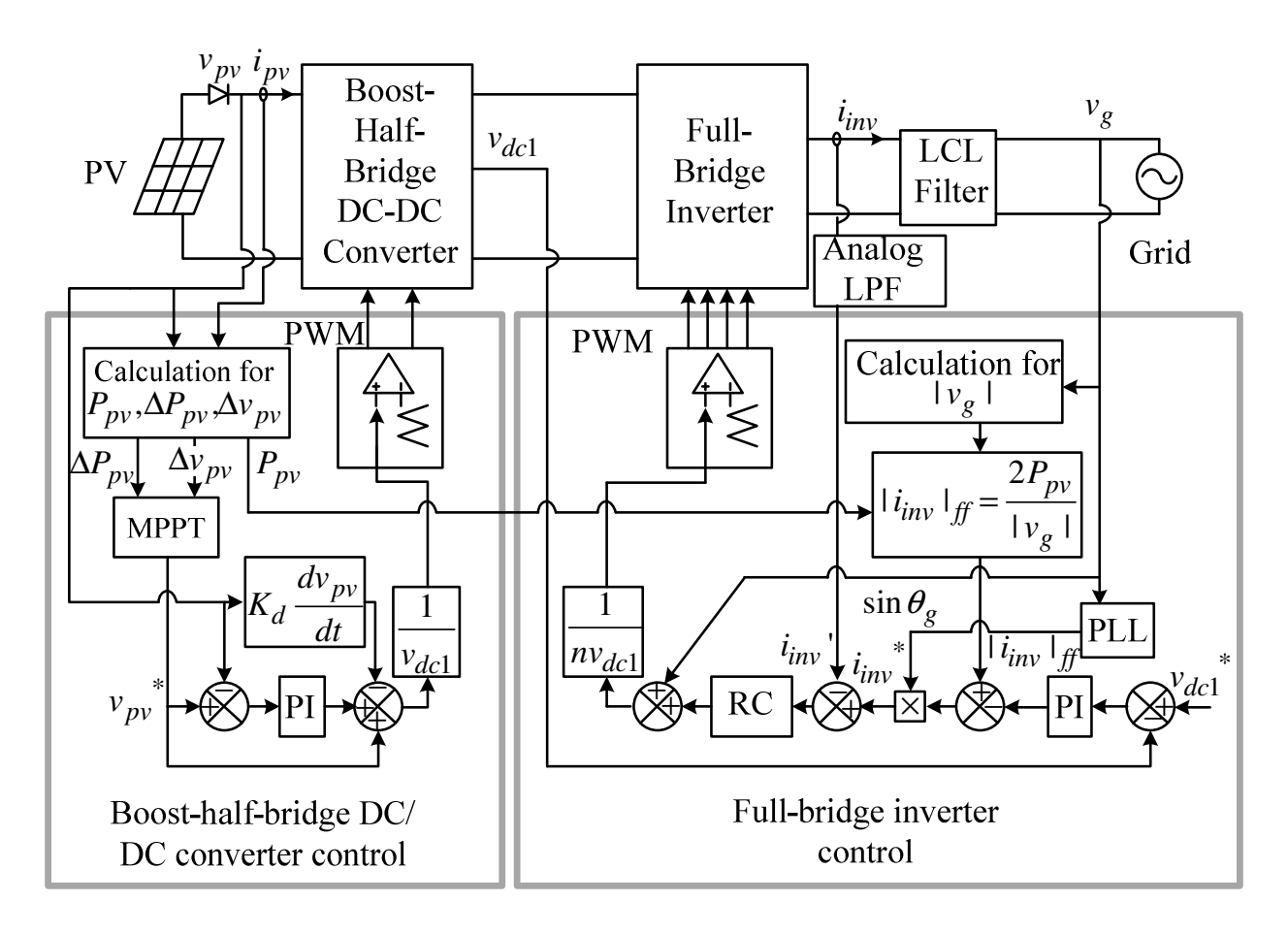


Figure 7.3. Architecture of the proposed PV micro inverter system control.

In order to achieve fast dynamic responses of the grid current as well as the DC link voltage, a current reference feed forward is added in correspondence to the input PV power P_{pv} . The magnitude of the current feed forward is expressed as

$$\left|i_{inv}\right|_{ff} = \frac{2P_{pv}}{\left|v_{g}\right|} \tag{7.3}$$

where $|v_g|$ is the magnitude of the grid voltage and can be calculated by

$$\left| v_g \right| = \frac{1}{2} \int_0^{\pi} v_g d\theta_g \tag{7.4}$$

7.4. Dynamics of the Boost-Half-Bridge Converter

7.4.1. Converter Parameters and Voltage Control

Table 7.1 summarizes the key parameters of the boost-half-bridge DC-DC converter. As aforementioned, the PV voltage is regulated instantaneously to the command generated by the MPPT function block. The continuous-time control block diagram is drawn in Figure 7.4. High bandwidth PI control is adopted to track the voltage reference $v_{pv}^{\ \ \ \ }$ and minimize the double-line-frequency disturbance from the LVS DC link. The capacitor voltage differential feedback is introduced for active damping of the input LC resonance [40].

Table 7.1. Boost-half-Bridge Converter Parameters

Input PV voltage (MPPT)	30 V~50V
Nominal PV power	210 W
Switching frequency	21.6 kHz
LVS DC link voltage	63 V
Transformer turns ratio	1:6
Transformer magnetizing inductors	0.7 mH:25.2 mH
Input inductor	200 uH

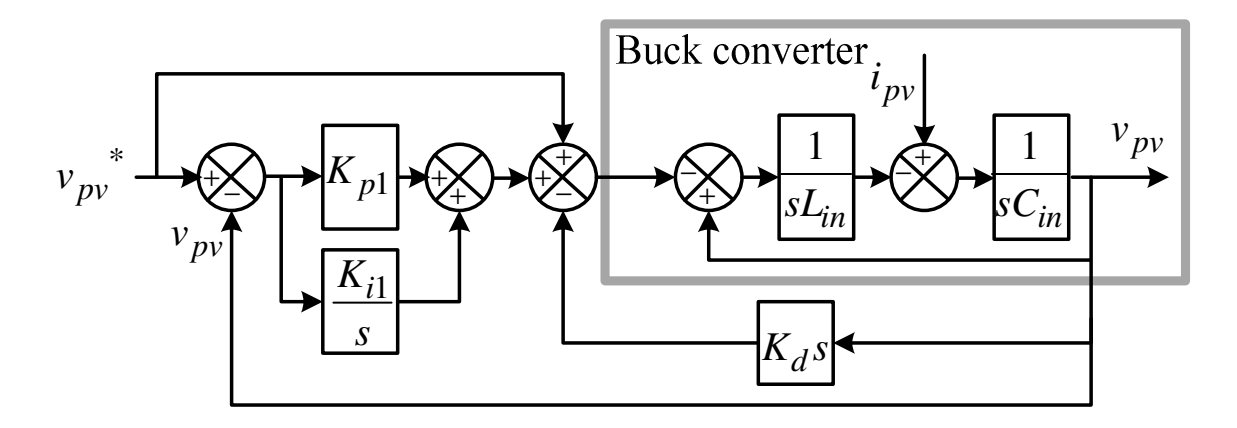


Figure 7.4. Block diagram of the PV voltage regulator.

Typically, the MPPT function block in a photovoltaic converter/inverter system periodically modifies the tracking reference of the PV voltage, or the PV current, or the modulation index, or the converter duty cycles. In most cases, these periodic perturbations yield step change dynamic responses in power converters. If the converter dynamics are disregarded in the MPPT control, undesirable transient responses such as LC oscillation, inrush current and magnetic saturation may take place. Consequently, the conversion efficiency can be deteriorated or even malfunction of the converter may occur.

Eq. (7.1) and (7.2) indicate that $v_{c1} \sim v_{c4}$ are changing dynamically in accordance with d_1 . It is worth noting that the charge and discharge of $C_1 \sim C_4$ caused by the uneven voltage distribution on the upper capacitors (C_1 and C_3) and the lower capacitors (C_2 and C_4) can only be conducted through the transformer magnetizing inductor. As a result, at any time, the charge and discharge rate of $C_1 \sim C_4$ must be limited such that the transformer flux is not saturated. Intuitively, this can be done by either introducing the transformer flux as a state variable into the inner PV voltage regulator or designing the outer MPPT block adaptively. For the sake of control simplicity and low cost, developing a customized MPPT method by carefully taking care of the boost-half-bridge converter dynamics would be more desirable.

7.4.2. Analysis of the Converter Dynamics

As previously discussed, the boost-half-bridge converter can be regarded as the integration of two sub-circuit topologies: 1) the boost converter; 2) the half-bridge converter. The PV voltage regulator depicted in Figure 7.4 has ensured that both the steady state and the dynamic response of the boost converter part are taken care of. Hence, the following analysis will be only concentrated on the dynamics of the half-bridge converter part.

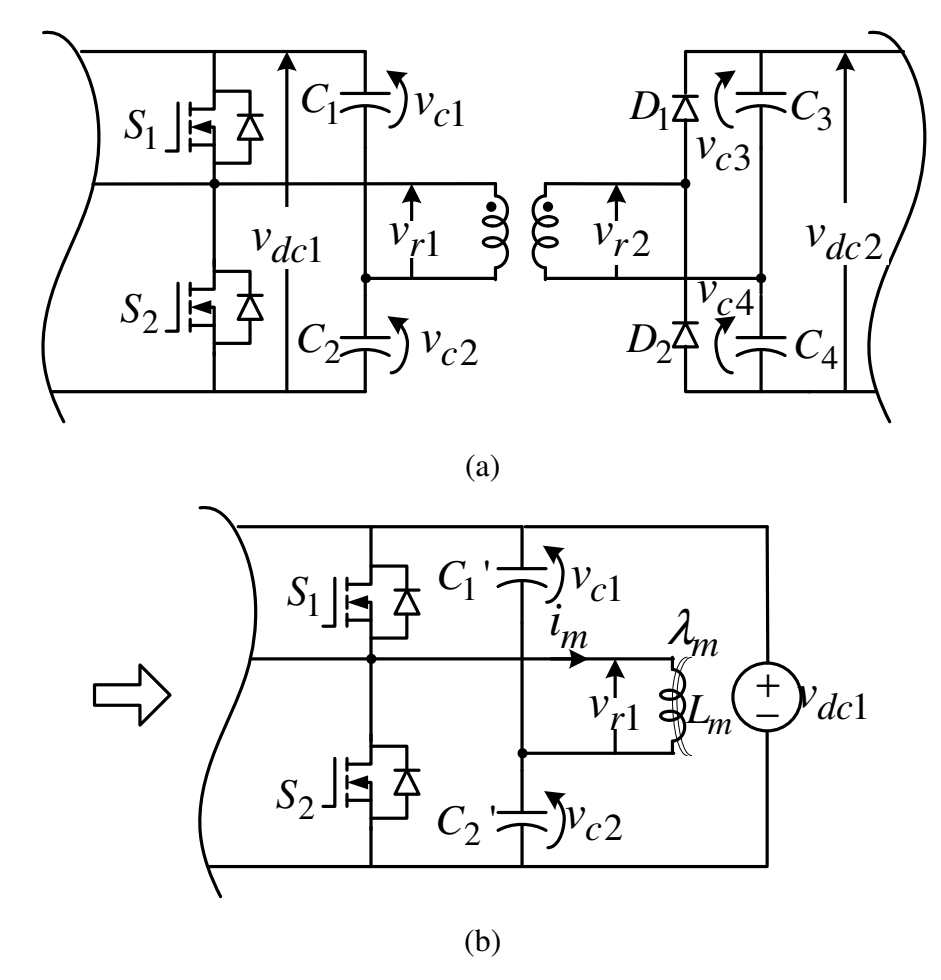


Figure 7.5. (a) Half-bridge converter part. (b) Equivalent circuit seen from the LVS DC link.

The major role of the half-bridge converter here is to transfer energy from the LVS DC link to the HVS DC link through the transformer. But besides that, it also allocates the amount of stored charges on the upper DC link capacitors (C_1 and C_3) and the lower DC link capacitors (C_2 and C_4).

Neglecting the effect of the transformer leakage inductance and power losses at this time, Figure 7.5 depicts the extracted half-bridge converter part and its equivalent circuit seen from the LVS DC link. As v_{dc1} is regulated to a constant DC, the LVS DC link in Figure 7.5(b) is simply connected to a constant voltage source for approximation. C_3 and C_4 are both reflected to the transformer primary and combined with C_1 and C_2 . C_1 ' and C_2 ' stand for the equivalent DC link capacitors, where C_1 '= C_1 + n^2C_3 and C_2 '= C_2 + n^2C_4 , respectively. L_m , i_m and λ_m denote the transformer primary magnetizing inductor, DC current and DC flux linkage, respectively. At the steady state, both i_m and λ_m are zero. But once the converter duty cycle d_1 is perturbed, i_m and λ_m will increase or decrease such that the electric charges can be transferred from C_1 ' to C_2 ' or vice versa. According to the Faraday's law, one has

$$v_{c1}(t)d_1(t) - v_{c2}(t)(1 - d_1(t)) = \frac{d\lambda_m(t)}{dt}$$
(7.5)

Define the duty cycle change rate $d_1'(t) = d(d_1(t))/dt$. Take derivative on both sides of (7.5), then

$$v_{dc1}d_1'(t) - \frac{dv_{c2}(t)}{dt} = \frac{d^2\lambda_m(t)}{dt}$$
 (7.6)

Furthermore, the capacitor charge and discharge equation can be expressed as

$$(C_1' + C_2') \frac{dv_{c2}(t)}{dt} = i_m(t) = \frac{\lambda_m(t)}{L_m}$$
(7.7)

Plug (7.7) into (7.6), then

$$\frac{d^2 \lambda_m(t)}{dt} + \frac{\lambda_m(t)}{L_m(C_1' + C_2')} - v_{dc1} d_1'(t) = 0$$
 (7.8)

Eq. (7.8) describes the dynamics of a typical 2nd-order system, where $d_1'(t)$ is the excitation and $\lambda_m(t)$ is the response. If d_1 is constant initially (at the steady state) and then perturbed by the MPPT operation, λ_m will start to oscillate with a frequency of $1/(2\pi\sqrt{L_m(C_1'+C_2')})$. Define the magnitude of λ_m as $|\lambda_m|$ and assume $d_1'(t) = d_1'$ as a constant, one has

$$|\lambda_m| = 2v_{dc1}L_m(C_1' + C_2')d_1'$$
(7.9)

Assume $|\lambda_m|_{\text{max}}$ is the maximum permissible flux linkage in the transformer for avoidance of the magnetic saturation, then the constraint for the duty cycle change rate is given by

$$d_{1}' < \frac{\left| \lambda_{m} \right|_{\text{max}}}{2v_{dc1}L_{m}(C_{1}' + C_{2}')} \tag{7.10}$$

7.5. Maximum Power Point Tracking (MPPT) Algorithm

7.5.1. MPPT with Ramp-Changed Voltage Command

Generally speaking, L_m and $(C_1'+C_2')$ are relatively large because of the high permeability of the transformer core and the required energy storage capability of the DC link capacitors to absorb the double-line-frequency power ripple. Therefore, the constraint given by (7.10) can hardly be satisfied if an MPPT method that produces a step-changed voltage reference is implemented. In order to strictly follow (7.10), a customized MPPT method that periodically generates a ramp-changed voltage command is developed.

Applying the system control provided in Figure 7.3, the simulation results of the boost-half-bridge converter are depicted in Figure 7.6. The step-changed voltage reference and the ramp-

changed voltage command are implemented for MPPT, respectively. Transformer leakage inductance and power losses are both taken into account in the simulation. From Figure 7.6, it is noticeable that λ_m has an average of zero with the double-line-frequency ripple when the PV voltage is constant. An oscillation of λ_m occurs once the PV voltage is perturbed by the MPPT operation. The slope of the voltage ramp in Figure 7.6(b) is chosen in consistency with (7.10). Here, the MPPT step size is selected as 0.3 V. The time duration of the voltage ramp in Figure 7.6(b) is denoted by t_{rp} . Here, $t_{rp} = 75$ ms. One can clearly see that with the ramp-changed voltage command, the transformer flux linkage is well confined within the permissible range.

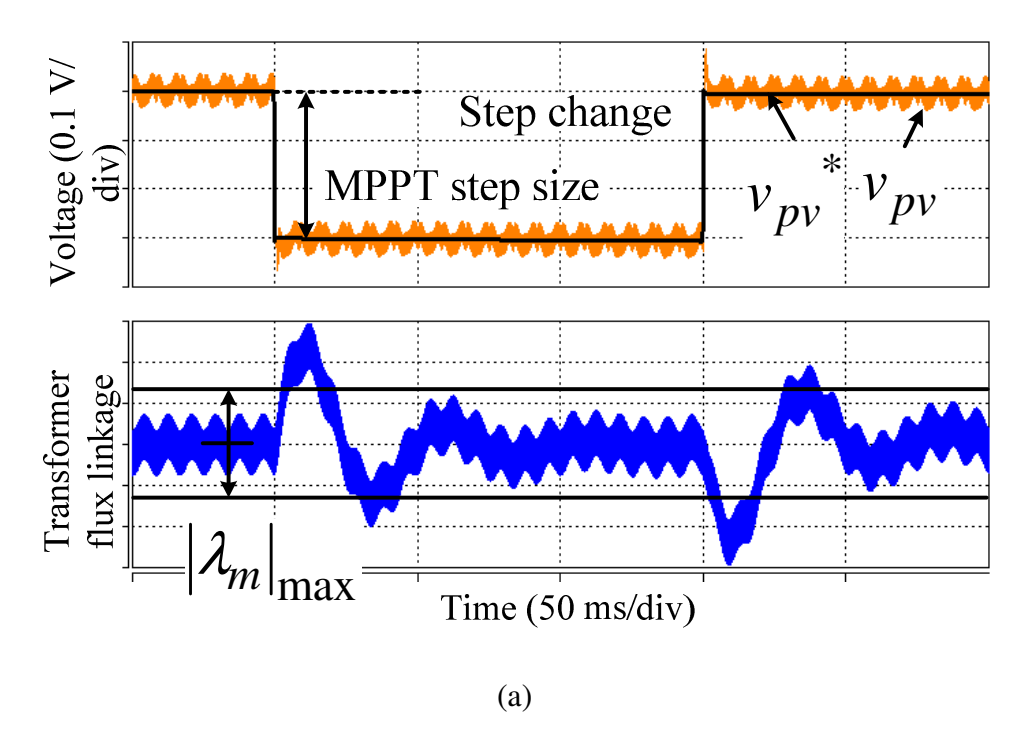
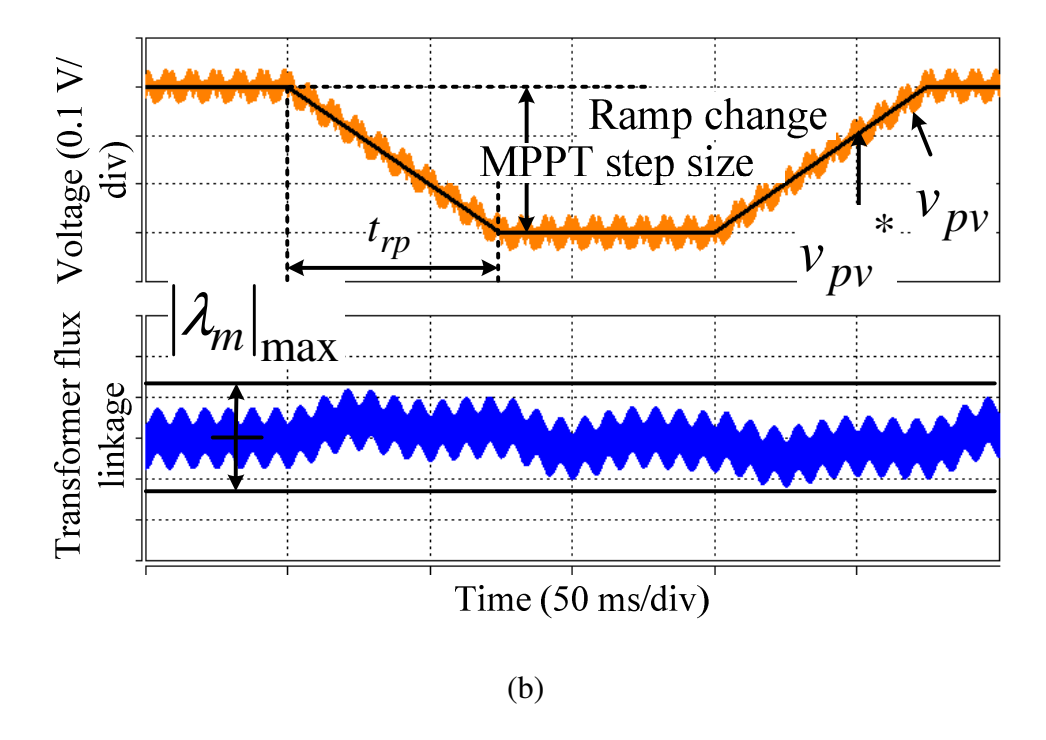


Figure 7.6. Dynamic responses corresponding to the different voltage command generation methods in the MPPT. (a) Using a step-changed voltage command. (b) Using a ramp-changed voltage command.

Figure 7.6 (cont'd).



7.5.2. Variable Step-Size MPPT Algorithm

For simplicity, it is assumed that the PV module is working under the standard irradiance (1000 W/m²) and the room temperature (25°C). Figure 7.7(a) sketches the operation curves of Sanyo HIT-210N, which best fits the proposed micro inverter. In Figure 7.7(b), dP_{pv}/dv_{pv} is illustrated. It is worth mentioning that some MPPT techniques calculate the step size online relying on the instantaneous values of ΔP_{pv} and Δv_{pv} in order to make the MPPT more adaptive [63], [77]. However, the sensed ΔP_{pv} and Δv_{pv} are vulnerable to noises, particularly when they are small. Therefore, an alternative method is adopted for robustness. Two points S_{pv1} and S_{pv2} on the dP_{pv}/dv_{pv} curve are selected to divide the PV operating points into three different zones, as Figure 7.7(b) shows. In Zone 0, PV output power is close to the MPP, where a fine tracking

step size is used to approach the exact MPP. In Zone 1 and Zone 2, a larger tracking step size is applied to boost up the tracking speed.

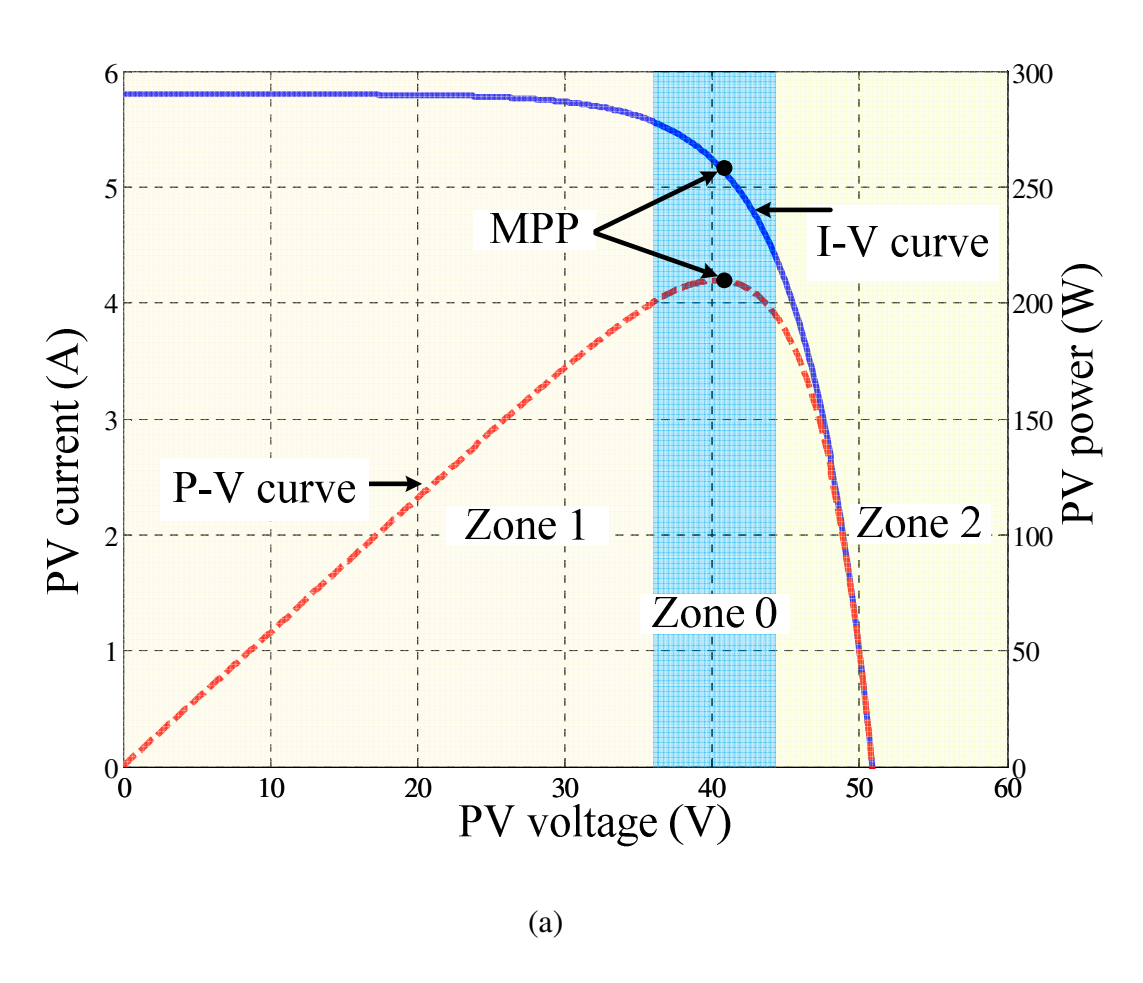
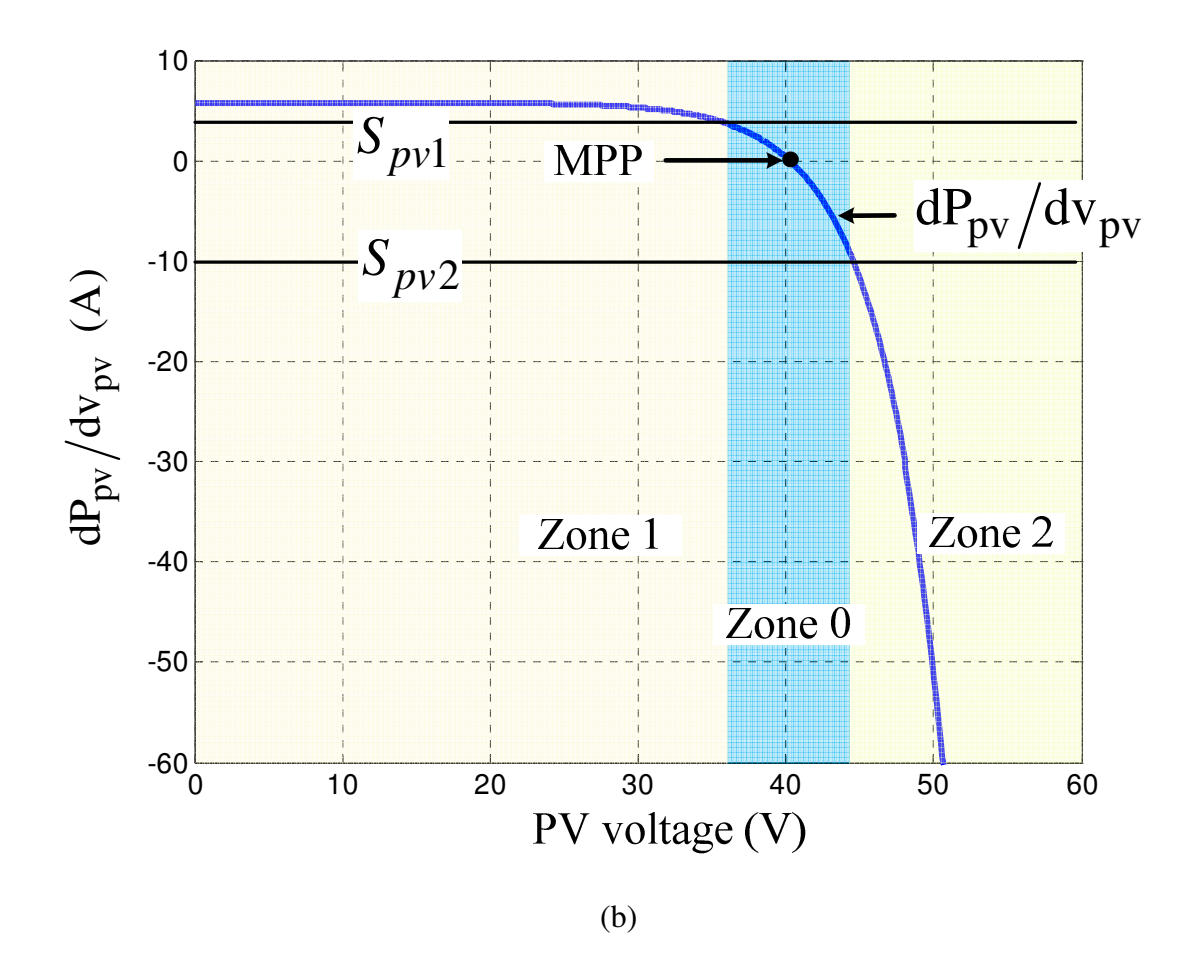


Figure 7.7. (a) I-V, P-V curves. (b) PV operation zone division based on dP_{pv}/dv_{pv}

Figure 7.7 (cont'd).



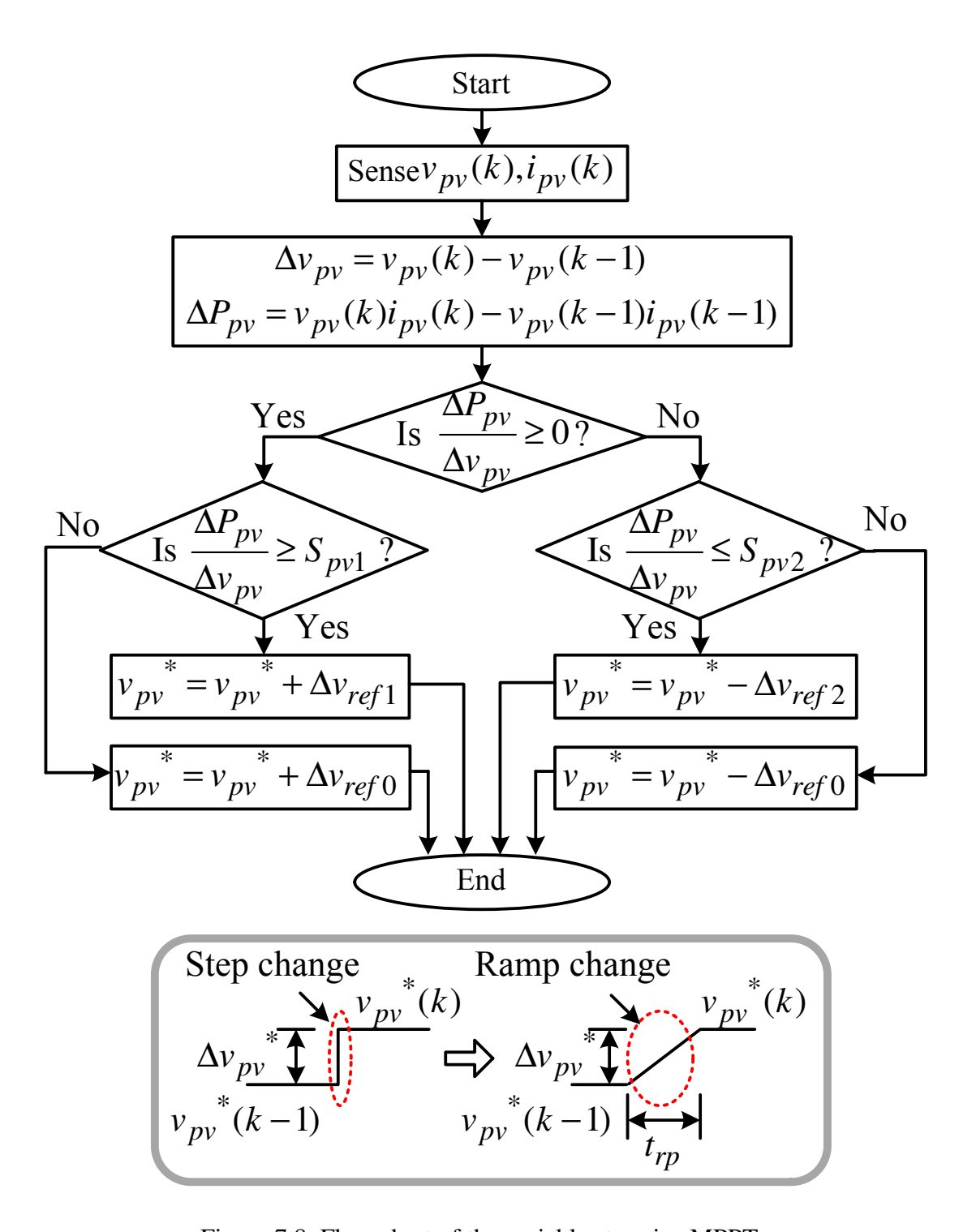


Figure 7.8. Flow chart of the variable step size MPPT.

7.6. Experimental Results

A 210 W boost-half-bridge PV micro inverter has been built and experimentally tested in the laboratory. The micro inverter is controlled by the 32-bit digital signal processor (TI TMS320F28035). One Sanyo PV module (HIT-210N) is selected as the low voltage power source. The validity of the boost-half-bridge DC-DC converter, the plug-in repetitive current controller, and the variable step size MPPT method are verified by the following experimental results.

7.6.1. Verification of the Boost-Half-Bridge DC-DC Converter

The experimental waveforms of the boost-half-bridge DC-DC converter are obtained in Figure 7.9.

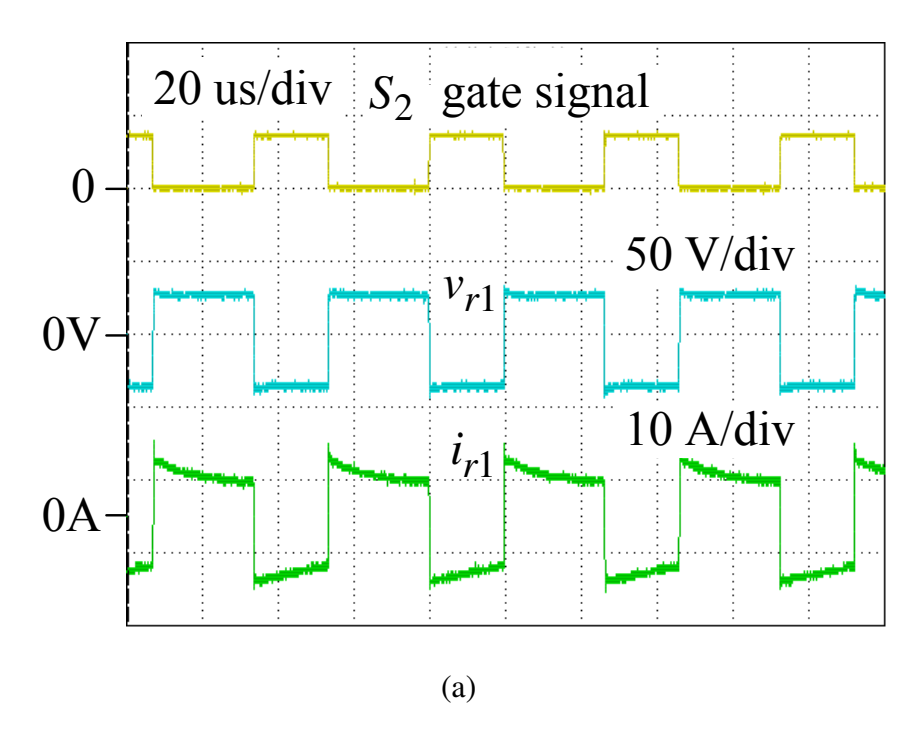
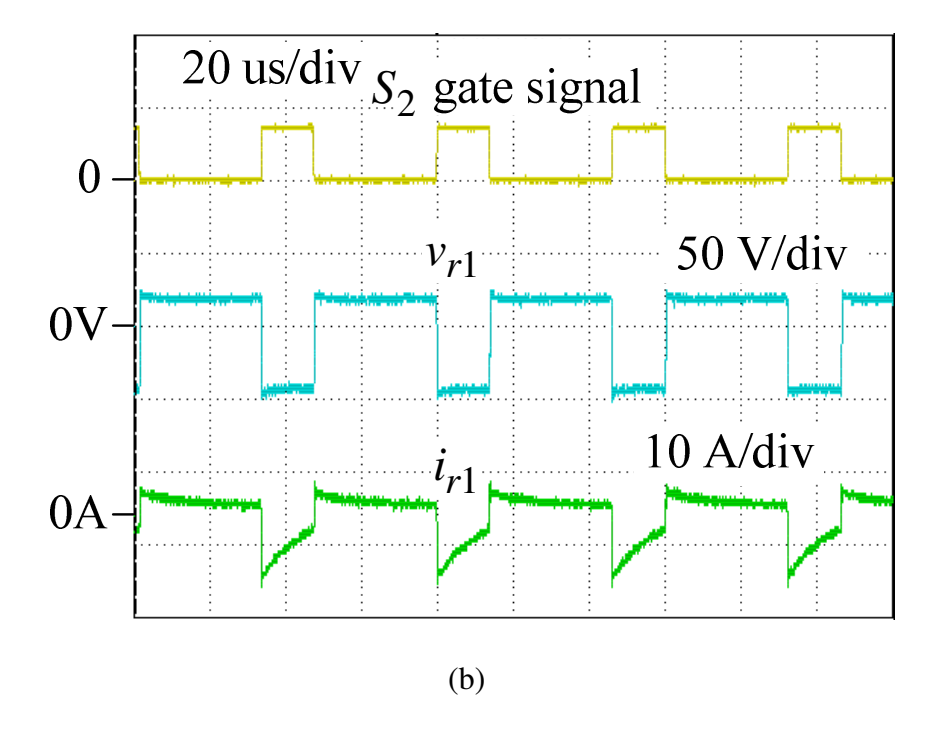


Figure 7.9. Transformer voltage and current responses of the boost-half-bridge converter. (a) $P_{pv} = 190 \text{ W}$, $v_{pv} = 36.8 \text{ V}$. (b) $P_{pv} = 74 \text{ W}$, $v_{pv} = 44.5 \text{ V}$.

Figure 7.9 (cont'd).



In Figure 7.9(a), the PV voltage is regulated to 36.8 V and the PV power is 190 W. In Figure 7.9(b), the PV voltage and power are 44.5 V and 84 W, respectively. The transformer leakage inductance is designed as very small such that when S_1 and S_2 are turning on/off, the transformer current reverses and reaches the opposite peak rapidly. From Figure 7.9(a), the transformer current shape is quite "square" at high power, indicating a small peak-to-average ratio or low conduction losses.

The conversion efficiency of the boost-half-bridge main circuit is summarized in Figure 7.10. It is measured based on the different input PV voltages and power levels. High efficiency $(97.0\%\sim98.2\%)$ is achieved over the entire input voltage range $(30 \text{ V}\sim50 \text{ V})$ when the PV power is above 30% of the nominal value. The peak efficiency is measured as 95.6% at $P_{pv}=160 \text{ W}$ and $v_{pv}=40 \text{ V}$ when the full-bridge inverter is included.

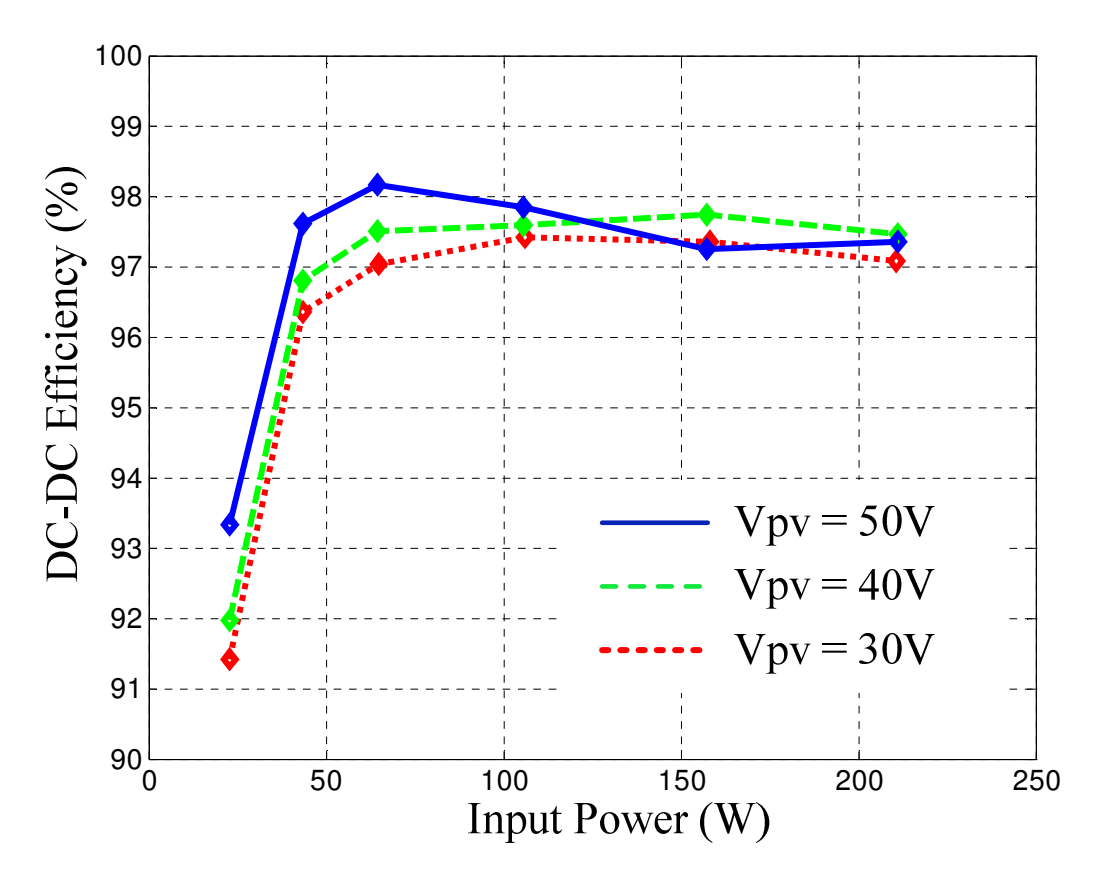


Figure 7.10. Efficiency chart of the boost-half-bridge DC-DC converter.

7.6.2. Verification of the Grid Current Dynamic Response

Figure 7.11 demonstrates the transient waveforms when the whole system is running and partial shading is suddenly applied to the PV module in order to generate an abrupt change of the input PV power. It can be observed that after the partial shading occurs, the LVS DC link voltage is still regulated stiffly and the power injected to the grid precisely follows the input power trajectory.

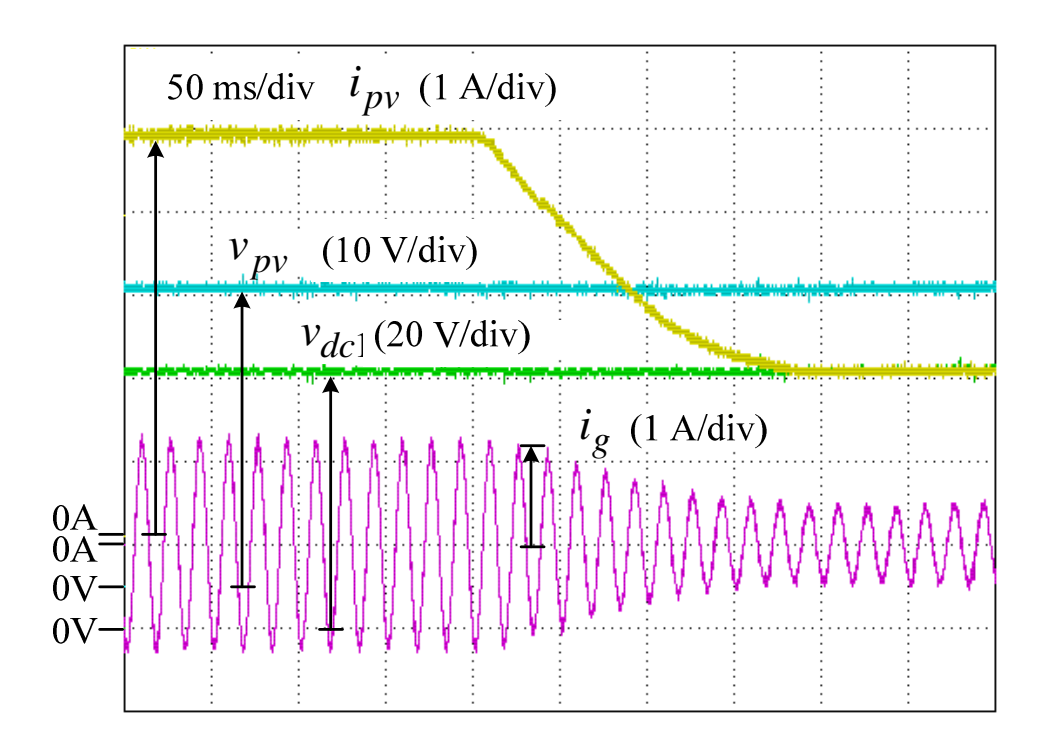
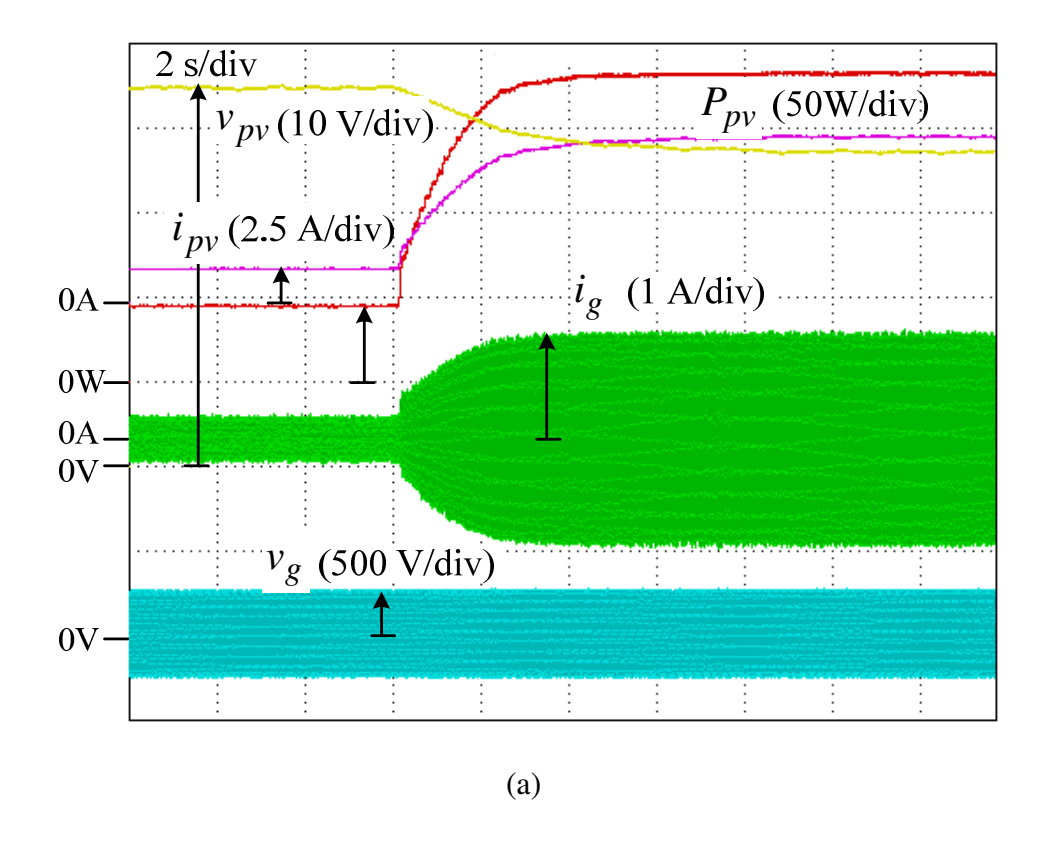


Figure 7.11. Transient responses of the micro inverter system under solar irradiance change $(840 \text{ W/m}^2 \text{ to partial shading}).$

7.6.3. Verification of the Variable Step-Size MPPT

As discussed in Chapter V, the variable step size MPPT with ramp-changed PV voltage reference is implemented experimentally. Thanks to the ramp-changed PV voltage, the system is able to run correctly and reliably. The MPPT response under solar irradiance change (partial shading to 880 W/m^2) is presented in Figure 7.12. It can be seen that the MPPT employs a larger step size 0.3 V right after the solar irradiance change to achieve fast tracking speed, and then shifts to a smaller step size 0.1 V for fine tracking. The steady state performance of the MPPT is verified by Figure 7.13. The PV voltage oscillates around the MPP within a very small range (0.5 V) at the steady state, providing an MPPT efficiency higher than 99.7%.

Figure 7.14 shows the fabricated prototype of the 210 W PV micro inverter.



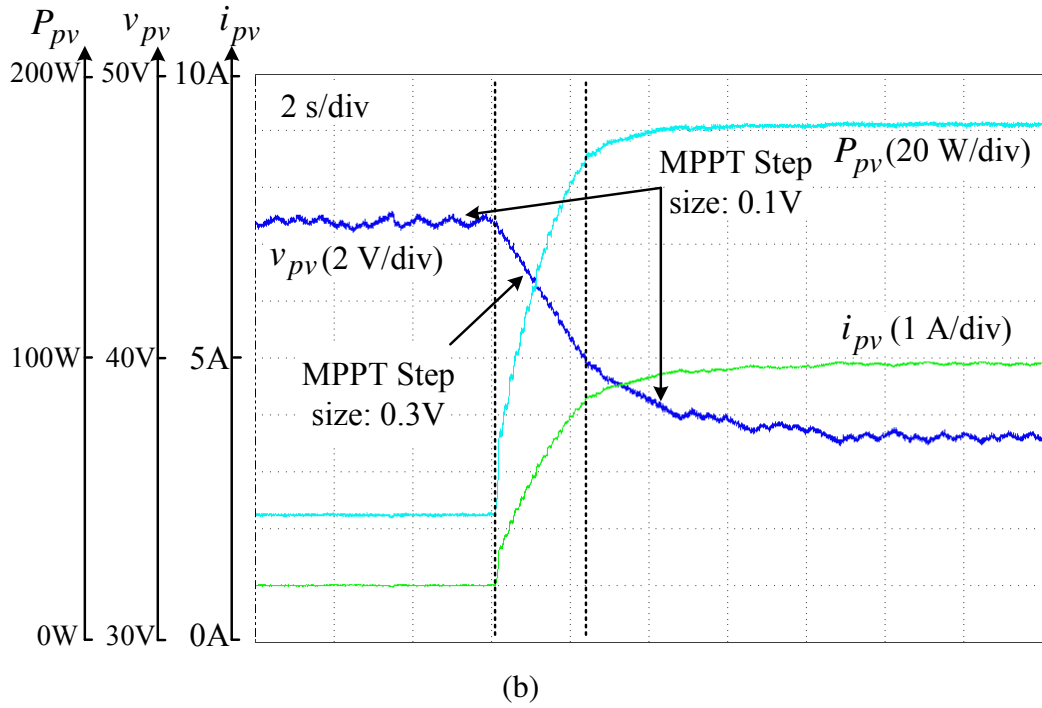
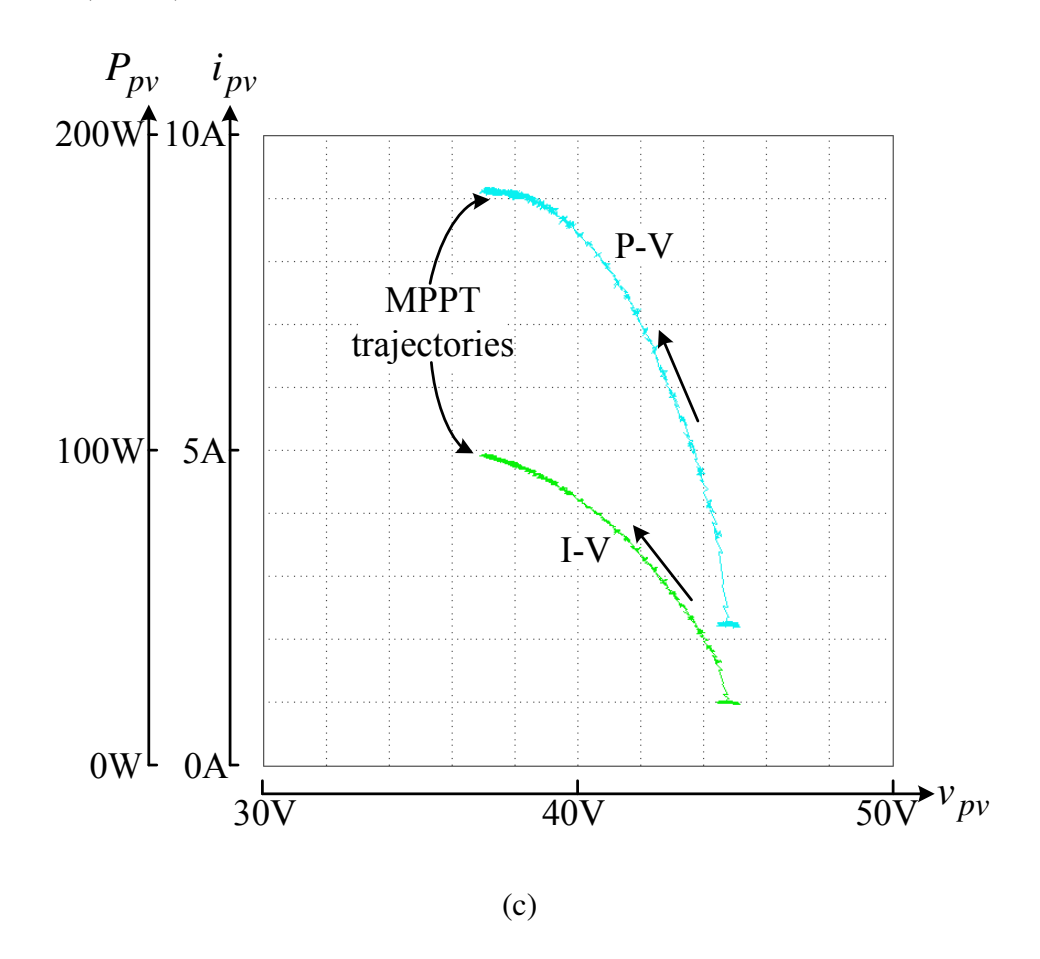
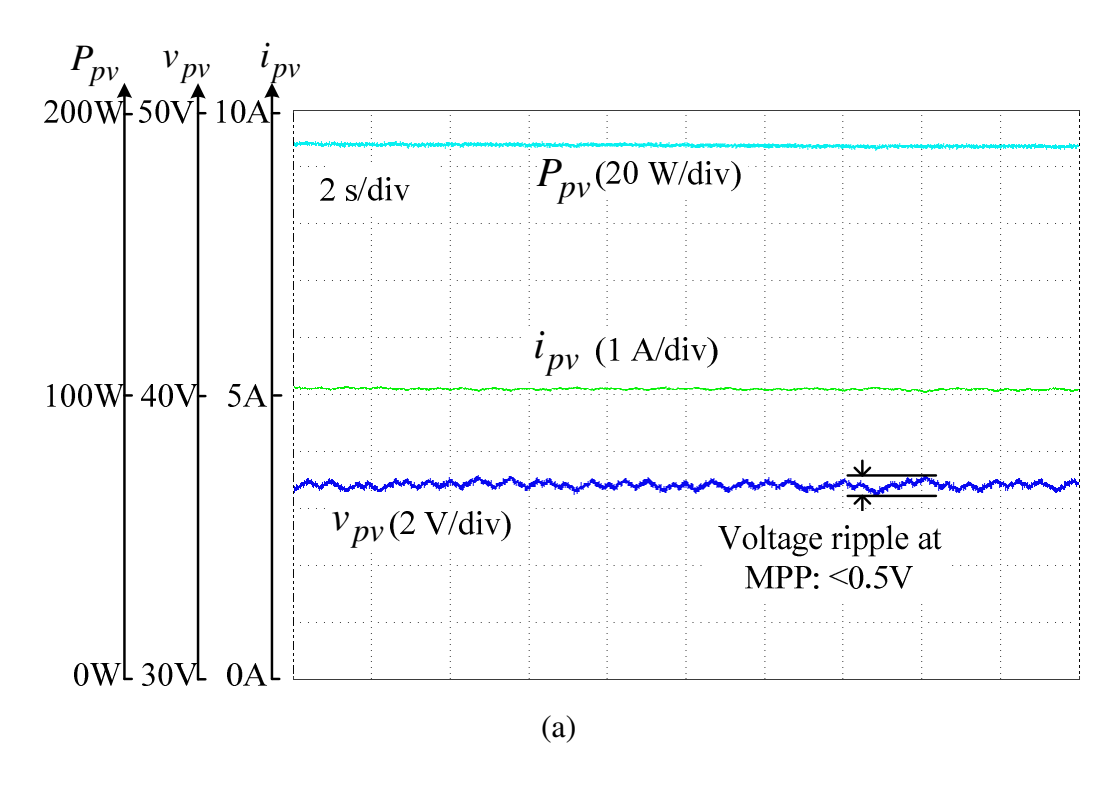


Figure 7.12. MPPT of the PV micro inverter system under solar irradiance change. (a) Input and output waveforms under solar irradiance change (partial shading to 880 W/m² @ 50°C). (b) Zoomed-in PV voltage, PV current and PV power in (a). (c) MPPT trajectories (P-V and I-V curves).

Figure 7.12 (cont'd).





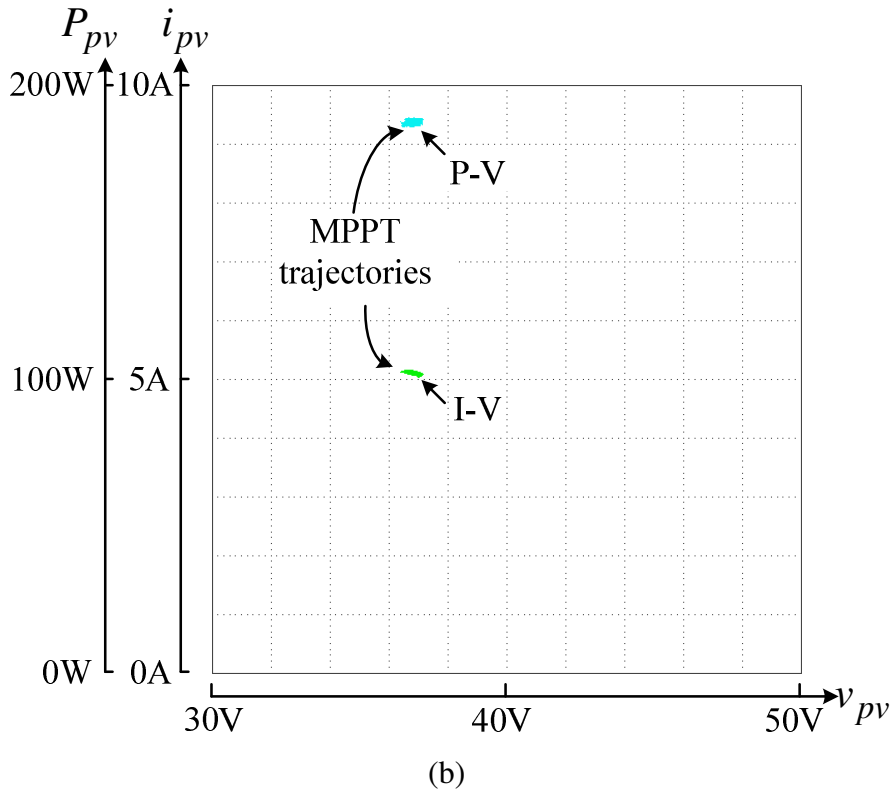


Figure 7.13. MPPT of the PV micro inverter system at the steady state. (a) PV voltage, PV current and PV power (solar irradiance: $900~\text{W/m}^2~\text{@}~50^\circ\text{C}$) (b) MPPT trajectories (P-V and I-V curves).



Figure 7.14. Prototype of the boost-half-bridge PV micro inverter

7.7. Summary

A novel boost-half-bridge micro inverter for grid-connected photovoltaic systems has been presented in this chapter. The repetitive control scheme discussed in Chapter 5 is utilized here for grid current regulation. The operation principles and dynamics of the boost-half-bridge DC-DC converter were analyzed and a customized MPPT control method was developed correspondingly. Simulation and experimental results of the 210 W prototype were shown to verify the circuit operation principles, current control and MPPT method.

Thanks to the minimal use of semiconductor devices, circuit simplicity and easy control, the boost-half-bridge PV micro inverter possesses promising features of low cost and high reliability. According to the experimental results, high efficiency (97.0%~98.2%) is obtained with the boost-half-bridge DC-DC converter over a wide operation range. Moreover, the current

injected to the grid is regulated precisely and stiffly. Finally, the customized MPPT method that generates a ramp-changed reference for the PV voltage regulation guarantees a correct and reliable operation of the PV micro inverter system. The variable step size technique provides a fast MPP tracking speed and a high MPPT efficiency (> 99.7%).

Chapter 8. Conclusion and Recommendation

8.1. Conclusion

This dissertation presents advanced inverter control techniques for uninterruptible power supply (UPS) systems and grid-connected renewable energy systems. This work has made the following contributions:

- Multi-loop control strategies have been designed and implemented with a three-phase four-wire online double conversion UPS system. A novel DC link voltage balancing technique with minimal required voltage sensors has been proposed. Good voltage regulation, input power factor correction, and fast dynamic response have been observed with linear load. When the system feeds nonlinear load, harmonic distortions can hardly be rejected, inspiring the study of more advanced control techniques.
- A high performance repetitive control strategy has been proposed for three-phase UPS inverters. A 4th-order linear phase IIR filter is proposed and synthesized for the repetitive control. Compared to the FIR filters which are widely used in the existing repetitive controllers, the proposed IIR filter exhibits great pass band flatness and a much faster high frequency roll-off rate. Benefiting from this feature, the proposed controller is able to eliminate harmonic distortions up to the 19th order. Hence, ultra low THD is guaranteed with the output voltage regulation even under heavily distorted nonlinear loads.
- A further improved synchronous-frame repetitive control approach for three-phase UPS inverterss is proposed. By placing the repetitive controller into three deliberately selected

synchronous rotating frames, all the odd harmonic distortions can be rejected. Conventional stationary-frame repetitive control schemes suffer the drawback of slow dynamic responses caused by the long control delay, but the proposed method minimizes the time delay to 1/6 of the fundamental period and significantly enhances the dynamic responses without sacrificing any steady state performance.

- Design and control of single-phase grid-connected inverter, which is usually as the grid-interfacing part in a photovoltaic inverter system, is studied. The feasibility of using a high-resonance-frequency LCL filter is investigated in order to achieve reduced filter size and cost. A proportional plus repetitive current control strategy is proposed for the grid current and power factor regulation. The advantages of the proposed current controller are verified by comparing to a conventional proportional + resonant controller.
- when a grid-connected inverter is interfacing a non-ideal infinite grid, in particular, a grid with complex impedance that is not negligible, careful modeling is required in order to design a stable and reliable inverter controller. A specific case of an offshore wind farm system is studied and the resonances issues caused by the parasitic inductance and capacitance of the incorporated long transmission cable are identified. A single-phase 120Vac emulator system is built for analysis and verification purposes. A cascaded notch filter based active damping control scheme is proposed for the offshore wind farm system. Verified on the emulator system, the proposed controller can effectively damp the resonances from the transmission cable. The impact from the cable parameters uncertainty to the control stability is studied and an auto damping technique is proposed to automatically measure the system resonance frequencies for more accurate notch filter frequency selection.

• A boost-half-bridge photovoltaic micro inverter associated with the control system has been proposed. The dynamic behavior of the front-end boost-half-bridge DC-DC converter has been examined. A customized MPPT technique which generates a rampchanged voltage command has been proposed and verified. High steady state MPPT efficiency and fast tracking speed during solar irradiance change have been obtained.

8.2. Recommendation for Future Work

The synchronous frame repetitive controller for three phase UPS systems introduced in Chapter 4 requires six times of dq transformation, which somehow consumes more resources in the digital signal processor compared with the stationary frame control scheme. However, the stationary frame repetitive control scheme usually requires much large delay which sacrifices the dynamic response. Hence, it is more attractive if the proposed synchronous frame control scheme can be equivalently transformed to a stationary counterpart, which should have the same steady state and dynamic performance but much less calculations. This work has not been done either in this dissertation or by other researchers. Therefore, it is recommended to do further research work on this.

In an offshore grid-connected wind farm system, which is discussed in Chapter 6, the long undersea cable parameters are typically of some extent of uncertainty and discrepancies must exist between the theoretical calculation and the reality. It is very desirable to have a reliable and robust auto compensation control scheme which can effectively and accurately deal with the resonance issues introduced from the cable transmission line effect. This dissertation proposes an auto damping scheme and has made some brief discussions and simulations. It is recommended to do further investigation on the auto compensation including more thorough analysis and experimental verifications.

In Chapter 7, the boost half bridge micro inverter system has limited control bandwidth due to the requirement for avoiding the transformer magnetizing inductor saturation. More research work can be done here to increase the DC-DC converter control bandwidth.

BIBLIOGRAPHY

BIBLIOGRAPHY

- [1] N. M. Abdel-Rahim and J. E. Quaicoe, "Analysis and design of a multiple feedback loop control strategy for single-phase voltage-source UPS inverters," *IEEE Transactions on Power Electronics*, vol. 11, no. 4, pp. 532-541, July. 1996.
- [2] S. J. Chiang, K. Chai, and Y. Tzou, "Design and implementation of single-phase three-wire rectifier-inverter for UPS applications," in *IEEE 2004 PESC*, 2004, pp. 1927-1932.
- [3] P. C. Loh, M. J. Newman, D. N. Zmood, and D. G. Holmes, "A comparative analysis of multiloop voltage regulation strategies for single and three-phase UPS systems," *IEEE Transactions on Power Electronics*, vol. 18, no. 5, pp. 1176-1185, Sep. 2003.
- [4] F. Kamran and T. G. Habetler, "A Novel on-line UPS with universal filtering capabilities," *IEEE Transactions on Power Electronics*, vol. 13, no. 3, pp. 410-418, May. 1998.
- [5] E. Kim, J. Kwon, J. Park, and B. Kwon, "Practical control implementation of a three-to single-phase online UPS," *IEEE Transactions on Industrial Electronics*, vol. 55, no. 8, pp. 2933-2942, August. 2008.
- [6] M. J. Ryan, W. E. Brumsickle, and R. D. Lorenz, "Control topology options for single-phase UPS inverters," *IEEE Transactions on Industry Applications*, vol. 33, no. 2, pp. 493-501, Mar/Apr. 1997.
- [7] S. B. Bekiarov and A. Emadi, "Uninterruptible power supplies: classification, operation, dynamics, and control," in *IEEE 2002 APEC*, 2002, vol. 1, pp. 597-604.
- [8] T. Kawabata, T. Miyashita, and Y. Yamamoto, "Dead beat control of three phase PWM inverter," *IEEE Trans. Power Electron.*, vol. 5, no. 1, pp. 21–28, Jan. 1990.
- [9] J. Rodríguez, J. Pontt, C. Silva, P. Correa, P. Lezana, P. Cortés, and U. Ammann, "Predictive current control of a voltage source inverter," *IEEE Trans. Ind. Electron.*, vol. 54, no. 1, pp. 495–503, Feb. 2007.
- [10] S. Kouro, P. Cortes, R. Vargas, U. Ammann, and J. Rodríguez, "Model Predictive Control—A Simple and Powerful Method to Control Power Converters," *IEEE Trans. Ind. Electron.*, vol. 56, no. 6, pp. 1826–1838, Jun. 2009.
- [11] R. Ghosh and G. Narayanan, "Control of three-phase, four-wire PWM rectifier," *IEEE Trans. Power Electron.*, vol. 23, no. 1, pp. 96–106, Jan. 2008.

- [12] P. C. Loh and D. G. Holmes, "Analysis of multiloop control strategies for LC/CL/LCL-filtered voltage-source and current-source inverters," *IEEE Transactions on Industry Applications*, vol. 41, no. 2, pp. 644-654, Mar/Apr. 2005.
- [13] E. Twining and D. G. Holmes, "Grid current regulation of a three-phase voltage source inverter with an LCL input filter," *IEEE Trans. Power Electron.*, vol. 18, no. 3, pp. 888–895, May 2003.
- [14] P. Mattavelli, "Synchronous-frame harmonic control for high-performance AC power supplies," *IEEE Transactions on Industry Applications*, vol. 37, no. 3, pp. 864-872, May/June. 2001.
- [15] A. V. Jouanne, P. N. Enjeti, and D. J. Lucas, "DSP control of high-power UPS systems feeding nonlinear loads," *IEEE Trans. Ind. Electron.*, vol. 43, no. 1, pp. 121–125, Feb. 1996.
- [16] S. Jiang, Y. Li, X. Lu, B. Ge and F. Z. Peng, "Practical control implementation for 100 kVA three-phase four-wire online voltage regulator," in *Proc. IEEE APEC*, Mar. 2011, pp. 749-756.
- [17] R. I. Bojoi, G. Griva, V. Bostan, M. Guerriero, F. Farina, and F. Profumo, "Current control strategy for power conditioners using sinusoidal signal integrators in synchronous reference frame," *IEEE Trans. Power Electron.*, vol. 20, no. 6, pp. 1402–1412, Nov. 2005.
- [18] D. N. Zmood, D. G. Holmes, and G. H. Bode, "Frequency-domain analysis of three-phase linear current regulators," *IEEE Transactions on Industry Applications*, vol. 37, no. 2, pp. 601-610, Mar/Apr. 2001.
- [19] B. A. Francis and W. M. Wonham, "The internal model principle for linear multivariable regulators," *Appl. Math. Opt.*, vol. 2, pp. 170-194, 1975.
- [20] S. Yang, B. Cui, F. Zhang, and Z. Qian, "A robust repetitive control strategy for CVCF inverters with very low harmonic distortion," in *Proc. IEEE APEC'07*, 2007, pp. 1673–1677.
- [21] K. Zhang, Y. Kang, J. Xiong and J. Chen, "Direct repetitive control of SPWM inverters for UPS purpose" *IEEE Trans. Power Electron.*, vol. 18, no. 3, pp. 784–792, May. 2003.
- [22] H. Deng, R. Oruganti and D. Srinivasan, "Analysis and design of iterative learning control strategies for UPS inverters," *IEEE Trans. Ind. Electron.*, vol. 54, no. 3, pp. 1739–1751, Jun. 2007.

- [23] Y.-Y. Tzou, S.-L. Jung, and H.-C. Yeh, "Adaptive repetitive control of PWM inverters for very low THD AC-voltage regulation with unknown loads," *IEEE Trans. Power Electron.*, vol. 14, no. 5, pp. 973–981, Sep. 1999.
- [24] Y.-Y. Tzou, R.-S. Ou, S.-L. Jung, and M.-Y. Chang, "High-performance programmable AC power source with low harmonic distortion using DSP-based repetitive control technique," *IEEE Trans. Power Electron.*, vol. 12, no. 4, pp. 715–725, Jul. 1997.
- [25] K. Zhou and D. Wang, "Digital repetitive learning controller for three-phase CVCF PWM inverter," *IEEE Trans. Ind. Electron.*, vol. 48, no. 4, pp. 820–830, Aug. 2001.
- [26] Y. Ye, K. Zhou, B. Zhang, D. Wang, and J. Wang, "High-performance repetitive control of PWM DC-AC converters with real-time phase-lead FIR filter," *IEEE Transactions on. Circuits and Systems–II: Express Briefs*, vol. 53, no. 8, pp. 768–772, Aug. 2006.
- [27] K. Zhou, K. Low, D. Wang, F. Luo, B. Zhang and Y. Wang, "Zero-phase odd-harmonic repetitive controller for a single-phase PWM inverter," *IEEE Trans. Power Electron.*, vol. 21, no. 1, pp. 193–201, Jan. 2006.
- [28] B. Zhang, D. Wang, K. Zhou, and Y. Wang, "Linear phase lead compensation repetitive control of a CVCF PWM inverter," *IEEE Trans. Ind. Electron.*, vol. 55, no. 5, pp. 1595–1602, Apr. 2008.
- [29] K. Zhou, D. Wang, B. Zhang, and Y. Wang, "Plug-in dual-mode-structure repetitive controller for CVCF PWM inverters," *IEEE Trans. Ind. Electron.*, vol. 56, no. 3, pp. 784–791, Mar. 2009.
- [30] G. Escobar, A. A. Valdez, J. Leyva-Ramos, and P. Mattavelli, "Repetitive-based controller for a UPS inverter to compensate unbalance and harmonic distortion," *IEEE Trans. Ind. Electron.*, vol. 54, no. 1, pp. 504–510, Feb. 2007.
- [31] T. Hornik and Q. C. Zhong, "A current-control strategy for voltage-source inverters in microgrids based on H∞ and repetitive control," *IEEE Trans. Power Electron.*, vol. 26, no. 3, pp. 943–952, Mar. 2011.
- [32] X. H. Wu, S. K. Panda, and J. X. Xu, "Design of a plug-in repetitive control scheme for eliminating supply-side current harmonics of three-phase PWM boost rectifier under generalized supply voltage conditions," *IEEE Trans. Power Electron.*, vol. 25, no. 7, pp. 1800–1810, Jul. 2010.
- [33] G. Escobar, M. Hernández-Gómez, P. R. Martínez and M. F. Martínez-Montejano, "A repetitive-based controller for a power factor precompensator," *IEEE Transactions on. Circuits and Systems-I: Regular Papers*, vol. 54, no. 9, pp. 1968–1976, Sep. 2007.

- [34] G. Escobar, J. Leyva-Ramos, P. R. Martínez and A. A. Valdez, "A repetitive-based controller for the boost converter to compensate the harmonic distortion of the output voltage," *IEEE Transactions on Control Systems Technolog*, vol. 13, no. 3, pp. 500–508, May. 2005.
- [35] P. Mattavelli and F. P. Marafao, "Repetitive-based control for selective harmonic compensation in active power filters," *IEEE Trans. Ind. Electron.*, vol. 51, no. 5, pp. 1018–1024, Oct. 2004.
- [36] R. Griñó, R. Cardoner, R. Costa-Castelló, and E. Fossas, "Digital repetitive control of a three-phase four-wire shunt active filter," *IEEE Trans. Ind. Electron.*, vol. 54, no. 3, pp. 1495–1503, Jun. 2007.
- [37] R. Castello, R. Grino and E. Fossas, "Odd-harmonic digital repetitive control of a single-phase current active filter," *IEEE Trans. Power Electron.*, vol. 19, no. 4, pp. 1060–1068, Jul. 2004.
- [38] G. Escobar, P. G. Hernandez-Briones, P. R. Martinez, M. Hernandez-Gomez and R. E. Torres-Olguin, "A repetitive-based controller for the compensation of 6l ± 1 harmonic components," *IEEE Trans. Ind. Electron.*, vol. 55, no. 8, pp. 3150–3158, Aug. 2008.
- [39] L. Li, L. Xie, W. Yan and Y. C. Soh, "Design of low-order linear-phase IIR filters via orthogonal projection" *IEEE Trans. Signal Processing*, vol. 47, no. 2, pp. 448–457, Feb 1999.
- [40] S. Yang, X. Ding, J. Liu and Z. Qian, "Analysis and design of a cost-effective voltage feedback control strategy for EPS inverters," in *Proc. IEEE PESC*, 2007, pp. 477–482.
- [41] S. Jiang, D. Cao, Y. Li, J. Liu and F. Z. Peng, "Low THD, fast transient, and cost-effective synchronous-frame repetitive controller for three-phase UPS inverters," *IEEE Transactions on Power Electronics*, vol. 27, no. 6, pp. 2994-3005, Jun. 2012.
- [42] S. Jiang, D. Cao and F. Z. Peng, "High performance repetitive control for three-phase CVCF PWM inverter using a 4th-order linear phase IIR filter," in *Proc. IEEE APEC*, Feb. 2012, pp. 225-231.
- [43] F. Blaabjerg, R. Teodorescu, M. Liserre, and A. Timbus, "Overview of control and grid synchronization for distributed power generation systems," *IEEE Trans. Ind. Electron.*, vol. 53, no. 5, pp. 1398–1409.

- [44] M. Liserre, T. Sauter, and J. Hung, "Integrating renewable energy sources into the smart power grid through industrial electronics," *IEEE Ind. Electron. Mag.*, vol. 4, no. 1, pp. 18–37, Mar. 2010.
- [45] R. Teodorescu, M. Liserre, and R. Rodriguez, *Grid Converters for Photovoltaic and Wind Power Systems. Hoboken, NJ: Wiley*, 2010.
- [46] M. Liserre, F. Blaabjerg, and S. Hansen, "Design and control of an LCL filter-based three-phase active rectifier," *IEEE Trans. Ind. Appl.*, vol. 41, no. 5, pp. 1281–1291, Sep./Oct. 2005.
- [47] R. Teichmann, M. Malinowski, and S. Bernet, "Evaluation of three-level rectifiers for low-voltage utility applications," *IEEE Trans. Ind. Electron.*, vol. 52, no. 2, pp. 471–481, Apr. 2005.
- [48] P. Channegowda and V. John, "Filter optimization for grid interactive voltage source inverters," *IEEE Trans. Ind. Electron.*, vol. 57, no. 12, pp. 4106–4114, Dec. 2010.
- [49] F. Blaabjerg, E. Chiarantoni, A. Dell'Aquila, M. Liserre, and S. Vegura, "Sensitivity analysis of a LCL-filter based three-phase active rectifier via a 'virtual circuit' approach," *J. Circuits, Syst., Comput.—Jubilee Special Issue on Power Electronics*, vol. 13, no. 4, pp. 665–686, Aug. 2004.
- [50] G. Shen, D. Xu, L. Cao, and X. Zhu, "An improved control strategy for grid-connected voltage source inverters with an LCL filter," *IEEE Trans. Power Electron.*, vol. 23, no. 4, pp. 1899–1906, Jul. 2008.
- [51] C. Olalla, R. Leyva, A. El Aroudi, and I. Queinnec, "Robust LQR control for PWM converters: An LMI approach," *IEEE Trans. Ind. Electron.*, vol. 56, no. 7, pp. 2548–2558, Jul. 2009.
- [52] T. Wang, Z. Ye, G. Sinha, and X. Yuan, "Output filter design for a gridinterconnected three-phase inverter," in *Proc. IEEE 34th Annu. Power Electron. Spec. Conf.*, Jun. 2003, vol. 2, pp. 779–784.
- [53] V. Blasko and V. Kaura, "A novel control to actively damp resonance in input LC filter of a three-phase voltage source converter," *IEEE Trans. Ind. Appl.*, vol. 33, no. 2, pp. 542–550, Mar./Apr. 1997.
- [54] M. Liserre, A. Dell'Aquila, and F. Blaabjerg, "Stability improvements of an LCL-filter based three-phase active rectifier," in *Proc. 33rd IEEE Annu. Power Electron. Spec. Conf.*, 2002, vol. 3, pp. 1195–1201.

- [55] A. Rahimi and A. Emadi, "Active damping in dc/dc power electronic converters: A novel method to overcome the problems of constant power loads," *IEEE Trans. Ind. Electron.*, vol. 56, no. 5, pp. 1428–1439, May 2009.
- [56] M. Liserre, R. Teodorescu, and F. Blaabjerg, "Stability of photovoltaic and wind turbine grid-connected inverters for a large set of grid impedance values," *IEEE Trans. Power Electron.*, vol. 21, no. 1, pp. 263–272, Jan. 2006.
- [57] I. J. Gabe, V. F. Montagner, and H. Pinheiro, "Design and implementation of a robust current controller for VSI connected to the grid through an LCL filter," *IEEE Trans. Power Electron.*, vol. 24, no. 6, pp. 1444–1452, Jun. 2009.
- [58] J. Dannehl, M. Liserre and F. W. Fuchs, "Filter-based active damping of voltage source converters with LCL filter," *IEEE Trans. Ind. Electron.*, vol. 58, no. 8, pp. 3623–3633, Aug. 2011.
- [59] S. Jiang and F. Z. Peng, "Repetitive current control of single-phase grid-connected inverter using a high-resonance-frequency LCL Filter," submitted to *IEEE ECCE* 2012.
- [60] S. Jiang, D. Cao, Y. Li and F. Z. Peng, "Grid-connected boost-half-bridge photovoltaic micro inverter system using repetitive current control and maximum power point tracking," *IEEE Transactions on Power Electronics*, vol. 27, no. 11, pp. 4711-4722, Nov. 2012.
- [61] S. B. Kjaer, J. K. Pedersen and F. Blaabjerg "A review of single-phase grid-connected inverters for photovoltaic modules," *IEEE Transactions on Industry Applications*, vol. 41, no. 5, pp. 1292-1306, Sep/Oct. 2005.
- [62] Q. Li and P. Wolfs, "A review of the single phase photovoltaic module integrated converter topologies with three different DC link configurations," *IEEE Transactions on Power Electronics*, vol. 23, no. 3, pp. 1320-1333, May. 2008.
- [63] R. Wai and W. Wang, "Grid-connected photovoltaic generation system," *IEEE Transactions on Circuits and Systems-I*, vol. 55, no. 3, pp. 953-963, Apr. 2008.
- [64] M. Andersen and B. Alvsten, "200 W low cost module integrated utility interface for modular photovoltaic energy systems," in *Proc. IEEE IECON*, 1995, pp. 572–577.
- [65] A. Lohner, T.Meyer, and A. Nagel, "A new panel-integratable inverter concept for grid-connected photovoltaic systems," in *Proc. IEEE ISIE*, 1996, pp. 827–831.
- [66] D. C. Martins and R. Demonti, "Grid connected PV system using two energy processing stages," in *Proc. IEEE Photovoltaic Specialists Conf.*, 2002, pp. 1649-1652.

- [67] T. Shimizu, K. Wada, and N. Nakamura, "Flyback-type single-phase utility interactive inverter with power pulsation decoupling on the dc input for an ac photovoltaic module system," *IEEE Trans. Power Electron.*, vol. 21, no. 5, pp. 1264–1272, Sep. 2006.
- [68] N. Kasa, T. Iida, and L. Chen, "Flyback inverter controlled by sensorless current MPPT for photovoltaic power system," *IEEE Trans. Ind. Electron.*, vol. 52, no. 4, pp. 1145–1152, Aug. 2005.
- [69] Q. Li and P.Wolfs, "A current fed two-inductor boost converter with an integrated magnetic structure and passive lossless snubbers for photovoltaic module integrated converter applications," *IEEE Trans. Power Electron.*, vol. 22, no. 1, pp. 309–321, Jan. 2007.
- [70] S. B. Kjaer and F. Blaabjerg, "Design optimization of a single phase inverter for photovoltaic applications," in *Proc. IEEE PESC*, 2003, pp. 1183–1190.
- [71] H. Li, F. Z. Peng and J. S. Lawler, "Modeling, simulation, and experimental verification of soft-switched bi-directional dc-dc converters," in *Proc. IEEE APEC*, 2001, pp. 736–742.
- [72] F. Z. Peng, H. Li, G. Su and J. S. Lawler, "A new ZVS bidirectional DC–DC converter for fuel cell and battery application," *IEEE Trans. Power Electron.*, vol. 19, no. 1, pp. 54–65, Jan. 2004.
- [73] H. Li and F. Z. Peng, "Modeling of a new ZVS bi-directional dc-dc converter," *IEEE Transactions on Aerospace and Electronic Systems*, vol. 40, no. 1, pp. 272–283, Jan. 2004.
- [74] D. Liu and H. Li, "A ZVS bi-directional DC–DC converter for multiple energy storage elements," *IEEE Trans. Power Electron.*, vol. 21, no. 5, pp. 1513–1517, Sep. 2006.
- [75] C. Yoon, J. Kim and S. Choi, "Multiphase DC–DC converters using a boost-half-bridge cell for high-voltage and high-power applications," *IEEE Trans. Power Electron.*, vol. 26, no. 2, pp. 381–388, Feb. 2011.
- [76] E. Koutroulis, K. Kalaitzakis, and N. C. Voulgaris, "Development of a microcontroller-based, photovoltaic maximum power point tracking control system," *IEEE Trans. Power Electron.*, vol. 16, no. 21, pp. 46–54, Jan. 2001.
- [77] A. K. Abdelsalam, A. M. Massoud, S. Ahmed and P. Enjeti, "High-performance adaptive perturb and observe MPPT technique for photovoltaic-based microgrids," *IEEE Trans. Power. Electron.*, vol. 26, no. 4, pp. 1010–1021, Apr. 2011.
- [78] N. Femia, G. Petrone, G. Spagnuolo, and M. Vitelli, "Optimization of perturb and observe maximum power point tracking method," *IEEE Trans. Power Electron.*, vol. 20, no. 4, pp. 963–973, Jul. 2005.

- [79] N. Femia, G. Petrone, G. Spagnuolo, and M. Vitelli, "A technique for improving P&O MPPT performances of double-stage grid-connected photovoltaic systems," *IEEE Trans. Ind. Electron.*, vol. 56, no. 11, pp. 4473–4482, Nov. 2009.
- [80] Y.-C. Kuo, T.-J. Liang, and J.-F. Chen, "Novel maximum-power-pointtracking controller for photovoltaic energy conversion system," *IEEE Trans. Ind. Electron.*, vol. 48, no. 3, pp. 594–601, Jun. 2001.
- [81] Y. H. Lim and D. C. Hamill, "Simple maximum power point tracker for photovoltaic arrays," *Electron. Lett.*, vol. 36, pp. 997–999, May 2000.
- [82] H. Patel and V. Agarwal, "MPPT scheme for a PV-fed single-phase single-stage grid-connected inverter operating in CCM with only one current sensor," *IEEE Trans. Energy Conv.*, vol. 24, no. 1, pp. 256–263, Mar. 2009.
- [83] S. Jain and V. Agarwal, "Comparison of the performance of maximum power point tracking schemes applied to single-stage grid-connected photovoltaic systems," *IET Electr. Power Appl.*, vol. 1, no. 5, pp. 753–762, Sep. 2007.
- [84] T. Esram and P. L.Chapman, "Comparison of photovoltaic arraymaximum power point tracking techniques," *IEEE Trans. Energy Conv.*, vol. 22, no. 2, pp. 439–449, Jun. 2007.
- [85] P. Bresesti, W. L. Kling, R. L. Hendriks and R. Vailati, "HVDC Connection of Offshore Wind Farms to the Transmission System," *IEEE Transactions on Energy Conversion*, vol 22, no. 1, pp. 37-43, Mar. 2007.
- [86] C. Meyer, M. Höing, A. Peterson and R. W. De Doncker, "Control and Design of DC Grids for Offshore Wind Farms," *IEEE Trans. Ind. Appl.*, vol. 43, no. 6, pp. 1475–1482, Nov./Dec. 2007.
- [87] S. M. Muyeen, R. Takahashi and J. Tamura, "Operation and Control of HVDC-Connected Offshore Wind Farm," *IEEE Transactions on Sustainable Energy*, vol. 1, no. 1, pp. 30-37, Apr. 2010.
- [88] X. I. Koutiva, T. D. Vrionis, N. A. Vovos and G. B. Giannakopoulos, "Optimal Integration of an Offshore Wind Farm to a Weak AC Grid," *IEEE Transactions on Power Delivery*, vol. 21, no. 2, pp. 987-994, Apr. 2006.
- [89] C-J. Chou, Y-K. Wu, G-Y. Han and C-Y. Lee, "Comparative Evaluation of the HVDC and HVAC Links Integrated in a Large Offshore Wind Farm—An Actual Case Study in Taiwan," *IEEE Trans. Ind. Appl.*, vol. 48, no. 5, pp. 1639–1648, Sep./Oct. 2012.

- [90] J. L. Agorreta, M. Borrega, J. L'opez and L. Marroyo, "Modeling and Control of N-Paralleled Grid-Connected Inverters With LCL Filter Coupled Due to Grid Impedance in PV Plants," *IEEE Transactions on Power Electronics*, vol. 26, no. 3, pp. 770-785, Mar. 2011.
- [91] M. Chinchilla, S. Arnaltes and J. C. Burgos, "Control of Permanent-Magnet Generators Applied to Variable-Speed Wind-Energy Systems Connected to the Grid," *IEEE Transactions on Energy Conversion*, vol 21, no. 1, pp. 130-135, Mar. 2006.
- [92] E. Twining and D. G. Holmes, "Grid current regulation of a three-phase voltage source inverter with an LCL input filter," *IEEE Trans. Power. Electron.*, vol. 18, no. 3, pp. 888–895, May. 2003.
- [93] J. Dannehl, C. Wessels and F. W. Fuchs, "Limitations of Voltage-Oriented PI Current Control of Grid-Connected PWM Rectifiers With LCL Filters," *IEEE Trans. Ind. Electron.*, vol. 56, no. 2, pp. 380–388, Feb. 2009.
- [94] X. Wang, X. Ruan, S. Liu and C. K. Tse, "Full Feedforward of Grid Voltage for Grid-Connected Inverter With LCL Filter to Suppress Current Distortion Due to Grid Voltage Harmonics," *IEEE Trans. Power Electron.*, vol. 25, no. 12, pp. 3119–3127, Dec. 2010.
- [95] J. W. Phinney, D. J. Perreault, and J. H. Lang, "Synthesis of lumped transmission line analogs," *IEEE Transactions on Power Electronics*, vol. 22, Issue 4, pp. 1531-1542, July 2007.
- [96] S. Jiang and F. Z. Peng, "Transmission-line theory based distributed Z-source networks for power conversion," in *Proc. of IEEE APEC 2011*, pp. 1138-1145, 2011.
- [97] J. M. Carrasco, L. G. Franquelo, J. T. Bialasiewicz, E. Galvan, R. C. P. Guisado, Ma A. M. Prats, J. I. Leon, and N. Moreno-Alfonso, "Power-Electronic Systems for the Grid Integration of Renewable Energy Sources: A Survey," *Industrial Electronics, IEEE Transactions on*, vol. 53, no. 4, pp. 1002-1016, 2006.
- [98] S. B. Kjaer, J. K. Pedersen, and F. Blaabjerg, "A review of single-phase grid-connected inverters for photovoltaic modules," *Industry Applications, IEEE Transactions on*, vol. 41, no. 5, pp. 1292-1306, 2005.
- [99] N. Flourentzou, V. G. Agelidis, and G. D. Demetriades, "VSC-Based HVDC Power Transmission Systems: An Overview," *Power Electronics, IEEE Transactions on*, vol. 24, no. 3, pp. 592-602, 2009.
- [100]B. Bolsens, K. De Brabandere, J. Van den Keybus, J. Driesen, and R. Belmans, "Model-based generation of low distortion currents in grid-coupled PWM-inverters using an LCL

- output filter," *Power Electronics, IEEE Transactions on*, vol. 21, no. 4, pp. 1032-1040, 2006.
- [101] T. Abeyasekera, C. M. Johnson, D. J. Atkinson, and M. Armstrong, "Suppression of line voltage related distortion in current controlled grid connected inverters," *Power Electronics, IEEE Transactions on*, vol. 20, no. 6, pp. 1393-1401, 2005.
- [102] Liu Fei, Zhou Yan, Duan Shanxu, Yin Jinjun, Liu Bangyin, and Liu Fangrui, "Parameter Design of a Two-Current-Loop Controller Used in a Grid-Connected Inverter System With LCL Filter," *Industrial Electronics, IEEE Transactions on*, vol. 56, no. 11, pp. 4483-4491, 2009.
- [103] S. Mariethoz and M. Morari, "Explicit Model-Predictive Control of a PWM Inverter With an LCL Filter," *Industrial Electronics, IEEE Transactions on*, vol. 56, no. 2, pp. 389-399, 2009.
- [104] Yen Chu-Sun, Z. Fazarinc, and R. L. Wheeler, "Time-domain skin-effect model for transient analysis of lossy transmission lines," *Proceedings of the IEEE*, vol. 70, no. 7, pp. 750-757, 1982.
- [105] R. Teodorescu, F. Blaabjerg, M. Liserre, and P. C. Loh, "Proportional-resonant controllers and filters for grid-connected voltage-source converters," *Electric Power Applications, IEE Proceedings* -, vol. 153, no. 5, pp. 750-762, 2006.
- [106] S. Zhang, S. Jiang, X. Lu, B. Ge and F. Z. Peng, "Resonance Issues and Damping Techniques for Grid-connected Inverters with Long Transmission Cable," *IEEE Transactions on Power Electronics*, vol. 29, no. 1, pp. 110-120, Jan. 2014.
- [107] S. Jiang, S. Zhang, X. Lu, B. Ge and F. Z. Peng, "Resonance Issues and Active Damping in HVAC Grid-Connected Offshore Wind Farm," in *Proc. IEEE ECCE*, Sep. 2013.
- [108] S. Zhang, S. Jiang, X. Lu, B. Ge and F. Z. Peng, "Auto-tuning based Resonance Damping of Gridconnected Voltage Source Inverters with Long Transmission Cable," in *Proc. IEEE ECCE*, Sep. 2013.